

# **Design and Characterisation Studies of Resistive Plate Chambers**

Submitted in partial fulfillment of the requirements  
for the degree of  
**Doctor of Philosophy**

by

**Satyanarayana Bheesette**  
**(Roll No. 04412701)**

Supervisors

**Prof. Raghava Varma, IIT Bombay**  
**Prof. Naba Mondal, TIFR, Mumbai**



**Department of Physics**  
**INDIAN INSTITUTE OF TECHNOLOGY BOMBAY, INDIA**  
**2009**



## **Dedicated to**

**My elder brother Shri Bheesette Venkataramana**

*... he vetoed our family's resolution during my early school years,  
proposing that I discontinue my studies and work to help raise family's meager income. Else ...*



# **Thesis Approval**

Thesis entitled **Design and Characterisation Studies of Resistive Plate Chambers** by **Satyanarayana Bheesette** is approved for the degree of **Doctor of Philosophy**.

## **Examiners**

(1) \_\_\_\_\_

(2) \_\_\_\_\_

## **Supervisors**

(1) \_\_\_\_\_

(2) \_\_\_\_\_

## **Chairperson**

\_\_\_\_\_

Date : \_\_\_\_\_

Place: \_\_\_\_\_



# **Declaration**

I declare that this written submission represents my ideas in my own words and where others' ideas or words have been included, I have adequately cited and referenced the original sources. I also declare that I have adhered to all principles of academic honesty and integrity and have not misrepresented or fabricated or falsified any idea/data/fact/source in my submission. I understand that any violation of the above will be cause for disciplinary action by the Institute and can also evoke penal action from the sources which have thus not been properly cited or from whom proper permission has not been taken when needed.

---

(Signature)

**Satyanarayana Bheesette**

---

(Name of the student)

**04412701**

---

(Roll number)

Date: \_\_\_\_\_



**INDIAN INSTITUTE OF TECHNOLOGY BOMBAY, INDIA**  
**CERTIFICATE OF THE COURSE WORK**

This is to certify that **Mr. Satyanarayana Bheesette** was admitted to the candidacy of the Ph.D. degree on **31.07.2005** after successfully completing all the courses required for the Ph.D. Degree Programme. The details of the course work are given below:

| Sr. No. | Course No. | Course Name   | Credits |
|---------|------------|---|---------|
| 1.      | PH403      | Quantum Mechanics I                                 | 8.0     |
| 2.      | PH801      | Classical Methods of Particles and Fields           | 8.0     |
| 3.      | PHs801     | Seminar   | 4.0     |
| 4.      | PH802      | Quantum and Statistical Mechanics: Advanced Methods | 8.0     |
| 5.      | PH803      | Computer Programming and Numerical Methods          | 8.0     |
| 6.      | PH804      | Laboratory Techniques                               | 8.0     |
| 7.      | HS699      | Communication and Presentation skills               | 4.0     |
| Total   |            |   | 48.0    |

Dy. Registrar (Academic)

IIT Bombay

Dated: \_\_\_\_\_



## Abstract

Important developments have occurred recently in neutrino physics and neutrino astronomy. Oscillations of neutrinos, and the inferred evidence that neutrinos have mass, are likely to have far-reaching consequences. This discovery has come from the study of neutrinos from the Sun and those produced in interactions of cosmic rays with the earth's atmosphere. The pioneering Homestake Mine Neutrino Experiment in the USA, the gigantic Super-Kamiokande detector and the KamLAND detector in Japan, the heavy-water detector at the Sudbury Neutrino Observatory in Canada, and a few other laboratories, together, have contributed in a very fundamental way to our knowledge of neutrino properties and interactions. Impelled by these discoveries and their implications for the future of particle physics, plans have been made world-wide, for new neutrino detectors, neutrino factories and long base-line neutrino experiments.

Indian scientists were pioneers in atmospheric neutrino experiments. In fact, neutrinos produced by cosmic ray interactions in the earth's atmosphere were first detected in the deep mines of the Kolar Gold Fields (KGF) in south India in 1965. In order to revive underground neutrino experiments in India, a multi-institutional collaboration has been formed with the objective of creating an India-based Neutrino Observatory (INO).

Considering the physics possibilities and given the past experience at KGF, the INO collaboration has decided to build a magnetised Iron CALorimeter (ICAL) detector with Resistive Plate Chambers (RPCs) as the active detector elements. In the first phase of its operation, ICAL will be used for atmospheric neutrino physics with the aim of making precision measurements of the parameters related to neutrino oscillations. The detector will be magnetised to a field of about 1.3 T, enabling it to distinguish the positive and negative muons and thus identifying muon-type neutrino and anti-neutrino produced events separately. This will be useful for ICAL to provide an exciting possibility to determine the ordering of the neutrino mass levels. Finally, this detector can also be used as the far-detector of a futuristic long-base-line neutrino experiment

using the neutrino beam from a neutrino factory. Good tracking, energy and time resolutions as well as charge identification of the detecting particles are the essential capabilities of this detector. The ICAL experiment will need about 30,000 RPCs each of about 200 cm × 200 cm in area.

RPCs are fast, planar, rugged and low-cost gas detectors which are being, and will be, used extensively in a number of high energy and astro-particle physics experiments. They find applications for charged particle detection, time of flight, tracking and digital calorimetry due to their large signal amplitudes as well as excellent position and time resolutions. A dedicated R&D programme is currently underway to design, develop and characterise large area RPCs, ultimately leading to their large scale and low-cost production required for the ICAL detector. In essence, this thesis outlines the successful completion of designing, building and characterising large size RPCs, for the first time in India.

To begin with, we developed a large number of single gap glass RPCs of 30 cm × 30 cm in area, using the glass procured from local market, and studied their operation in the streamer mode (using a gas mixture of R134a : Isobutane : Argon in the ratio of 62 : 8 : 30). The results obtained from the characterisation studies of these chambers were consistent with those reported in the literature. However, we were faced with a serious problem as far as stability of their operation is concerned. They died of sudden aging when operated continuously. In order to understand this problem, we studied extensively the glass, gas and other components of the RPC detector using a number of different techniques. We subsequently fabricated a large number of RPCs of 100 cm × 100 cm in area and operated them in the avalanche mode (using a gas mixture of R134a : Isobutane : SF<sub>6</sub> in the ratio of 95.15 : 4.51 : 0.34), without facing any aging problems. These chambers show typical efficiencies of over 98% and timing resolutions of about 1 ns.

A sophisticated gas mixing and distribution system, which works on four input gases, has been designed and fabricated as part of this R&D work. It features mass flow controllers to precisely mix the gases to the required proportion and 0.3 mm diameter stainless steel capillaries to control the mixed gas into 16 pneumatically controlled output channels. We have also developed an open loop gas recovery system using fractional condensation technique and studied its performance. We have devel-

oped a suitable paint and an automated painting plant for glass electrode coating. We have also indigenously designed and fabricated polycarbonate spacers, buttons and gas nozzles which are needed to fabricate the RPC gas gaps as well as developed appropriate jigs and tools used during the RPC detector assembly and quality control.

We have subsequently designed and built a detector stack of 12 RPCs of  $100\text{ cm} \times 100\text{ cm}$  in area, along with a state-of-the-art, front-end electronics, trigger, data acquisition, control and monitoring systems. The stack is in un-interrupted operation now for about a couple of years. The stack is currently tracking about 6 cosmic ray muons per second. Some of the parameters that are monitored using this data on day to day basis are the RPC efficiencies using cosmic ray muons, absolute and relative timing resolutions as well as the stability of RPCs based on the monitoring data of the individual strip rates. Apart from studying various characteristics and long-term stability of the RPCs under test, the stack is also being used to study and optimise a number of parameters concerning the RPC gap, chamber design, gas mixture and readout electronics.

The cosmic ray muon tracks are used to build a tomography of the RPCs, which make up the detector stack. Pitch (30 mm) of the pickup strips used for the RPC readout as well as the dead space due to the button-shaped spacers (11 mm in diameter) are accurately mapped using this analysis. We have also studied the distribution of the residuals between the track and hit pick-up strip coordinates as well as the impact position distribution of the cosmic ray muons on both readout planes of RPC detectors. The width of the residual distribution was found to be as expected for pick-up strip widths of 28 mm. The average strip multiplicity for the cosmic ray muon data was also obtained to be a little over 1, again confirming to the expected value. We have also established the up-down tracking capability of the stack for charged particles, using the cosmic ray muon data.

The individual strip counting rates (or noise rates) provide an excellent measure for monitoring the long-term stability of the RPC detectors. We have also shown that the noise rates reflect the effect of 24-hour day-night variations in the ambient conditions faithfully. This opens up the possibility of gain correction of the RPCs using their noise rates.

Finally, we have recently succeeded in fabricating and testing glass RPCs of  $200\text{ cm} \times 200\text{ cm}$  in area - the designed RPCs for the ICAL detector. All the characterisation

studies that we have completed so far - including those on the effect of SF<sub>6</sub> on the RPC performance, have concluded that these chambers are performing excellently and make them a perfect choice as active detector elements for the ICAL experiment.

The thesis contains six chapters and three appendices and is organised as follows. Chapter 1 begins with a brief history of neutrinos, their description in the Standard Model of particle physics, discovery of their oscillation and inferred mass. We then outline the aims of a large number of ongoing neutrino detectors, along with their current status. Physics potential of a typical magnetised calorimeter type of neutrino detector is summarised, before describing the ICAL detector in which RPCs are going to be deployed in huge numbers. Chapter 2 is devoted to the principle of operation and detector physics of RPCs. Starting with an introduction to particle detectors, we discuss the design, principle of operation, operating modes, types and designs of RPCs. We end this chapter with a review of their applications and deployment in various ongoing and planned experiments. Chapter 3 discusses the entire research and development work involved in design, fabrication and characterisation of large area RPCs, including the problems and challenges which were overcome during the course of this work. Development of a large number of techniques, systems, components, tools and jigs needed for the above work is also highlighted. A large detector stack consisting of RPCs equipped with an indigenously developed electronics and data acquisition system was built as a prototype for the ICAL detector as well as to study the long-term stability of these devices. We describe this detector in detail in Chapter 4. Chapter 5 deals entirely with the data analysis and results from the prototype detector, beginning with a short description of a ROOT based data analysis code that we have developed. In Chapter 6, we summarise our work as well as propose future outlook in terms of deployment and readout issues of these large area RPCs, detailed device level simulations and physics analysis of muon data from the detector stack. Appendix A deals with details on neutrino oscillations. We have compiled data sheets of various materials that we have used during this work, in addition to other technical details and information together in Appendix B. Finally, the list of publications, including conference papers and technical notes resulting from this work, are included in Appendix C.

Keywords: Neutrino physics, INO, ICAL, Particle detectors, Glass Resistive Plate Chambers



# Table of Contents

|          |  |           |
|----------|--|-----------|
| <b>1</b> | <b>Introduction</b>                                | <b>1</b>  |
| 1.1      | History of neutrino . . . . .                      | 1         |
| 1.2      | Neutrino in the Standard Model . . . . .           | 2         |
| 1.3      | Neutrino oscillations . . . . .                    | 4         |
| 1.4      | Properties of neutrinos . . . . .                  | 5         |
| 1.5      | Why study neutrinos? . . . . .                     | 6         |
| 1.6      | Sources of neutrinos . . . . .                     | 7         |
| 1.7      | Status and goals of neutrino experiments . . . . . | 9         |
| 1.8      | Physics with Magnetised Iron Calorimeter . . . . . | 12        |
| 1.9      | The Magnetised Iron Calorimeter . . . . .          | 14        |
| 1.9.1    | Basic parameters . . . . .                         | 15        |
| 1.9.2    | The Magnet . . . . .                               | 17        |
| 1.9.3    | Detector readout scheme . . . . .                  | 19        |
| 1.10     | Chapter summary . . . . .                          | 20        |
| <b>2</b> | <b>Detector Physics of RPCs</b>                    | <b>21</b> |
| 2.1      | Brief history of particle detectors . . . . .      | 21        |
| 2.2      | Resistive Plate Chambers . . . . .                 | 25        |
| 2.3      | Basic principle of operation . . . . .             | 26        |
| 2.4      | Operating modes . . . . .                          | 30        |
| 2.4.1    | Avalanche Mode RPCs . . . . .                      | 32        |
| 2.4.2    | Streamer Mode RPCs . . . . .                       | 32        |
| 2.5      | Types of RPCs . . . . .                            | 34        |
| 2.5.1    | Trigger RPCs . . . . .                             | 34        |
| 2.5.2    | Timing RPCs . . . . .                              | 35        |
| 2.6      | RPC designs . . . . .                              | 35        |
| 2.6.1    | Single gap RPC . . . . .                           | 36        |
| 2.6.2    | Double gap RPC . . . . .                           | 36        |
| 2.6.3    | Multi-gap RPC . . . . .                            | 37        |
| 2.6.4    | Hybrid RPC . . . . .                               | 38        |
| 2.6.5    | Micro RPC . . . . .                                | 39        |

|          |   |            |
|----------|---|------------|
| 2.6.6    | Special RPCs . . . . .                                      | 39         |
| 2.7      | Applications and deployment . . . . .                       | 40         |
| 2.8      | Chapter summary . . . . .                                   | 42         |
| <b>3</b> | <b>Development and characterisation of RPCs</b>             | <b>43</b>  |
| 3.1      | Our early work and results . . . . .                        | 44         |
| 3.1.1    | Small RPC prototype designs and fabrication . . . . .       | 44         |
| 3.1.2    | Gas mixtures and gas system . . . . .                       | 46         |
| 3.1.3    | Cosmic ray muon telescope . . . . .                         | 47         |
| 3.1.4    | Data acquisition system . . . . .                           | 48         |
| 3.1.5    | Preliminary results . . . . .                               | 51         |
| 3.2      | Tracking of cosmic ray muons . . . . .                      | 57         |
| 3.3      | RPC aging problem . . . . .                                 | 60         |
| 3.4      | Long-term stability tests of RPCs . . . . .                 | 63         |
| 3.5      | Development of gas systems . . . . .                        | 68         |
| 3.5.1    | Overview of the gas system . . . . .                        | 69         |
| 3.5.2    | Calibration of the gas systems . . . . .                    | 74         |
| 3.6      | Gas recovery and recycling system . . . . .                 | 75         |
| 3.6.1    | Principle of operation . . . . .                            | 78         |
| 3.6.2    | Technical details of the unit . . . . .                     | 79         |
| 3.6.3    | Performance studies of the unit . . . . .                   | 81         |
| 3.7      | RPC materials and assembly procedures . . . . .             | 82         |
| 3.7.1    | Characterisation of electrode glass samples . . . . .       | 83         |
| 3.7.2    | Glass electrode coating . . . . .                           | 87         |
| 3.7.3    | Development of spacers, buttons and nozzles . . . . .       | 92         |
| 3.7.4    | Vacuum jig for RPC gas gap assembly . . . . .               | 92         |
| 3.7.5    | Studies on a suitable insulating film . . . . .             | 95         |
| 3.7.6    | Development and characterisation of pickup panels . . . . . | 96         |
| 3.7.7    | Design and development of RPC casings . . . . .             | 100        |
| 3.8      | Development of large area RPCs . . . . .                    | 100        |
| 3.9      | Development of RPCs for ICAL detector . . . . .             | 102        |
| 3.9.1    | Studies of SF <sub>6</sub> on the RPC performance . . . . . | 103        |
| 3.10     | Chapter summary . . . . .                                   | 107        |
| <b>4</b> | <b>ICAL prototype detector stack</b>                        | <b>109</b> |
| 4.1      | Assembly of 100 cm × 100 cm RPCs . . . . .                  | 110        |
| 4.2      | Construction of the detector stack . . . . .                | 111        |
| 4.3      | Segmentation of the prototype detector . . . . .            | 112        |
| 4.4      | Gas system for the prototype detector . . . . .             | 113        |
| 4.5      | Power supply and monitor systems . . . . .                  | 113        |

|          |   |            |
|----------|---|------------|
| 4.6      | Electronics and data acquisition system . . . . .           | 116        |
| 4.6.1    | Fast preamplifiers . . . . .                                | 117        |
| 4.6.2    | Analog and digital front-end electronics . . . . .          | 119        |
| 4.6.3    | Back-end control and DAQ system . . . . .                   | 120        |
| 4.7      | Validation of front-end electronics . . . . .               | 121        |
| 4.8      | Trigger schemes and the system . . . . .                    | 123        |
| 4.9      | On-line data acquisition software . . . . .                 | 126        |
| 4.10     | Ambient parameter monitor system . . . . .                  | 127        |
| 4.11     | On-line utilities and services . . . . .                    | 128        |
| 4.12     | Chapter summary . . . . .                                   | 129        |
| <b>5</b> | <b>Data analysis and results</b>                            | <b>131</b> |
| 5.1      | <i>BigStack</i> : The ROOT based software package . . . . . | 132        |
| 5.2      | Basic data analysis procedure . . . . .                     | 133        |
| 5.3      | Charge and timing studies of the RPCs . . . . .             | 134        |
| 5.4      | Muon tracking and detailed analysis . . . . .               | 137        |
| 5.4.1    | Tracking efficiencies of the RPCs . . . . .                 | 139        |
| 5.4.2    | Distribution of track impact position . . . . .             | 140        |
| 5.4.3    | Study of RPC cluster size . . . . .                         | 141        |
| 5.4.4    | Residual distribution of muon tracks . . . . .              | 142        |
| 5.4.5    | RPC <i>tomography</i> using cosmic ray muons . . . . .      | 143        |
| 5.5      | Long-term monitoring of detector stack . . . . .            | 143        |
| 5.6      | Ambient parameters and the RPC performance . . . . .        | 145        |
| 5.7      | Preliminary physics studies using muon data . . . . .       | 147        |
| 5.8      | Chapter summary . . . . .                                   | 147        |
| <b>6</b> | <b>Summary and future outlook</b>                           | <b>149</b> |
| 6.1      | Summary . . . . .   | 149        |
| 6.2      | Future outlook . . . . .                                    | 155        |
| <b>A</b> | <b>Neutrino oscillations</b>                                | <b>157</b> |
| <b>B</b> | <b>Technical information</b>                                | <b>161</b> |
| B.1      | Gases used in ICAL detector . . . . .                       | 161        |
| B.2      | Paint used in spray painting technique . . . . .            | 162        |
| B.3      | GE LEXAN polycarbonate material . . . . .                   | 162        |
| B.4      | Garware EMCL insulating film . . . . .                      | 163        |
| B.5      | Data format of the on-line DAQ software . . . . .           | 164        |
| <b>C</b> | <b>Publications and proceedings</b>                         | <b>167</b> |
| C.1      | Publications and communications . . . . .                   | 167        |

|                               |            |
|-------------------------------|------------|
| C.2 Proceedings . . . . .     | 168        |
| C.3 Technical notes . . . . . | 170        |
| <b>Bibliography</b>           | <b>171</b> |
| <b>Acknowledgements</b>       | <b>178</b> |

# List of Figures

|     |  |    |
|-----|--|----|
| 1.1 | Standard Model of Particle Physics showing the electric charge (right) and mass for each particle in MeV (top left corner). . . . .  | 3  |
| 1.2 | Schematic illustration of the status of masses and mixing of neutrino eigenstates. The flavour content is indicated by different shading; the $\nu_e$ contribution shown in the third mass eigenstate is an upper bound. The mass squared differences as obtained from the data are also shown. . . . .                    | 6  |
| 1.3 | Schematic view of a part of the ICAL detector showing its constructional details along with an RPC. . . . .  | 17 |
| 1.4 | Schematic view of one of the (three) completed ICAL detector modules along with the RPC detector handling trolleys shown on either side. The top view of the magnet coils is also shown. . . . .   | 19 |
| 2.1 | Schematic of Pestov counter [27]. . . . .  | 24 |
| 2.2 | Constructional schematic of a <i>basic</i> Resistive Plate Chamber. . . . .  | 28 |
| 2.3 | Schematic of an avalanche and the electric field variations caused by the avalanche charge carriers inside the RPC. $E_0$ is the uniform field applied across the electrodes. $E_1$ , $E_2$ and $E_3$ are the effective fields at the tip, centre and tail of the avalanche charge distribution respectively [34]. . . . . | 29 |
| 2.4 | Schematic images of the development of avalanche in an RPC [34]. . . . .   | 33 |
| 2.5 | Schematic images of the development of streamer in an RPC [34]. . . . .  | 34 |
| 2.6 | Schematic of a double gap Resistive Plate Chamber [42]. . . . .  | 37 |
| 2.7 | Schematic of a multi-gap Resistive Plate Chamber [47]. . . . .   | 38 |
| 2.8 | Schematic of a hybrid Resistive Plate Chamber [46]. . . . .  | 39 |
| 2.9 | Simplified schematic of a micro Resistive Plate Chamber [48]. . . . .  | 39 |
| 3.1 | One of the first fully assembled small area prototype RPC gas gaps (left panel) along with various RPC assembly jigs developed locally (right panel). . . . .  | 46 |
| 3.2 | Assembly scheme of scintillator paddle based cosmic muon telescope (left panel) and its signal timing chart (right panel). . . . .   | 47 |

|      |  |    |
|------|--|----|
| 3.3  | A cosmic ray muon telescope set up (left panel) and close-up view of its precise alignment along with the RPC under test (right panel). RPC is seen in bright orange colour as its pickup panels are covered with a Kapton tape. The <i>finger</i> (2 cm wide) paddle and a pair of veto paddles which surround it, are all mounted on top of the RPC. . . . . | 49 |
| 3.4  | Logic diagram of the trigger signal generation and data acquisition system. The entire system is built using off-the-shelf commercial NIM and CAMAC modules. . . . .   | 50 |
| 3.5  | Oscilloscope trace of a typical RPC pulse produced by a cosmic ray charged particle. It may be noted that this RPC signal in the streamer mode is about 70 mV in amplitude and its <i>opening width</i> is about 50 ns. . .  | 52 |
| 3.6  | Electrical representation of an RPC gas gap (left panel) [96] and its V–I characteristics (right panel). The RPC <i>turn-on</i> point at high voltage of about 8 kV may be noted. This is also the starting point of the plateau region as will be seen later. . . . .   | 53 |
| 3.7  | Two most important characteristics of glass RPCs: noise rate (left panel) and efficiency (right panel) as a function of its applied voltage. . . . .   | 54 |
| 3.8  | Charge collection linearity characteristics of glass RPCs. While the charge distributions (histograms) as a function of applied voltages are shown in the left panel, the right panel represents the charge linearity plot. . . . .  | 55 |
| 3.9  | Charge-Time correlation plot of a small glass RPC is shown in the right panel. Shown in the left panel are timing distributions (histograms) of scintillator paddle (bottom) and the RPC (top). These plots indicate comparable time resolutions for a scintillator paddle and the RPC. . . . .  | 56 |
| 3.10 | Time response (left panel) and absolute timing resolution (right panel) of a small glass RPC. . . . .  | 57 |
| 3.11 | Comparison of timing resolutions of an RPC. Shown in the left panel is the timing distribution (histogram) plot of an RPC with reference to a scintillation paddle, while in the right panel is with reference to another RPC. . . . .   | 58 |
| 3.12 | Muon tracking set up using RPC stack. Shown in the right panel is the close-up view of the stack of 10 RPCs mounted in a rack. . . . .   | 58 |
| 3.13 | Some interesting cosmic ray particle tracks recorded by a small RPC detector stack, measuring about one cubic foot. Only eight strips from one of the two detector pickup planes per RPC were instrumented in this setup. . . . .  | 60 |
| 3.14 | A few of the extracted RPC parameters from the data recorded by the stack. . . . .   | 61 |
| 3.15 | Efficiency time profile plot of an RPC undergoing the aging process. The drop in the efficiency is rather sudden. . . . .  | 62 |

|      |   |    |
|------|---|----|
| 3.16 | Noise history of two RPCs showing signs of aging. Differential noise rate is shown in the top panel, while the bottom panel shows their integrated noise. . . . .   | 63 |
| 3.17 | AFM pictures of damaged glass electrode surfaces [101]. The scans are carried out on $2\text{ }\mu\text{m} \times 2\text{ }\mu\text{m}$ areas. . . . .  | 64 |
| 3.18 | SEM pictures of damaged glass electrode surfaces (left panel). In the right panel we show SEM scan of a raw glass surface for reference. . . . .  | 64 |
| 3.19 | Long-term stability monitoring plots of $J_2$ and $J_3$ RPCs spanning over two years. Initial test data is not shown. . . . .   | 65 |
| 3.20 | Effect of temperature and relative humidity on RPC characteristics. While the behaviour chamber current is shown in the left panel, we show their effect on the RPC noise rate and efficiency in the right panel. . . . .   | 67 |
| 3.21 | Schematic diagram (left panel) and a photograph (right panel) of this first generation gas mixing and distribution system. . . . .  | 69 |
| 3.22 | Schematic diagram (left panel) and a photograph (right panel) of the second generation gas mixing and multi-channel distribution system. . . . .  | 70 |
| 3.23 | Schematic diagrams of MFC calibration schemes for the gas mixing and distribution systems. Shown in the left panel is water downward displacement method and linear gas flow method is represented in the right panel. . . . .  | 74 |
| 3.24 | MFC calibration plots using flow through tube method. Shown in the figure clock-wise starting from top left are the calibrations for R134a, Argon, Isobutane and $\text{SF}_6$ gases. . . . .   | 76 |
| 3.25 | Schematic diagrams of the purifier unit (left panel), condenser unit (middle panel) and a picture of the completely assembled gas recycling unit (right panel). . . . .   | 81 |
| 3.26 | Comparative study of Asahi Float (top left panel), Japanese (top right panel) and Modi (bottom panels) glass samples using AFM technique. All the scans are taken over a $10\text{ }\mu\text{m} \times 10\text{ }\mu\text{m}$ glass surface area. While the surface quality scale for the Asahi Float and Japanese glass is 0 - 30 nm, the scale is 0 - 200 nm in case of Modi glass. . . . . | 84 |
| 3.27 | Comparative study of Japanese, Asahi Float and Modi glass samples using SEM technique. Shown in the figure from left to right respectively, are scans at a couple of regions on each glass sample. . . . .  | 84 |
| 3.28 | Reflectance studies of various glass samples using UV radiation. Reflectivity (%) as a function of wavelength (nm) for glass samples from Asahi Float, Germany, Modi, Saint Gobian and Japan are shown. . . . .   | 85 |
| 3.29 | Comparative study of glass samples using transmittance test. . . . .  | 86 |
| 3.30 | Comparative study of density of glass samples from different manufacturers. . . . .   | 86 |

|      |   |     |
|------|---|-----|
| 3.31 | Surface resistivity plot of the graphite-based paint is shown in the left panel. The value settles to a stable value within a few days due to curing of the paint. The jig used to measure the surface resistivity is shown in the right panel. . . . .   | 88  |
| 3.32 | Prototype plant for automatic spray painting of glass sheets. While the glass plate mounted on a bed moves on X-direction, the spray gun is provided the movement in Y-direction. . . . .   | 90  |
| 3.33 | Contour plots of resistivity of 100 cm × 100 cm glass sheet painted by the automatic plant. Each division on the axes corresponds to about 6.25 cm. . . . .   | 90  |
| 3.34 | Conceptual designs of spacer (left panel), button (middle panel) and gas nozzle (right panel). Intricate details in the designs of these seemingly simple components may be noted. For example, various cut-outs and holes in the button design increase glue contact area with the glass sheets. . . . . | 93  |
| 3.35 | Vacuum jig used for assembly of gas gaps. Shown in the left panel is the conceptual diagram, while the actual set up is shown in the right panel. . . . .   | 94  |
| 3.36 | Test results of characterisation studies of various insulating film samples. . . . .  | 96  |
| 3.37 | Experimental set up for measurement of characteristic impedance of pickup strips. . . . .   | 98  |
| 3.38 | Typical signals seen on oscilloscope during measurement of characteristic impedance of pickup strips. The snapshots from left to right and clock-wise direction correspond to termination resistances of open, 100 Ω, 51 Ω, 48.2 Ω and 47 Ω respectively. . . . .   | 99  |
| 3.39 | Honeycomb panel with milled copper pickup strips shown (left panel) and partially assembled RPC using aluminum honeycomb panel. . . . .   | 101 |
| 3.40 | A fully assembled RPC of dimensions 100 cm × 100 cm along with the front-end electronics mounted (left panel) and its efficiency plateau (right panel). . . . .   | 101 |
| 3.41 | A 200 cm × 200 cm RPC being fabricated (left panel) and three such RPCs are under test in a cosmic ray test stand (right panel). . . . .  | 102 |
| 3.42 | Preamplifier output traces of a 200 cm × 200 cm RPC (left panel) and distribution (histogram) of their peak pulse heights (right panel). . . . .  | 103 |
| 3.43 | Time profile of noise rate of a 200 cm × 200 cm RPC channel, along with the ambient temperature. . . . .  | 104 |
| 3.44 | Oscilloscope screen shots of signal from RPC, operated without (left panel) and with (right panel) gas mixture containing SF <sub>6</sub> . . . . .   | 105 |
| 3.45 | RPC current characteristics without and with SF <sub>6</sub> gas mixture. . . . .   | 105 |

|      |   |     |
|------|---|-----|
| 3.46 | Effect of SF <sub>6</sub> in the gas mixture on RPC charge yield. The plot shown in the left panel is a superposition of charge distributions of RPC operated at various SF <sub>6</sub> concentrations. In the right panel, we show the extracted parameters of the distributions, such as most probable and maximum charge. . . . . | 106 |
| 3.47 | Effect of SF <sub>6</sub> in the gas mixture on RPC efficiency (left panel) and noise rate (right panel) characteristics. . . . .   | 106 |
| 3.48 | Effect of SF <sub>6</sub> in the gas mixture on RPC timing characteristics. While the time response plot is shown in the left panel, time resolution as a function of SF <sub>6</sub> fraction in the gas mixture is shown in the right panel. . . . .  | 107 |
| 4.1  | Mechanical assembly drawings of 100 cm × 100 cm RPCs used for constructing the ICAL prototype detector stack. . . . .   | 111 |
| 4.2  | Fully installed ICAL prototype detector stack along with the gas system (left) and DAQ and power supply systems (right). The front-end electronics racks are built on either side of the detector stack - one each for X- and Y-readout planes. . . . .   | 111 |
| 4.3  | Segmentation scheme of the ICAL prototype detector stack. Only the X-readout plane view is shown here for brevity. . . . .  | 112 |
| 4.4  | Commercial components based high voltage (left panel) and low voltage (right panel) power supply systems for the ICAL prototype detector stack. . . . .   | 114 |
| 4.5  | Low voltage distribution scheme and networks for the preamplifiers (left panel), analog (middle panel) and digital (right panel) front-end subsystems. . . . .  | 115 |
| 4.6  | Screen shots of low voltage (left panel) and high voltage (right panel) power supply system monitor consoles. These are made accessible on the intranet for facilitating remote monitoring and control. . . . .   | 115 |
| 4.7  | Schematic diagram of the front-end and data acquisition systems for the ICAL prototype detector stack. The back-end is based on the CAMAC modular instrumentation standard. . . . .   | 116 |
| 4.8  | Signal flow of the data acquisition system shown using the actual circuit boards. The DAQ sections that these groups of boards represent from left to right are preamplifiers, analog front-end, digital front-end, routers and back-end respectively. . . . .  | 118 |
| 4.9  | HMC based 8-in-1 two-stage preamplifier: the circuit board (left panel) and its gain characteristics (right panel). About 100 such boards were needed to instrument the prototype detector stack. . . . .   | 118 |

|      |  |     |
|------|--|-----|
| 4.10 | Signal flow diagram of the analog and digital front-end sections. Inputs shown at the top of the diagram are the analog signals from the preamplifiers. The daisy-chained control signals from the previous station are shown to enter from the left and exit to the next station from the right side of the diagram. . . . .  | 120 |
| 4.11 | Output pulse characteristics of preamplifier. As may be noted from the figure, the pulse amplitude is about -120 mV and pulse width at a threshold of -20 mV is about 18 ns. . . . .   | 122 |
| 4.12 | Performance studies of the front-end electronics using simultaneous measurements and analysis of RPC parameters using the DAQ system and oscilloscope. The plot in the right panel takes-off from -20 mV on the x-axis, which is the set threshold for the DAQ system. . . . .   | 122 |
| 4.13 | Logic diagram of the generation of in-situ trigger signal using the RPC strip signals. Level-0 and level-1 of this three tier trigger system are implemented in the front-end, while level-2 (final) stage is implemented in the back-end . . . . .  | 126 |
| 4.14 | Barometric pressure, temperature and humidity sensors (left panel) and the monitoring console of these devices (right panel). . . . .  | 127 |
| 4.15 | A screen shot of INO's on-line web based ELOG book. Apart from plain text, the ELOG entries could comprise of tables, plots, pictures and even audio-video objects. . . . .  | 129 |
| 5.1  | A few typical cosmic ray muon events recorded by the prototype detector stack. Shown in the left panel is a single muon track passing through the entire detector. The event in the middle panel is of two muon tracks, both partially tracked by the detector. The right panel demonstrates the capability of the detector to capture particle interactions inside its volume.                              | 133 |
| 5.2  | Typical efficiency plateau plot of a 200 cm × 200 cm RPC operated in avalanche mode with binary gas mixture of Freon (R134a) and Isobutane. The cosmic ray telescope was intended to be aligned on the strip (S32). But, geometrical mis-alignment of telescope and the SF <sub>6</sub> -less gas mixture contribute to <i>apparently</i> large cross-talk on the neighbouring strips (S31 and S33). . . . . | 134 |
| 5.3  | Typical charge and timing characteristics of an RPC. It may be noted that the charge distribution is of a single strip, while the timing data is obtained from an entire readout plane by logically summing up all the strip signals. . . . .  | 135 |
| 5.4  | Absolute time resolution plots of all the RPCs in the prototype detector stack. . . . .  | 136 |

|      |   |     |
|------|---|-----|
| 5.5  | Relative time resolution plots of all the RPCs in the prototype detector stack. . . . .   | 138 |
| 5.6  | $\chi^2/ndf$ distribution plots. Clock-wise, starting from top-left plot are for: all the fit tracks, $\chi^2/ndf < 4.0$ , all the re-fit tracks and finally $0.06 \leq \chi^2/ndf < 0.7$ . . . . .   | 140 |
| 5.7  | Track impact position distribution of an RPC in the stack using cosmic ray muon data. . . . .   | 142 |
| 5.8  | Typical cluster size or strip multiplicity distribution plot of an RPC. . . . .   | 143 |
| 5.9  | Residual distribution of cosmic ray muon track position through an RPC.<br>Most of hits are distributed within 20 mm, and the RMS is about 6 mm. . . . .  | 144 |
| 5.10 | Surface map or tomograph of an RPC using cosmic ray muons. . . . .  | 145 |
| 5.11 | Typical strip noise rate time profile (left panel) and distribution plots (right panel). It may be noted that the mean value of the distribution corresponds to the noise count for 10 secs of an RPC strip of $100\text{ cm} \times 3\text{ cm}$ in dimension. We therefore obtain a nominal counting rate of about $0.2\text{ Hz/cm}^2$ from this plot. . . . . | 145 |
| 5.12 | Applied voltage and chamber current profile plot of an RPC in the detector stack. As the RPC is powered by a differential high voltage, monitored voltages and currents for both polarity supplies are plotted. The average chamber current is about 50 nA. . . . .   | 146 |
| 5.13 | Correlation between ambient laboratory temperature and RPC strip rates.<br>Shown in the left panel is the time profile of noise rate and temperature, while in the right panel we show the scatter plot of the same data. . . . .   | 146 |



# List of Tables

|     |  |     |
|-----|--|-----|
| 1.1 | Specifications of the ICAL detector and its active detector elements . . . . .   | 16  |
| 2.1 | Summary on the deployment of RPCs in the past and current experiments. Area is given in m <sup>2</sup> , while the gap (width) in mm. . . . .  | 41  |
| 3.1 | Summary of RPC cross-talk measurements using pickup strips of 30 mm in width . . . . .   | 57  |
| 3.2 | Summary of MFC calibration equations for individual gases using water displacement and flow through tube methods. Flow rate value $y$ SCCM is set in order to obtain an actual flow rate of $x$ SCCM. . . . .  | 76  |
| 3.3 | Requirement of various gases in the ICAL detector . . . . .  | 77  |
| 3.4 | Summary of our EDS studies on glass samples from various manufacturers. . . . .  | 85  |
| 3.5 | Summary of our studies on screen printing technique on glass electrodes using special inks. . . . .  | 91  |
| 3.6 | Summary of characteristic impedance measurements of RPC pickup strips. .   | 98  |
| 3.7 | Summary of capacitance measurements of RPC pickup strips. . . . .  | 98  |
| 5.1 | Summary of time resolution measurements of the RPCs in the stack. All the time units are in ns. Columns of particular interest are absolute and relative sigmas. . . . .   | 137 |
| 5.2 | Tracking efficiencies of the RPCs in the stack as determined by the tracking of cosmic ray muon events. The layer-wise efficiencies are calculated as the ratio of the number of strip hits on the cosmic ray muon track to the number of tracks passed through the detector stack (and through that layer). . . . . | 141 |
| 5.3 | Average cluster sizes of all the RPCs in the prototype detector stack. . .   | 142 |
| B.1 | Important properties of gases used in ICAL detector. Note <sup>1</sup> : Triple point: -49.4°C at 2.2 bar, Sub. point: -63.9°C. . . . .  | 161 |
| B.2 | Specifications of the paint used for spray painting of glass electrodes. . .   | 162 |
| B.3 | Technical specifications of the GE made LEXAN polycarbonate material. .  | 162 |
| B.4 | Technical specifications of the Garware made EMCL grade insulating film.   | 163 |

|   |     |
|---|-----|
| B.5 Event data format. Packet size: 167 words. . . . .  | 164 |
| B.6 Monitor data format. Packet size: 52 words. . . . . | 165 |

## Abbreviation Notation and Nomenclature

|   |   |
|---|---|
| CERN                                    | European Organization for Nuclear Research (Geneva)                 |
| LHC                                     | Large Hadron Collider   |
| $e^-$                                   | Electron  |
| $e^+$                                   | Positron  |
| $\mu$                                   | Muon  |
| $p$                                     | Proton  |
| $n$                                     | Neutron   |
| $\pi$                                   | Pion  |
| $W^\pm$                                 | Vector boson  |
| $\nu_e$                                 | Electron neutrino   |
| $\nu_\mu$                               | Muon neutrino   |
| $\nu_\tau$                              | Tau neutrino  |
| $\bar{\nu}_e$                           | Electron anti-neutrino  |
| $\bar{\nu}_\mu$                         | Muon anti-neutrino  |
| $\nu_1, \nu_2, \nu_3$                   | Neutrino mass eigenstates   |
| $\theta_{12}, \theta_{13}, \theta_{23}$ | Neutrino mixing angles  |
| $\delta_{ij}^2$                         | Neutrino mass squared differences                                   |
| $\delta_{atm}$                          | Mass squared difference measured by atmospheric neutrino experiment |
| $\delta_{sol}$                          | Mass squared difference measured by solar neutrino experiment       |
| L                                       | Distance travelled by the neutrino                                  |
| E                                       | Energy of the neutrino  |
| CC                                      | Charged-Current (interaction)                                       |
| CP                                      | Charge conjugation and Parity (symmetry)                            |
| CPT                                     | Charge conjugation, Parity and Time reversal (symmetry)             |
| GZK                                     | Greisen-Zatsepin-Kuzmin (limit)                                     |
| GWth                                    | Giga Watt thermal   |
| eV                                      | Electron Volt   |
| $\alpha$                                | Townsend coefficient  |
| $\beta$                                 | Attachment coefficient  |
| FWHM                                    | Full Width at Half Maximum  |
| HV                                      | High Voltage  |
| PVC                                     | Poly Vinyl Chloride   |
| ABS                                     | Acrylonitrile Butadiene Styrene                                     |
| DAQ                                     | Data Acquisition  |
| NIM                                     | Nuclear Instrumentation Module                                      |
| CAMAC                                   | Computer Automated Measurement and Control                          |
| VME                                     | Versa Module Europa   |



# Introduction

We begin this chapter by tracing the discovery of the incredible neutrino - *the most tiny quantity of reality ever imagined by a human being*<sup>1</sup>. We then introduce their description in the Standard Model of particle physics, the concept of neutrino oscillations and some of their properties. The motivation to study neutrinos from various sources and current results of some important experiments has been reviewed, besides highlighting some of the outstanding problems in field of neutrino physics and neutrino astronomy [1]. We then list neutrino physics issues that can be addressed by a magnetised iron calorimeter, before moving on to describe one, in which Resistive Place Chambers (RPCs) as active detector elements are going to be deployed on an unprecedented scale.

## 1.1 History of neutrino

According to Big Bang, neutrinos were born around 14 billion years ago - soon after the birth of the universe and are now the second most abundant particles in the universe - next only to photons. However, theoretically they were proposed in 1930 by Wolfgang Pauli to explain nuclear beta decay. Early studies of beta decay, revealed a continuous energy spectrum, unlike the discrete energy spectra observed in a two body radioactive decay. As repeated search [2] failed to detect the third particle, Niel Bohr had even begun to contemplate abandoning the law of energy conservation in nuclear processes [3]. Pauli postulated that an undetected neutral particle - which was escaping detection, could carry away the observed difference between the energy and

---

<sup>1</sup>as one of its co-discoverers, Frederick Reines described them.

momentum of the initial and final particles [4]. The name *neutrino* is due to Enrico Fermi who, in 1934 took the neutrino hypothesis seriously, and proposed his theory of weak interactions.

Hans Bethe and Rudolf Peierls in 1934 used Fermi's theory to show that the interaction cross section of neutrinos and matter would be about 20 orders of magnitude smaller than typical nuclear cross sections ( $\sim$ barns) and hence concluded "there is no practically possible way of observing the neutrino" [5]. But, in a series of experiments [6] in 1956, Frederick Reines and Clyde Cowan conclusively proved their existence through the inverse beta decay weak interaction process where an *electron-type* anti-neutrino,  $\bar{\nu}_e$  created in a nuclear reactor is captured by a proton  $p$  giving rise to a positron  $e^+$  and a neutron  $n$ .

$$\bar{\nu}_e + p \rightarrow e^+ + n \quad (1.1)$$

Apart from electron-type neutrinos which are produced in nuclear beta decay, the separate identity of *muon-type* neutrinos was proved in 1962 by Leon Lederman *et al* by first detecting interactions of the muon neutrino [7]. When a third type of charged lepton, the tau, was discovered in 1975 at the Stanford Linear Accelerator, it too was expected to have an associated neutrino. First evidence for this third neutrino type came from the observation of missing energy and momentum in tau decays analogous to the beta decay. The first detection of tau neutrino in 2000 by the DONuT collaboration [8], made it the latest particle of the Standard Model to have been directly observed.

A result of fundamental importance to neutrino physics is the precise measurement of the decay width of the  $Z$ -boson which is saturated by (and hence indicates the existence of only) three active light neutrino flavours with masses less than half the  $Z$ -boson mass. The existence of sterile neutrinos which do not participate in the weak interaction but which could be created through flavour oscillation cannot be ruled out from these measurements [9].

## 1.2 Neutrino in the Standard Model

The Standard Model is a consistent framework that embodies all of our current understanding of fundamental particles and forces, except gravity. It describes the way fun-

damental particles interact. The Standard Model incorporates twelve building blocks of matter (Fermions) - six leptons and six quarks, and their antiparticles along with four force carriers (Bosons). The fermions are also grouped into generations. In general, fermion masses increase with generation (Figure 1.1).

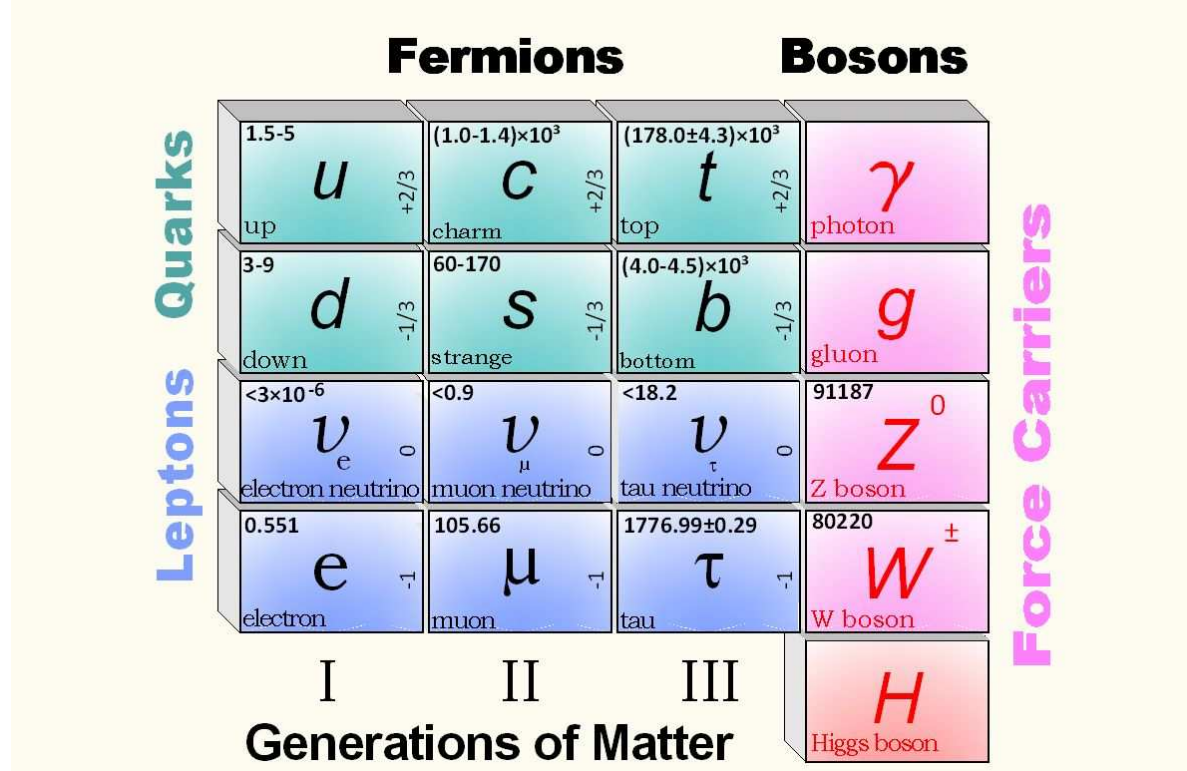


Figure 1.1: Standard Model of Particle Physics showing the electric charge (right) and mass for each particle in MeV (top left corner).

The quarks have fractional charge and interact primarily through the colour force, though they experience all other basic interactions. Their binding through the colour interaction is what gives rise to the proton, the neutron and all other hadrons. The charged leptons do not interact via the colour force, but experience the electromagnetic and weak force. All matter and energy interact through gravity, however. Although we do not have a quantum theory of gravitation, string theory holds promise of not only quantizing gravity but also unifying all four fundamental interactions. The other building blocks of Standard Model are the gauge bosons, namely, the gluons, the photons and the  $W^\pm$  and the  $Z$ -boson that mediate the various interactions. In the Standard Model fundamental particles acquire mass by interacting with the Higgs field [10]. The Higgs boson is yet to be discovered and its discovery is the main goal of the LHC experiments.

Within the Standard Model, the three neutrinos (and their anti-particles) are massless. Neutrinos interact with matter only through the weak force. It is precisely this lack of interaction strength that makes the neutrinos experimentally elusive. According to the Standard Model, an electron neutrino can not change to neutrino from another family as the lepton flavour number is conserved. Since the predictions of Standard Model have stood up till date to increasingly precise tests in laboratory experiments, the observation of neutrino mass and oscillation (see below) turned out to be a fundamental issue central to neutrino physics and to the Standard Model as well.

## 1.3 Neutrino oscillations

As mentioned above, many important observations on neutrinos from several key experiments all fall in line, if neutrinos have mass and the neutrino *flavour* states (electron, muon and tau) which participate in the weak interactions are mixtures of *mass* eigenstates with different masses ( $m_1$ ,  $m_2$  and  $m_3$ ). In general the two bases - flavour and mass states, are connected by a unitary matrix. The quantum mechanical evolution of the flavour states leads to the phenomenon of neutrino oscillations, which was first proposed by B.Pontecorvo [11] [12]. In fact, the idea of neutrino oscillations is rooted in quantum mechanics. The neutrinos switch identities, or oscillate into other flavours, as they propagate. Appendix A deals with details on neutrino oscillations.

Experiments using a variety of sources of neutrinos (Section 1.6), clearly indicate that neutrinos do exhibit such flavour oscillations. Results from these experiments determine or constrain the extent of mixing as well as the differences between the squared masses. In particular, while the absolute masses themselves are not constrained by such observations, data indicate that at least two of the neutrinos must be massive, and with different masses. This is in fact the first confirmed evidence for physics beyond the Standard Model of particle physics. Moreover, the estimated smallness of the neutrino mass (of the order of eV or much smaller) may have its origins near or beyond the scale of Grand Unified Theories (GUTs), thus probing physics beyond the reach of present day accelerators.

## 1.4 Properties of neutrinos

Neutrinos interact only by the weak interaction. It is very hard to uniquely identify neutrino interactions among the background of cosmic ray interactions and even radioactivity (depending on neutrino energy). Neutrinos traveling through matter, in general, are not directly observable because they do not possess electric charge and therefore cannot ionise matter. They do interact via the weak interaction in electric charge changing reactions (charged current interaction) or electric charge preserving reactions (neutral current interaction).

The existence of a neutrino mass strongly suggests the existence of a tiny neutrino magnetic moment of the order of  $10^{-19}$  Bohr magneton allowing the possibility that neutrinos may interact electromagnetically as well.

Experimental results show that nearly all neutrinos have left-handed helicities (spins anti parallel to momenta), and all anti neutrinos have right-handed helicities. In the massless limit, it means that only one of the two possible helicities is observed for either particle.

Before the idea of neutrino oscillations came up, it was generally assumed that neutrinos travel at the speed of light. However, for massive particles, this can not be true. The neutrinos from the supernova were detected within a time window that was consistent with a speed of light for the neutrinos. So far, the question of neutrino masses cannot be decided based on measurements of the neutrino speed.

While the experimental results show that neutrinos have mass, their absolute mass scale is still not known. This is due to the fact that neutrino oscillations are sensitive only to the difference in the squares of the masses.

A schematic of the present status of masses and mixing is shown in Figure 1.2 as obtained from a combined analysis of the experiments on solar, atmospheric, reactor and accelerator neutrinos. The present data does not distinguish between the two possible mass orderings:  $m_3^2 > m_2^2 > m_1^2$  (direct),  $m_2^2 > m_1^2 > m_3^2$  (inverted). In Figure 1.2, the direct or normal mass hierarchy is assumed; in the case of the inverted hierarchy, the  $\nu_3$  state would be the lightest.

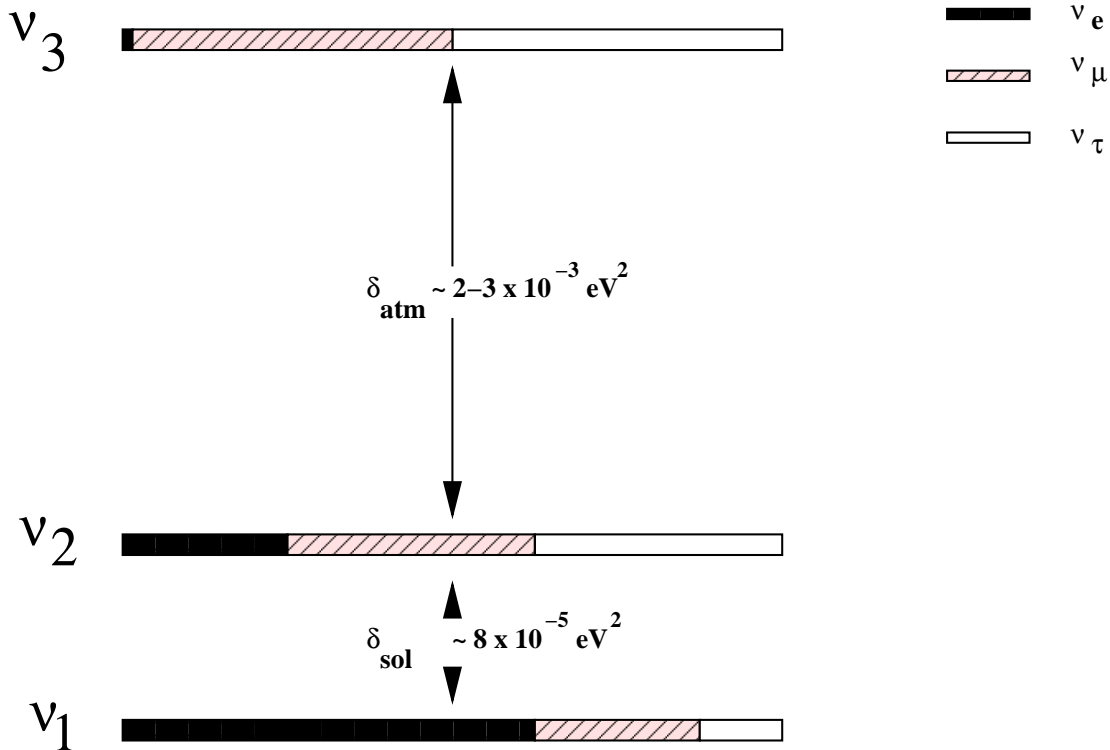


Figure 1.2: Schematic illustration of the status of masses and mixing of neutrino eigenstates. The flavour content is indicated by different shading; the  $\nu_e$  contribution shown in the third mass eigenstate is an upper bound. The mass squared differences as obtained from the data are also shown.

## 1.5 Why study neutrinos?

In astronomy, neutrino is of scientific interest because it can make an exceptional probe for environments that are typically concealed from the standpoint of other observation techniques, such as optical and radio observation [14].

The first such use of neutrinos was proposed for observation of the core of the Sun. Direct optical observation of the solar core is impossible due to the diffusion of electromagnetic radiation by the huge amount of matter surrounding the core. On the other hand, neutrinos generated in stellar fusion reactions at the core pass through the sun with few interactions. While photons emitted by the solar core may require some 40,000 years to diffuse to the outer layers of the Sun, neutrinos can virtually cross this distance at nearly the speed of light.

Neutrinos are also useful for probing astrophysical sources beyond our solar system. Neutrinos are the only known particles that are not significantly attenuated by their travel through the interstellar medium. Optical photons can be obscured or dif-

fused by dust, gas and background radiation. High-energy cosmic rays, in the form of fast-moving protons and atomic nuclei, are not able to travel more than about 100 Mpc due to the GZK cutoff. Neutrinos can travel this and greater distances with very little attenuation.

Another important use of the neutrino is in the observation of core collapse supernovae, the explosions that end the lives of highly massive stars. The core collapse phase of a supernova is an almost unimaginably dense and energetic event. It is so dense that no known particles are able to escape the advancing core front except for neutrinos. The usefulness of neutrinos as a probe for this important event in the death of a star cannot be overstated.

Neutrinos could also be used for studying quantum gravity effects. Because they are not affected by either the strong interaction or electromagnetism, and because they are not normally found in composite particles or prone to near instantaneous decay it might be possible to isolate and measure gravitational effects on neutrinos at a quantum level.

## 1.6 Sources of neutrinos

The sources of naturally occurring neutrinos are both terrestrial and extraterrestrial. They are also produced using particle accelerators and in nuclear reactors. Each of these sources provide information, sometimes overlapping, that is extremely important in understanding the intrinsic properties of the neutrinos and their sources. The energy spectrum of naturally produced neutrinos starts from fractions of electron-volts and spans an impressive range.

1. **Big-Bang:** The standard model of the Big-Bang predicts, like for the photons, a cosmic background of neutrinos. Even though they are very numerous - about 330 neutrinos per  $\text{cm}^3$ , their energy is so small (about 0.0004 eV), that no experiment has been able to detect them as yet.
2. **Atmospheric neutrinos:** Atmospheric neutrinos result from the interaction of cosmic rays with atomic nuclei in the Earth's atmosphere, creating showers of particles, many of which are unstable and produce neutrinos when they decay.

This process is represented by:

$$\pi \rightarrow \mu + \nu_\mu ; \quad \mu \rightarrow e + \bar{\nu}_e + \nu_\mu \quad (1.2)$$

The atmospheric neutrino flux, which is approximately  $10^3 / \text{m}^2 / \text{s}$ , peaks just below a GeV and falls thereafter faster than  $1/E^2$ .

3. **Solar neutrinos:** According to the Standard Solar Model, when four protons fuse to become one helium nucleus, two of them have to convert into neutrons, and each such conversion releases one electron neutrino, which is represented by the following equation:



Every second, about 65 billion solar neutrinos pass through every square centimeter on Earth that faces the sun. Since neutrinos are insignificantly absorbed by the mass of the Earth, the surface area on the side of the Earth opposite the Sun receives practically the same number of neutrinos as the side facing the Sun.

4. **Supernovae:** Most of the energy produced in supernovae is radiated away in the form of an immense burst of neutrinos. Because neutrinos interact so little with matter, it is thought that a supernova's neutrino emissions carry information about the innermost regions of the explosion. A second and more important neutrino source is the thermal energy of the newly formed neutron core, which is dissipated via the formation of neutrino-anti neutrino pairs of all flavors. These processes may be represented by the following equations. Approximate neutrino flux observed from SN1987a Supernova was  $10^{12} / \text{m}^2 / \text{s}$ .

$$p + e \rightarrow n + \nu_e ; \quad e^+ + e^- \rightarrow \nu + \bar{\nu} \quad (1.4)$$

5. **Geologically produced neutrinos:** Some of the isotopic constituents of the earth are naturally radioactive, especially those with half lives of the order of the geological age. Neutrinos are produced as a result of this natural radioactivity. In particular, the decay chains of Uranium-238 and Thorium-232 isotopes, as well

as Potassium-40, include beta decays which are accompanied by the emission of anti-neutrinos and neutrinos. They can provide information on the Earth's interior. The flux of the geologically produced neutrinos is about  $5 \times 10^{10} / \text{m}^2/\text{s}$ .

6. **Nuclear reactors:** Nuclear reactors are the major source of human-generated neutrinos. They have been the first to be detected and also the first to be used to put some limits on the neutrino oscillation. Anti-neutrinos are made in the beta-decay of neutron-rich daughter fragments in the fission process. The average nuclear fission releases about 200 MeV of energy, of which roughly 6% is radiated away as anti-neutrinos. A standard nuclear power reactor produces about  $2 \times 10^{20} \bar{\nu}_e / \text{GWth}$ . Nuclear bombs also produce very large quantities of neutrinos.
7. **Particle accelerators:** Some particle accelerators have been used to make neutrino beams. The technique is to smash protons into a fixed target, producing charged pions or kaons. These unstable particles are then magnetically focused into a long tunnel where they decay while in flight. Because of the relativistic boost of the decaying particle the neutrinos are produced as a beam rather than isotropically. The newly built neutrino beam at the J-PARC accelerator laboratory in Tokai, Japan is one such example. Efforts to construct an accelerator facility where neutrinos are produced through muon decays are also ongoing. Such a setup is called a neutrino factory.

## 1.7 Status and goals of neutrino experiments

Neutrino physics experiments in the last several decades have provided many new and significant results.

- **Solar and atmospheric neutrinos:** The observation of the deficit in electron neutrinos from the Sun, relative to the expectations from the Standard Solar Model, constitutes the Solar Neutrino problem. The combination of deficit in charged current interactions and the detection of all the predicted number of neutrinos in neutral current interactions indicate that the solution to this problem is through neutrino oscillations. The other problem involves the atmospheric  $\nu_\mu$ , whose

deficit relative to the atmospheric  $\nu_e$  is accounted for by a mass squared difference, which is an order of magnitude larger than the relevant value to solar neutrino data, and yet another large mixing between states. These observations thus imply the existence of at least two non-zero masses for neutrino mass eigenstates.

- **Beta decay and double beta decay:** In contrast to neutrino oscillation-sensitive experiments, these yield direct mass limits. So far, there is only an upper limit of  $2.2 \text{ eV}/c^2$  on the dominant mass eigenstate for electron neutrinos involved in tritium beta decay [15].
- **Cosmological data:** Cosmological experiments, apart from limiting the number of light neutrino flavour, set fairly robust upper limits on the sum of all the active neutrino masses [16].
- **Neutrinos from Supernova:** The observation of neutrinos from the Supernova SN1987a has confirmed many qualitative features of the stellar collapse scenario. While the number of observed events is statistically small some conclusions can be drawn on the properties of the neutrinos. The measurements also confirm, in a broad sense, our understanding of supernova explosions.
- **Other neutrino properties:** Stringent upper limits also exist for neutrino magnetic moments, decay rates, and other such properties.

In spite of these remarkable results, there are several outstanding issues of fundamental importance. In fact, there has been a paradigm shift in the nature of the goals to be pursued in neutrino physics. From a search for an understanding of the particle physics and the astrophysics, the focus has shifted to one where increasingly precise measurements of neutrino mass and mixing matrix parameters are sought. These are primarily measurements of neutrino oscillation parameters. Specifically, the challenges are:

1. To observe the neutrino oscillation pattern - periodic changes in the neutrino flux with minima and maxima - over at least one full period, in order to make a precise measurement of the oscillation parameters.

2. To improve the existing upper limit on the mixing angle  $\theta_{13}$  and to ascertain if its value is different from zero. This has tremendous implications for observing terrestrial matter-dependent oscillation effects as well as CP violation in the leptonic sector. It is known that these effects are small; however, this is a question of fundamental and deep significance which may be probed in future long-baseline neutrino experiments.
3. To determine whether the leptonic CP phase  $\delta$  is non-zero, and if so, obtain some measure of its magnitude, provided  $\theta_{13} \neq 0$ .
4. To determine whether the mixing angle  $\theta_{23}$  is maximal, if not explore how well its octant can be determined.
5. To obtain unambiguous evidence for matter effects and determine the sign of the mass-squared difference  $\delta_{32}$  involved in atmospheric neutrino oscillations. This can be determined through precision experiments sensitive to matter effects during propagation of the neutrinos through the earth. This has implications for building theoretical models that can accommodate the observed neutrino oscillation parameters.
6. Do neutrinos decay? This is unlikely as a dominant scenario to explain the known data. However, they may still be allowed in combination with dominant neutrino oscillations.
7. What is the absolute scale of neutrino mass? Direct mass measurements from beta decay place an upper limit of about 2.2 eV. Model dependent interpretation of the astrophysical results limits the sum of the neutrino masses to around 0.5 eV. Neutrino-less double beta decay, if observed, will also determine the mass scale.
8. Are the neutrinos different from their anti-particles (Dirac) or are they their own anti-particles (Majorana particles)? There is a strong theoretical prejudice that neutrinos are Majorana particles. Only charge-neutral fermions can be Majorana particles and hence neutrinos are the only candidates within the Standard Model. Hence there is great interest in establishing this by an unambiguous observation of neutrino-less double beta decay.

9. How many species of neutrinos exist? The number of active species with masses less than half the mass of the  $Z$ -boson is limited to three by LEP experiments. However, recent results suggests the existence of at least one more relatively light species, which has to be sterile (that is, cannot experience weak interactions), since there cannot be more than three light active species.
10. Does the neutrino have a non-zero magnetic moment? A non-zero magnetic moment is possible now that the neutrinos are known to be massive. The determination of its magnitude is therefore of fundamental importance, and may also have an impact on the solar neutrino problem.
11. The observed *knee and ankle* features of the cosmic ray spectrum are as yet not understood. The sources and mechanism responsible for this may lead to production of very high energy neutrinos, and if this is the case, a study of high – PeV and higher – energy neutrinos may provide the vital clues to resolve this important question.

## 1.8 Physics with Magnetised Iron Calorimeter

Impelled by the discoveries mentioned in the previous section and their implications for the future of particle physics, plans have been made - world-wide - for new neutrino detectors, neutrino factories and long base-line neutrino experiments.

The Indian initiative in cosmic ray and neutrino Physics experiments goes back several decades. The first atmospheric neutrino induced muon events were recorded at the Kolar Gold Fields (KGF) underground laboratory nearly forty five years ago [17]. In fact, the resurrection of Indian experimental neutrino physics programme was made possible by the experience gained here. A multi-institutional Neutrino Collaboration has been formed with the objective of creating an India-based Neutrino Observatory (INO). The observatory will have a large underground cavern, with an all round rock cover of 1 km, to house the ICAL detector and a smaller one for experiments with more compact detectors. The access will be through a tunnel. The preferred location is Singara, located about 100 km from Mysore in South India [18].

The INO collaboration has proposed to build a massive magnetised Iron Calorime-

ter (ICAL) detector inside the INO cavern. The ICAL is contemplated as both a detector for atmospheric neutrinos and as well as a future end-detector for a neutrino factory beam. In both cases, the primary detection mechanism is via detection of muons produced in charged current neutrino interactions such as  $\nu_\mu + n \rightarrow \mu^- + p$ . The detector will comprise of layers of iron sheets interleaved with the planar active detector elements, which are Resistive Plate Chambers (RPCs). The detector will be magnetised to a field of about 1.3 T, which allows for charge discrimination of muons.

The atmospheric neutrino physics program possible with ICAL is substantial. It is possible to observe a clear signal of oscillation by observing one full oscillation period so that the *precision of the parameters*,  $\delta_{32}$  and  $\theta_{23}$ , can be improved to 10%. We can also use atmospheric neutrinos to *probe CPT invariance* which is one of the fundamental paradigms of quantum field theories, of which the Standard Model is one. Apart from their charge discrimination capability, iron calorimeters have a large range in sensitivity to  $L/E$  variations compared to water Cerenkov detectors and can substantiate the evidence of neutrino mass and oscillation already observed by Super-K experiment, via the observation of dips and peaks in the event rate versus  $L/E$ . When used as an end-detector for a high  $\gamma$  Beta Beam or a neutrino factory, the ICAL-CERN distance matches the *magic baseline*, so that results are insensitive to the CP phase  $\delta$ . The major physics goals of the ICAL detector are summarised below [19]:

- To re-confirm the occurrence of oscillation in atmospheric muon neutrinos and significantly improve measurement of the oscillation parameters, through the explicit observation of the first oscillation swing in  $\nu_\mu$  disappearance as a function of  $L/E$ . A broad range in both path length  $L$  and energy,  $E$ , and indeed in their ratio,  $L/E$ , possible with atmospheric neutrinos, offers the opportunity to probe a large range of  $\delta_{32}$ .
- To observe matter dependent effects, using magnetised ICAL detector's ability to distinguish neutrino- and anti-neutrino-initiated processes by detecting the charge of the produced muons. Determining the *sign of*  $\delta_{32}$  and the magnitude of  $\theta_{13}$ , using the matter effect. It is not known if  $\theta_{13}$  is different from zero. This has tremendous implications for observing Earth matter-dependent oscillation effects as well as CP violation in the leptonic sector. If this angle is exactly zero,

neither of these effects will be seen.

- A new way of distinguishing whether the muon neutrino deficit observed by previous experiments is due to oscillations of muon neutrinos to tau neutrinos or to sterile ones. A sterile neutrino does not have a charged lepton partner and immune to the weak interactions, unlike the other three known active neutrinos ( $\nu_e$ ,  $\nu_\mu$  and  $\nu_\tau$ ).
- Probing CPT violation in the neutrino sector using atmospheric neutrinos and putting bounds on them. The atmospheric neutrino data involve both the particle and the antiparticle channels and are therefore suitable for studying CPT violation. As the atmospheric neutrino experiments are probing mass squared differences and not the absolute neutrino mass, these will be the quantities which might be restricted by the data. The interest in CPT violation arises due to a recently suggested scheme which is capable of solving all neutrino anomalies without the use of a light sterile neutrino [20].
- Constraining the long range leptonic forces. These are a special class of long range forces which distinguish between leptonic flavours and have far reaching implications for the neutrino oscillations. In turn we may use them as a probe of such forces.
- To study multi-TeV cosmic ray muons through pair-meter technique. The technique [21] is used to measure the energy and frequency of electron-positron pair cascades produced by the passage of a high energy muon in dense matter. Such studies in the high energy (TeV-PeV) region can throw light on possible extensions of the Standard Model.

## 1.9 The Magnetised Iron Calorimeter

The primary focus of ICAL at INO is to study interactions involving atmospheric *muon neutrinos and anti-neutrinos*. This requires the construction of a detector that is sensitive to the energy, direction and sign of the electric charge of muons, produced by charged-current (CC) interactions of neutrinos with the detector material. This detector (perhaps upgraded in terms of fiducial volume) will also be a suitable choice as

a far-end detector of a long-base-line experiment. Based on the physics goals of the ICAL detector, the following criteria was used for selecting an appropriate design for the detector system.

- A large target mass to achieve a statistically significant number of neutrino interactions in a reasonable time-frame for the confirmation of atmospheric neutrino oscillation.
- To explicitly detect the oscillation pattern in the  $L/E$  spectrum of atmospheric muon neutrinos, the energy  $E$  and direction  $\theta$  of the incoming neutrino have to be accurately measured in each event. The energy of the neutrino can be estimated by measuring the energies of muon and the hadrons produced in each event. The direction of the neutrino can be estimated from the direction of the muon produced from the  $\nu_\mu$  charged-current interaction. The energy and angular resolution of the detector should therefore be good enough so that  $L/E$  can be measured with an accuracy better than half of the modulation period.
- In order to estimate the distance traversed by the neutrino, it is necessary to establish the flight direction (up vs. down) of the muon produced by the neutrino with high efficiency. Different techniques like increase of curvature in a magnetic field, multiple scattering along the track or the measurement of timing in successive detector layers can be used to achieve this. Of these the time-of-flight technique is the most effective and allows excellent up-down discrimination for a detector with a time resolution ( $\sigma$ ) of 1 ns or better.
- Identification of the electric charge of muons so as to distinguish between neutrino and anti-neutrino interactions. Charge determination is necessary to achieve most of the physics goals mentioned above.
- Compactness, ease of construction and modularity which allows the possibility of phasing.

### 1.9.1 Basic parameters

The ICAL detector with a target mass of about 100 kt will be ideal to address the physics goals listed above. To begin with we are proposing a detector of about 50 kt,

which may be enlarged to its final size of 100 kt in stages. The detector will have a modular structure of total lateral size 48 m × 16 m and will consist of a stack of 151 horizontal layers of 56 mm thick low carbon iron plates interleaved with 40 mm gaps to house the active detector layers. The height of the detector will be 14.5 m. The ICAL detector will be subdivided into three modules of size 16 m × 16 m. Salient features of the ICAL detector and its active detector elements are summarised in the Table 1.1.

Table 1.1: Specifications of the ICAL detector and its active detector elements

| ICAL Parameters                    |                           |
|------------------------------------|---------------------------|
| No. of modules                     | 3                         |
| One module dimensions              | 16 m × 16 m × 14.5 m      |
| Complete detector dimensions       | 48 m × 16 m × 14.5 m      |
| No. of iron layers                 | 151                       |
| Iron plate thickness               | 56 mm                     |
| Gap for RPC trays                  | 40 mm                     |
| Magnetic field                     | 1.3 T                     |
| RPC Parameters                     |                           |
| No. of RPC layers                  | 150                       |
| RPC unit dimensions                | 1840 mm × 1840 mm × 24 mm |
| Readout strip width                | 30 mm                     |
| No. of RPC units/Road/Layer        | 8                         |
| No. of Roads/Layer/Module          | 8                         |
| No. of RPC units/Layer             | 192                       |
| Total no. of RPC units             | 28800                     |
| No. of electronic readout channels | 3,686,400                 |

The iron structure for this detector will be self supporting with the layer above resting on the layer immediately below using steel spacers located every 2 m along the X-direction. This will create 2 m wide roads along the Y-direction for the insertion of RPC trays. There will be a total of 8 roads per module in a layer. The details of the detector design are shown in Figure 1.3 [22].

Considering the overall size of the apparatus and the large active detector area of about 100,000 m<sup>2</sup>, it is desirable that such a detector should be of low cost, modular in construction with elements of a size suitable for mass production on a time scale consistent with the requirement that the detector be internationally competitive. This modular structure will allow early operation with the completed modules while constructing others.

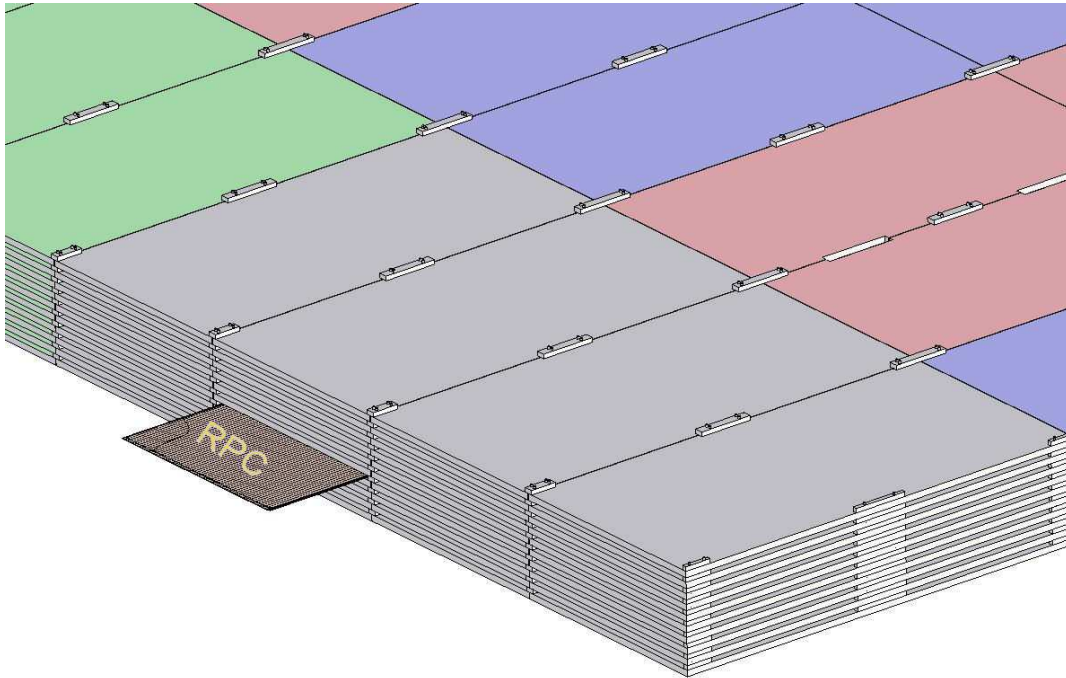


Figure 1.3: Schematic view of a part of the ICAL detector showing its constructional details along with an RPC.

## 1.9.2 The Magnet

The ICAL magnet provides target nucleons for neutrino interactions as well as it serves as a medium in which secondary charged particles can be separated on the basis of their magnetic rigidity so that their momenta can be estimated. The magnetised iron calorimeter will consist of about 50 kt of low carbon iron. The carbon percentage should be 0.1% or less in order to have a good magnetic characteristics.

The design criteria for the ICAL magnet are basically the following:

- **Field uniformity:** The performance of the detector will be the best when the magnetic field is uniform. We adopt a gap-less toroidal design for the magnet. In this design the magnetic field is predominantly inside the iron and field leakage outside is minimal.
- **Field orientation:** Minimum number of changes in the field orientation will be the criteria to be decided by simulation and event reconstruction.
- **Modularity:** Even in the basic design with 50 kt of iron, the detector and the magnet will be made in three modules. The modules can be added at any stage later, either singly or in pairs.

- **Optimum copper-to-iron ratio:** The copper to iron ratio decides the cost and the electrical power consumption. If we take a larger ratio then the power consumption is low resulting in lower running cost but higher fixed cost. The heat dissipation in the coil depends on the volume of copper used. A small amount of copper reduces the copper cost but dissipates a large amount of heat which has to be removed by using low conductivity water (LCW) flow through hollow copper conductors.
- **Access for maintenance:** Modularity is of utmost importance from the point of view of accessibility to provide maintenance.

In the toroidal (gap-less) design, the copper coil goes through two rectangular slots in the stack of iron plates. Four coils will be installed in the central zone of each detector module. Figure 1.4 shows the arrangement of the iron blocks with the coil slots in the ICAL magnet. The length, breadth and the positions of the slots are chosen to generate a uniform field in as large a volume of iron as possible. The design also facilitates easy insertion/removal of active detector trays. The small cross-section of the copper conductor ( $10\text{ mm} \times 10\text{ mm}$ ) and of the coil ( $625\text{ mm} \times 80\text{ mm}$ ) ensure negligible loss of fiducial volume of the detector. The coil dimensions are going to be gigantic  $8\text{ m} \times 14.5\text{ m}$ . We propose to use a hollow copper conductors cooled by low conductivity water flowing through them. Additionally, heat generated by the magnet coil can also be dissipated by conduction through the iron plates and by radiation from the iron surface.

A coil with 40,000 amp-turns is needed for producing a field of 1.3 T in one module. We have used a 3D commercial code MagNet 6.0 [23] to design the magnet and compute the magnetic field. The variation of the field over the entire set of plates is expected to be within 0.3%, the field varying by less than 0.15% over a height of  $\pm 5\text{ m}$  from the centre. The variation of the field is quite uniform in the X-direction, varying by less than 0.25% but in the Y-direction it starts falling beyond the length of the coil slot ( $\pm 4\text{ m}$ ) [19].

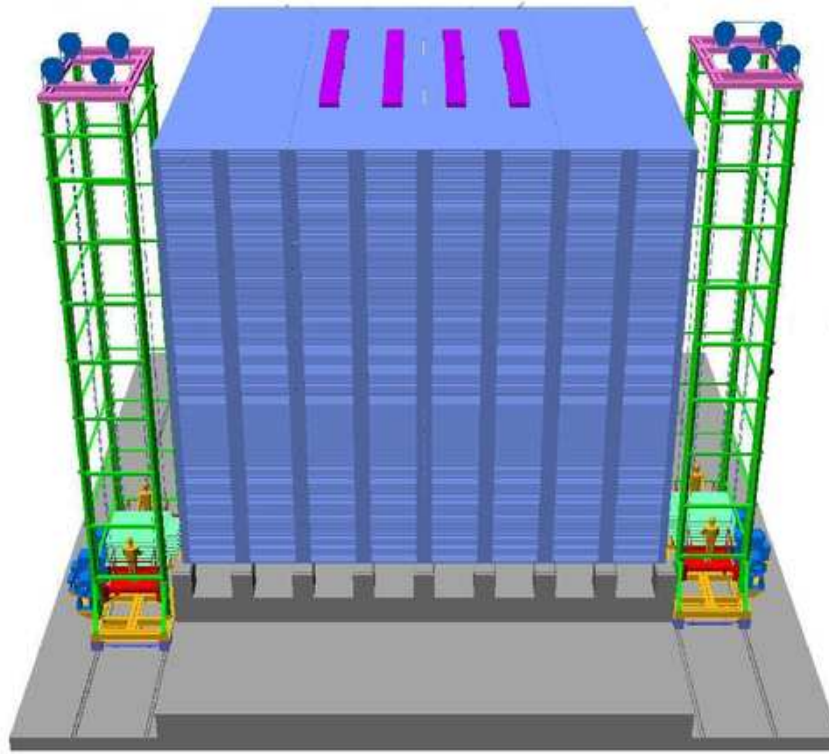


Figure 1.4: Schematic view of one of the (three) completed ICAL detector modules along with the RPC detector handling trolleys shown on either side. The top view of the magnet coils is also shown.

### 1.9.3 Detector readout scheme

In order to achieve most important requirements of the ICAL detector readout system - time resolution of under 1 ns and spatial resolution of better than 1 cm for the detector, the Resistive Plate Chambers (RPCs) were chosen as the active detector elements. Being planar in their geometry, RPCs are highly suitable for detectors requiring large coverage. They are easy to construct using commonly available materials, rugged, amenable for large scale industrial production and easy to operate over long periods of time - all of which are highly desirable in case of ICAL detector. While the RPCs can be constructed using bakelite or glass as electrode materials, we have at present opted for glass mainly due to the fact that it is readily available in the local industry, has good surface finish and is less expensive.

The basic RPC detector elements for ICAL will be 1.84 m in length and 1.84 m wide. Eight such elements will cover a road of  $16 \text{ m} \times 2 \text{ m}$ . A total of 28800 elements therefore will be needed to complete the entire detector. The readout of the RPCs will be performed by external orthogonal pick-up strips of 30 mm in pitch. Table 1.1 summarises

the specifications of the ICAL detector and the RPC elements.

A dedicated R&D programme was initiated by the INO collaboration to design and develop large area glass RPCs. This work along with detailed characterisation of the RPCs, forms the subject of this thesis report.

## 1.10 Chapter summary

We have given a brief motivation and background for the RPC detector work described in subsequent chapters. While not comprehensive in scope, we have highlighted many interesting results obtained so far from the large number of neutrino experiments. We have also, hopefully, put into perspective the major open issues and challenges ahead. We have then briefly summarised the physics potential of the proposed ICAL detector and its design. Finally, we have introduced the topic of this thesis report - design and characterisation of Resistive Plate Chambers (RPCs), which are going to be deployed in huge numbers in the ICAL detector.

# Detector Physics of RPCs

Resistive Plate Chambers (RPCs) are parallel plate gas detectors built using electrodes of high volume resistivity such as glass or bakelite (phenol-formaldehyde polymer). RPCs are simple to construct and operate, yet rugged, well adapted to inexpensive industrial production. The main features of these detectors are large signal output, excellent time as well as position resolutions and low cost per unit area of coverage. The field has enjoyed very active progress in recent years, including the development of avalanche mode of operation, extension of the counting rate capabilities up to about 10 MHz/cm<sup>2</sup>, improvement of the time resolution for minimum ionising particles to about 50 ps and position resolutions to a few tens of  $\mu\text{m}$  [41]. These new developments have further expanded the range of their applications in particle physics experiments and opened up new and diverse applications such as medical imaging and reliable high-rate tracking of Minimum Ionising Particles (MIPs).

We begin this chapter with a brief history of particle detectors in general and of RPCs in particular. We then introduce the basic principle and main modes of operation of the RPCs. RPCs are deployed as trigger detectors as well as timing detectors. RPCs with imaginative designs are also being developed to suit specific and diverse applications. We therefore review various designs of these versatile detectors. We conclude this chapter by presenting a survey of their applications and world-wide deployment.

## 2.1 Brief history of particle detectors

The discovery of X-rays and radioactivity in the 1890s heralded the birth of particle detectors. H.Becquerel's photosensitive paper, which was blackened by the radi-

ation released by uranium salt was possibly the first documented particle detector. E.Rutherford and E.Marsden used a scintillating screen to detect scattered alpha particles. Other early particle detectors used to reconstruct the tracks of charged particles were emulsions and the spark-, cloud-, streamer- and bubble chambers in which the particle tracks were photographed. The technology of particle detectors has, with time, evolved from these optical methods to electrical methods [34]. Detectors that record the ionisation produced by charged particles in gaseous medium have started finding applications. They were typically used to record the position of the track and the time of its passage. Gaseous detectors such as wire or drift chambers [24] have successfully replaced the scintillation counters in experiments, particularly requiring high spatial resolution. The amount of ionisation created inside the active volume of these gaseous detectors could also be used to determine the charge and velocity of the intercepted particle.

A large fraction of gaseous detectors presently in use have wire-like anode electrodes. This geometry leads to a strong dependence of the electric field on the distance  $r$  from the wire, quite often having  $1/r$  dependence. The amplification in the wire detectors is limited to the region around the wire - usually to dimensions of the order of the wire diameter, and all electrons need to drift into this region before amplification and the signal generation sets in. The electric field near the cathodes is instead quite low. This geometry thus allows to achieve extremely good spacial resolution ( $\sim 100 \mu\text{m}$ ) as in the case of multi-wire proportional chambers or drift chambers. On the other hand, the time resolution of wire detectors is rather poor due to fluctuations in the drift time of the primary electrons. The time dependent signal on the anode wire depends on the spatial distribution of the primary ionisation produced by the minimum ionising particle (MIP). This introduces a time jitter, limiting the time resolution of wire based detectors to a few nanoseconds. In fact, scintillator detectors generally outperform the wire based gaseous detectors as far as time resolution is concerned [38].

A better time resolution is achievable if a strong uniform electric field is used instead of that of a charged wire. Here the avalanche amplification sets in instantly for all primary clusters right after primary ionisation. The intrinsic detector time resolution is then dominated by the spatial variation of the primary interaction leading to a temporal spread, avalanche statistics and noise induced triggering time fluctuations are thus

minimised. The first gas detector taking advantage of the improved time resolution in strong uniform electric fields was the Keuffel Spark Counter, a gaseous avalanche detector with parallel plate geometry, that was introduced as early as 1948 [25].

Spark Counters generally consist of two planar metal electrodes with a high voltage applied to them. The gap between the plates is filled with a gas mixture. The passage of a charged particle leaves a trail of free charge carriers (primary ionisation) in the gas, which trigger avalanches of charge carriers in the electric field. At a certain size, the avalanches transform into streamers, where photons produced by the recombination process, contribute to the spread of free charge carriers. At a later stage, a conducting plasma filament connecting the two electrodes is formed. Through this channel, the electrodes are discharged and a spark is created. The rapidly growing anode current is transformed by a resistor into a fast voltage signal and this signal can be taken as a time flag for the arrival of the charged particle. The spark mode of operation leads to large signals that need no further amplification, avoiding electronic time jitter [34]. It offered a time resolution of around 1 ns which was far better than any of the Geiger-Müller Counters that were commonly used at that time and had a timing resolution of around 100 ns. This development opened the possibility for the construction of accurate timing systems to measure the velocity of fast charged particles. However, the standard spark chamber has an area of the order of a few cm<sup>2</sup> only because as the area increases, the discharge energy in a spark becomes large enough to damage the surface of the counter electrodes. Spark Counter had metal electrodes and needed a switching-off circuit that prevented the electrodes from being short-circuited by the spark produced in the gas. It therefore had a quite long dead time ( $\sim 1$  s), which posed limits on the maximum detection rate it could sustain. In addition, it worked with low-pressure gas and had a very short operating span [34].

To overcome these problems, a new type of spark chamber introduced resistive plate electrodes and special gas mixtures for photon absorption in 1971 [26]. The discharge in the detector causes a voltage drop between the two electrodes. The resistivity of around  $10^9 \Omega\text{-cm}$  of the electrodes limits the discharge to an area around the primary avalanche and because the high voltage drops only locally, the remaining counter area is still sensitive to charged particles. The electrodes gets recharged with a time constant that is much longer than the typical time scale of the avalanche development. It

then turns out that the multiplication process is self-extinguishing when resistive electrodes are used. Moreover, if organic gases with high ultra violet absorption capability are used then charge diffusion in the gas will be prevented and the actual area of the detector which suffers from the voltage drop is localised around the primary ionisation region. The main advantage of the use of resistive electrodes is that high voltage switching off circuits are no longer necessary and consequently a higher detection rate can be achieved. The energy in the sparks is much smaller than in the case of metallic electrodes and therefore larger electrode surfaces can be used.

The first detector mounting resistive electrodes was the Planar Spark Chamber (PSC), which was built by Pestov. The signal was extracted by means of copper strips glued on the anode. The Pestov Spark Counter [27] [28] with a 0.1 mm gap achieved a time resolution of 25 ps. However, the very thin gap (0.1 mm) combined with the high values of the electric field (500 kV/cm) demand a very good surface smoothness of the electrodes. Moreover, the detector has to be operated at a large overpressure of 12 bar. This ensures a sufficiently large number of primary electron-ion pairs in the thin gap to result in a good detection efficiency. Figure 2.1 shows a simple schematic of a Pestov counter.

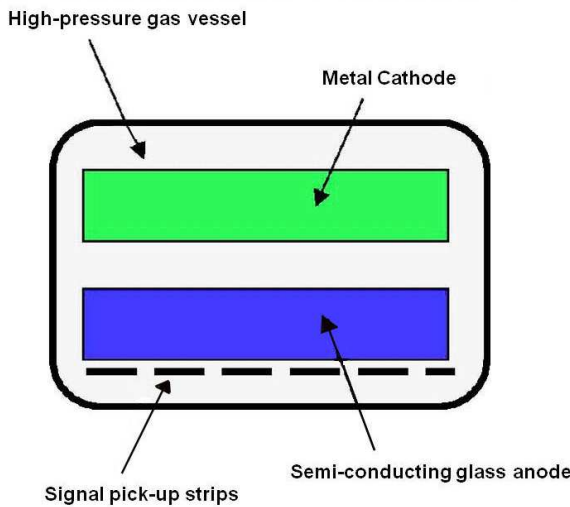


Figure 2.1: Schematic of Pestov counter [27].

A Parallel Plate Avalanche Chamber (PPAC) [30] is a single gap gaseous detector very similar to the Spark Counter. However, they are operated in avalanche mode; streamers and discharges are unwanted side effects in this type of detector. It normally

consists of two planar electrodes made of metal, or metalized ceramic or plastic, kept apart at a fixed distance of 0.5 to 2 mm by precise spacers. Its advantages include a fast response and an increased rate capability of up to  $10 \text{ MHz}/\text{cm}^2$ . The time resolution is 100 to 250 ps. Depending on the gas mixture used, a gain of  $10^3$  to  $10^4$  can be reached with a very low discharge probability of  $10^{-5}$  for minimum ionizing particles. The PPAC signals are small (about 100 fC on average) which results in a low signal-to-noise ratio. To account for a good detection efficiency, the front-end electronics has to be very low-noise and very sensitive, which often results in compromising the fast rise time needed for timing purposes. The possibility of using this technology for large scale applications therefore is questionable.

## 2.2 Resistive Plate Chambers

The Resistive Plate Chamber (RPC) was introduced in 1981 by R. Santonico and R. Cardarelli [31] as a practical alternative to the remarkable localised discharge spark counters, which ultimately achieved a time resolution of 25 ps. RPC is based on essentially the same principle as that of Pestov's Planar Spark Chamber. Nevertheless drastic simplifications were introduced in its realisation. These included absence of high pressure gas, lower requirements of mechanical precision and use of plastic materials instead of glass. The resulting detector, was found to be free from damaging discharges by construction and provided a time resolution of the order of 1 ns. Together these merits made RPCs of potential interest in a different and wider range of applications in modern experiments. In particular it has replaced plastic scintillators, based on cost considerations, whenever large detecting areas are needed in low counting rate environments.

An RPC is a particle detector utilising a constant and uniform electric field produced by two parallel electrode plates, atleast one of which is made of a material with high bulk resistivity. A gas mixture with a high absorption coefficient for ultraviolet light is flown through the gap between the electrodes. When the gas is ionised by a charged particle crossing the chamber, free charge carriers that are deposited in the gas gap trigger avalanches of electrons in the externally applied electric field and originate a discharge. Due to the high resistivity of the electrodes, the electric field is suddenly

dropped down in a limited area around the point where the discharge occurred. Thus the discharge is prevented from propagating through the whole gas volume. The sensitivity of the counter remains unaffected outside this small area. On the other hand, due to the ultra-violet absorbing component of the gas mixture, the photons produced by the discharge are not allowed to propagate in the gas. This prevents secondary discharges from originating at other points of the detector. The propagation of the growing number of electrons induces a current on external strip electrodes.

RPCs exhibit much better time resolution than wire chambers or limited streamer tubes. This is an obvious advantage arising from the uniform field as opposed to the  $1/r$  field in the wire chambers, which introduces large time fluctuations due to the electron drift motion. Very sophisticated versions of RPCs are being built recently, in which extremely flat electrodes of semi-conducting glass and high pressure gas were utilised. These detectors provide time resolutions considerably better even than those attainable by scintillators and fast photomultipliers.

## 2.3 Basic principle of operation

The task of a detector system in general is to identify and to measure the momenta and/or energies of different particles, which leave their signatures in the detectors. The physical process upon which any gas detector is based is ionisation: the passage of a charged particle through a gas volume gives rise to the production of electron-ion pairs. The drift velocity of electrons is much higher compared to that of ions. If an intense enough electric field is applied throughout the gas volume then the primary electrons produce further ionisations. This multiplication mechanism results in a distribution of free charge in the gas which has the characteristic shape of an avalanche. Recombination processes usually take place during the avalanche development. Photons are produced in such recombinations and they can in turn start the development of secondary avalanches. These are mainly produced along the axis of the primary avalanche. The regime in which several secondary avalanches are produced causing large amounts of free charge in the gas is called streamer regime. Moreover, if the ion-electron plasma is so large as to connect the two electrodes, then the so called spark is created. The propagation of the growing number of charges induces a signal on a read

out electrode.

The RPC detector in its simplest configuration is shown in Figure 2.2. Two planar electrodes made out of a resistive material (typically glass or bakelite) having bulk resistivity of  $10^{10} - 10^{12} \Omega\text{-cm}$  are spaced by a few mm. Other resistive materials such as cellulose, melamine laminate with phenolic plates, PVC, ABS etc. have also been used by researchers. The electrodes are connected to a high voltage power supply in order to create a uniform and intense electric field (about 5 kV/mm) in the gap between them. A thin layer of graphite is coated over the external surface of the electrodes to permit uniform application of the high voltage. The electrodes are kept apart by means of small polycarbonate cylindrical spacers having a diameter of  $\sim 10$  mm and a bulk resistivity greater than  $10^{13} \Omega\text{-cm}$ . A gas mixture could consist of Argon, Isobutane and an electronegative gas like Freon (R134a). Argon acts as target for ionising particles while Isobutane, being an organic gas, helps to absorb the photons that result from recombination processes thus limiting the formation of secondary avalanches far from the primary ones. An electronegative gas may serve the purpose of limiting the amount of free charge in the gas. This type of gas mixture is particularly important when one wants to avoid the onset of streamers. The surface resistivity of the graphite coating is high enough to render it *transparent* to the electric pulses generated by the charge displacement in the gas gap. For this reason electric signals can be induced on metallic strips capacitively coupled to the gap. The strips are mounted on the external surface of the gap from which they are separated by a layer of mylar insulator. Two different sets of strips oriented in orthogonal directions may be arranged on both sides of the detector to obtain measurements in both planes. The strips behave like transmission lines with typical characteristic impedance of about  $50\Omega$ .

High resistivity of the electrodes prevents high voltage supply from providing the electric charge that would be necessary to maintain the discharge between the electrodes. Therefore the electric field drops drastically in the region of the discharge causing it to extinguish. This behaviour can be understood by observing that the typical duration of the discharge is 10 ns while the time constant ( $\tau$ ) with which the electrodes are recharged is independent of the detector surface dimensions and is of the order of  $\rho\epsilon$  [32], where  $\rho$  and  $\epsilon$  are the resistivity and dielectric constant of the glass. Assuming  $\rho = 5 \times 10^{12} \Omega\text{-cm}$  and  $\epsilon = 4 \times \epsilon_0$  then  $\tau \approx 1.8$  s. The large difference between  $\tau$  and

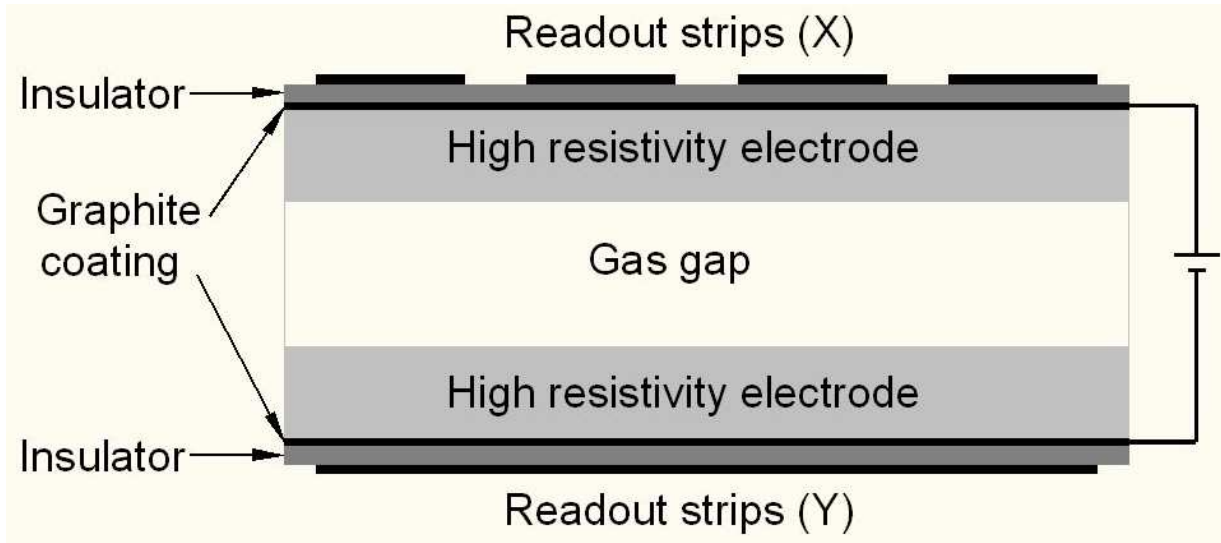


Figure 2.2: Constructional schematic of a *basic* Resistive Plate Chamber.

the typical discharge time in the detector ensures that the electrodes behave like insulators during the discharge. Hence only a limited area (typically about  $0.1 \text{ cm}^2$ ) of their surface suffers from a high voltage drop. This area stays inactive for a time interval of order  $\tau$ . This represents the detector dead time in the region of the primary ionisation. Counting rate capability of an RPC is governed by these characteristic times. Glass RPCs can therefore handle counting rates of up to about  $500\text{Hz}/\text{m}^2$  with a dead-time of less than 1%. Since typical bulk resistivity of bakelite is two orders of magnitude lower than that of glass, the rate capability of bakelite RPCs is proportionately higher.

One would expect a simple description of the avalanche propagation in the RPC as the electric field configuration in the gas gap is very simple. However, it turns out that the physical processes are very complex. The detailed simulation of the time development of the signal needs a dynamic calculation of the electric field that is sensed by the electrons in the avalanche and that gets contributions from the positive and negative avalanche charges. Especially at the final stages of the avalanche development this space charge field can easily reach the same strength as the applied electric field. At the two zones at the tip and at the tail of the electron distribution the total electric field is increased by the space charge field. At the center of the avalanche, in the region of maximum electron density, the total electric field is strongly decreased. This space charge effect is schematically shown in Figure 2.3. For avalanches approaching  $10^8$  electrons (the Raether limit), the high-field regions generate the conditions for the

development of the cathode and anode (backward and forward) streamers, while the lower field region causes the reduction of gas gain seen by the avalanche (avalanche saturation effect). Both phenomena - avalanche saturation and streamers, share a common physical origin and are normally simultaneously present.

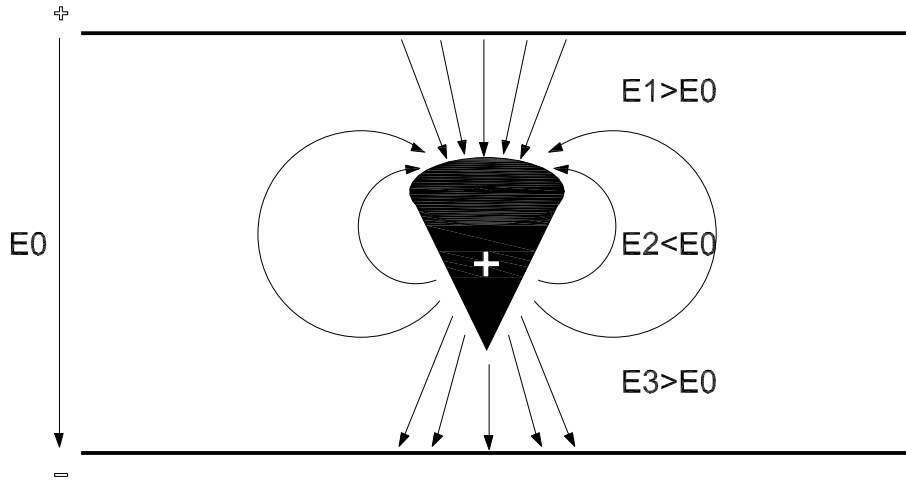


Figure 2.3: Schematic of an avalanche and the electric field variations caused by the avalanche charge carriers inside the RPC.  $E_0$  is the uniform field applied across the electrodes.  $E_1$ ,  $E_2$  and  $E_3$  are the effective fields at the tip, centre and tail of the avalanche charge distribution [34].

Even though RPCs are being developed, studied and deployed for about three decades, there are still disagreements about the explanation of several aspects of their performance. Since the introduction of timing RPCs with gas gaps of a few hundred microns and very high applied field strengths ( $\sim 100$  kV/cm), a seeming disagreement between the high efficiencies of the device and the rather low measured signal charges was observed. To explain the observed detection efficiencies, a large density of primary clusters in the used gases is necessary, which contradicts experimental values [34]. A large ionisation density provides a higher probability for the traversing particles to create electrons close to the cathode. The avalanches then travel almost the whole gas gap (cathode to anode) and can thus reach sufficient sizes to cross the detection threshold. Even in the case of a large ionisation density, the gas gain has to be extremely large to increase the number of avalanches that cross the threshold and thus explain the observed efficiencies [34]. This raises other questions: assuming exponential growth of the avalanches, the average avalanche charge would be up to seven orders of magni-

tude larger than the measured values. A very strong space charge effect is required to explain the small observed charges of around 1 pC [33] and an avalanche may not progress under such extreme conditions without developing into a streamer [35]. Another disagreement concerns the shape of the charge spectra. While the statistics of avalanche multiplication predicts a shape following a power law, measurements show a peak that becomes more pronounced at higher voltages.

## 2.4 Operating modes

RPCs may be operated in the avalanche mode (also called limited proportional mode) or in the streamer mode. In the avalanche mode, the release of the primary charge by the incoming ionising radiation is followed by the propagation and multiplication of the electrons corresponding to a Townsend avalanche. At a large gas gain a change occurs in the avalanche dynamics. Then the avalanche charge carriers influence the electric field in the gas gap and hence their own propagation and multiplication. This is called the space charge effect. When the gas gain is increased further, photons start to contribute to the propagation of the avalanche and streamers appear. At a later stage, a conductive channel is formed between the two electrodes, through which the local electrode surfaces are discharged. A weak spark may be created. While in the avalanche mode RPCs streamers are an unwanted side effect, streamer mode RPCs make use of the large current pulses induced by the streamers which simplifies the read out of the device.

The formation of the electric signal in the RPC is essentially based on the process of electron multiplication. Following the passage of an ionising particle through its gas gap, a certain number of primary electrons are created; they are grouped into clusters each of which is created by a single ionisation. The  $n_0$  electrons of a given cluster are accelerated by the electric field and start the multiplication in the gas. This process is characterised by the parameter  $\alpha$  (first Townsend coefficient), which represents the number of ionisations per unit length, and by  $\beta$  which is the attachment coefficient, i.e. the number of electrons that are captured by the gas per unit length. The parameter  $\beta$  becomes particularly important in the presence of electronegative gases. If  $x$  is the distance between the anode and the point where the cluster is produced then the number

of electrons that reach the anode will be given by [36]:

$$n = n_0 e^{\eta x} \quad (2.1)$$

where,

$$\eta = \alpha - \beta \quad (2.2)$$

The gain factor of the detector therefore is defined as:

$$M = \frac{n}{n_0} \quad (2.3)$$

Operating regimes of the RPCs - avalanche or streamer, can be distinguished by the value of  $M$ . If  $M$  is greater than  $10^8$ , then primary ionisations will give rise to streamers with high probability. On the contrary values of  $M$  much lower than  $10^8$  are low enough to prevent formation of additional secondary avalanches and the simple charge multiplication phenomenon occurs. In this case smaller amounts of charge are created and the detector is said to operate in avalanche mode. Transition into streamer regime by an RPC designed to operate in the avalanche mode is often a severe problem to deal with. This was shown [37] to depend both on the initial electric field (set up by the bias voltage) as well as by the field produced by primary avalanche.

As suggested by Y.N.Pestov, a planar detector with resistive electrodes can be modeled as a set of discharge cells which to the first order can be considered independent of each other. The simple expression of the capacitance of a planar condenser leads to the result that the area of such cells is proportional to the total average charge  $Q$  that is produced in the gas gap [38]:

$$S = \frac{Qd}{\epsilon_0 V} \quad (2.4)$$

where,  $d$  is the gap thickness and  $V$  is the voltage applied to the electrodes. This expression explains the important role played by the parameter  $Q$  in the maximum detection rate that an RPC is capable to sustain efficiently: the smaller the value of  $Q$ , the smaller the surface of the discharge cells and therefore the higher the rate capability. The average charge produced in the gas gap for an RPC operating in the streamer

mode is  $\sim 100$  pC, while in the avalanche mode the value is about 1 pC. Operation in the avalanche mode requires, however sophisticated front-end electronics. Indeed the basic idea in this mode is to transfer a large fraction of the gain factor characterising the streamer regime from the gas gap to the front-end electronics. The latter must provide large amplification factors and at the same time a large bandwidth in order not to spoil the detector intrinsic time resolution.

### 2.4.1 Avalanche Mode RPCs

High rate applications and detector aging issues made the operation in avalanche mode popular. This is achieved by substantial reduction of the charge produced in the gas gap. The counting rate capability of RPCs is improved by more than an order of magnitude if the occurrence of streamers is suppressed by operating the detector in the avalanche mode [39]. This was also facilitated by the development of new highly quenching  $C_2F_4H_2$ -based gas mixtures or with addition of small fraction of  $SF_6$  to the gas mixtures. The  $C_2F_4H_2$  gas in particular exhibits other attractive features like a moderately high density (resulting in high primary ionisation) and a low operating voltage [40]. While the physics of streamers is difficult to study, the avalanche mode is amenable for detailed simulations of the physics processes in RPCs.

Schematic images of the development of an avalanche in an RPC and the electric field deformations caused by the avalanche charges at large gain are shown in Figure 2.4.  $E_0$  is the applied uniform electric field across the gas gap. Some gas atoms are ionised by the passage of a charged particle through the gas gap (top-left panel). An avalanche is started. The avalanche size is sufficiently large to influence the electric field in the gas gap (top-right panel). The electrons reach the anode plate. The ions drift much slower due to their substantially lower drift velocities (bottom-left panel). The ions reach the cathode. The charges in the resistive layers influence the field in a small area around the position where the avalanche is developed (bottom-right panel).

### 2.4.2 Streamer Mode RPCs

As the streamer signals are quite large (between 50 pC and a few nC), no amplification is needed and the signals can be discriminated against the detection threshold directly.

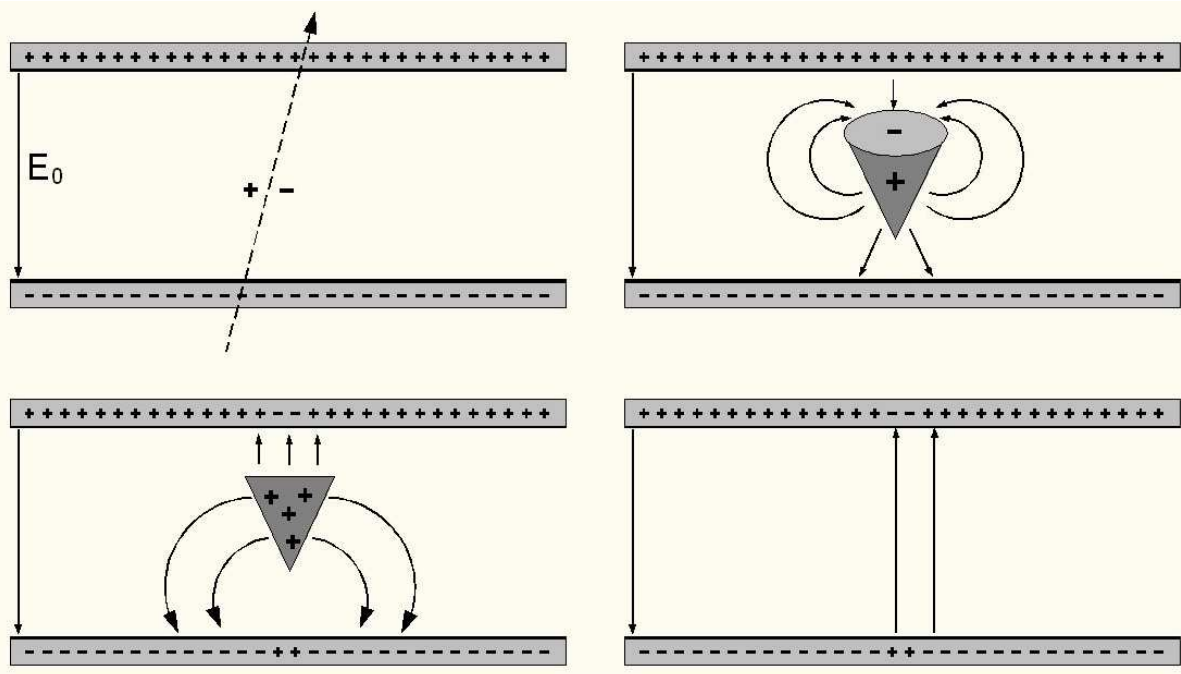


Figure 2.4: Schematic images of the development of avalanche in an RPC [34].

Thus the read out of streamer mode RPCs is quite simple. Double gap chambers operated at electric fields of 40 kV/cm in streamer mode and with 2 mm wide gaps reach efficiencies of 99% and a time resolution around 1 ns. However, the rate capability is limited to a few hundred Hz/cm<sup>2</sup>.

Schematic images representing various stages of development of a streamer in an RPC are shown in Figure 2.5. The top-left panel shows the development of an avalanche, as in the case of avalanche mode represented by Figure 2.4. The avalanche charges lead to a high field distortions in the gas gap. Moreover, high energetic photons start to contribute to the avalanche development and cause a rapid spread of the avalanche: a streamer evolves (top-right panel). A weak spark may also be created at this stage. The local electrode area is discharged (bottom-left panel). The area is localised due to high bulk resistivity of the electrode material. The electric field is strongly decreased around the spot where avalanche is formed. The detector develops a blind spot (bottom-right panel).

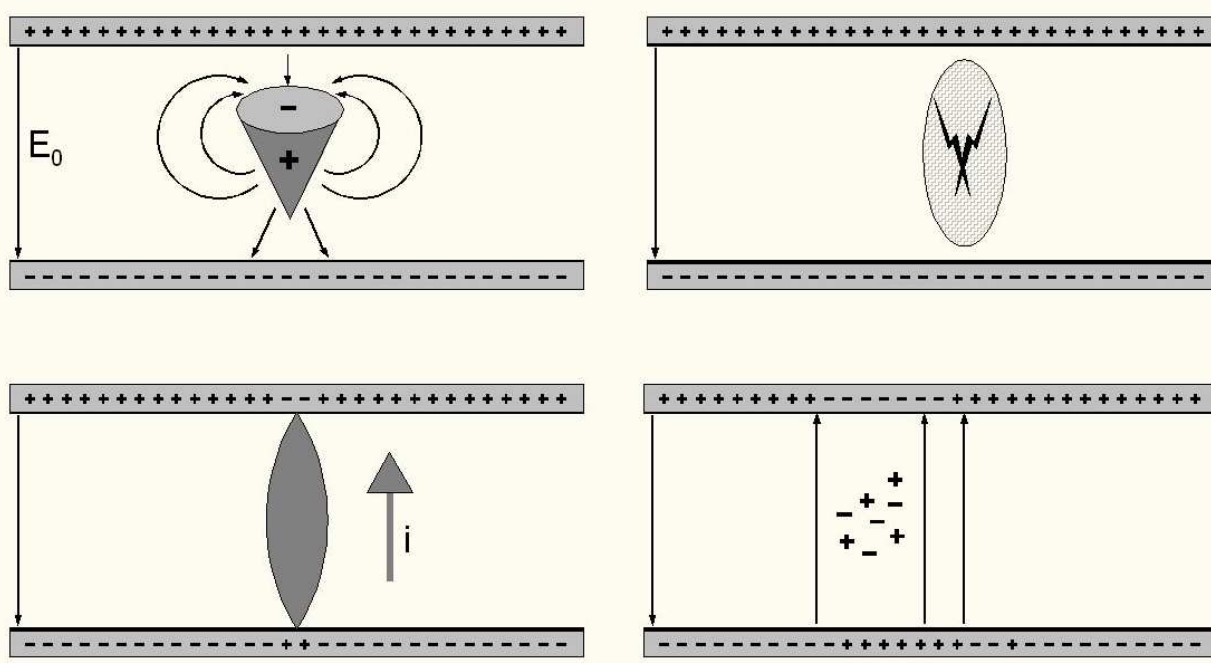


Figure 2.5: Schematic images of the development of streamer in an RPC [34].

## 2.5 Types of RPCs

RPCs are usually classified as trigger or timing depending on their application in an experiment. While, the distinction is largely subjective, the timing RPCs are expected to provide much better timing resolution compared to trigger RPCs and hence the former are typically used as Time-Of-Flight (TOF) detectors in many experiments. Trigger RPCs on the other hand typically are used to detect the passage of Minimum Ionising Particles (MIPs) such as muons and signaling the other co-detectors and their data acquisition systems to record the data.

### 2.5.1 Trigger RPCs

Large area RPCs with 2 mm single or double gaps operated in avalanche mode provide above 98% efficiency up to a particle flux of several kHz/cm<sup>2</sup>. Typically this type of RPCs are used as trigger RPCs. For example in an accelerator experiment, in order to identify the beam bunch responsible for a muon event in the detector(s) and thereby limiting random coincidences from background hits, a time resolution of around 1 ns is needed. This is easily achieved by deploying RPCs as trigger detectors.

## 2.5.2 Timing RPCs

Large area timing RPCs with a gas gap of 0.2 to 0.3 mm are widely used in multi-gap configurations and provide 99% efficiency, time resolution down to 50 ps with very small amount of cross-talk. This performance is kept at least up to an electrode area of 800 cm<sup>2</sup> per readout channel and seems to be independent of the number of gas gaps (at least up to 5). Performance of RPCs if operated in the avalanche mode with an electric field in the gas gap of 100 kV/cm, is comparable to existing scintillator-based Time-Of-Flight (TOF) technology. A very significant feature of timing RPCs is the much lower - up to an order of magnitude, price per detector channel. The possibility of simultaneous two-dimensional measurement of the avalanche position with  $\sim$ mm accuracy and time measurement with a resolution  $\sigma$  of  $\sim$ 50 ps has been recently demonstrated in even single-gap counters. They are therefore increasingly finding use in relatively small but accurate TOF systems [41].

The principle of operation of timing RPCs may be described as follows. The initial current grows exponentially in time until the discriminating level is reached. The time delay between the primary ionisation and the signal detection is independent from the position occupied by the initial charges in the gap, thus providing excellent timing. The observed timing jitter depends only on the variation of the initial current (avalanche and cluster statistics) and inversely on the current growth rate  $\alpha v$ , where  $\alpha$  is the first Townsend coefficient and  $v$  is the electron drift velocity. It is also concluded that in the first approximation, the timing resolution should be independent of the discriminator level. Both this effect and the inverse dependence on  $\alpha v$  have been experimentally confirmed [41].

## 2.6 RPC designs

The combination of resistive and/or metallic electrodes, signal-transparent semi-conductive electrode coats, highly isolating layers between the electrodes and signal pick-up panels, and different kinds of pick-up panels endows the RPCs with a rich variety of configurations, tunable to a large variety of requirements. We describe in brief various designs of RPCs below [41].

## 2.6.1 Single gap RPC

The original RPC design, included a single gas gap delimited by bakelite resistive electrodes. However, a number of improvements have taken place in the chamber since then. Glass electrodes, enjoying a mechanical rigidity and better surface quality compared to bakelite have also been considered subsequently and remain in popular use today. Electrical potential to the resistive electrodes is applied via a semi-resistive layer. Since this layer is transparent to the induced signals, it allows us to operate both the signal pick-up electrodes at ground potential. The inherent advantage of this design is absence of high-voltage capacitors and thus avoiding the need for high voltage insulation of the strips.

Most standard 2 mm gap RPCs reach a time resolution ( $\sigma$ ) of 1 - 1.5 ns, independent of the operating mode of the chamber. These results are normally obtained by using a simple leading-edge discrimination technique. Most of the RPC detector applications do not require determination of hit position of the charged particles better than about 1 cm. Therefore, usually little effort is made to optimise the signal pickup hardware for obtaining the best position resolution from an RPC detector. It was however shown that a single gap (of width 8 mm) RPC equipped with signal pick-up strips of 0.38 mm in pitch is capable of yielding a position resolution of about 115  $\mu\text{m}$  FWHM [44].

## 2.6.2 Double gap RPC

Double gap designs having a larger number of elements (such as gas gaps and pickup electrodes), allow for more varied chamber structures than the single gap ones. The double gap structure was introduced to improve the detection efficiency along with the avalanche mode of operation, which extends its counting rate capabilities. A schematic drawing of a double gap RPC is shown in Figure 2.6.

Alternately, double gap RPCs are also made of two independent gas gaps with a common pick-up panel sandwiched in the middle [43]. The avalanches produced in either or both of the gas gaps induce signals in the common pick-up strips. This design provides ease of construction and operational redundancy apart from most of the advantages of the design shown in Figure 2.6.

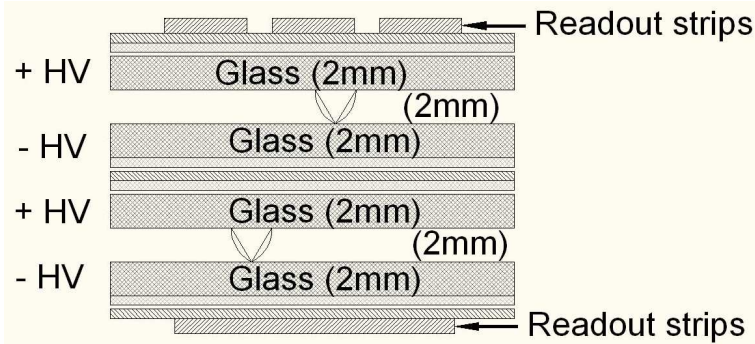


Figure 2.6: Schematic of a double gap Resistive Plate Chamber [42].

### 2.6.3 Multi-gap RPC

While the construction of the single gap RPCs is simple and well suited for most applications, there are some inherent drawbacks in its design - particularly when operated in the avalanche mode. There is only one - merged avalanche in the single gap RPC. Further, size of this avalanche is dominated by avalanche fluctuations. Ideally, the traversing particle's interaction inside the gas gap should take place close to the cathode so that clusters of ionisation are produced. Therefore, the statistical nature of ionisation process within distance (from the point of interaction to the anode) results in considerable time jitter.

In order to alleviate the problems mentioned above, a novel construction method, denominated *multi-gap RPC* was introduced, being specially suited for the construction of counters with more than a single gas gap. A schematic drawing of a multi-gap RPC is shown in Figure 2.7.

The most prominent feature of this design is the inclusion of resistive, electrically floating electrodes that divide the gas volume into a number of individual gas gaps, without the need of any conductive electrodes. According to its inventors the steady-state requirement for a null total current on each of the dividing electrodes stabilizes their potential at a value that equalizes the currents flowing in and out by adjusting the gas gain in the neighboring gaps. Intermediate plates are *transparent* for avalanche signals; thus induced signals on external anode and cathode are *analogue sum* of avalanches in all gaps. The avalanches in different gaps have the same time development. Possible drawbacks of this design are the large voltages required, and the fact that at low ionising particle fluxes the stabilising mechanism may be dominated

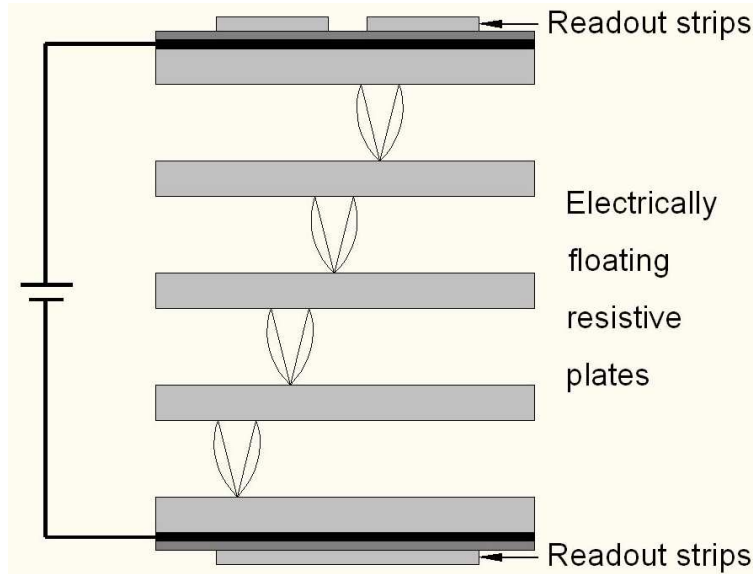


Figure 2.7: Schematic of a multi-gap Resistive Plate Chamber [47].

by the dark counting rate. For the purpose of comparing efficiency of a multi-gap RPC with that of a single gap RPC, the following expression is used [41]:

$$\epsilon_{1gap} = 1 - \bar{\epsilon}_{1gap} \approx 1 - \sqrt[n]{(1 - \bar{\epsilon}_{ngap})} \quad (2.5)$$

where,  $n$  are the number of gaps in a multi-gap RPC,  $\epsilon_{1gap}$  is the efficiency per one gap,  $\bar{\epsilon}_{1gap}$  is the inefficiency per gap and  $\bar{\epsilon}_{ngap}$  is the inefficiency of the multi-gap RPC.

## 2.6.4 Hybrid RPC

Metallic and resistive electrodes may be combined and still retain the main property of the RPC: the total absence of violent discharges. The only requirement is that no gas gap will be delimited by two metallic electrodes. Actually, the gas counter formed by two parallel metallic electrodes defining a gas gap is called the Parallel Plate Chamber (PPC). It has found wide applications in the detection of heavy ions, where wire-mesh electrodes were used, and proposed long ago for high-rate applications [45]. However, due to the violent nature of the discharges, this type of counter never found wide acceptance in high energy physics applications. A schematic example of a hybrid RPC is shown in Figure 2.8.

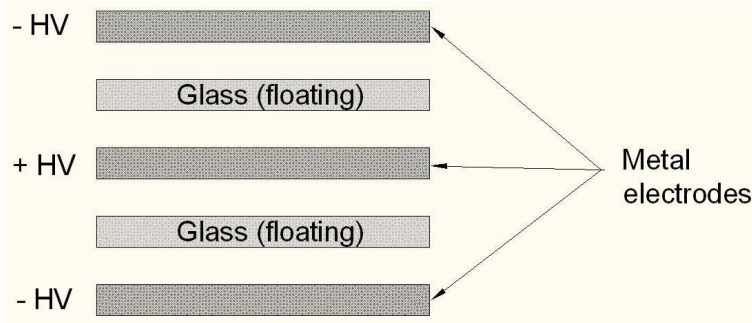


Figure 2.8: Schematic of a hybrid Resistive Plate Chamber [46].

### 2.6.5 Micro RPC

A schematic drawing of a micro RPC with a  $100\ \mu\text{m}$  gap, equipped with a solid X-ray converter and anodic strips placed at a pitch of  $30\ \mu\text{m}$  is shown in Figure 2.9. Results obtained under irradiation by a soft X-ray beam collimated by a  $30\ \mu\text{m}$  wide slit showed that mostly a single pick-up strip was hit, yielding a resolution of at least  $30\ \mu\text{m}$  FWHM in the digital counting mode. The reasons for this result are the good localisation of the primary charge given by the solid converter and the fact that most of the charge in the avalanche is developed very close to the anode. Due to its exponential growth in space, the avalanche yields a very narrow induced charge profile.

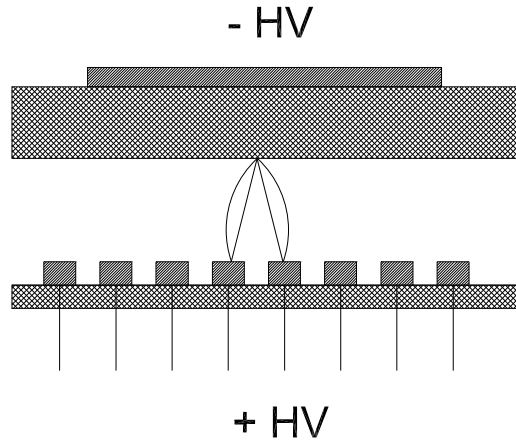


Figure 2.9: Simplified schematic of a micro Resistive Plate Chamber [48].

### 2.6.6 Special RPCs

High counting rate detectors can be built by combining classical metallic counter structures like PPC or PPAC with low resistive anodes ( $\rho = 4 \times 10^7\ \Omega\cdot\text{cm}$ ). The resultant de-

signs yield stable and discharge-free detectors. A micro RPC (Figure 2.9) with a Silicon cathode of low bulk resistivity ( $\rho = 10^4 \Omega\text{-cm}$ ) and metallic anode reaches the intrinsic counting rate limitation of metallic counters [29], indicating that no further reduction of the electrode resistivity below  $10^7 \Omega\text{-cm}$  is required for very high rate RPCs.

## 2.7 Applications and deployment

Large, RPC based detector systems had been deployed in several major experiments in the past. RPCs of many designs, employing a variety of materials, construction techniques and operating modes are also in extensive use in the experiments currently in operation as well as being prototyped for a large number of future experiments. By virtue of their flexibility in design and construction, RPC detectors are tunable and adaptable to a variety of applications and environments. Therefore, they are increasingly preferred over the other competing technologies for the accelerator as well as cosmic ray experiments and as trigger as well as timing detectors. A brief summary on the deployment of RPCs in the past and current experiments is given in Table 2.1.

Single and double gap RPCs operated in the streamer mode have so far found application in large scale high energy physics experiments such as L3 at CERN [49], BaBar at SLAC [50], BELLE at KEK [86] [51], ARGO experiment [52] at the Yang Ba Jing high altitude cosmic ray laboratory, OPERA experiment at LNGS [53], BESIII experiment [54] [55] at IHEP and the muon arm of the ALICE experiment at CERN [56]. RPCs were also used previously in NADIR, FENICE [57], E771 [58], WA92, E831, MINI [59], Cover\_Plastex [60] [61] [62] in the UK, Pierre Auger Cosmic Ray Observatory in the USA [63] and EAS-TOP [64] experiments.

RPCs operated in avalanche mode are being used on a large scale for the muon trigger systems of the ATLAS [65] [66] [67] ( $6550 \text{ m}^2$  with 355,000 read out channels), CMS [68] [69] and LHCb [70] [71] experiments on the Large Hadron Collider (LHC) at CERN to provide information on the presence of muons. Single gap trigger RPCs with 2 mm gas gaps, bakelite resistive plates and applied electric field of 50 kV/cm are used and provide above 98% efficiency and around 1 ns time resolution. Good time resolution is needed to provide bunch crossing identification for the 40 MHz proton-proton collision rate at the LHC.

Table 2.1: Summary on the deployment of RPCs in the past and current experiments. Area is given in m<sup>2</sup>, while the gap (width) in mm.

| Experiment    | Application | Area | Electrodes | Gap  | Gaps | Mode      |
|---------------|-------------|------|------------|------|------|-----------|
| BaBar         | Trigger     | 2000 | Bakelite   | 2    | 1    | Streamer  |
| Belle         | Trigger     | 2200 | Glass      | 2    | 2    | Streamer  |
| ALICE-Muon    | Trigger     | 140  | Bakelite   | 2    | 1    | Streamer  |
| ATLAS         | Trigger     | 6550 | Bakelite   | 2    | 1    | Avalanche |
| CMS           | Trigger     | 2953 | Bakelite   | 2    | 2    | Avalanche |
| STAR          | Timing      | 50   | Glass      | 0.22 | 6    | Avalanche |
| ALICE-TOF     | Timing      | 150  | Glass      | 0.25 | 10   | Avalanche |
| OPERA         | Trigger     | 3200 | Bakelite   | 2    | 1    | Streamer  |
| YBJ-ARGO      | Trigger     | 5630 | Bakelite   | 2    | 1    | Streamer  |
| BESIII        | Trigger     | 1200 | Bakelite   | 2    | 2    | Streamer  |
| HARP          | Timing      | 10   | Glass      | 0.3  | 4    | Avalanche |
| COVER-PLASTEX | Timing      | 16   | Bakelite   | 2    | 1    | Streamer  |
| EAS-TOP       | Timing      | 40   | Bakelite   | 2    | 1    | Streamer  |
| L3            | Trigger     | 300  | Bakelite   | 2    | 2    | Streamer  |
| HADES         | Timing      | 8    | Glass      | 0.3  | 4    | Avalanche |
| FOPI          | Timing      | 6    | Glass      | 0.3  | 4    | Avalanche |
| PHENIX        | Trigger     | ?    | Bakelite   | 2    | 2    | Avalanche |
| CBM TOF       | Timing      | 120  | Glass      | 0.25 | 10   | Avalanche |
| NeuLAND       | Timing      | 4    | Glass      | 0.6  | 8    | Avalanche |

One of the most successful large scale implementation of timing RPCs is the 160,000 channel, 150 m<sup>2</sup> area Time-Of-Flight barrel of ALICE experiment's particle identification detector (PID) at CERN [72] [73]. This detector employs multi gap RPCs made of glass resistive plates which are separated by 0.25 mm. The applied high voltage to the RPCs leads to an electric field of around 100 kV/cm in the gas gaps. These detectors reach efficiencies of 99% and time resolutions of better than 90 ps. Multi gap timing RPCs are also implemented in the HARP experiment at CERN [74] [75], STAR [76] [77] and PHENIX [78] experiments at RHIC, HADES [79] [80] and FOPI [81] experiments at GSI, Darmstadt. RPC systems for the CBM [82] and NeuLAND [83] experiments are under development and construction at the Facility for Antiproton and Ion Research (FAIR), GSI, Germany. The NeuLAND RPCs are made of two stacks of five glass electrodes (four gas gaps) each. The stacks are surrounded by steel absorber plates which are used for neutron detection.

## 2.8 Chapter summary

Standard RPC detectors today find a wide application in high energy physics and astroparticle physics experiments. They are fast, rugged, relatively free of potentially damaging discharges and affordable. They offer two operation modes with similar efficiency and time resolution characteristics. The corresponding signal charges are tunable - ranging from a few pC for the fast signal in avalanche mode to a range of 50 pC to a few nC in the streamer mode. Commonly used 2 mm wide single gap RPCs provide detection efficiency of about 95% for minimum ionising particles. Efficiencies above 99% also are routinely reached by the use of two or more gaps sharing the same readout structure. A good time resolution, from 1 to 2 ns, is also routinely achieved in either operation mode. State-of-the-art RPCs reach counting rates up to a few kHz/cm<sup>2</sup> in the avalanche mode and up to a few hundred Hz/cm<sup>2</sup> in the streamer mode.

Timing RPCs, made with glass electrodes that define several thin (0.1 to 0.3 mm) gas gaps, have reached time resolutions of 50 ps, opening perspectives for affordable high-granularity time-of-flight detectors. This performance is kept at least up to an impressive electrode area of 800 cm<sup>2</sup> per readout channel and seems to be independent of the number of gas gaps (at least up to 5). They usually provide scalable efficiencies of about 45% per 0.1 mm gap. Very high rate operation (10 MHz/cm<sup>2</sup> at a gain of  $5 \times 10^4$ ) was demonstrated for two different counter constructions, both featuring medium resistivity electrodes ( $10^4$  to  $10^7$  Ω-cm).

An excellent position resolution of 30 μm FWHM for X-rays in digital readout mode has also been reported. These new developments may open new applications in medical imaging and reliable high-rate tracking of minimum ionising particles.

---

## Development and characterisation of RPCs

The India-based Neutrino Observatory (INO) collaboration is planning to build a massive 50 kt magnetised Iron Calorimeter (ICAL) detector, to study atmospheric neutrinos and to make precision measurements of the parameters related to neutrino oscillations. About 30,000 glass Resistive Plate Chambers (RPCs) of about  $2\text{ m} \times 2\text{ m}$  in size are going to be deployed as active elements for the ICAL detector. An aggressive R&D program to develop and characterise these large area glass RPCs was undertaken. Starting our work with chambers of  $30\text{ cm} \times 30\text{ cm}$  in size, we went on to fabricate a large number of glass RPC prototypes of  $100\text{ cm} \times 100\text{ cm}$  in size and have studied in detail, their performance and long term stability. We have essentially concluded the detector R&D programme for the ICAL detector recently by successfully fabricating and characterising  $2\text{ m} \times 2\text{ m}$  RPCs.

In this chapter, we describe the design and development of three generations of RPCs along with their characterisation and performance results. We have put in intense efforts to indigenously develop and produce a variety of materials and components required for fabrication of RPCs. We have also designed and optimised a number of fabrication jigs and quality control procedures for assembling the gas gaps. In this chapter we discuss these developments. One of the major problems we faced during this R&D work was the aging of RPCs, while they were operated in the streamer mode. We will also highlight this crucial, but an issue yet to be completely comprehended.

## 3.1 Our early work and results

We started our RPC detector R&D by fabricating and testing chambers of  $30\text{ cm} \times 10\text{ cm}$  in area. The very first chamber was assembled - without gluing, using *E*-shaped spacers between the glass electrodes to create uniform gap between them. The chamber was not even closed on sides. It was tested by housing it inside a drift chamber shell, through which gas was flown. The next version was made by machining an acrylic frame from a single sheet and gluing the glass electrodes within the frame. The chamber is closed and the gas ports were created by laterally milling the outer margins of the acrylic frame. These chambers did not work well.

The first successful attempt was when we built and operated several RPCs of  $30\text{ cm} \times 30\text{ cm}$  in size. We have used a number of materials which were gifted by our collaborators and other researchers during our initial R&D work. But we have developed our first gas system, cosmic ray telescope, data acquisition system, assembly jigs and other facilities ourselves. We describe this work and early results in the following sections.

### 3.1.1 Small RPC prototype designs and fabrication

We have used 2 mm thick standard Asahi [84] float glass procured from the local market in Mumbai. We have chosen float glass over bakelite due to its excellent surface uniformity achieved without the surface treatment, resulting in better field uniformity and therefore less noisy operation. We found the standard deviation of the thickness measurements on 2 mm glass sheets using ultrasound thickness gauge to be less than  $20\text{ }\mu\text{m}$ . The glass sheets after passing through mechanical and dimensional tolerance tests, were cleaned of any possible oil deposits using liquid soap (*Labolene*) solution. The insulator spacers used for maintaining precise and electrically isolated gap between the glass electrodes as well as *T*-shaped frames used for supporting the electrodes and for forming an enclosed gas volume were made up of special PVC material, brand named *NORYL* [85]. We have used these materials of the design employed in the Belle experiment [86]. The spacers between the electrodes were arranged in staggered manner in order to make the gas flow inside the chamber uniform. The glass plates, spacers, frames, gas inlet and outlet nozzles are all assembled using a special 3M Scotch-Weld 2216 or DP-190 epoxy. This adhesive was chosen for its excellent shear

and peel-off strengths as well as its non-reactive properties with most of the detector gases. The leak tests of the finished chambers were performed either by maintaining overpressure of about 20 mbar for gas tightness or by using a hand-held Freon gas leak checker of model GH-202F [87]. Chambers which show leaks of typically more than 10 ppm level are re-glued.

High voltage is applied across the electrodes by means of a semi-resistive coating. We devised the following procedure for coating the glass electrodes. We mixed a locally available dry colloidal graphite powder (of Grade 40019 [88]) and industrial lacquer in about 1 : 8 ratio by weight along with thinner used for consistency. This mixture was sprayed uniformly on the cleaned glass electrode surfaces using a standard paint spray gun typically used in the auto shop. We obtained a *low*, but uniform, resistance of 100 - 200 k $\Omega$ /□ using this technique.

The signal pick-up panels were made up of poly-isocyanurate foam board [89] with reinforced poly-aluminum foil facers on both sides. While on one side of these materials, strips of required pitch were milled, the other surface was used as the ground reference for the picked up signal. Mylar sheets were used for achieving the necessary insulation between the RPC's electrode surfaces and the pickup strip panels which were mounted in contact with either side of the gas gap for the RPC operation.

Gas inlet and outlet ports were implemented by fabricating special nozzles which have standard nipples for holding the plastic gas tube on one side, while the other side of the nozzle was pressed flat to be able to slide in between the electrodes of the chamber.

We fabricated more than a dozen *small area* chambers of dimension 30 cm × 30 cm. We also made a couple of *large area* chambers of dimension 120 cm × 90 cm. Design of the small and large area chambers was identical. We have developed a number of useful jigs and tools to ascertain the quality of raw materials as well as various fabrication stages of the glass RPCs. The jigs helped us in achieving speed and consistency in the RPC production. We have also standardised all the assembly procedures of the chambers. One of the early small area prototype chambers is shown in Figure 3.1 along with some of the RPC assembly jigs developed locally.

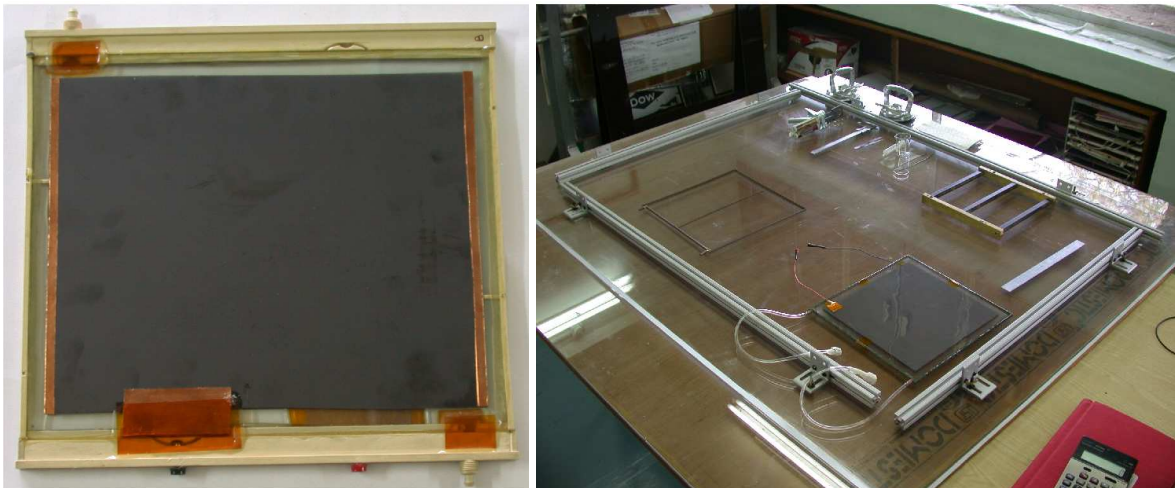


Figure 3.1: One of the first fully assembled small area prototype RPC gas gaps (left panel) along with various RPC assembly jigs developed locally (right panel).

### 3.1.2 Gas mixtures and gas system

The choice of a suitable gas mixture for RPCs is governed by factors such as low working voltage, high gain, linearity and high rate capability. For a minimum working voltage, noble gases are usually chosen since they require the lowest electric field intensities for avalanche formation. Because of its higher specific ionisation and lower cost, Argon is usually preferred. But excited Argon atoms formed in the avalanche, de-excite emitting high energy photons. These photons are capable of further ionising the gas and causing cascaded avalanches, which is often undesirable. This problem is usually solved by adding polyatomic gases, such as Isobutane to the gas mixture. These molecules act as quenchers by absorbing the photons and then dissipating this energy through dissociation or super-elastic collisions, where the kinetic energy of the two molecules in the final state is more than that in the initial state. The gas quenching can be increased further by adding a judicious amount of electronegative gases such as Freon (R134A is its eco-friendly substitute). These gases trap the unbound (to the electron cluster) but energetic electrons from the gas volume before they can initiate a new avalanche. Of late, SF<sub>6</sub> is being preferred to Freon, especially if the avalanche mode of operation is desired. It is also found that the problem of RPC aging which is known to be caused due to water vapour contamination in a Freon based gas mixture, is not observed if SF<sub>6</sub> is used. We have used Freon, Isobutane and Argon [90] gas mixture in the ratio of 62 : 8 : 30 by volume for most of our preliminary studies.

A gas mixing unit capable of mixing these four individual gas components and control the mixed gas flow through the detector chambers has been designed and developed with the help of a local industry [91]. The mixing unit has provision either to flow the mixed gas directly into the detector chambers or to store it in a pre-mix gas cylinder (15 litres in capacity) for a later use. We have used rota meters for gas dispensing instead of more sophisticated mass flow meters in order to reduce the overall cost of the unit. Complete details of the design and fabrication of this unit are given in Section 3.5. A microcontroller based gas bubble counter was developed and mounted on the output gas line of the chamber for monitoring the gas flow rate through the chamber along with a differential pressure gauge. During normal operation, approximately one volume (of the chamber) change of gas per day is adequate. We used steel tubing for gas supply lines from the gas mixing unit to the RPC test stand. We used standard Norton Tygon [92] flexible plastic tubes for short connections within the test stand.

### 3.1.3 Cosmic ray muon telescope

All the prototype chambers have been tested for their performance using a scintillator paddle based cosmic ray muon telescope. A schematic of this telescope arrangement as well the logic and timing sequence of generation of the cosmic ray muon trigger are shown in Figure 3.2.

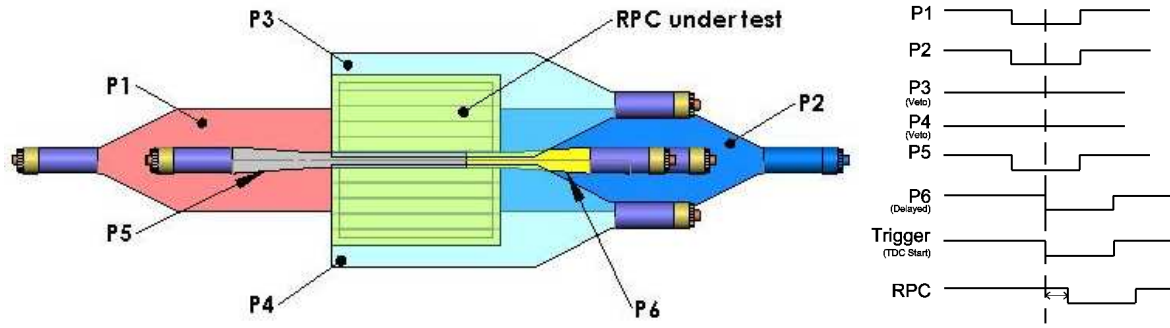


Figure 3.2: Assembly scheme of scintillator paddle based cosmic muon telescope (left panel) and its signal timing chart (right panel).

The telescope consists of four ( $P_1, P_2, P_5$  and  $P_6$ ) cosmic ray muon trigger and two ( $P_3$  and  $P_4$ ) veto paddles. The areas of these scintillator paddles are  $60\text{ cm} \times 20\text{ cm}$ ,  $60\text{ cm} \times 20\text{ cm}$ ,  $30\text{ cm} \times 3\text{ cm}$ ,  $30\text{ cm} \times 2\text{ cm}$ ,  $40\text{ cm} \times 20\text{ cm}$  and  $40\text{ cm} \times 20\text{ cm}$  respectively. A paddle is made up of a scintillator tile of 1 cm in thickness, which is

optically coupled to a Photo Multiplier Tube (PMT) for converting the scintillation light into an electrical signal. When the PMT is operated with a calibrated high voltage, the paddle gives a signal indicating the passage of a cosmic ray muon or any other charged particle through its scintillator tile volume. The geometry of the telescope using these paddles has been set up such that we define a window of about  $14\text{ cm} \times 2\text{ cm}$  for the cosmic ray muons to pass through the telescope as well as through one of the pickup strips of the RPC under test. Narrow ( $P_5$  and  $P_6$ ) paddles are used to define the telescope geometry precisely. Veto paddles are used to prevent generation of triggers when in addition to the area of interest, particles intercept rest of the RPC area, which is not under study. We record the data from RPC pickup strips whenever a cosmic ray muon particle has passed through the telescope window. This is indicated by a trigger signal, which is generated according to the following logic equation:

$$\text{Trigger} = P_1 \cdot P_2 \cdot \bar{P}_3 \cdot \bar{P}_4 \cdot P_5 \cdot P_6 \quad (3.1)$$

A suitable telescope support structure has been designed and built employing light-weight aluminum extruded channels [93]. This has allowed us to quickly and accurately rearrange the telescope to meet day-to-day requirements based on the type of study that we want to perform. Provision has also been made to align the paddles and the RPC under test using a laser pointer for a better geometrical alignment. This test set up is shown in the Figure 3.3.

The stability of the cosmic ray muon telescope is vital for reliability and accuracy of the measurements that we make on the RPC performance. One of the easiest ways to ascertain this is by monitoring the individual counting rates of the paddles as well as various coincidence logic signal rates of the telescope. This is achieved by a dedicated data acquisition system operated on continuous basis. The scintillator paddle based cosmic ray muon telescope was found to exhibit excellent stability.

### 3.1.4 Data acquisition system

A data acquisition system for RPC testing has been designed and developed using NIM and CAMAC standard electronics. A certain level of redundancy was built into the data acquisition system, in order to monitor the stability of the cosmic ray muon



Figure 3.3: A cosmic ray muon telescope set up (left panel) and close-up view of its precise alignment along with the RPC under test (right panel). RPC is seen in bright orange colour as its pickup panels are covered with a Kapton tape. The *finger* (2 cm wide) paddle and a pair of veto paddles which surround it, are all mounted on top of the RPC.

telescope as well as for acquisition of various operating parameters from the RPC under test in parallel. For example, the telescope monitor system could also be used as a backup for the RPC test system.

The telescope scintillator paddle signals were converted to NIM level logic signals by feeding them into discriminator modules operating with a threshold of  $-30\text{ mV}$  and producing a logic pulse of  $50\text{ ns}$  in width. The cosmic ray muon trigger signal was formed by the logic shown in Figure 3.4 using NIM logic circuits. This consists of 4-input *AND* of  $P_1$ ,  $P_2$ ,  $P_5$  and  $P_6$  paddles and 2-input *OR* of the veto paddles  $P_3$  and  $P_4$  in the first stage. Outputs from this first stage are *ANDED* again to generate the final trigger. The paddle signal into the logic circuit from  $P_6$  is deliberately delayed with respect to others, so as to eliminate possible accumulation of jitter of individual paddle signals on the final trigger. Using this trick, we can make sure that the timing resolution of telescope is limited by just one of the paddles (i.e. the one that completes the telescope trigger criteria).

The RPC pickup strips (mentioned in Section 3.1.1) act as transmission lines of characteristic impedance of about  $110\Omega$ . We match this to the standard  $50\Omega$  coaxial cable impedances by placing suitable impedance matching circuits on the signal lines. Analog signals from the RPC strips are directly fed in as inputs to a CAMAC charge ADC

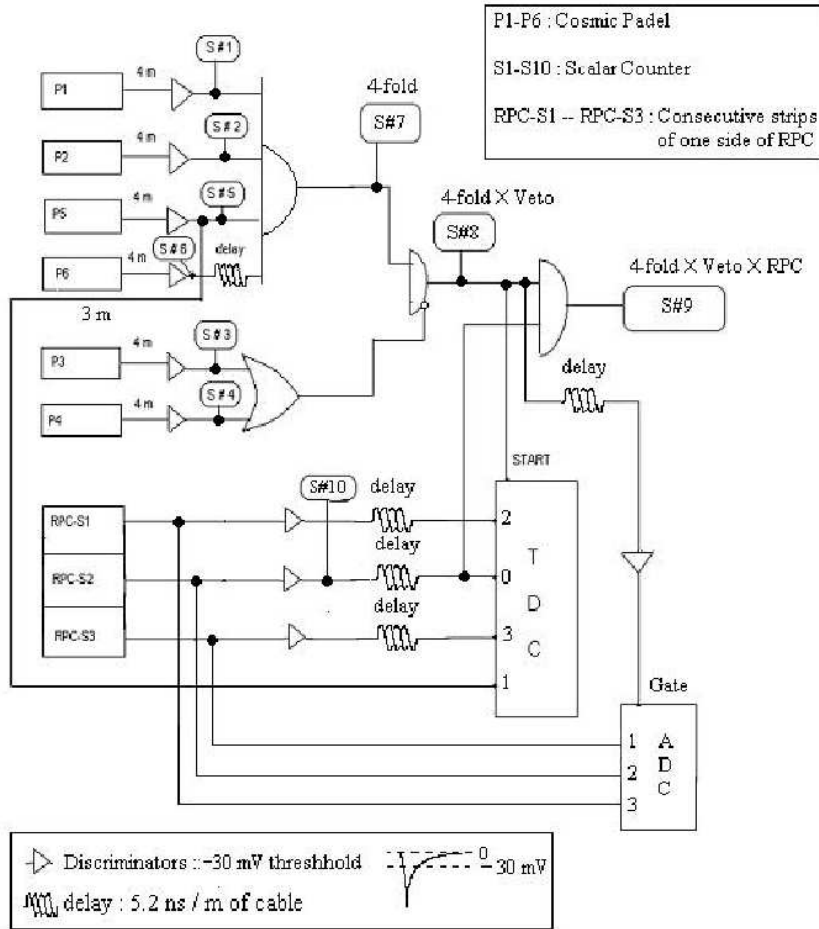


Figure 3.4: Logic diagram of the trigger signal generation and data acquisition system. The entire system is built using off-the-shelf commercial NIM and CAMAC modules.

module. These signals in parallel are also fed into discriminators for logic conversion. The NIM logic outputs of the RPC strips are again fed in as inputs to a CAMAC TDC module. The efficiency of a RPC strip channel is determined by the ratio of its coincidences with the triggers and the triggers themselves, both of which are counted simultaneously. The cosmic ray muon trigger signal is also used as a common START for the TDC module as well as a GATE signal for the ADC module. All the individual paddle signals, RPC signals as well as other coincidence signals were counted using scaler module channels.

The entire data acquisition system electronics was housed in a NIM and a CAMAC crate. The telescope monitor and RPC data acquisition CAMAC crates were individually controlled by dedicated PC hosts, in which the on-line data acquisition system software run. While the telescope monitor system collects, displays and stores all scaler

counters' data at equal chosen time intervals continuously, the RPC system waits for the cosmic ray muon trigger, to initiate data acquisition for that event. On trigger, the timing (TDC), charge (ADC) and rates (scalers) data were acquired, displayed and stored.

The data collected by the on-line systems was analysed using standard physics analysis software packages such as PAW [94] and ROOT [95]. Apart from this, various slow monitor parameters such as ambient temperature, relative humidity, gas flow into the RPC, applied high voltage, chamber current etc. are also recorded so that we can easily correlate various results or problems with recorded observations.

### 3.1.5 Preliminary results

In this section, we present some of the preliminary results obtained from several 30 cm × 30 cm chambers that we have built and operated in the streamer mode. We started our studies by studying some of the basic operating characteristics of the chambers, such as RPC pulse profiles, voltage–current relationship, individual counting (or noise) rates of the RPC and so on.

Figure 3.5 shows oscilloscope trace of an RPC signal (Channel 2) captured on a cosmic ray muon trigger signal (Channel 1). The trigger signal is a NIM level logic signal. The RPC signal shape is typical for a pulse produced by a gaseous chamber. While the prominent pulse is due to the streamer produced inside the chamber, we also notice a tiny pulse preceding the streamer pulse. This is the avalanche pulse, produced always with an excellent timing (with low jitter). However, on the flip side its pulse height is very small compared to the streamer pulse and hence needs external electronic amplification, if we want to build electronics based on this signal.

Typical d.c. characteristics of our glass RPCs operated in streamer mode are shown in Figure 3.6. Shown in the left panel is the electrical equivalent circuit representation of the RPC, while in the right panel, we show the V–I characteristics of the RPC. The RPC gas gap is represented by a parallel combination of spacer (Ohmic) resistance and gas ionisation volume of the gap (represented by a Zener diode). At lower applied voltages, the primary ionisations in the gas gap do not lead to development of avalanches. Therefore, the gas gap offers infinite resistance (Equation 3.2). The current flowing through the chamber then is entirely determined by the spacer resis-

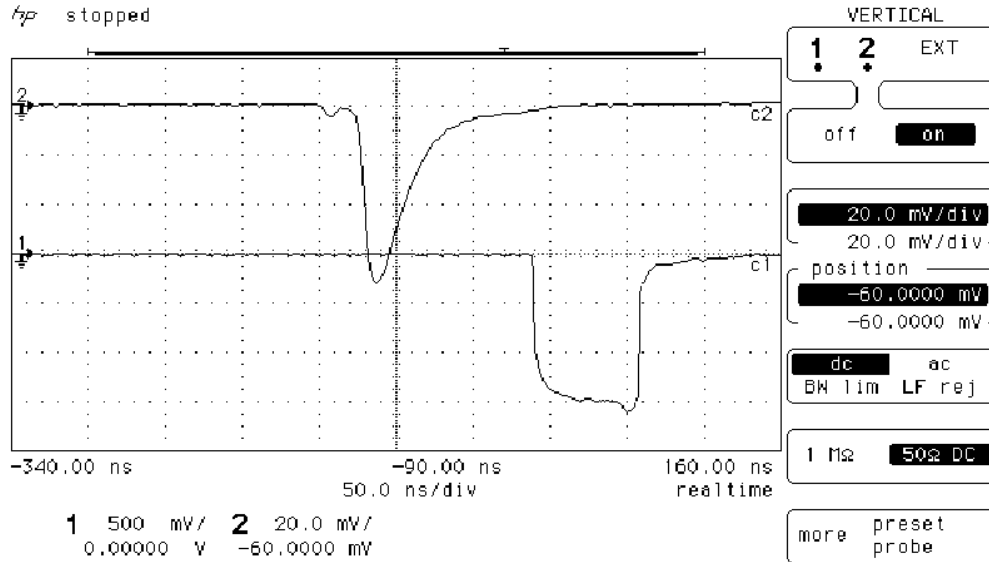


Figure 3.5: Oscilloscope trace of a typical RPC pulse produced by a cosmic ray charged particle. It may be noted that this RPC signal in the streamer mode is about 70 mV in amplitude and its *opening width* is about 50 ns.

tance (Equation 3.3). Starting from the chamber's turn-on point, the slope of the curve changes drastically as the ionisation volume almost seizes to offer any Ohmic resistance (Equation 3.4). The current flowing through the chamber in this case is determined by the glass resistance (Equation 3.5).

- At lower voltage:

$$R_{Gas\ gap} \approx \infty \quad (3.2)$$

$$\frac{dV}{dI} = R_{Spacer} \quad (3.3)$$

- At higher voltage:

$$R_{Gas\ gap} \approx 0 \quad (3.4)$$

$$\frac{dV}{dI} = R_{Glass} \quad (3.5)$$

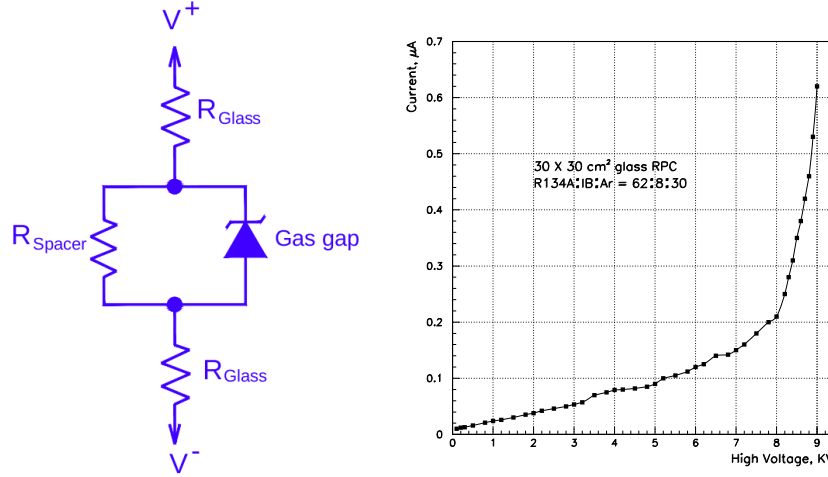


Figure 3.6: Electrical representation of an RPC gas gap (left panel) [96] and its V–I characteristics (right panel). The RPC *turn-on* point at high voltage of about 8 kV may be noted. This is also the starting point of the plateau region as will be seen later.

Noise rate of an RPC is the total counting rate of all its signals above a certain discriminator threshold. These signals are produced by the cosmic ray charged particles of all energies, due to the surrounding stray radioactivity as well as due to the dark current of the chamber. This rate per unit cross-sectional area of a particular RPC should be consistent when averaged over a reasonable period of time. The noise rate serves as a good measure to monitor the long-term stability of the chamber as well as its dark current. For instance, if the dark current of a RPC increases drastically, there will be a sharp increase in the noise rate. This might result in reduction of the actual voltage potential difference across the electrodes and hence the chamber's gain as well as its efficiency. Left panel of Figure 3.7 shows a fairly linear dependence of the noise rate of the RPC on the applied high voltage. As the field is increased, even ionisation created by lower energy particles are also amplified enough to be detected which results in increased noise rate.

The efficiency of a particle detector element is related to its ability to respond to external radiation by producing a fast and well-discriminated signal. RPCs with a higher efficiency help in detecting the track of a particle passing through the detector more accurately and efficiently. Typically this measurement is done in the laboratory using cosmic ray muons (minimum ionising particles) tagged by a scintillator paddle based telescope. The efficiency of the glass RPC as determined in our test system is defined as the ratio of number of cosmic ray muon triggers recorded in the RPC to the

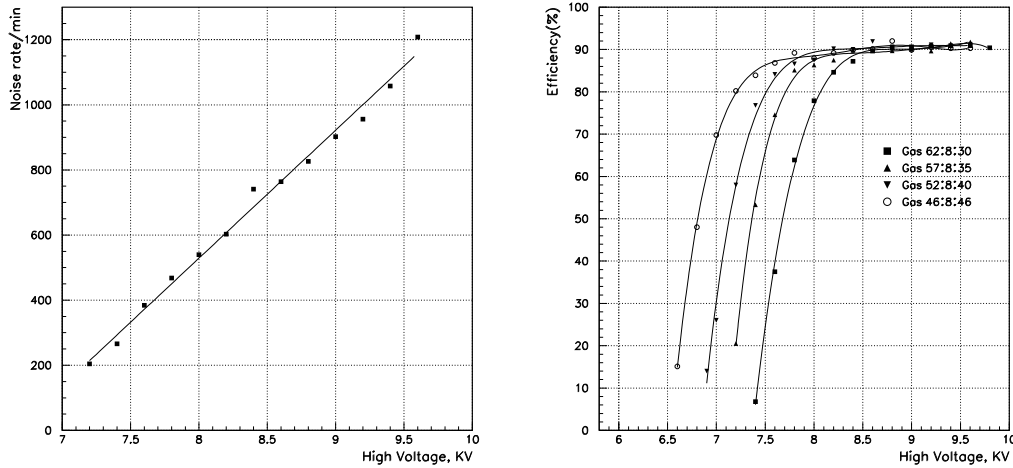


Figure 3.7: Two most important characteristics of glass RPCs: noise rate (left panel) and efficiency (right panel) as a function of its applied voltage.

actual number of muon trigger signals generated by the telescope.

The right panel of Figure 3.7 shows a plot of these efficiencies recorded from an RPC as a function of high voltage applied between the glass electrodes and for different gas mixtures. We have obtained efficiencies of over 90% on plateau for all the gas mixtures. It may be noted that as the Freon concentration is increased, we need higher electrode voltages in order to maintain the same efficiency. This is due to the fact that Freon has a high electron affinity and higher concentration of Freon reduces the streamer size. In these studies the Argon concentration is decreased in order to makeup for the increase in Freon concentration while leaving the Isobutane concentration unchanged.

Typical charge distributions of a small area RPC operated at increasing applied voltages - represented by plots from bottom right to top left, are shown in the left panel of Figure 3.8. All the studies result in good Gaussian distributions and produce clean fits. In the right panel, we show these fitted mean charges and their standard deviations as function of operating high voltages. The plot indicates the expected linear response while the standard deviations (represented by the lower fitted line in the plot) of the charge distributions are fairly constant. We can conclude from this behaviour that the RPC is operating with a good and linear energy resolution.

A typical RPC timing distribution measured with respect to cosmic ray muon telescope trigger signal is shown by the left panel in Figure 3.9. The lower plot shown for reference in this panel is of one of the telescope scintillator paddles, while the upper

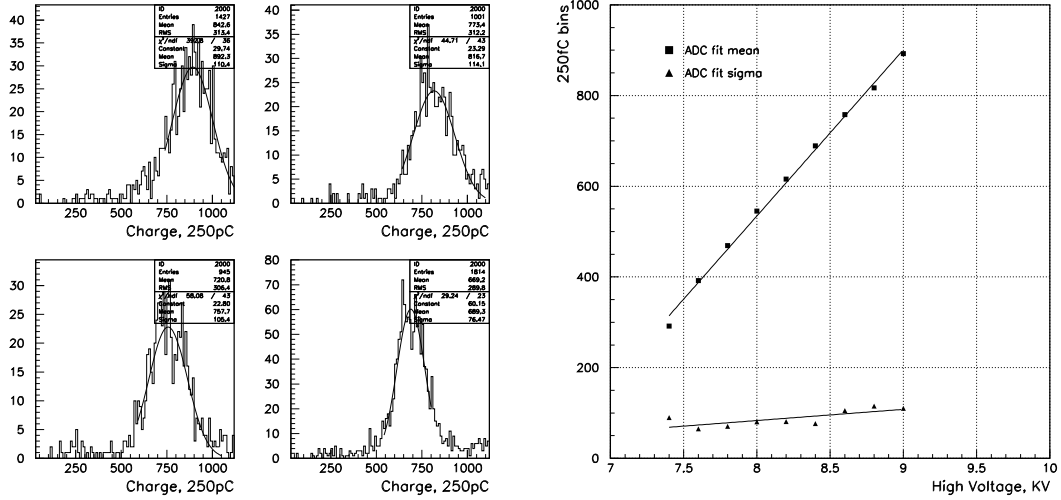


Figure 3.8: Charge collection linearity characteristics of glass RPCs. While the charge distributions (histograms) as a function of applied voltages are shown in the left panel, the right panel represents the charge linearity plot.

plot is of one of the strips of an RPC. The right panel of this figure shows a scatter plot of charge versus timing information for the same signal. It is expected that a signal of larger charge should have better (faster) rise time and hence better timing information, and vice versa. This correlation is well demonstrated by this plot. In fact, this data could also be used to correct for the *time-walk* from the actual RPC timing data.

The left panel of Figure 3.10 is the time response plot of a typical RPC as a function of its operating voltage. The gain of the chamber increases with the applied voltage and for the same amount of primary ionisation, the mean rise time improves exponentially. This is called timing response of the detector. The timing is measured through the spread in its temporal response to a charged particle passing through its gas volume, with better time response giving smaller time spread leading to a more accurate time measurement. This capability of the RPC is crucial for recording directionality of incoming particle unambiguously. The right panel of Figure 3.10 shows the timing resolution plot of a typical RPC. As can be seen from the plot, the timing resolution also improves exponentially with increase of operating high voltage and reaches the telescope timing resolution (about 1.2 ns) on the plateau. Shown in the plot with a linear fit is the timing resolution of the cosmic ray muon telescope, which is the reference for the timing measurement.

To further investigate RPC timing, we set up two RPCs in a cosmic ray test stand,

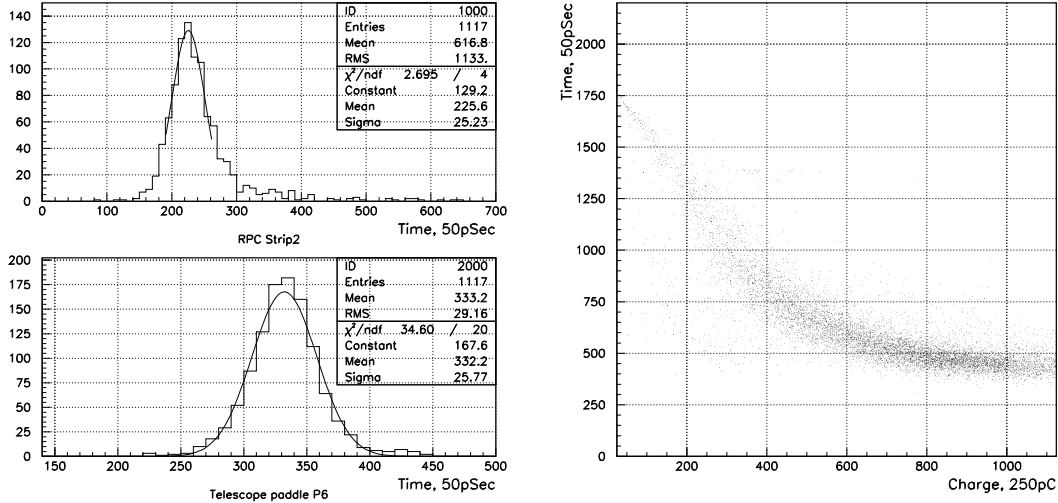


Figure 3.9: Charge-Time correlation plot of a small glass RPC is shown in the right panel. Shown in the left panel are timing distributions (histograms) of scintillator paddle (bottom) and the RPC (top). These plots indicate comparable time resolutions for a scintillator paddle and the RPC.

sharing the same telescope. The trigger was modified to add one of these RPCs' signal to the scintillator trigger. We have obtained timing distribution of the other RPC using this modified trigger as the timing reference. As shown in Figure 3.11, we have obtained a timing resolution of about a nano second when measured with reference to another RPC signal.

The spatial resolution of the detector is mainly determined by the pitch of the pickup strips. However, usable value of this parameter is limited by the cross-talk between the adjacent strips. The electrical characteristics and thickness of the pickup strips, surface resistivity of graphite coat, gas composition used as well the driving scheme of the picked up signals contribute significantly to the cross-talk. Table 3.1 summarises our measurements on cross-talk between adjacent strips for different concentrations of R134a gas in the mixture as well as telescope window widths. The telescope windows (widths) shown in the table are centred on a single RPC pickup strip of 30 mm in width. The chambers that we had fabricated have shown cross-talk of about 7% between the adjacent pickup strips.

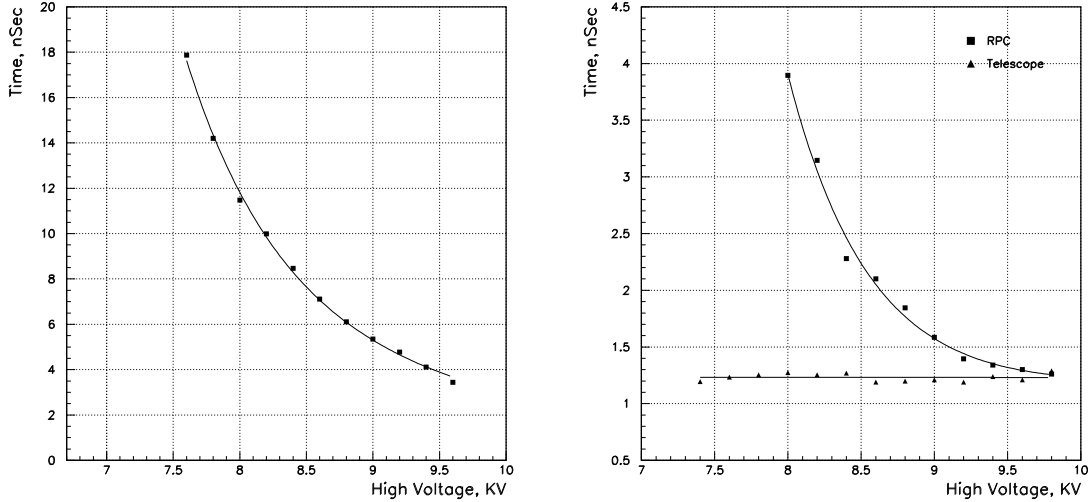


Figure 3.10: Time response (left panel) and absolute timing resolution (right panel) of a small glass RPC.

Table 3.1: Summary of RPC cross-talk measurements using pickup strips of 30 mm in width

| Gas composition<br>Ar:IB:R134A | Telescope window<br>(mm) | Cross-talk<br>(%) |
|--------------------------------|--------------------------|-------------------|
| 62:8:30                        | 10                       | 6.8               |
| 62:8:30                        | 15                       | 6.7               |
| 62:8:30                        | 20                       | 6.2               |
| 57:8:35                        | 20                       | 6.5               |
| 52:8:40                        | 20                       | 5.9               |
| 46:8:46                        | 20                       | 6.0               |

## 3.2 Tracking of cosmic ray muons

The RPCs for this experiment were fabricated using the same materials, fabrication procedures and parameters that of those described in the previous sections. Float glass of thickness 2 mm and size 30 cm × 30 cm was used. RPCs fabricated using glass which was procured from different manufacturers were used in the set up. This was done in order to make a comparison of the RPCs made using the glass from different vendors and to monitor their relative long-term performance.

The cosmic ray muon telescope seen in the left panel of Figure 3.12 was set up using seven scintillator paddles. These include one narrow paddle of 2 cm in width to define the telescope window such that it centres on an individual signal pickup

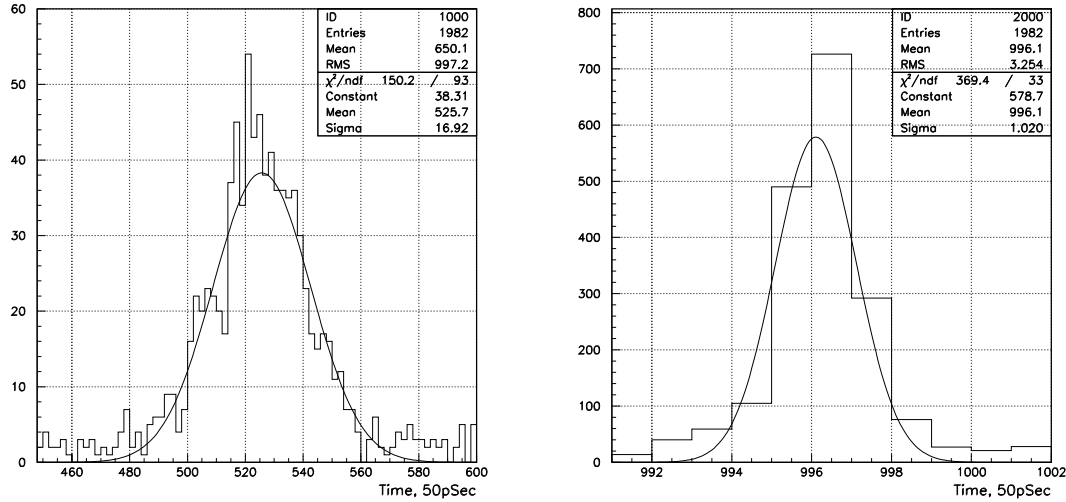


Figure 3.11: Comparison of timing resolutions of an RPC. Shown in the left panel is the timing distribution (histogram) plot of an RPC with reference to a scintillation paddle, while in the right panel is with reference to another RPC.

strip of interest. Two more paddles are used to veto triggers in which RPC is hit with particles passing outside the strip of interest as well. This arrangement has allowed measurement of cross-talk between adjacent strips.

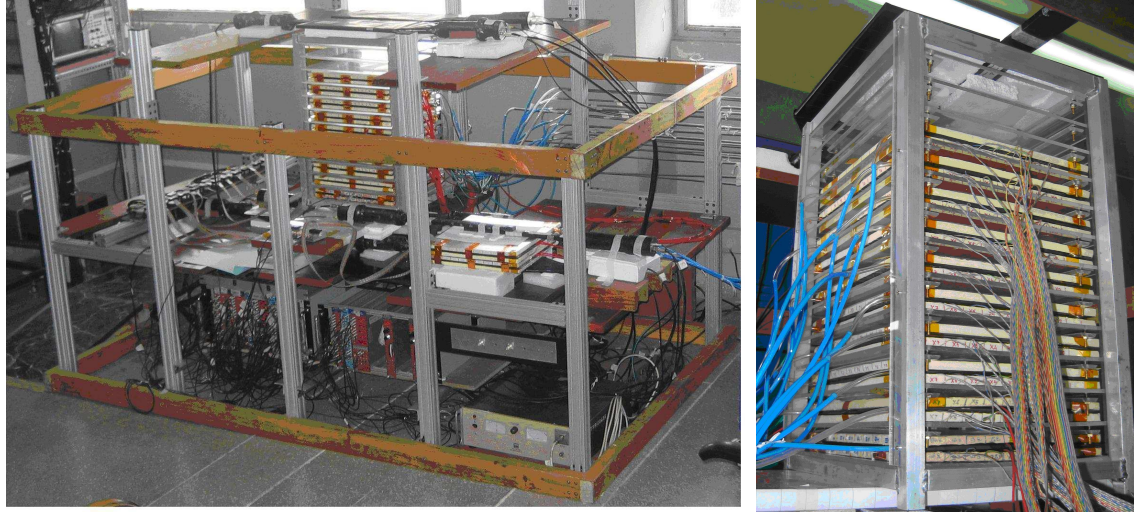


Figure 3.12: Muon tracking set up using RPC stack. Shown in the right panel is the close-up view of the stack of 10 RPCs mounted in a rack.

A suitable rack to house RPCs of the above size was fabricated. The rack allows easy access to any individual chamber in the stack. It also integrates a spring loaded mechanism to keep the signal pickup panels pressed uniformly against the gas gaps. A stack of 10 RPCs, as seen in the right panel of Figure 3.12 were mounted in the above

mentioned rack such that the signal pickup strips of all the chambers were well aligned geometrically. The chambers were operated in the streamer mode, using a mixture of argon, Isobutane and freon (30 : 8 : 62 by volume). The operating high voltage for the tests was fixed at 8.6 kV using a high voltage mainframe system, controlled via a PC Ethernet interface. The high voltage supply current was monitored on-line to diagnose any possible instability in the RPCs.

The signals from the pickup strips were transmitted through twisted pair cables onto patch panels, where the line impedances are transformed in order to match to those of the NIM electronics. The RPC strip analog signals were fed to discriminator and latch modules. The cosmic ray telescope trigger signal was used as the strobe signal for the latch modules, which record binary information on the presence or absence of a signal on the RPC strip of interest for every trigger. The noise rates of the RPC strips of interest were counted with scalers using the corresponding logic signals. The logic signals from the strips were also used to record the timing information from the RPC, with respect to the cosmic muon trigger, with the help of TDC modules. The strips of only one pickup panel per RPC were read out. We have developed an on-line data acquisition software, which records event data on trigger, reconstructs and displays the tracks, saves event data for further analysis etc. The software runs monitoring jobs such as trigger rate and RPC strip noise rate counters in the background. The software also offers a host of off-line facilities such as replaying the recorded data, binning and generating data histograms in the Microsoft Excel data format etc.

Figure 3.13 shows some interesting cosmic ray muon induced tracks recorded using the above set up. Muons arriving at different angles could be captured simply by relocating the telescope window. This experiment has demonstrated that even these small prototype chambers were capable of effectively tracking cosmic ray muons [97].

The information recorded in these tests was also used to extract other parameters of interest, such as efficiency, noise rate and timing of individual RPCs and their long term stability. Figure 3.14 shows total hit distributions of various RPCs in the stack with reference to cosmic ray triggers, their individual computed efficiencies and strip hit multiplicity distribution patterns of a couple of RPCs. While the strip hit multiplicity plot shown on left is an ideal one, the RPC whose plot is shown on the right seems to show a highly undesirable level of cross-talk between the strip of interest and

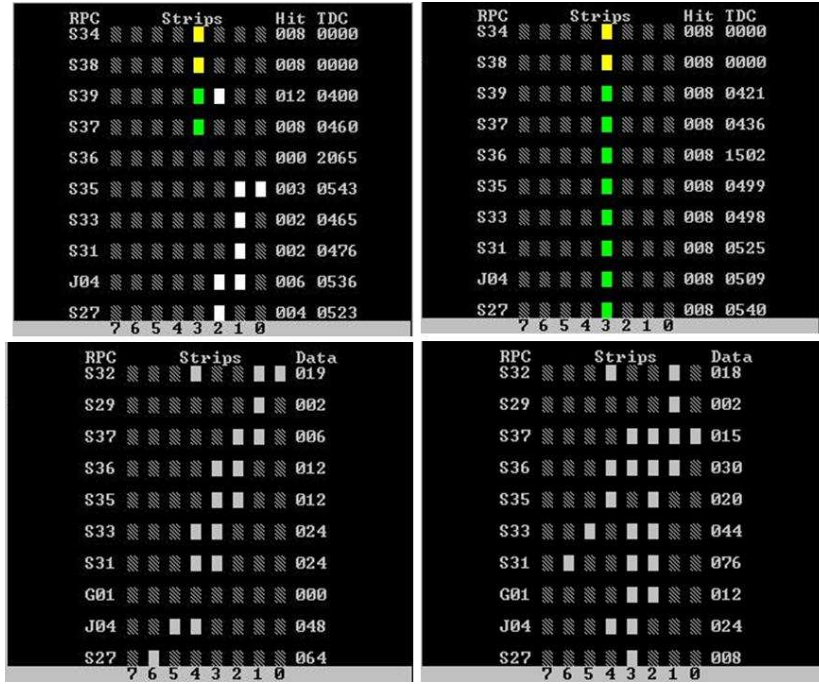


Figure 3.13: Some interesting cosmic ray particle tracks recorded by a small RPC detector stack, measuring about one cubic foot. Only eight strips from one of the two detector pickup planes per RPC were instrumented in this setup.

its neighbour. Parameters such as temperature, barometric pressure and relative humidity were also monitored on-line in order to collate and correlate the dependence of chamber performance on these ambient parameters.

### 3.3 RPC aging problem

As described in the previous sections, we have fabricated a number of prototype glass RPCs of various designs and studied their performance in detail. The results obtained from most of the chambers at the beginning were on expected lines and their measured parameters were in good agreement with those reported in the literature. However, we soon started facing a serious problem with regard to the long-term stability and performance of these chambers.

While the newly fabricated chambers initially showed good efficiency, timing, V-I characteristics as well as noise rates, their performance was found to degrade suddenly - after a few weeks of continuous operation. While the efficiencies dropped (Figure 3.15), their chamber current and noise rates used to shoot up. This problem has been reported in the literature [98]. We have shown in the Figure 3.16, differential (top

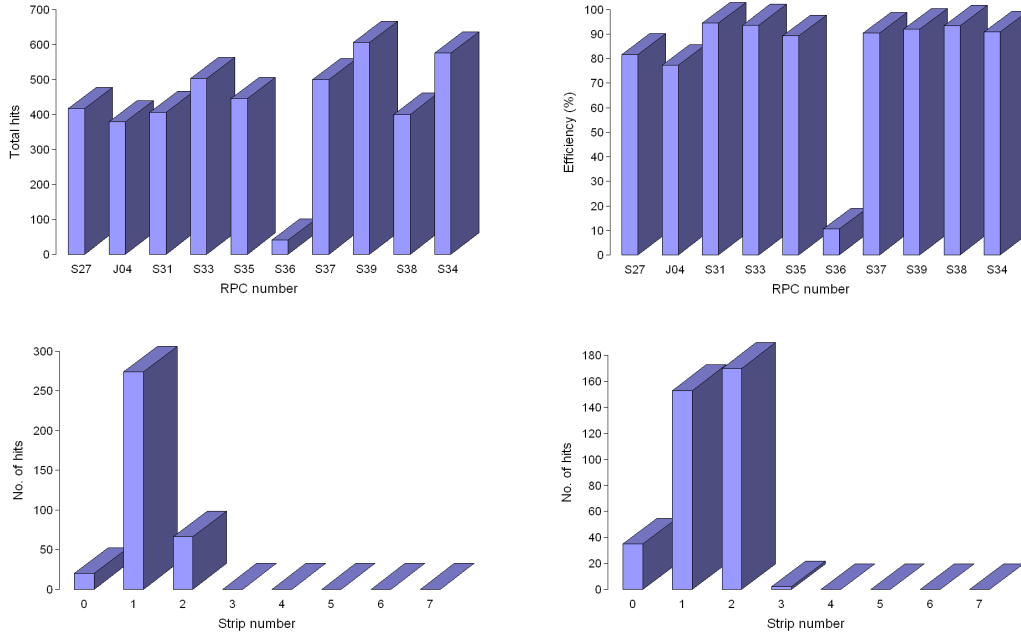


Figure 3.14: A few of the extracted RPC parameters from the data recorded by the stack.

panel) and integrated (bottom panel) noise rate history of two glass RPCs which were being operated simultaneously. Sudden changes in the slopes of integrated noise rate plots of both the chambers, further accelerating the aging process, are clearly visible.

The reason that was suggested for this problem is possible contamination of the detector gas with impurities - moisture being the most responsible. Controlled studies have shown that moisture contamination to a level of 1000-2000 ppm in the detector gas can damage the RPC after about two weeks of continuous operation. While some forms of this damage could be reversed by switching back to the dry gas, other forms cause irreversible damage to the chamber [99]. We have also tried the following recipe [100] for recovering the damaged chambers, with limited success. The method involved flushing the chamber for a day with Argon gas, bubbled through water containing about 3% ammonia, followed by a few weeks of training the chamber with dry gas. Chamber parameters such as the efficiency and noise rate could be recovered close to their original values, but the chamber could not sustain the performance for long after the recovery.

One of the plausible chemical reactions causing damage to the electrodes is formation of Hydrogen Fluoride (HF) inside the gas gap. The Freon (R134A) gas which is present in the gas mixture, decomposes under electrical discharge and produces a sig-

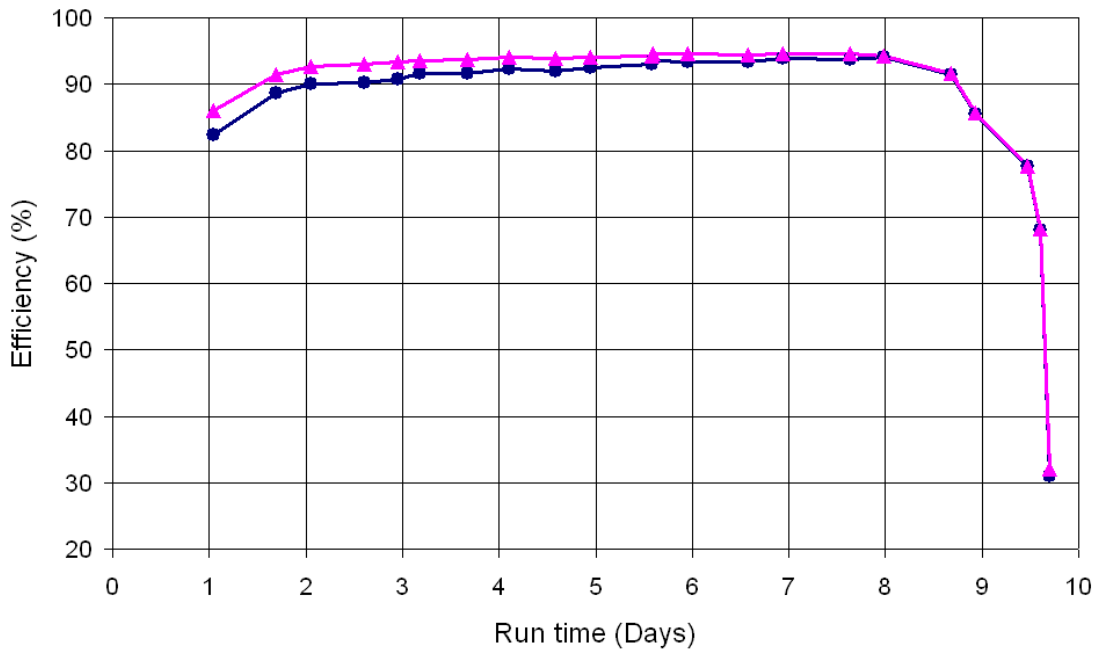


Figure 3.15: Efficiency time profile plot of an RPC undergoing the aging process. The drop in the efficiency is rather sudden.

nificant concentration of Fluoride radicals. These radicals react with traces of moister present in the gas mixture to form the Hydrogen Fluoride. HF is an aggressive acid. Due to its high chemical reactivity, it causes damage to the inner surfaces of the glass electrodes. The work-function of the electrode surfaces is reduced and thus leads to field emission of electrons from the cathode. This in turn reduces the electric field inside the chamber below the efficiency plateau and causes a permanent efficiency drop. This regenerative process is also responsible for sudden rise in the noise rate, caused by severe field disturbances and local discharges inside the gas volume.

This was confirmed by studying the damaged electrodes using an Atomic Force Microscope (AFM) (Figure 3.17) and a Scanning Electron Microscope (SEM) (Figure 3.18). We have noticed deposits of about 500 nm in area and about 100 nm in thickness on the inner surfaces (which were in contact with the gas in the chamber) of the glass electrodes. An elemental analysis using X-Ray Diffraction (XRD) technique on the samples has shown that while the Fluorine content in the raw glass was about 4% by weight, in the damaged electrode sample it had increased to about 38%.

We have also taken direct measurements of moisture levels on the input gas lines using a commercial moisture meter [102]. We have noticed higher moisture levels in

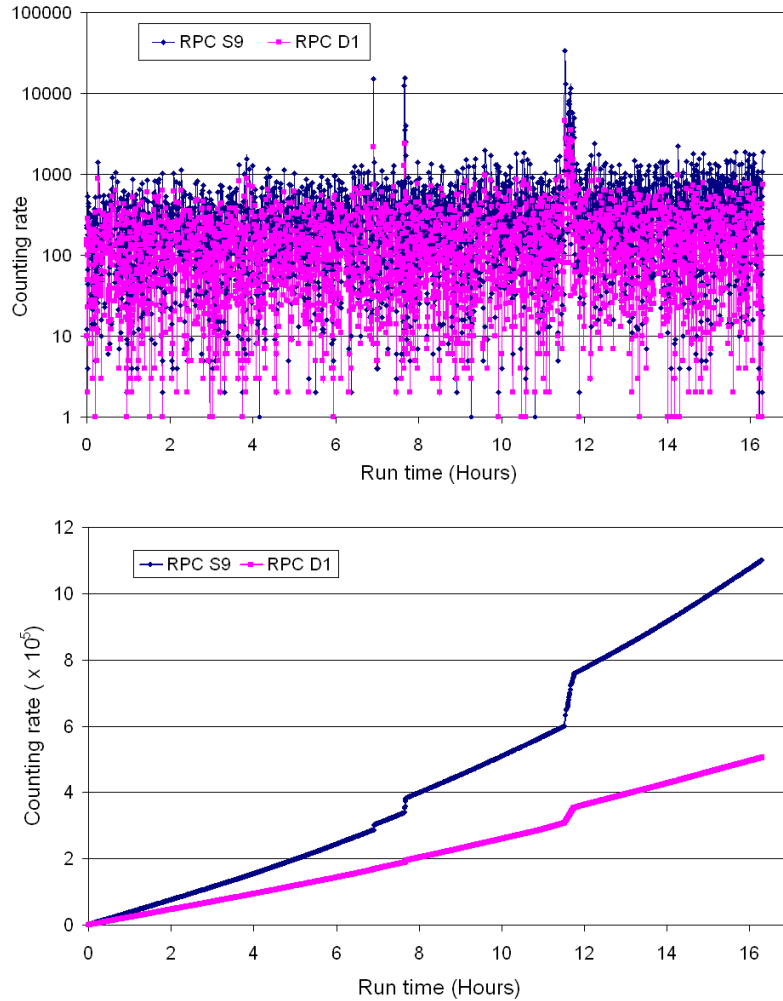


Figure 3.16: Noise history of two RPCs showing signs of aging. Differential noise rate is shown in the top panel, while the bottom panel shows their integrated noise.

the R134A gas (400 ppm), while the moisture levels in the Argon and Isobutane gas seem to be under reasonable limits (60 ppm and 140 ppm respectively). We have subsequently installed silica gel and molecular sieve cartridges on the input gas lines to filter out the moisture from the bottled gases. We have also installed a dehumidifier in the laboratory.

## 3.4 Long-term stability tests of RPCs

Although glass RPCs operating in the streamer mode are known to be stable and have a long lifetime as evidenced by the successful operation of these chambers in the Belle and other experiments, as reported in the previous section, our RPCs had shown signs

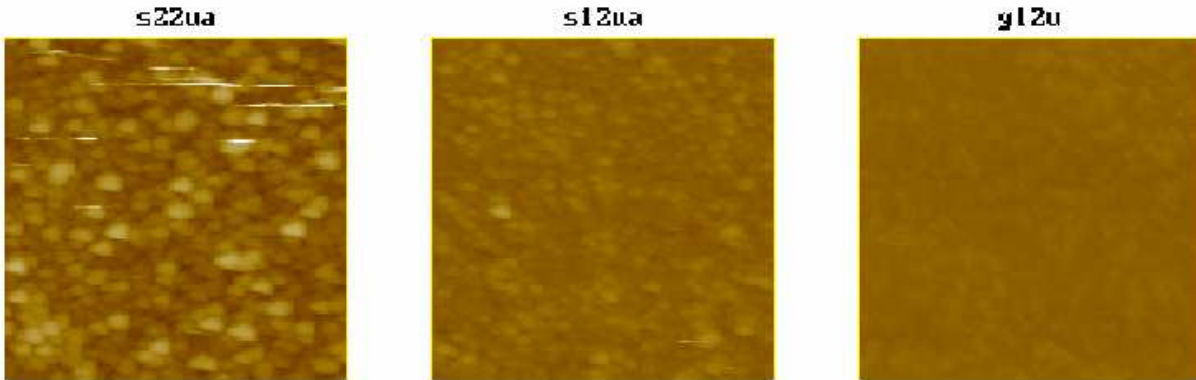


Figure 3.17: AFM pictures of damaged glass electrode surfaces [101]. The scans are carried out on  $2\text{ }\mu\text{m} \times 2\text{ }\mu\text{m}$  areas.

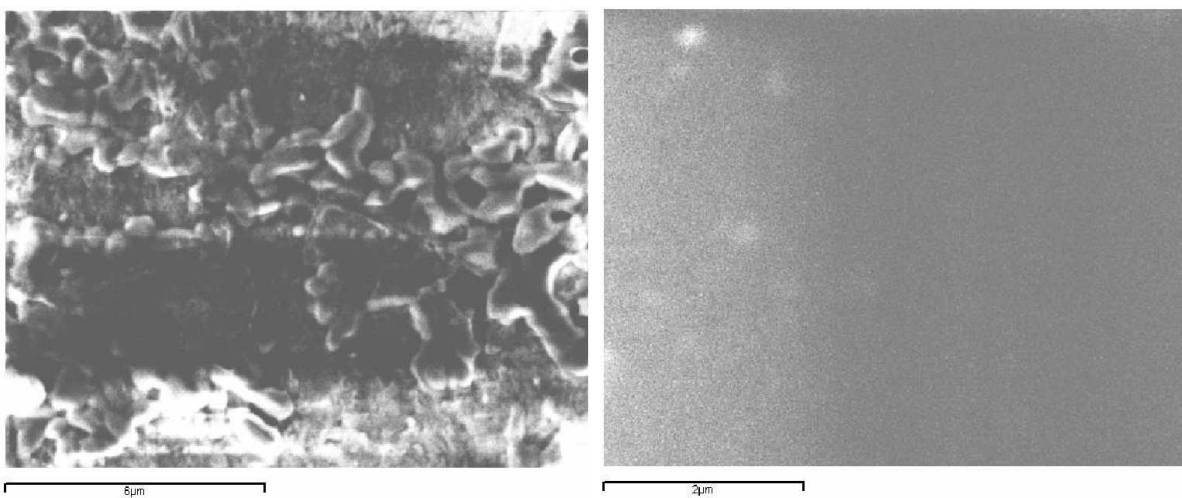


Figure 3.18: SEM pictures of damaged glass electrode surfaces (left panel). In the right panel we show SEM scan of a raw glass surface for reference.

of early detector aging. Studies on the long-term operation are mandatory, in view of their deployment in the ICAL experiment that will be taking data for several years.

While the problem of short lifetime of the glass RPCs produced by us was being investigated, we had fabricated a few RPCs of dimensions  $40\text{ cm} \times 30\text{ cm}$  using glass sheets procured from Japan. The same procedure for fabrication as well as testing as in the case of earlier RPC prototypes were followed for these new chambers using Japanese glass as well. Two of these chambers (named *J2* and *J3*) were operated in the avalanche mode, in which a gas mixture of Freon (R134a) and Isobutane in the proportion 95.5 : 4.5 by volume was used. The chambers were operated at an applied voltage of 9.3 kV. Since the pickup signals in the avalanche mode were in the range of few millivolts across a  $50\text{ }\Omega$  load in amplitude, external amplification has been provided by

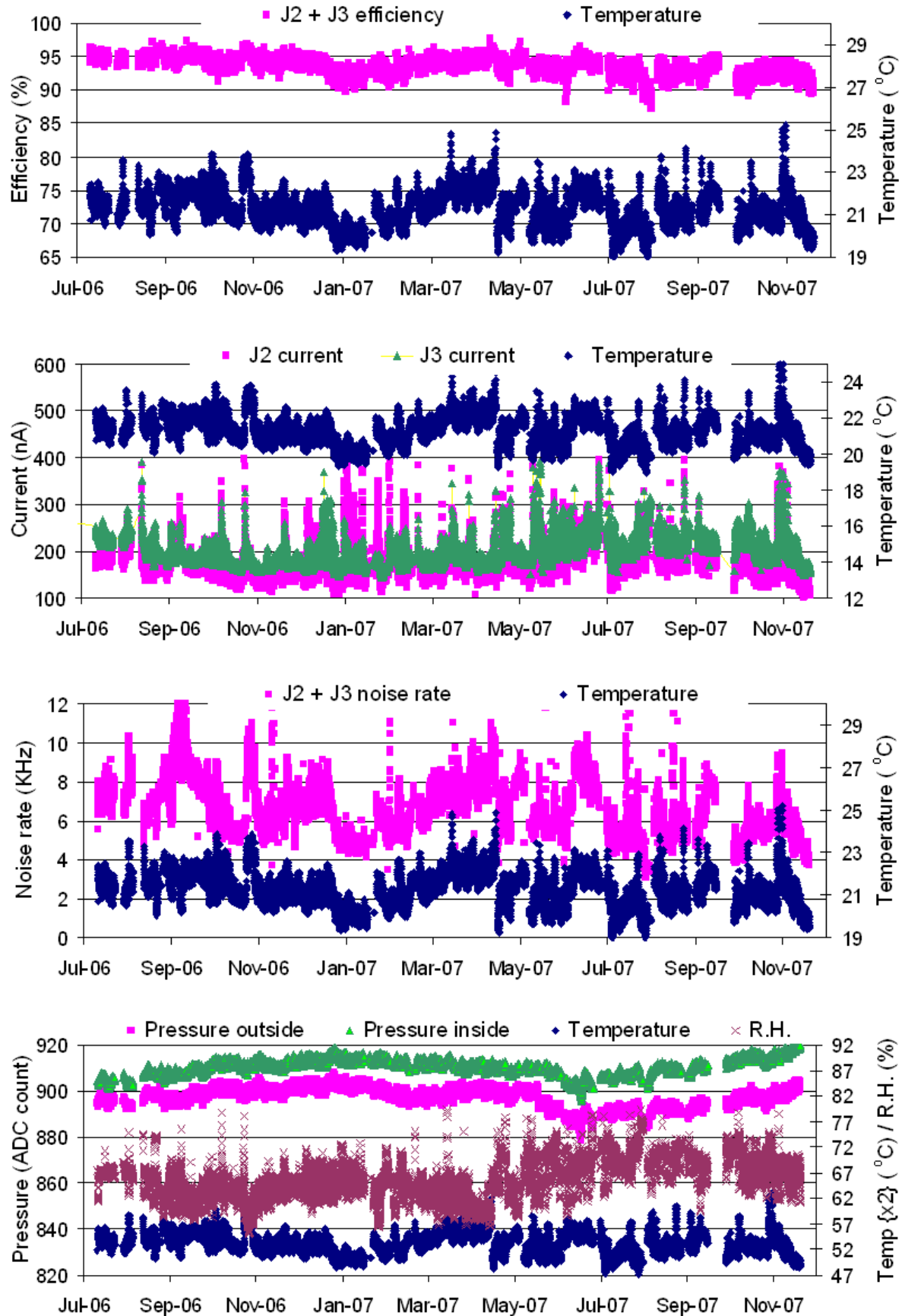


Figure 3.19: Long-term stability monitoring plots of  $J_2$  and  $J_3$  RPCs spanning over two years. Initial test data is not shown.

preamplifiers of gain 10. The rest of the electronics down-stream and data acquisition chain was the same as that used earlier.

A comprehensive monitoring system for the periodic recording of the chamber currents of these two RPCs as well as the ambient parameters such as temperature, pressure and relative humidity both inside and outside the laboratory has been designed and implemented. Using these data, several correlations between the ambient parameters and the RPC operating characteristics could be established. As can be seen from the plots in the Figure 3.19, all the vital characteristics of these chambers remained stable even after a period of two years. Shown in the top three plots are the their combined efficiency, individual chamber currents and ORed noise rate. Laboratory temperature is also plotted along with each of these RPC characteristics, as it is one of the characteristic ambient parameters representing 24-hour cycle. All the concurrently recorded ambient parameters - temperature, barometric pressures and relative humidity are shown in the bottom plot for cross-reference.

These tests have indicated that the aging problem associated with the previous RPCs was related to their operating mode - streamer mode and/or the gas mixture used. We have again repeated these studies on a large area RPC (of dimensions 100 cm × 100 cm) operating in the streamer mode using the streamer gas mixture. The chamber's efficiency dropped suddenly after surviving barely for a few weeks. This has essentially reconfirmed our earlier conclusions on the issue of detector aging.

We had an interesting data on the effect of ambient conditions on the RPC characteristics from an unintended experiment! There was an unscheduled shutdown of the Institute's air conditioning system. The temperature and relative humidity in the RPC laboratory, where RPCs J2 & J3 were being tested for their long-term stability, rose steadily during the next couple of hours. Chamber currents of J2 and J3 also started rising quickly. Shown in left panel of Figure 3.20 is the complete data during this period. As can be seen, in about two hours after the air-conditioning system failure, the laboratory temperature rose to about 75.5 °F; but the rate of increase was slow and linear. In the case of relative humidity, the rise was faster and the value reached saturation in about an hour. The bulk of the increase in chamber current seems to be due to an increase in relative humidity and is due to surface leakage. It is therefore understood that the pattern of current increase will be specific to the chamber due to variations in

their packaging and insulation considerations.

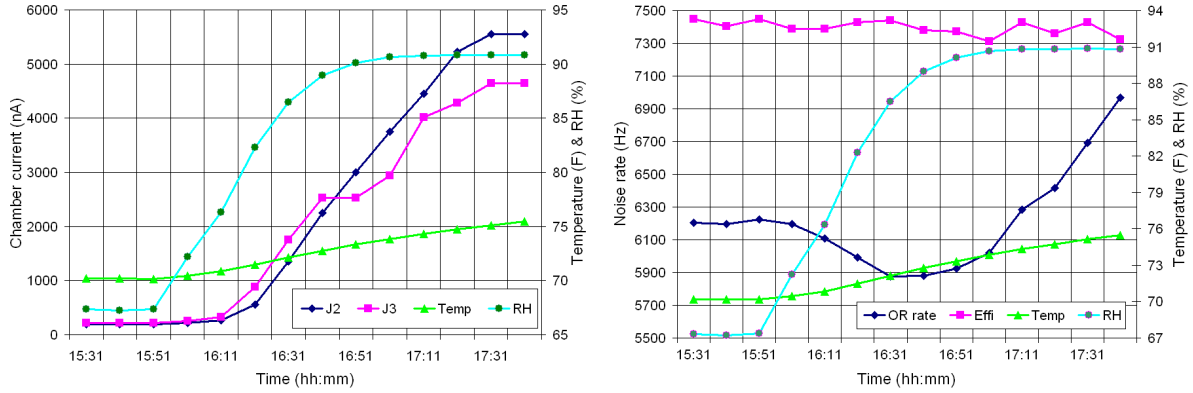


Figure 3.20: Effect of temperature and relative humidity on RPC characteristics. While the behaviour chamber current is shown in the left panel, we show their effect on the RPC noise rate and efficiency in the right panel.

It is interesting to note that typically, it takes about half an hour for an increase of relative humidity to be reflected on the chamber currents. Though the rate of increase of chamber current is not uniform with respect to the rate of increase of relative humidity, a ballpark figure of 200 nA per unit percentage rise in relative humidity is obvious. This value depends on the surface area of an RPC and its design. The chamber currents saturate along with relative humidity.

The right panel of Figure 3.20 shows the variation of noise rate and efficiency during this period. The noise rate variation has an interesting behaviour. Starting from the outage, the noise rate drops till about the time when the relative humidity saturates. From there on, it increases steadily. During this later period, the rate of increase of noise rate with respect to the lab temperature was about 600 Hz/°F. The increase of the chamber's noise rate with temperature can be ascribed to the increase of spurious pulses due to the decrease of dead time of the chamber. This follows from the reduction of glass resistivity, which decreases exponentially with temperature according to the following relationship [104]:

$$\rho = \rho_{20} 10^{(20-T)/25} \quad (3.6)$$

where,  $T$  is the temperature in °C and  $\rho_{20} = 10^{13}$  Ω-cm represents the glass resistivity at 20 °C. The rate capability of glass RPC improves with temperature, due to the lowering of glass resistivity.

The all important characteristic, the RPC efficiency, does not seem to vary appreciably with these drastic changes in the ambient conditions. There is a drop of about 1% in the efficiency at most.

## 3.5 Development of gas systems

Proper and efficient functioning of the RPC detector demands pre-mixing or on-line mixing of individual gases, in an appropriate proportion, together with a controlled flow of mixed gases through the detector. This is usually achieved either by using gas mixing and distribution systems or gas recovery and recycling systems. In the former, the gas mixture leaving the detector is collected in a manifold and vented to atmosphere, whereas in the latter, it is collected and re-circulated after appropriately purifying it and adding small amounts of fresh gases.

We have designed and developed two generations of gas mixing and distribution systems. The first one features a single output channel and employs rota-meters to mix the input gas in the required proportion. The mixed gas is stored in a reservoir cylinder and subsequently allowed to flow through the output channel. The salient features of this system are described below.

The input gases are controlled through two-stage gas regulators mounted on the cylinders. The gases are then passed through silica dryer cartridges installed on the steel gas lines, where common contaminants such as water vapour, oil traces etc. are removed. The gases then enter the rota-meters, which are used to control the gas flow rate through the line precisely. Individual solenoid valves mounted after the rota-meters are used to allow the individual gases enter the bulkhead interface. A three-way solenoid valve on the bulkhead is used to let the mixed gas flow on-line into the detector under test or to fill up the pre-mixed gas cylinder for later use. Another three-way valve further down-stream allows either the pre-mixed gas stored in the cylinder through the detector or let the cylinder be evacuated. Either the bulkhead interface or the pre-mix gas cylinder can be evacuated using the vacuum pump. A schematic diagram and a photograph of this first generation gas mixing and distribution system is shown in Figure 3.21.

Even though, we have used this system extensively for the initial phase of our de-

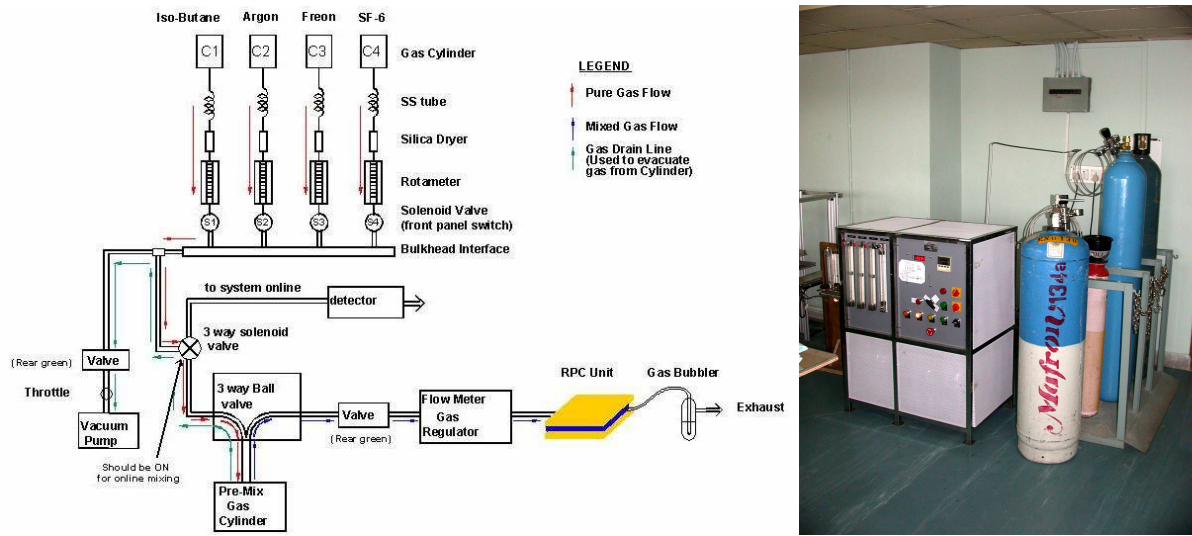


Figure 3.21: Schematic diagram (left panel) and a photograph (right panel) of this first generation gas mixing and distribution system.

tector R&D programme, the utility of the first generation system was limited to gas flow in only one detector chamber. Parallel connection of RPCs on the single output channel of the system did not result in uniform flow through the chambers as their individual resistances to the gas flow are different. We have therefore designed a rotameter based six channel distribution system as an add-on unit to the gas mixing system. We have also mounted an additional alumina based moisture filter on the gas system's output line. The alumina is reactivated from time to time using the built in electric heating element.

In the next phase of development, we have designed a Mass Flow Controller (MFC) based on-line gas mixing and multichannel distribution system [103]. This system is capable of mixing four input gases (Argon, Freon (R134a), Isobutane and SF<sub>6</sub>) on-line by the volumetric method, and distributing it simultaneously to sixteen individually controlled output channels. Equal gas flow rate in each of output channels is maintained by using capillary tubes which serve as flow resistors. The return gas from the chambers is collected in a common manifold and is vented out to the atmosphere. The gas system is described in the following sections.

### 3.5.1 Overview of the gas system

Broadly, the on-line gas mixing and multichannel distribution system comprises of a gas purifier column, a gas mixing unit, distribution panel and an exhaust manifold.

Safety and isolation bubblers, moisture meters, controls for monitoring and remote operation, and a set of gas cylinders together with manual and pneumatic valves are the other important parts of this system. A schematic diagram and a photograph of this second generation gas mixing and distribution system are shown in Figure 3.22. The molecular sieve in the purifier column absorbs moisture and purifies the gas flowing through it. The mass flow controller (MFC) based mixing unit ensures controlled flow of gas. Flow resistor (i.e., capillary tube)-based distribution panel allows for connecting sixteen RPCs in parallel and maintains uniform flow in all of them. While the safety bubblers serve to protect the RPCs from getting over pressurised, the isolation bubblers prevent back diffusion of air into the RPC and also indicate the gas flow. All the gas to be vented is collected in an exhaust manifold and a single output is provided to vent out the used gas into atmosphere. This manifold has a pressure sensor to indicate the difference between room pressure and the exhaust pressure. In addition to the above, a provision for on-line monitoring of input gas pressure and moisture content is provided, together with a possibility of setting and monitoring the gas flow through MFCs. This is displayed in standard cubic centimeters per minute (SCCM). Flow rates of individual gases calibrated in SCCM are settable from and displayed on the front-panel.

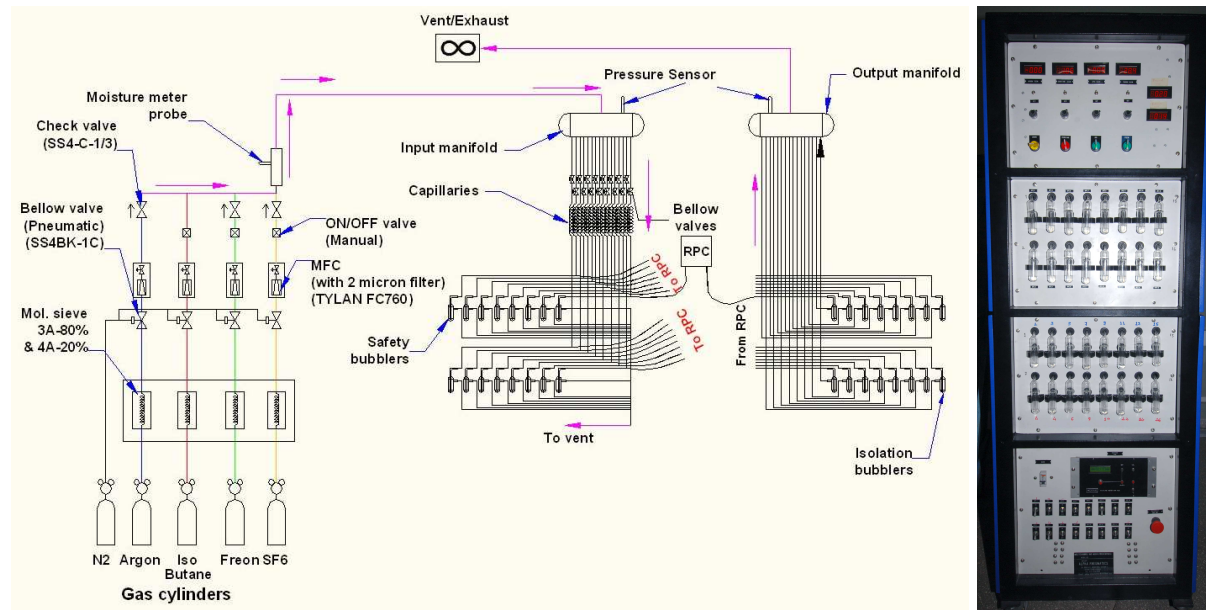


Figure 3.22: Schematic diagram (left panel) and a photograph (right panel) of the second generation gas mixing and multi-channel distribution system.

A detailed description of the design and functioning of each of the components in

the gas system is provided below.

1. Input gases: The pressures of gases to be mixed are controlled at the output of the respective cylinders by using two-stage pressure regulators. R134a and Isobutane gases are in liquid form for which low pressure input regulators of range 0 - 5 kg/cm<sup>2</sup> are used, while 200 kg/cm<sup>2</sup> pressure regulators are used for Argon and SF<sub>6</sub>. The output range of all these regulators is 0 - 5 kg/cm<sup>2</sup>. Depending on the mode of RPC operation, either avalanche or streamer, appropriate gases at optimum pressure are allowed to flow into the purifier column.
2. Gas purifier columns: Although the input gases used are 99.9% pure, moisture and other impurities may have diffused through valves and other accessories due to long transit time and storage. This calls for a need to purify the gases being used. Four in-situ rechargeable molecular sieve based columns (one for each input gas) are mounted on the input gas lines in order to absorb moisture, oil traces and other contaminants from the gases. These columns are made of stainless steel and have two built-in heaters of 500 watts each. Each column is charged with 300 grams of molecular sieve absorbents of Type 3Å (80%) and Type 4Å (20%); the Argon column has a 13X type absorbent in addition to these.
3. Mixing unit: The outputs from purifiers enter the mixing unit, which consists of pneumatic valves, mass flow controllers, mixing line, check valves, bellow-sealed valves and a probe for moisture measurement. The pneumatically controlled bellow-sealed valves are activated by a pressure of about 4 bar. A dry nitrogen gas or an air compressor is used for maintaining this pressure. All the valves used in the system are of normally-closed type.
4. Mass flow controllers: Following the pneumatic valves, are model FC-760 [105] mass flow controllers, which are used to measure and control the flow of gases [106]. They are designed and calibrated to control a specific type of gas at a particular range of flow rates. Each of these MFCs has a built-in 2 µm dust filters. The control input to MFCs and the output from the same are both DC voltages (0 - 5 volts) which are linearly proportional to the mass flow. They are displayed as SCCM (Standard Cubic Centimeters per Minute) units. A ten-turn potentiometer

is used for adjusting the mass flow, and the set value is displayed by an LED on the front panel of the system.

5. Mixing line and moisture measurement probe: Predetermined volumes of various gases from MFCs get mixed in the stainless steel tubing as they flow past a moisture measurement probe. This probe is a microprocessor based capacitive type commercial sensor [107] with dew point display. It measures the moisture content in the gas that is being mixed on-line. The sensitivity range of this device is  $-800^{\circ}\text{C}$  to  $-250^{\circ}\text{C}$  dew point. Even as the moisture content is measured, gases get mixed in the sensor volume and further mixing occurs along the stainless steel tubing as the gas flows through it and enters a distribution manifold.
6. Distribution system: The flow resistor-based distribution system comprises of a manifold and pressure transducers. Gas mixture entering the manifold is mixed further in a small cylinder which provides higher cross section and residence time. A pressure transducer-gauge of range  $0 - 1 \text{ kg/cm}^2$  is mounted here to indicate the pressure at which the gas mixture is being dispensed. This transducer operates on 15 volts DC and gives a current output of  $4 - 20 \text{ mA}$ , which is displayed on the front panel. The manifold then feeds the gas into sixteen selectable channels, isolated by pneumatically activated valves, with control switches at the bottom front panel. Uniform and approximately equal flow of gas mixture in all chambers is facilitated and ensured by flow resistors. Flow resistors are two meter long stainless steel capillaries having an inner diameter of  $300 \mu\text{m}$ . Since the pressure gradients across these tubes are similar and very large compared to a typical RPC's input to output pressure gradient, the gas flow into each RPC will be the uniform [108]. These capillaries also allow the gas to mix thoroughly by providing a long residence time. When a viscous fluid undergoes laminar flow through a tube, a pressure gradient which is proportional to the volume flow rate is set up between the ends of the tube according to the Hagen-Poiseuille equation [109]:

$$\Phi = \frac{\pi R^4 \Delta P}{8\eta L} \quad (3.7)$$

where,  $\Phi$  is the voluminal gas flow rate ( $\text{m}^3/\text{s}$ ),  $R$  is the capillary radius (m),  $\Delta P$  is the differential pressure (Pa),  $\eta$  is the dynamic fluid viscosity of gas (Pa-s) and  $L$  is the total length of the capillary tube in the x-direction (m). There are sixteen such capillaries wherein, one end is connected to one pneumatically controlled valve after the mixing cylinder and other end is connected in parallel to the RPC and safety bubbler. The mixed gas is then distributed into sixteen individually selectable parallel gas outlets. A fine particle filter [110] is mounted on this line to purify the mixed gas further, before it enters the RPCs.

7. Safety bubblers: Safety bubblers mounted on individual output lines take care of the back pressure and protect the RPCs from possible damage due to over pressure. Each of these bubblers is made of borosilicate glass and is connected to a stainless steel tube by a flexible Tygon tube. Every bubbler has a 25 mm column (typically about 5 ml) of silicone diffusion pump oil (DC704 [111]), which has a density of 1.08 g/cc and a very low vapour pressure at room temperature. This bubbler prevents over pressurisation of RPC that might occur due to blockages in the flow path, by relieving the excess gas to bubble through the oil. Thus, under proper flow conditions, gas should not bubble through safety bubblers. The outlets of all these are connected to a common vent.
8. Isolation bubblers: These bubblers are similar to a safety bubblers in dimension, and serve to prevent back diffusion of air into the RPC. There are sixteen such bubblers in the system. The gas mixture flowing out of each RPC flows through one isolation bubbler. The absence of bubbling in these bubblers implies malfunctioning of the channel or a leakage in the RPC or a joint in the line. The output from all bubblers is fed into a output/exhaust manifold and then vented out.
9. Exhaust manifold: The return gas from all connected chambers is collected into this manifold, and a single output is provided to vent the used gas into the atmosphere. This manifold also has a pressure sensor to indicate the system pressure with reference to the ambient room pressure as well as a high precision moisture meter. Since we monitor the moisture levels in the gas both on the input and output lines, we will be able to detect whether the moisture was present in the input

gases or acquired the same as the gas has flown through the gas system and the RPCs.

10. Remote control and monitoring: The required flow rates of individual gases in the system can be set and monitored through a PC interface. Other important system parameters such as pressures at various stages of the unit can also be monitored using this interface.

### 3.5.2 Calibration of the gas systems

As described earlier, MFCs are used to measure and control the flow of gases. They are designed and calibrated to control a specific type of gas at a particular range of flow rates. Normally, the rating on MFCs is the one that corresponds to the flow of Nitrogen gas, and hence, calibrating the MFCs for different gases being flown through them is a prerequisite. All the MFCs employed in our gas mixing system are calibrated by water downward displacement method and cross-calibrated by linear gas flow method. These two calibration schemes are schematically shown in Figure 3.23.

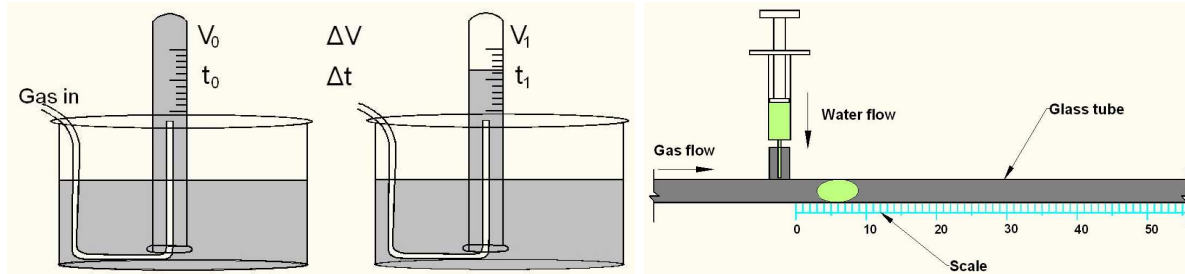


Figure 3.23: Schematic diagrams of MFC calibration schemes for the gas mixing and distribution systems. Shown in the left panel is water downward displacement method and linear gas flow method is represented in the right panel.

MFCs need a 0 - 5 volts DC signal for their operation, and the flow through them increases linearly with the applied voltage. The sensing voltage is again a 0 - 5 volts DC, corresponding to the actual flow through MFC. The MFC under calibration is first set to, say, 5 volts, and the gas under test (Argon, for example) is passed through it into a measuring jar filled with water. This jar is then inverted into a container filled with water. The gas tube from the MFC output is carefully inserted, and the gas collected in the jar from one known level to other known level together with the time taken for the same are recorded. The level difference divided by the time is the average flow rate

during calibration period. Then the voltage is set to say 2.5 volts and again the above procedure is repeated and time and level difference are recorded. This procedure may be repeated for many values of the MFC (input) voltages. Flow rates thus calculated and the corresponding voltages are plotted to obtain the calibration curve for the gas under test. This procedure is repeated for other gases with different MFCs. Once all the MFCs are calibrated, the proportion (by volume) of various gases in the mixture are decided, depending on the mode of RPC operation, and the flows are adjusted accordingly. All the MFCs were calibrated accurately using this data and has resulted in smooth and reliable functioning of the gas system.

In addition, cross-calibration of the MFCs was performed using an alternate method. A gas tube of uniform inner diameter 6 mm and length 1.5 m was taken. A small hole is made on its wall close to one end of the tube where the gas connection from the system is made. A droplet of water is introduced into the tube using this hole. Now, just like in the previous calibration method, one of the MFCs is set at a known flow rate, while all other gas inlets are closed. The gas that enters the glass tube pushes the water drop forward, whose speed depends on the flow rate set on the MFC. The position of the drop in the tube and the corresponding time is recorded at several points as the drop travels forward. Using the differential data, the volume flowing through the tube is calculated at several points and the measured average gas flow is obtained unlike a single measurement as in the earlier water displacement method. These measurements are repeated at several set gas flow rates as well as for different gases (Figure 3.24). The plots show excellent linearity between the gas flows set on the gas unit and the actual flow measured by the flow through tube method.

Using the plots shown above we obtain the MFC calibration equations (Table 3.2) for individual gases, using which we set their required proportions in the gas mixture according to the total flow rate of the mixture.

## 3.6 Gas recovery and recycling system

Even though the gases create and control ionisation in radiation detectors, none are consumed in the process. However, a small fraction may undergo a permanent chemical change and do need to be replaced. A small flow of gas mixture - about a few

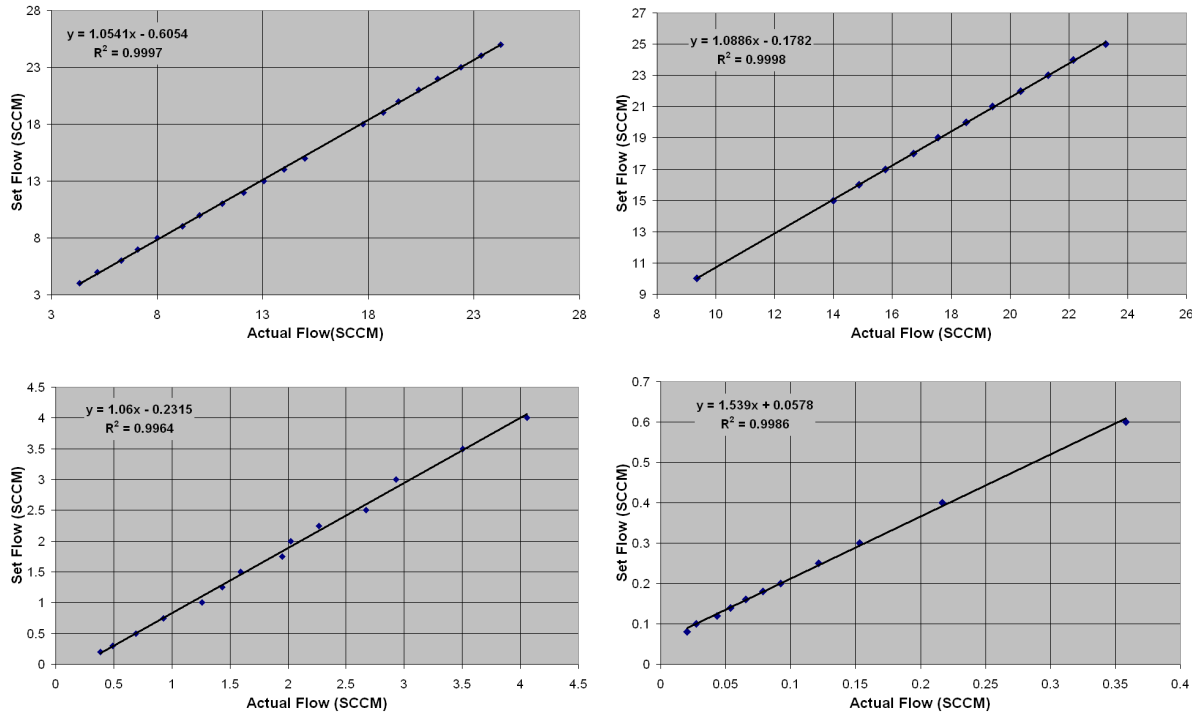


Figure 3.24: MFC calibration plots using flow through tube method. Shown in the figure clock-wise starting from top left are the calibrations for R134a, Argon, Isobutane and SF<sub>6</sub> gases.

detector volume changes per day, must therefore be maintained to flush out the contamination. As per the design of the gas mixing and distribution systems described above, the gas mixture, after its passage through RPCs is discarded and let into atmosphere. This practice is apparently very convenient for few RPCs. But when the number of RPC detectors deployed is large - as in the case of ICAL detector, the quantity of gases thrown out becomes large (see Table 3.3) and poses the following problems:

Table 3.2: Summary of MFC calibration equations for individual gases using water displacement and flow through tube methods. Flow rate value  $y$  SCCM is set in order to obtain an actual flow rate of  $x$  SCCM.

| Gas             | Water displacement method | Flow through tube method |
|-----------------|---------------------------|--------------------------|
| Argon           | $y = 1.0495x - 1.0205$    | $y = 1.0886x - 0.1782$   |
| R134a           | $y = 1.0482x - 0.1825$    | $y = 1.0541x - 0.6054$   |
| Isobutane       | $y = 1.0321x - 0.0651$    | $y = 1.06x - 0.2315$     |
| SF <sub>6</sub> | $y = 1.0155x - 0.0048$    | $y = 1.539x + 0.0578$    |

Table 3.3: Requirement of various gases in the ICAL detector

| Total gas volume of ICAL: $28800 \times 184 \text{ cm} \times 184 \text{ cm} \times 0.2 \text{ cm} \approx 195,000 \text{ litres}$ |           |          |         |          |         |         |
|--|-----------|----------|---------|----------|---------|---------|
| Gas  | Avalanche | Streamer | Max.(%) | Vol.(L)  | Density | Wt.(kg) |
| Argon  | 0.0       | 30.0     | 30.0    | 58503.2  | 1.784   | 104.4   |
| R134a  | 95.5      | 62.0     | 95.5    | 186235.1 | 4.25    | 791.5   |
| Isobutane  | 4.3       | 8.0      | 8.0     | 15600.8  | 2.51    | 39.2    |
| SF <sub>6</sub>  | 0.2       | 0.0      | 0.2     | 390.0    | 6.164   | 2.40    |

1. Cost of gases: Some of the constituent gases are very expensive. Exhausting them to the atmosphere will contribute to a huge running cost.
2. Pollution: Hazardous and toxic gas products generated due to corona discharge inside the RPC during its operation, are harmful to health and unsafe to be let out without adsorbing or conversion to safer compounds. RPC exhaust contains SF<sub>6</sub> and Freon (R134a) whose Global Warming Potentials (which cause the green-house effect) are 22400 and 4200 times greater, respectively, than CO<sub>2</sub>. They are highly stable and remain in the atmosphere for very long time, closer to ground.
3. Storage hazards: A large amount of space is needed for storage of gas cylinders to cope up with the consumption. The space near the detector is always at a high premium.
4. Pressure instability: If the gas mixture is directly discharged into the atmosphere, the RPC pressure regulation system may get affected by changes in atmospheric pressure.
5. Performance: To minimize the vent loss, the number of volume changes is always kept to a bare minimum, which might result in degradation of performance.

A solution to above mentioned problems is to reuse the exhaust gas mixture from RPC detectors. Presently the closed-loop technique is the only available method for this purpose [112]. In this method, the RPC exhaust gas mixture is re-circulated with elaborate pressure/flow controls system. In-situ gas analysis is performed, unwanted components are removed and lost quantities are topped up. This is a very effective technique but the equipment involves extensive instrumentation and therefore may

turn out be very expensive for many applications. We are developing an open-loop method as an alternative to the re-circulation method [113]. We have targeted to recover 95% of the exhaust gases while limiting the impurities up to a maximum of 1000 ppm for this system in the first phase.

### 3.6.1 Principle of operation

In this method, gases are separated, purified, stored and reused. Separation of gases from the mixture is accomplished by using differences in their physical and chemical properties. Appendix B.1 lists important properties of commonly used RPC gases, in which the differences in their properties are quite evident. For example: Isobutane and Freon (R134a) can be liquefied at temperatures above  $-30^{\circ}\text{C}$ , whereas Argon and  $\text{SF}_6$  are still in gas phase at that temperature. R134a is a highly saturated compound but Isobutane retains substantial chemical affinity. In the gas phase  $\text{SF}_6$  is 2.5 times heavier than Argon.

Differences between characteristics of gases are employed to separate gases from one another and purify them for reuse. At first, Isobutane and R134a are separated by condensation. The suitable temperature-pressure for condensation is given by Clausius-Clapeyron Equation for the boiling point in the vapour-liquid system:

$$T_B = \left[ \frac{R \ln(P_0) - \ln(101.325)}{\Delta H_{vap}} + \frac{1}{T_0} \right]^{-1} \quad (3.8)$$

where,  $T_B$  is the boiling point ( $^{\circ}\text{K}$ ),  $R$  is the ideal gas constant ( $8.314 \text{ J}/^{\circ}\text{K}\cdot\text{mol}$ ),  $P_0$  is the absolute vapour pressure of gas at a given temperature (KPa),  $\Delta H_{vap}$  is the heat of vapourisation ( $\text{J}/\text{mol}$ ) and  $T_0$  is the gas temperature ( $^{\circ}\text{K}$ ).

During the separation of condensable gases parameters such as the pressure, temperature and surface activation are maintained in such way that only one gas is adsorbed, condensed and trapped. For Isobutane, this temperature is typically  $-13^{\circ}\text{C}$  at 0.5 bar. After removal of Isobutane, the residual gas mixture flows to the next zone where conditions ( $-26^{\circ}\text{C}$  and 0.5 bar) are set for Freon (R134a) to condense. Liquefied Freon is in equilibrium with its gas at partial pressure of 1 bar at  $-26^{\circ}\text{C}$ . The gas mixture finally coming out of the fractional condensation section is comprised of non-condensable gases such as Argon and  $\text{SF}_6$  along with washed off vapours of condensed

gases (R134a and Isobutane).

In the next stage, Argon + SF<sub>6</sub> mixture is allowed to settle under a low turbulence condition. As densities of Argon and SF<sub>6</sub> are quite different, the heavier gas (SF<sub>6</sub>) settles to bottom of the tank. Argon is collected from the top. Argon is subsequently adsorbed in a column of type 4Å molecular sieve. When dealing with small quantities of gas, a batch purifier (with low purge loss) is recommended. For continuous recovery of large flow rates of Argon, a dual column Tandem operated purifier is suitable. In either case molecular sieves are regenerated by raising it to an appropriate temperature.

The remaining volume of gases consists of traces of SF<sub>6</sub> and of condensable gases. The efficiency of recovery achieved by open or closed loop extraction of RPC exhaust gases is in the range of 90% to 95% under optimum conditions. For a large detector setup such as ICAL, operating on even one volume change per day basis, a 5% loss amounts to discharging about 50 kg of R134a and 0.5 kg of SF<sub>6</sub> into the atmosphere every day. These emissions are equivalent to creating nearly 50,000 m<sup>3</sup> of Carbon dioxide daily. Gas emissions need to be completely converted to safer compounds. We designed a scheme and developed a prototype unit to test the same.

Gases such as R134a and SF<sub>6</sub> are stable compounds. In order to decompose them, the mixture is first activated by adding of 50% oxygen and 2% Argon and under typical RF plasma conditions of 13.56 MHz, 1 Torr pressure and 0.2 W/cm<sup>2</sup> power density. The chemical reaction takes place on the surface of a Silicon electrode. Main product of this reaction is SiF<sub>4</sub> (gas), which is further hydrolysed to form HF solution and Silicon Hydroxide sludge. More than 90% of effluent gas mixture can be effectively removed by this method [114].

### 3.6.2 Technical details of the unit

*Separation of gases:* The process equipment employed for open gas recovery consists of a gas purifier and a gas condenser. The gases coming out of the RPC enter the purifier unit through an isolation bubbler which also serves as flow counter. The gas flows further into a chamber which provides capacitance to compensate fluctuations in flow rates. An impedance in the form of micro-bore capillary connects the gas to a receiver chamber maintained at an absolute pressure of 700 mbar. Capillary impedance regu-

lates flow into the receiver and does not allow the development of a negative pressure differential inside the RPC. A safety outlet is provided in the form of a bubbler to avoid back pressure build-up inside the RPC. The vacuum column is charged with activated alumina which reacts with and fixes the radicals present in the gas stream. Oil free diaphragm pumps send the gas mixture from the vacuum column and feed it to the pressure chamber. The vacuum chamber is fitted with a vacuum transmitter and the switch set at 690 - 710 mbar absolute pressure. The pressure chamber is also equipped with a pressure transmitter and switch set at 1.5 - 1.6 bar absolute pressure. The pressure chamber also contains 3Å type molecular sieve to reduce the water vapour contamination down to 2 ppm.

The gas mixture flows into a refrigerated chamber where two columns are maintained at  $-13^{\circ}\text{C}$  and  $-26^{\circ}\text{C}$  respectively. The compressor [115] model SC12CL with Freon R404 is used to create a source temperature of  $-35^{\circ}\text{C}$ . The first column contains activated Palladium catalyst (on Alumina). The adsorption surface is typically  $200 \text{ m}^2/\text{gm}$ . Isobutane is extracted to 10 ppm level in this column. The second column contains copper granules and is maintained at  $-26^{\circ}\text{C}$ . Freon condenses in this column. A check valve adjusted at 1.5 bar absolute pressure is placed at the outlet on the gas line. This valve maintains sufficient back pressure essential for condensation.

Overflow gas returns to the purifier and enters the Argon extraction column. Here Argon (free of moisture) is absorbed in the type 4Å molecular sieve. This column has to be thermally regenerated for removal of adsorbed Argon. Residual gas is settled in a container with activated carbon. At the lower end,  $\text{SF}_6$  is tapped out for further concentration and recovery. The unrecovered gas flows out to the vent exhaust through an indicator-cum-isolation bubbler.

All columns except that of activated alumina have to be regenerated after a certain usage time which depends on the concentration of gases. Activated alumina needs to be replaced as it gets consumed in the process of cleaning of radicals.

*Reuse of extracted gases:* Isobutane and Freon R134a are collected at  $-13^{\circ}\text{C}$  and  $-26^{\circ}\text{C}$  in their respective columns. To transfer the liquids into their containers, a sequence of valve operation is carried out. The valves are of the all metal solenoid type suitable for low temperature application. In the beginning a valve located inside the refrigerated chamber is opened. At the same time, the release valve connecting the

transfer chamber outlet to the vacuum chamber is also opened. Under a pressure differential, liquefied gas flows into the insulated transfer chamber. After a few seconds, both valves are closed.

The insulated chamber is heated to about 27 °C (+10 °C above room temperature) by electric heaters. Pressure, measuring about 4 bar (for Isobutane) and 7 bar (for R134a), develops inside the transfer chamber(s). At this point, the solenoid valve connecting the transfer chamber to the liquefied gas container is opened. The gas pressure inside the container is 3 bar (Isobutane) and 5 bar (R134a) at 17 °C which is close to the typical room temperature. Under the pressure gradient, liquefied gas flows from the transfer chamber into the liquid container. The lower valve is now closed and the release valve opened. Evaporated gas flows back into the vacuum chamber and joins the incoming RPC exhaust for the next cycle of recovery.

Shown in Figure 3.25 - left to right, are the schematic diagrams of the purifier unit, condenser unit and a picture of the completely assembled gas recycling unit.

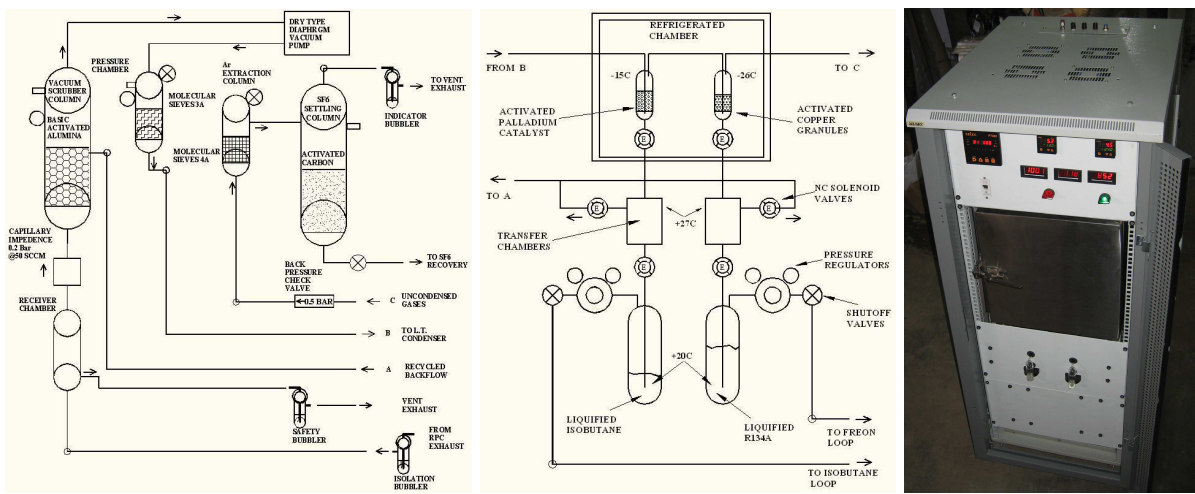


Figure 3.25: Schematic diagrams of the purifier unit (left panel), condenser unit (middle panel) and a picture of the completely assembled gas recycling unit (right panel).

### 3.6.3 Performance studies of the unit

*Volumetric method for estimating gas recovery:* The three identical bubblers connected in the gas stream indicate the amount of flow rate passing through. The number of bubbles counted by isolation bubbler in a given amount of time should be equal to sum of bubbles coming out of the safety and indicator bubblers, in the absence of leakage

through the system. At this stage, refrigeration is started. At around  $-24^{\circ}\text{C}$ , the flow in the indicator bubbler starts dropping. As soon as equilibrium is reached between pressure-vacuum and temperature, the flow in the indicator bubbler drops to less than 10% of its original value. The measurement indicates that more than 90% gas is collected in the recovery system. As there is no pressure increase the collected gas must be in the liquid phase.

*Isobutane measurement:* Isobutane content in the gas mixture is about 1% to 5%. Removal of Isobutane, therefore does not significantly change the total volume of gas. A Matheson gas detector (model 8057) with minimum 100 ppm sensitivity for Isobutane was used to estimate the presence of Isobutane at test points during its passage through the recovery system. It is found that Isobutane was completely absorbed by activated carbon. It was found that Isobutane is completely extracted from 1% to 100 ppm by condensation.

## 3.7 RPC materials and assembly procedures

RPC fabrication involves deploying a large number of materials as well as many assembly procedures. So the production of high performance and reliable chambers involves choosing the right type and quality of materials as well as optimisation of various assembly and quality control procedures involved in the fabrication. The materials comprise of glass used for electrodes, individual gases used for mixing and flowing the gas mixtures for the operation of the chambers, spacers, buttons, gas nozzles etc. which are needed for the assembling the chamber, resistive coat on the electrodes, epoxies used for gluing together different types of materials, pickup panels used for external signal pickup from the chambers, polyester films used for insulating the pickup panels from the resistive coated electrodes, to name a few. We have studied a number of different types and qualities of these materials and optimised most of them. We have continuously improved the quality of the RPCs by incorporating the results of these studies in fabrication and testing of the chambers.

We have also designed and developed a large number of assembly and quality control procedures and invented a number of useful jigs that are extremely useful in the production of good quality detectors. Coating of resistive paint on the electrodes, as-

sembling and gluing of chambers, leak testing of the finished chambers are some of the important assembly procedures. We have worked closely with various R&D institutions as well as many industrial houses in developing these materials and designing and developing the assembly procedures.

### 3.7.1 Characterisation of electrode glass samples

Drawing a reasonable conclusion from the long-term studies of RPCs fabricated using Japanese glass that the electrode glass seems to be one of the crucial factors in the aging of RPCs, we have initiated detailed characterisation studies on various glass samples that we have so far utilised for fabricating the RPCs. The motivation was twofold. While we certainly believe that these studies will throw light on possible reasons for the sudden aging of our RPCs, we also want to find out, on a comparative scale, the main characteristics of the glass that make a good electrode. We have mainly studied glass samples made by some local glass manufacturers such as Modi, Asahi float and Saint Gobian as well as those from Italy, Germany and Japan [116].

Figure 3.26 shows Atomic Force Microscope (AFM) surface scans of these glass samples. While the Modi glass surface seem to be bad on a relative scale, surface quality of the Asahi glass is comparable to that of the Japanese glass. We have also scanned these samples on a Scanning Electron Microscope (SEM) whose results are shown in Figure 3.27. There are no appreciable differences on the surface quality among these glass samples. It is however interesting to note a couple of observations from these studies. These scans indicate a debris of tissues used for cleaning of these glass samples as impurities with a high carbon concentration. The Modi sample shows a flaw in terms of a very clear diffraction pattern on the sample.

We show in the Table 3.4, fractional percentages of weights of various elements present in the glass samples obtained using the Energy Dispersive X-ray Spectroscopy (EDS) technique. The data is shown for a couple of samples each of different brands of glass. Within the instrument tolerances, we find that the glass samples show consistent values of various constituent elements among them.

Due to the technique of float glass manufacturing, the quality of two surfaces of the glass is not identical. While the surface, which is in contact with molten tin - on which the glass floats during its manufacture, is relatively smooth, the surface that is

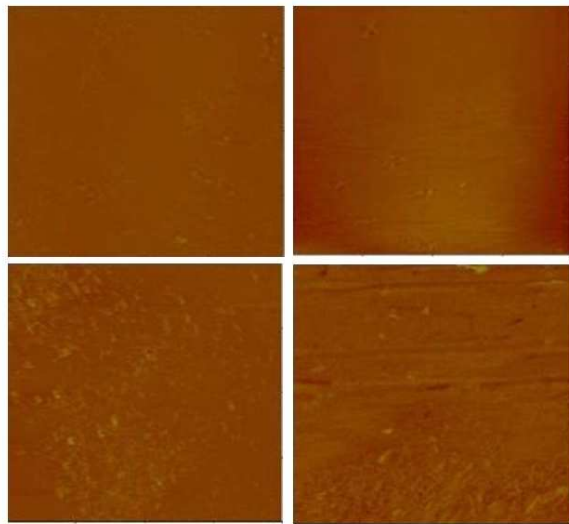


Figure 3.26: Comparative study of Asahi Float (top left panel), Japanese (top right panel) and Modi (bottom panels) glass samples using AFM technique. All the scans are taken over a  $10 \mu\text{m} \times 10 \mu\text{m}$  glass surface area. While the surface quality scale for the Asahi Float and Japanese glass is 0 - 30 nm, the scale is 0 - 200 nm in case of Modi glass.

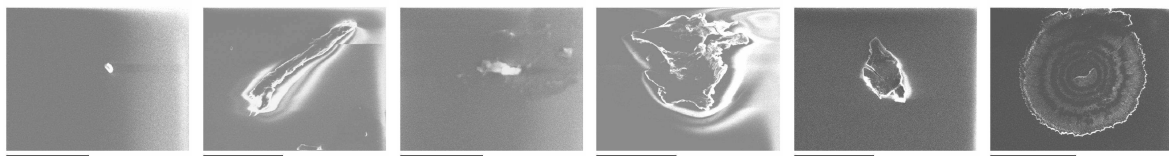


Figure 3.27: Comparative study of Japanese, Asahi Float and Modi glass samples using SEM technique. Shown in the figure from left to right respectively, are scans at a couple of regions on each glass sample.

exposed to the air is rough. It is advisable that we keep two smooth surfaces of the top and bottom electrode glasses facing the gas volume for a better performance of the detector. We have devised a scheme using the reflectance of glass surfaces for the UV radiation to mark and compare the smooth and rough surfaces. Shown in Figure 3.28 are results of these tests on various glass samples where we could clearly identify these two surfaces. This distinction is clearest in the case of the Japanese glass samples.

We have also studied the transmittance of these glass samples using a light source of UV and visible spectrum. These results are shown in Figure 3.29. All the glasses show the expected behaviour, including the sudden drop of transmittance at the UV spectrum boundary. Even though the Japanese glass shows marginally better trans-

Table 3.4: Summary of our EDS studies on glass samples from various manufacturers.

| Element   | Modi     |          | Asahi    |          | Japanese |          |
|-----------|----------|----------|----------|----------|----------|----------|
|           | Sample 1 | Sample 2 | Sample 1 | Sample 2 | Sample 1 | Sample 2 |
| Oxygen    | 71.0     | 72.6     | 69.9     | 70.1     | 72.9     | 73.4     |
| Sodium    | 8.6      | 3.3      | 7.7      | 7.8      | 7.6      | 7.2      |
| Magnesium | 1.8      | 1.8      | 2.3      | 2.4      | 1.9      | 1.5      |
| Silicon   | 17.8     | 15.7     | 19.0     | 18.6     | 16.9     | 17.1     |
| Calcium   | 0.9      | -        | 0.7      | 0.7      | -        | 0.4      |
| Carbon    | 6.7      | -        | -        | -        | -        | -        |
| Aluminum  | -        | -        | 0.5      | 0.4      | 0.7      | 0.5      |

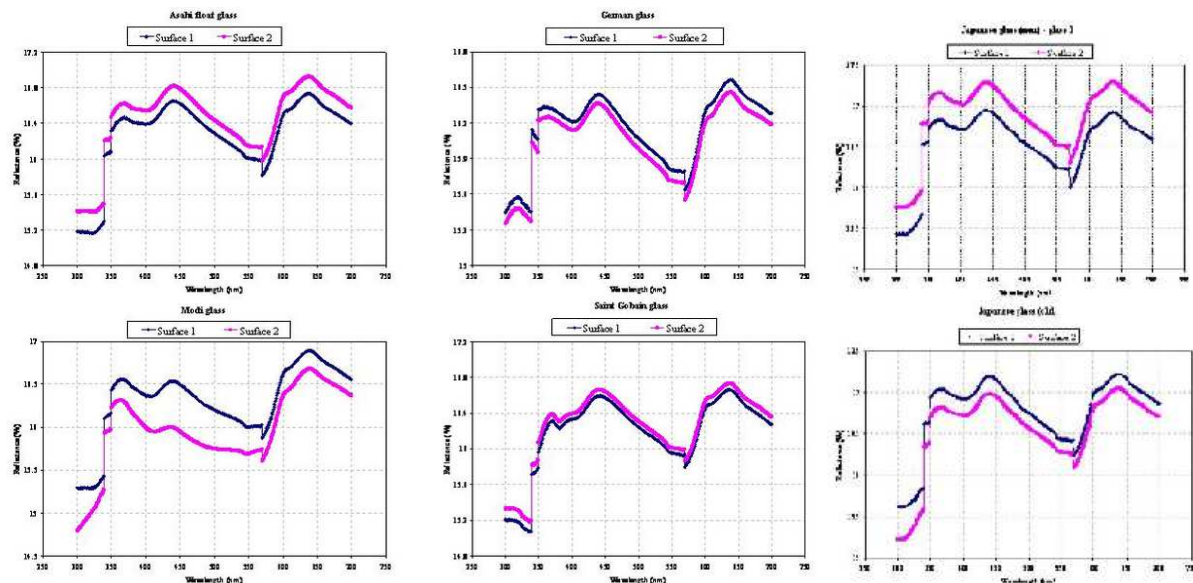


Figure 3.28: Reflectance studies of various glass samples using UV radiation. Reflectivity (%) as a function of wavelength (nm) for glass samples from Asahi Float, Germany, Modi, Saint Gobian and Japan are shown.

mittance by about 10%, we do not believe that this is a significant difference among the samples. So, we conclude that using various surface scan, elemental analysis or the transmittance tests, we do not find any significant differences among various glass samples.

Another characterisation study that was carried out on various glass samples was their density measurement. This study was driven by the conviction that a simple characteristic such as density might indicate a possible major difference in the glass composition which in turn might throw some light on the possible role of glass electrodes in the RPC aging phenomenon. The density of the glass samples was computed

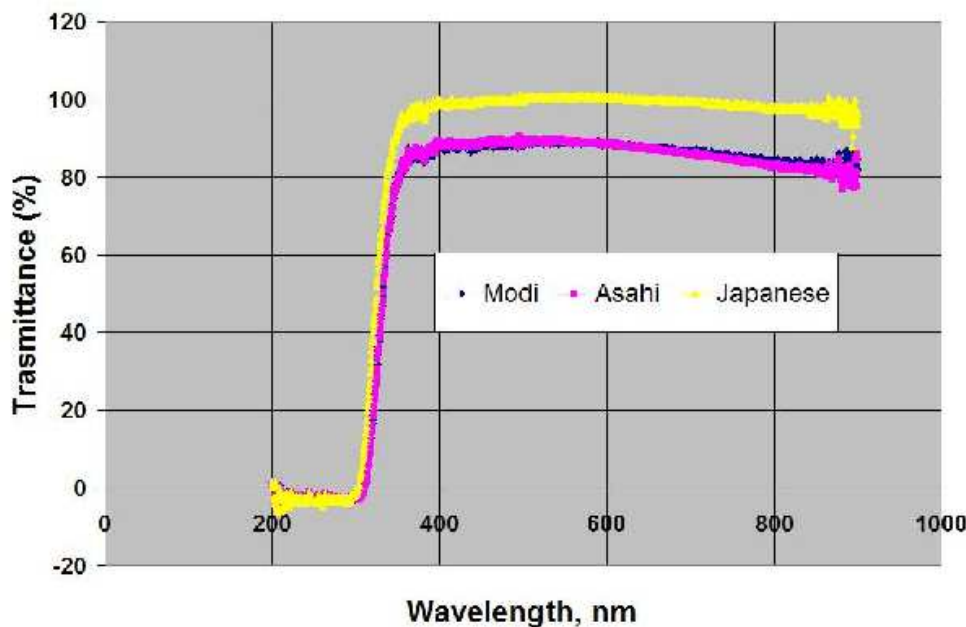


Figure 3.29: Comparative study of glass samples using transmittance test.

by precisely measuring the dimensions of the sample, calculating its volume and by measuring the mass of the samples. We show a summary of our studies on glass density measurements in Figure 3.30. We again find that there are no significant differences in density among the various samples, even though the density of German glass is significantly lowest among the samples that we have studied. The density of the Japanese glass is a shade smaller than that of Indian glasses.

| Saint Gobian |        |         |         | German     |        |         |                  | Japanese              |        |         |         |
|--------------|--------|---------|---------|------------|--------|---------|------------------|-----------------------|--------|---------|---------|
| Sample no.   | Volume | Weight  | Density | Sample no. | Volume | Weight  | Density          | Sample no.            | Volume | Weight  | Density |
| SG1          | 5.1009 | 12.8276 | 2.5148  | G1         | 4.8079 | 10.6978 | 2.2250           | J1                    | 4.2826 | 10.7103 | 2.5009  |
| SG2          | 5.0110 | 12.5467 | 2.5039  | G2         | 4.8282 | 10.7368 | 2.2238           | J2                    | 4.2911 | 10.6816 | 2.4892  |
| SG3          | 4.9628 | 12.4893 | 2.5166  | G3         | 4.9211 | 10.9445 | 2.2240           | J3                    | 4.2144 | 10.4389 | 2.4770  |
| SG4          | 5.0790 | 12.7575 | 2.5118  | G4         | 4.8027 | 10.6503 | 2.2176           | J4                    | 4.1877 | 10.3865 | 2.4802  |
| SG5          | 5.0659 | 12.7342 | 2.5137  | G5         | 4.9294 | 10.9600 | 2.2234           | J5                    | 4.1752 | 10.3920 | 2.4890  |
| Average      |        | 2.5122  | Average |            |        | 2.2228  | Average          |                       |        |         | 2.4873  |
| Modi         |        |         |         | Asahi      |        |         |                  | New Japanese          |        |         |         |
| Sample no.   | Volume | Weight  | Density | Sample no. | Volume | Weight  | Density          | Sample no.            | Volume | Weight  | Density |
| M1           | 4.6903 | 11.8039 | 2.5166  | A1         | 5.4973 | 13.7945 | 2.5093           | JN1                   | 4.7247 | 11.7209 | 2.4808  |
| M2           | 4.6336 | 11.6363 | 2.5113  | A2         | 5.2471 | 13.1615 | 2.5083           | JN2                   | 4.6282 | 11.5423 | 2.4939  |
| M3           | 4.5710 | 11.4635 | 2.5079  | A3         | 5.2233 | 13.0981 | 2.5076           | Average               |        |         | 2.4873  |
| M4           | 4.5802 | 11.4710 | 2.5045  | A4         | 5.2539 | 13.1530 | 2.5035           | All volumes are in cc |        |         |         |
| M5           | 4.6084 | 11.5331 | 2.5026  | A5         | 5.2421 | 13.1274 | 2.5042           | Weight in gm          |        |         |         |
| Average      |        | 2.5086  | Average |            |        | 2.5066  | Density in gm/cc |                       |        |         |         |

Figure 3.30: Comparative study of density of glass samples from different manufacturers.

### 3.7.2 Glass electrode coating

The resistive coating of the outer surfaces of the electrodes plays a very crucial role in the operation of the RPC detector. While the surface resistivity of this coating should be small enough so that the bias voltage that is required for the RPC operation can be applied on these coats, it should be high enough to render it *transparent* to electric pulses generated by the charge displacement in the gas gap. This way, the charges produced inside the gas gap on passage of a particle, can induce electric signals on the external metallic pickup strips, which are capacitively coupled to the gap. There is another important consideration of this electrode coat on the performance of the RPC. Every charged particle passing through the RPC, produces a tiny charge spot of about  $0.1 \text{ cm}^2$  in area. This area is too small to result in any noticeable cross-talk between two adjacent pickup strips on which signals are induced. However, if the surface resistivity of the graphite coat is *too* small, the induced charge is less localised and spreads laterally across the graphite coat, producing large cross-talks between the pickup strips and thus severely affecting the position resolution of the detector. Y.Hoshi *et al.* [119] showed that the cluster size of an RPC exponentially decreases with the surface resistivity of its electrode coating. The cluster size of 30 mm at a surface resistivity of  $20 \text{ k}\Omega/\square$  reduces to about 8 mm as the resistivity is increased to  $1 \text{ M}\Omega/\square$ . On the other hand, thin coats with surface resistivities of  $0.1 - 1 \text{ M}\Omega$  result in time constants that are comparable to the charge movement duration [117].

Needless to say that the uniformity of response across the RPC is dependent on the uniform resistivity of the coating across the surface of the electrodes. It is also important (for the long term stability of the RPCs) that the binding strength of the coat to the electrodes is strong. Studies by G.Aielli *et al.* [118] have indicated that degradation of the anode graphite coating is one of the main factors for long-term aging of the RPC. In order to prevent damage to the painted surfaces due to handling, a thin insulating PET film is glued on the painted surfaces. Finally, the materials used, as well as the technique employed, for coating should be adaptable for large scale industrial production.

Several types of materials and a variety of application methods for obtaining this coating can be found in the literature. The Monolith [120] [121] collaboration has used a silk screen printing method by which the coat could be controlled precisely. Other

techniques such as metal oxide paints, anti-static paints, graphite varnishes [122], adhesive graphite foils [123], special inks [124] and commercial automobile paints are also used. We had started with a graphite paint prepared using colloidal grade graphite powder (3.4 gm), *Duco-lacquer* (25 gm) and *Duco-thinner* (40 ml) and sprayed on the glass electrodes using an automobile spray gun. While the graphite powder of appropriate grade provides the required surface resistivity, the lacquer binds the graphite to the smooth glass surface. A thinner is added to obtain the required consistency of the mixture that allows spraying using a spray gun. A uniform graphite coat of stable surface resistivity (100–200 k $\Omega/\square$ ) could be obtained by this method. Shown in the left panel in Figure 3.31 is a plot of the surface resistivity measurements of a painted glass for over a month. The surface resistivity of the coat drops swiftly during the first few days of application, essentially due to evaporation of the thinner from the coat, and remains reasonably stable thereafter. Even though this method worked well for the quick fabrication of small prototype RPCs, one of the problems using this method was that the paint came unstuck from the glass with time and handling.

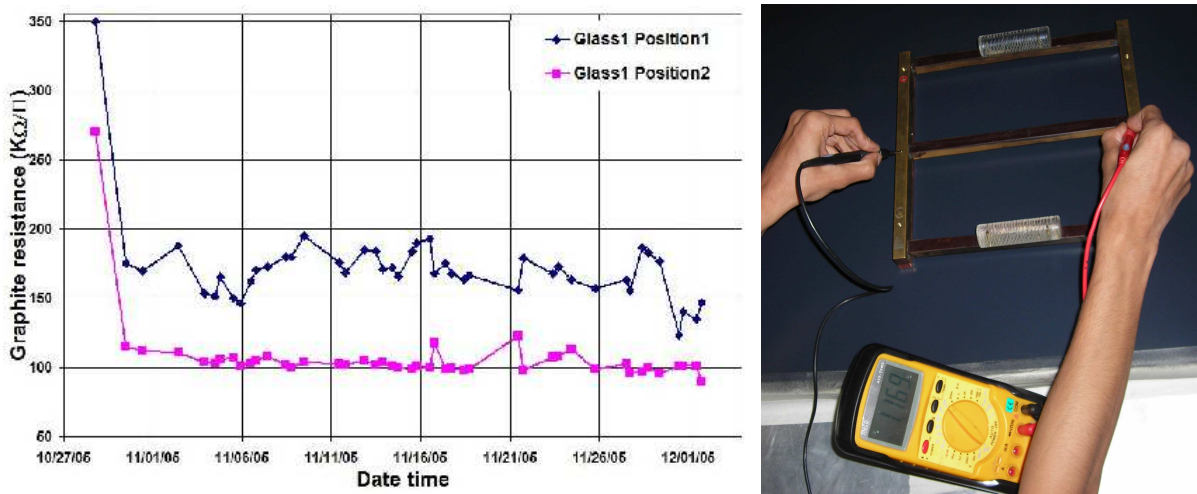


Figure 3.31: Surface resistivity plot of the graphite-based paint is shown in the left panel. The value settles to a stable value within a few days due to curing of the paint. The jig used to measure the surface resistivity is shown in the right panel.

The data is obtained with the help of an indigenously developed novel jig (shown in the right panel of Figure 3.31), which allows quick measurements without causing damage to the painted surfaces. It works on the following principle: The resistance,  $R$  of a surface film of thickness,  $t$  as measured between two conductors of length,  $L$  and separated by width,  $W$  is proportional to  $L \div (W \times t)$ . So for a given square of side,

$L$  (which is equal to  $W$ ),  $R$  is independent of  $L$  (and  $W$ ) and depends only inversely on  $t$ . The jig essentially consists of two conducting bars fixed in frame so as to form a square. Provision is made to measure the resistance across these conducting bars, using a multimeter. The resistance value is directly read as  $\Omega/\square$ . The jig is intentionally made heavy so that it makes good surface contact with coat and thus provides reliable measurements. Jigs of small and big squares were fabricated so that the resistivity measurements on both fine and coarse length scales could be made.

Subsequently we developed a special conductive paint in collaboration with an Indian paint company [125]. This paint uses modified acrylic resin as a binder, conductive black as pigment and aromatic hydrocarbons and alcohols as solvents. We have devised the following procedure for painting the glasses. We have found that cleaning of the raw glass received from the factory, is a very important factor for expected performance and long-term operation of the RPC. The glass plates are first cleaned using ethyl-alcohol and rinsed with distilled water. We then apply a soap solution (*Labolene*) on the glass sheets and clean them thoroughly using distilled water after soaking for about 10 minutes. The spraying of paint is done with a gun of nozzle size of 1.3 - 1.6 mm and at a pressure of about  $4 \text{ kg/cm}^2$ , maintaining the glass plate at a distance of about 15 - 25 cm from the gun. While at room temperature, the painted surface dries in about 10 minutes, it takes about 18 hours for complete drying. The required surface resistivity could be obtained by fine tuning the quantity of thinner in the paint mixture. Detailed specifications of the paint mixture developed, is given in the Appendix B.2.

Painting of huge number of large area RPCs using the manual method would be quite impractical and result in piece to piece variations in the surface resistivity or the thickness of the paint. We have therefore developed an automatic system to paint the glasses with the help of a local industry [126], a prototype of which is shown in the Figure 3.32. A rudimentary scheme using infrared radiation for curing of the paint was also developed. Work is underway to improvise both these systems, making them suitable for the large scale production of painted glasses.

Detailed studies are done on the surface resistivity of the glass electrodes coated using the automatic plant. We used two jigs -  $36 \text{ cm}^2$  and  $1000 \text{ cm}^2$  in area, to measure the values for two ranges in coated areas and also took data placing the jig in two orthogonal orientations in order to average the values obtained. Shown in Figure 3.33

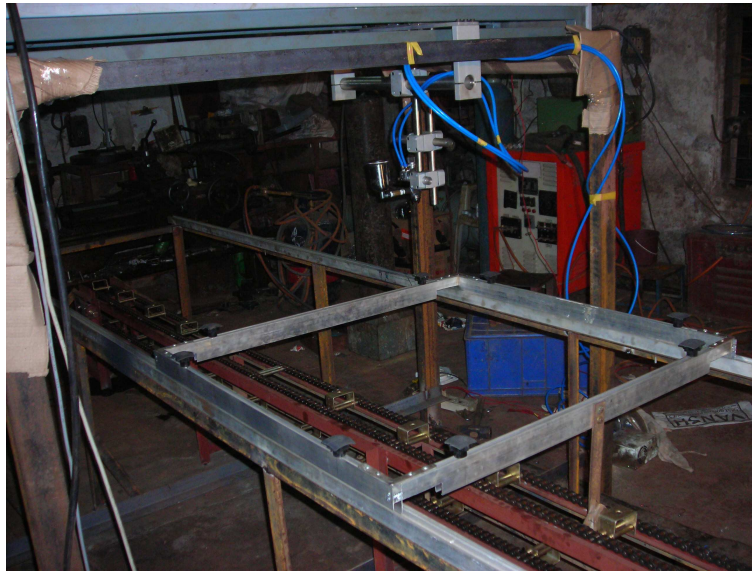


Figure 3.32: Prototype plant for automatic spray painting of glass sheets. While the glass plate mounted on a bed moves on X-direction, the spray gun is provided the movement in Y-direction.

are contour plots of the resistivity obtained from 100 cm × 100 cm glass sheet in the two orientations of the jig. As can be seen from the plots, the measurements obtained are close to the design values and are uniform over the surface, except close to the edges [127].

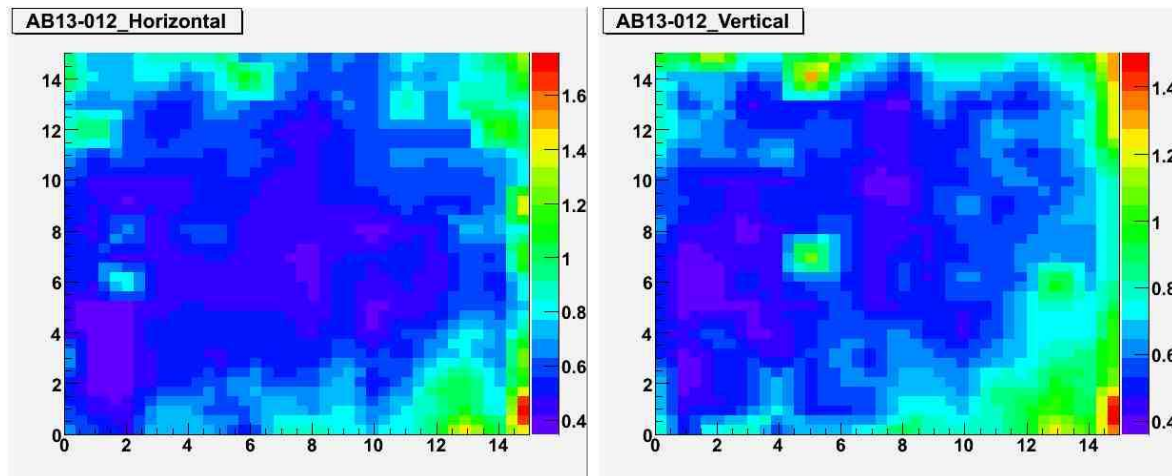


Figure 3.33: Contour plots of resistivity of 100 cm × 100 cm glass sheet painted by the automatic plant. Each division on the axes corresponds to about 6.25 cm.

An alternate method for obtaining a resistive coat on the RPC electrode is to screen print on the glass or on a PET sheet and then glue it on the glass surface. We have developed these techniques in collaboration with a local industry [128]. The coating was done using the screen printing ink Carbon Heat DC-1000M and DC-20 [129]. This

ink is normally used in keyboard contacts, jumper circuits and carbon through holes. It has good reliability of conductive film, high wear resistance, adhesion and solder resistance. A surface resistivity of a few hundred  $\text{k}\Omega/\square$  could be obtained on a  $100 \mu\text{m}$  thick polyester sheet of dimensions  $0.7 \text{ m} \times 1.2 \text{ m}$ . Curing was done for about 30 minutes at  $150^\circ\text{C}$  temperature. The main differences between the screen printing ink and spray painting paint are that the former has to be of high viscosity (in the range of 350 - 400 centipoises) and hence needs long drying (using infrared heat) time.

Table 3.5 summarises our studies done using the inks mentioned above, mixed in different ratios. We have used a screen printing machine of  $1.2 \text{ m} \times 0.7 \text{ m}$  in size to paint a PET sheet of about  $30 \text{ cm} \times 20 \text{ cm}$  in dimensions and used a screen printing mesh size of 77 threads/cm. After some trials, a 20% : 80% mixture was found to give a resistance of  $5 - 10 \text{ M}\Omega/\square$ , which was reduced to  $1 - 1.5 \text{ M}\Omega/\square$  after curing the paint with an infrared lamp. The lamp was maintained at  $670^\circ\text{C}$  and the PET sheet was passed under it 5 times at  $6 \text{ m/min}$  speed. We have subsequently coated two polyester films of about  $29'' \times 36''$  in dimension as well as few glasses of about  $30 \text{ cm} \times 30 \text{ cm}$  using paint mixture consisting of 14% of DC20 and 86% of DC1000M. The glasses were cured in a heat furnace at  $150^\circ\text{C}$  for about 45 minutes. We found that the uniformity and adhesiveness of the coating was extremely good. Studies are underway to fine tune the paint layer thickness and uniformity for obtaining the designed resistivity and longevity. We are currently also working on an appropriate curing technique.

Table 3.5: Summary of our studies on screen printing technique on glass electrodes using special inks.

| DC-20<br>Percentage by weight | DC-1000M<br>Percentage by weight | Resistance<br>$\Omega/\square$ | Remarks                  |
|-------------------------------|----------------------------------|--------------------------------|--------------------------|
| 0                             | 100                              | < 50M                          | With 10% Sericol Vionyl  |
| 10                            | 90                               | < 500M                         |                          |
| 20                            | 80                               | 5-10M                          | After drying             |
| 50                            | 50                               | 4.8K                           |                          |
| 100                           | 0                                | 160                            |                          |
| 40                            | 60                               | 5-7K                           | Single coat              |
| 40                            | 60                               | 3.1-4.3K                       | Double coat              |
| 30                            | 70                               | 40K                            | On paper with no reducer |
| 30                            | 70                               | 30K                            | On polyester             |

### 3.7.3 Development of spacers, buttons and nozzles

Resistive Plate Chambers are essentially of a parallel plane geometry detectors. The chamber is constructed by mounting two glass electrodes of required area and thickness, parallel to each other and separated precisely by the required gap between them. The chamber volume is realised by closing all the four edges of the above assembly with spacers of T-shaped cross-section. These detectors are always operated in a continuous gas flow mode. So, the spacers used for closing the detector volume, the buttons used for maintaining the required gap and mechanical rigidity as well as the gas nozzles required for letting the gas in and out of the detector chamber are the most important components for construction of an RPC. We identified and studied a variety of materials as well as produced a number of designs for these components and optimised them. We then collaborated with a local industrial house [130] and produced these components using polycarbonate material. The specifications of this material is given in Appendix B.3.

While the spacers were produced using a die, the buttons and gas nozzles were manufactured using injection molding procedure. All the required tooling was designed by us in coordination with the industrial fabricator. We have subjected the finished products through stringent mechanical and other quality control tests. We have taken a significantly large number of measurements on every dimension of these components and systematically analysed the data as part of the quality control procedure. We have also fabricated RPCs to demonstrate the suitability of these components in the RPC fabrication. This had required a few iterations in the fabrication steps before achieving the final products that met our specifications. We have finally achieved tolerances of  $5\text{-}8\mu\text{m}$  in various dimensions of the spacers, buttons and nozzles. We have used these indigenously developed components throughout in our on-going detector R&D programme. Figure 3.34 shows from left to right, the conceptual designs of spacer, button and gas nozzles [131].

### 3.7.4 Vacuum jig for RPC gas gap assembly

One of the most crucial aspects of fabricating the RPC gas gap is to mount the two glass electrodes parallel to each other. This ensures a uniform field across the entire

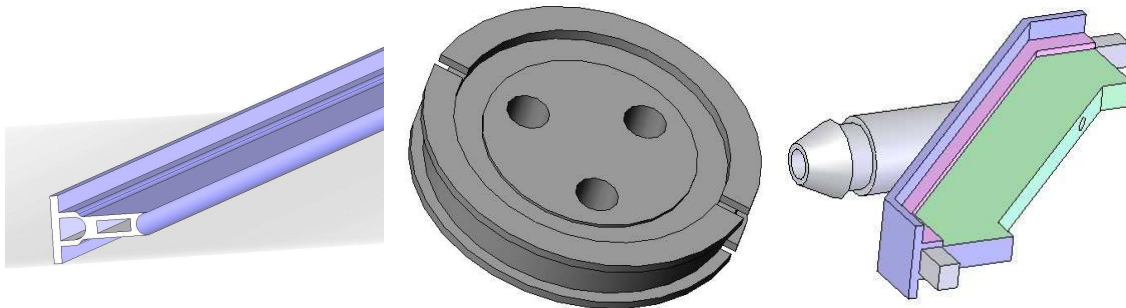


Figure 3.34: Conceptual designs of spacer (left panel), button (middle panel) and gas nozzle (right panel). Intricate details in the designs of these seemingly simple components may be noted. For example, various cut-outs and holes in the button design increase glue contact area with the glass sheets.

area of the chamber when high voltage is applied to the electrodes. As mentioned in Section 3.7.3, polycarbonate buttons are used to maintain this precise gap between the electrodes. It is equally important that these buttons are glued perfectly on either sides to the electrodes so that they will provide rigidity and mechanical strength required for the assembly to overcome the pressure exerted by the gas flowing through the chamber.

In order to achieve the above goals, the following procedure is used. First, the bottom glass sheet is placed on a perfectly even working platform. This platform itself is mounted on a rigid stand using ball bearings, such that it can make a complete rotation around its axis. The precise amount of glue is dispensed at the designated *grid* points on the glass, where the buttons are going to be located. The buttons are then placed at these points. Glue is again applied on the top side of the buttons and the top electrode glass is placed on the buttons. The glass sheets are handled with help of a multiple suction cup assembly, which is anchored to and moved using a chain pulley block. In order that the buttons are glued well on both sides to the glass electrodes, heavy metal or lead blocks are placed at many places on the assembly. Though this method is widely used, it is not a suitable for fabrication of large area chambers, because it is difficult to apply uniform pressure across entire area of the chamber.

We have therefore developed a very elegant and inexpensive jig to overcome this problem based on a novel technique [132]. This is depicted by Figure 3.35. Four ports are provided on the RPC fabrication table, just outside the four corners of the chambers. These ports are connected in parallel using plastic pipes and connected to a specially

designed bubbling jar. The glass jar has three pipes mounted using its cap a flange. One pipe of large diameter is fixed in such a way that one of its ends is deep inside the jar and the other end is open to air. The pipe which is connected to the RPC fabrication table ports is fixed in such a way that one of its ends is inside the bubbler jar. Finally, the third tube is connected to a vacuum pump on one end while the other end is placed just below the cap of the bubbler jar. The jar is filled up with water in such a way that the large pipe is in water and the water level of about 80 mm is maintained below the tube which is connected to the RPC fabrication table.

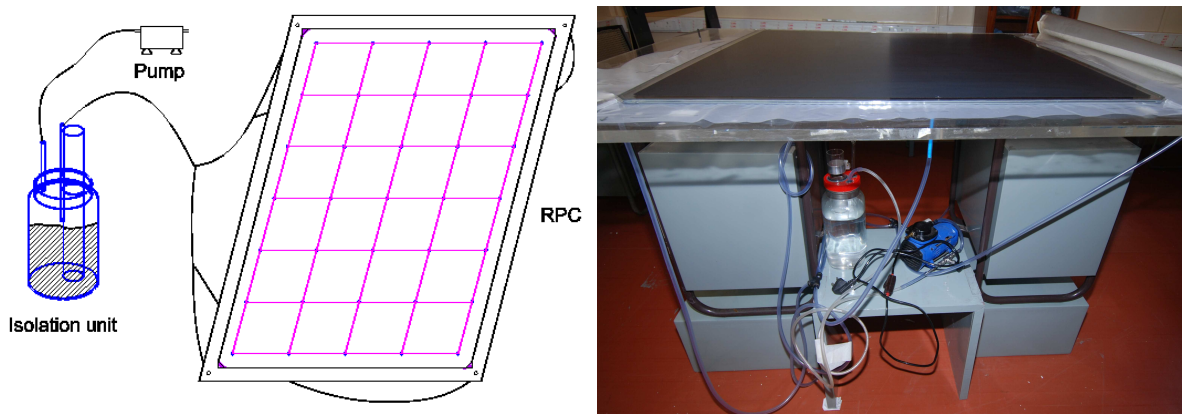


Figure 3.35: Vacuum jig used for assembly of gas gaps. Shown in the left panel is the conceptual diagram, while the actual set up is shown in the right panel.

After the buttons are glued to the glass sheets, the assembly is covered with a polythene sheet on the top and it is sealed to the table on all four sides. The vacuum pump is then switched on. The pump first removes the air from the volume above the water level in the bubbler jar, followed by the air from the volume created by the polythene sheet. As this process continues, the atmosphere exerts pressure on the polythene sheet, which in turn keeps the two glass electrodes firmly pressed against the buttons separating them. Meanwhile, since a low pressure volume is generated above the water level, atmospheric pressure pushes the water level up in the bubbler jar till the top water level touches the lower end of the pipe, that is connected to the RPC fabrication table. From this stage onwards, the volume created by the polythene sheet is not evacuated and the pump only runs just to maintain the equilibrium pressure which was attained. This way the two glass sheets are held together tightly, and parallel to each other, with the gap decided by the buttons. The pump is usually run for several

hours, till the glue is completely set. After the two glass sheets are glued together along with the buttons, the edge spacers and gas nozzle assemblies are glued on one side of the gas gap. When the glue sets on this side, the gap is rotated upside-down using the mechanism mentioned above, and the edges on the other side are glued. This simple jig was found to be an invaluable tool for large area RPC gas gap fabrication and found to result in zero failures while fabrication.

### 3.7.5 Studies on a suitable insulating film

As per the constructional design of the RPC (Section 2.3), the bias voltage required to produce a high electric field across the electrodes is applied using the semi-resistive coating on the outer surfaces of the glass sheets. On passage of a charged particle, the chamber produces charge inside the gas volume due to primary ionisation followed by avalanche multiplication. This charge induces readout signals on the metallic strips of the pickup panel, which are mounted on either side of the chamber and are nominally at ground potential. The RPC electrodes are isolated from the pickup panels using insulating films. Typically, a PET film is glued on to the resistive coat for mechanically protecting the coat as well as for primary insulation from the high potential. In addition, one or more mylar films are placed between the RPC gas gap and the pickup panels. Mylar is a bi-axially oriented, thermoplastic film [133] produced from ethylene glycol and dimethyl terephthalate (DMT).

While we have used mylar films to begin with, we have surveyed local industry to find a suitable replacement, which offers the insulation properties comparable to that of mylar films and hence provides the least leakage current paths. We have studied and characterised mainly two grades (Garfilm ER/ERE and Garfilm) of  $100\ \mu\text{m}$  polyester films [134]. The studies essentially comprised of obtaining voltage - current characteristics of a *standard* RPC, with different mylar sheets samples. The results of these are plotted in Figure 3.36. As can be seen from the plot, the ER grade film is as good as the mylar sheet, the EMCL grade even fares better in terms of its insulating properties [135]. Based on these test results, we have chosen the EMCL grade film, whose technical specifications are given in Appendix B.4.

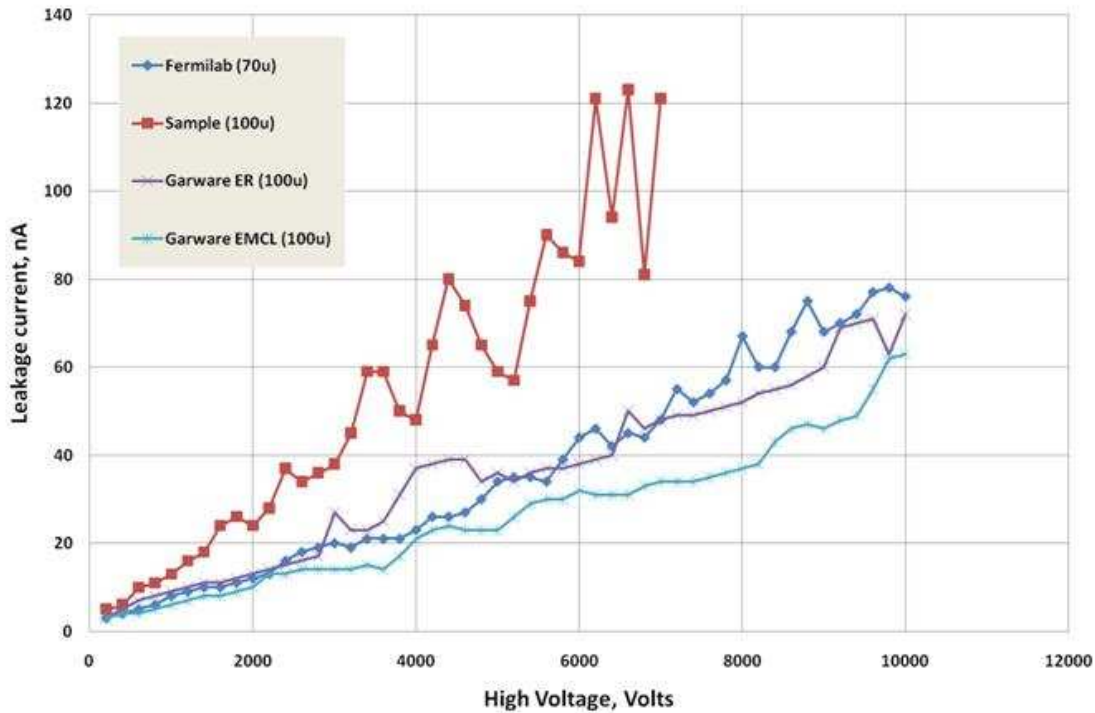


Figure 3.36: Test results of characterisation studies of various insulating film samples.

### 3.7.6 Development and characterisation of pickup panels

Pickup panels are mounted on either side of the RPC detector volume. The charge produced inside the gas volume due to passage of a charged particle through the chamber, induces signals on the strips of the pickup panels due to capacitive coupling. A good design of the pickup panel is crucial not only in terms of its mechanical dimensions, but also in terms of its electrical properties. Pickup panels are typically designed using a dielectric medium between two metallic layers. The metallic layer facing the RPC detector volume is segmented as per the required spatial resolution from the chamber. As far as the mechanical properties are concerned, it is ideal to have the thin pickup panels so that the overall thickness of the finished chamber is minimized. On the other hand as far as the electrical properties are concerned, it will be ideal to have the characteristic impedance of the strips so formed match that of the front-end electronics so that signal reflections are minimised. Another important consideration is the attenuation of the pickup strips, which should be minimised as well. To begin with, we have used pickup panels made of 12 mm thick foam on either side of which aluminum foils are pasted. Pickup strips of about 30 mm are realised by machining the aluminum foil on one side

of the composite. The foil on the other side is used as a common reference plane during the signal conditioning by the front-end electronics. The characteristic impedance of these strips is typically about  $110 \Omega$ . Since the typical input impedance of the front-end electronics is  $50 \Omega$ , this requires use of impedance matching circuits between the pickup strips and front-end electronics. We have also designed and developed pickup panels which use G10 panels which are typically used to fabricate electronic printed circuit boards (PCBs).

However, based on cost and other considerations, we have developed panel boards made of 5 mm thick foam laminated with aluminum foil on both sides. This was done in collaboration with a local industry [136]. The density of the polyurethane(PUR) foam is  $40 \text{ kg/m}^3$ . While the aluminum foil is 0.2 mm thick, the adhesive film which binds the foil with the foam is  $33 \text{ g/m}^2$ (GSM). These panels were machined to form the pickup strips of required pitch as mentioned above. A number of measurements were performed to determine the characteristic impedance of the transmission line formed by the pickup strip and ground plane, the dielectric constant of the foam and the signal attenuation along the strips.

We use the experimental set up shown in Figure 3.37 to measure the characteristic impedance of the pickup strips. A waveform generator is used to send a pulse through a  $50 \Omega$  cable. This cable is matched to a pair of twisted pair lines of characteristic impedance of  $110 \Omega$  using an impedance matching network. While one line goes to an oscilloscope for measurement, the other is connected to the pickup strip whose characteristic impedance we want to obtain. A variable resistor is connected between the two plates of the pickup and adjusted such that the reflection from the far end disappears. This is the characteristic impedance of the strip. This value can be calculated using the dimensions of the pickup strip and the dielectric constant of the foam material [36]. Our measured values were found to agree well with the calculated values. A typical sequence of signals seen on the oscilloscope for a case of un-terminated strip to the matched termination resistor values are shown in Figure 3.38 in the clock-wise direction starting from the leftmost trace. The measurements are done for strips of different widths and at different signal frequencies. We can also estimate the capacitance of the strips and hence the dielectric constant of the foam by using the strip as a capacitor in a mono-shot circuit. We summarised the measurements on characteristic

impedance in Table 3.6. The results of the strip capacitance measurements are given in Table 3.7.

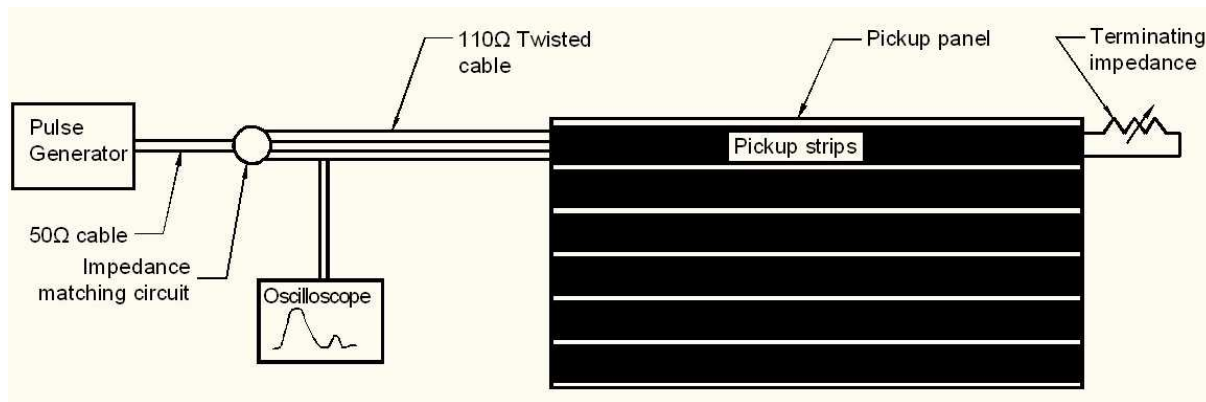


Figure 3.37: Experimental set up for measurement of characteristic impedance of pickup strips.

Table 3.6: Summary of characteristic impedance measurements of RPC pickup strips.

| Pulse frequency (kHz) | $Z_c (\Omega)$ |
|-----------------------|----------------|
| 4.0                   | 117.1          |
| 2.0                   | 114.6          |
| 1.33                  | 100.0          |

Table 3.7: Summary of capacitance measurements of RPC pickup strips.

| $R_{ext} (k\Omega)$ | $t_w (\text{nS})$ | $C_{ext} (\text{pF})$ |
|---------------------|-------------------|-----------------------|
| 10                  | 283.6             | 59.1                  |
| 20                  | 550.0             | 57.3                  |
| 30                  | 817.2             | 56.7                  |
| 40                  | 1071.0            | 55.8                  |
| 80                  | 2162.0            | 56.0                  |

In addition, there is also a requirement for designing a suitable arrangement for providing mechanical support and rigidity to the RPC detector. When using foam based pickup panels, this requirement is met by designing a box-like structure using aluminum around the RPC. This has resulted in increase in the thickness of the RPC, in addition to the increased cost of its fabrication. The design of the ICAL detector structure is carried out assuming a minimum thickness for the active detector elements

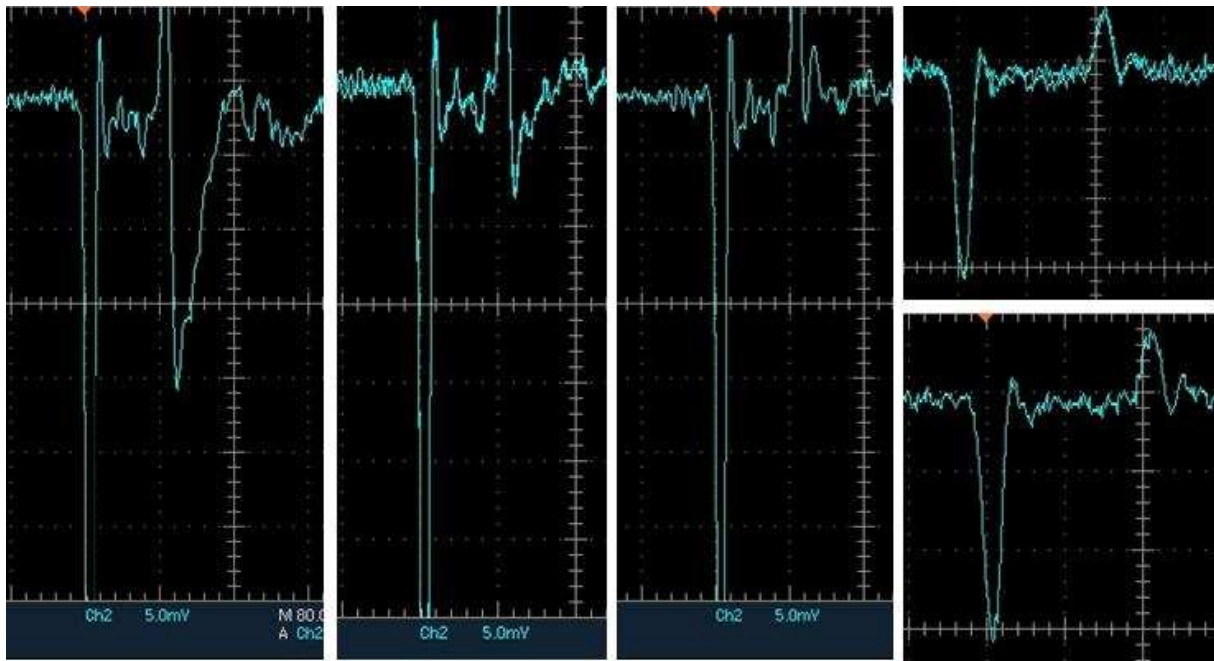


Figure 3.38: Typical signals seen on oscilloscope during measurement of characteristic impedance of pickup strips. The snapshots from left to right and in clock-wise direction correspond to termination resistances of open,  $100\ \Omega$ ,  $51\ \Omega$ ,  $48.2\ \Omega$  and  $47\ \Omega$  respectively.

in order to accommodate 150 of these layers as well as to minimise the magnetic field variations inside the structure. Due to the reasons mentioned above, it was decided to work on development of a solution that combines the two functions, namely that of pickup panels and of the support structure for RPCs.

We have finally developed plastic honeycomb panels of 5 mm in thickness, laminated on one side by  $100\ \mu\text{m}$  thick aluminum sheet and the other side by  $50\ \mu\text{m}$  thick copper sheet, with the help of a local industry [137]. Pickup strips of 30 mm in width are realised by employing the same machining technique on the copper sheet. Aluminum side acts as the signal reference layer. The honeycomb panels were found to be an excellent solution for the mechanical support to the RPC, since it offered better rigidity to the detector with much lesser weight than that of aluminum. The characteristic impedance of these pickup strips turned out to be  $50\ \Omega$ , which has also eliminated the need for any impedance matching circuits between the pickup strips and the front-end electronics.

### 3.7.7 Design and development of RPC casings

Resistive Plate Chambers are planar geometry detectors. The RPC gas gaps (or volumes) which will be used for the ICAL detector are about  $4 \text{ m}^2$  in area, but are only 8 mm thick. This extremely disproportionate and heavy detector module (weighing about 30 kg) poses serious problems in terms of mechanical rigidity and difficulties in the packing, transportation and installation of the modules in the detector. In addition, in spite of gluing the glass sheets together with a matrix of buttons throughout the area and using spacers on the four edges, the chamber tends to bulge outwards when the gas is flown through the chamber. The problem becomes more severe, in the detector as many modules will be cascaded in series in order to implement the gas flow using minimum number of gas channels and thus increasing differential pressure across the chamber gas ports further. These considerations call for a suitable and light weight casing for the chamber. In our case, the RPC case in addition to providing the mechanical strength required for the gas gap, will also house the pickup panels, gas and high voltage connections to the chamber as well as various front-end electronics components. We have designed and tested an aluminum based RPC case to begin with, but could not achieve the desired results in terms of the mechanical strength and other considerations. We subsequently replaced the aluminum panels by aluminum honeycomb panels. This design change seems to have solved the problem and we could achieve all the required results. In order to even improve the mechanical strength further, we have bent the top and bottom panels of the casing with a radius of curvature of 10 mm and mounted the panels in the assembly such a way that the parabolas face outwards. Shown in Figure 3.39 is a detector being assembled in a RPC case which was fabricated using the aluminum honeycomb panels.

## 3.8 Development of large area RPCs

Having learnt the science and technology of RPC design through fabrication and characterisation of small prototype chambers, as well as having developed all the materials, processes and infrastructure needed for detector R&D of ICAL experiment magnitude, we have taken the next logical step to develop larger area RPCs of  $100 \text{ cm} \times 100 \text{ cm}$  in dimensions. We used 3 mm thick Asahi Float glass sheets which were procured lo-



Figure 3.39: Honeycomb panel with milled copper pickup strips shown (left panel) and partially assembled RPC using aluminum honeycomb panel.

cally. We measured its bulk resistivity ( $\rho$ ) to be  $2 \times 10^{12} \Omega\text{-cm}$ . We have essentially used the materials, followed the procedures and utilised the infrastructure described in the previous sections of this chapter.

The glass sheets were coated with the special paint that we had developed and applied using the automatic plant. The polycarbonate spacers, buttons and gas nozzles were used for the assembly of the gas gap, which was set in place by using the vacuum jig. Machined plastic honeycomb panels mounted orthogonally on either side of the gas gap, were used for signal pickup. Finally the chamber was packed inside a case made of aluminum honeycomb panels. We show in Figure 3.40, a photograph of the fully assembled such RPC along with its efficiency plateau characteristics obtained using a cosmic ray muon telescope.

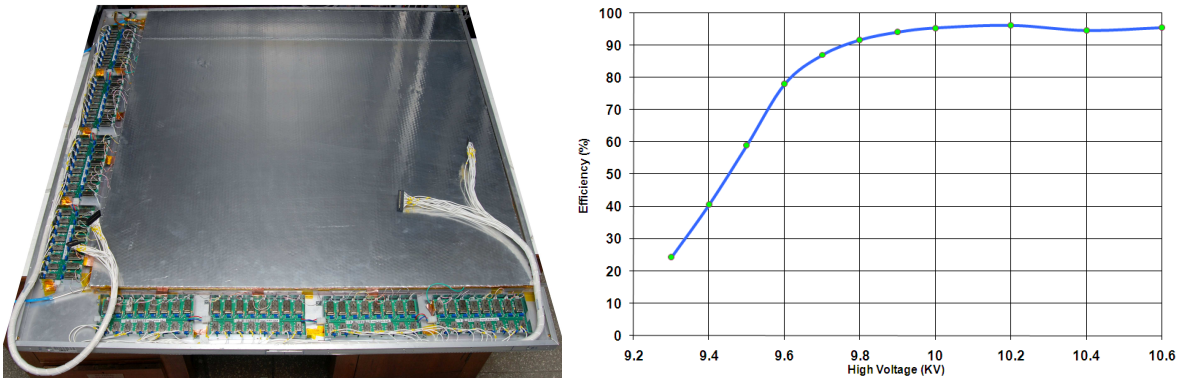


Figure 3.40: A fully assembled RPC of dimensions  $100 \text{ cm} \times 100 \text{ cm}$  along with the front-end electronics mounted (left panel) and its efficiency plateau (right panel).

We have built 12 chambers of this type and individually characterised them in a

cosmic ray test stand. These chambers were arranged in a detector stack and is in continuous operation now for about two years tracking cosmic ray muons. The data obtained from this detector has helped us improve our understanding of the RPC design, characteristics, long-term stability etc. The construction and readout system of this detector stack is dealt with in Chapter 4 and results obtained from the same are discussed in Chapter 5.

### 3.9 Development of RPCs for ICAL detector

As mentioned in Chapter 1, the ICAL detector proposes to use about 30,000 RPCs of  $184\text{ cm} \times 184\text{ cm}$  in dimensions. Therefore, our final aim was to build RPCs of this size and study their performance and long-term stability in operation, so that they can be successfully produced in large numbers and used in the ICAL detector. These RPCs are comparable to some of the largest area chambers in the world.

We essentially followed the same procedure which we have streamlined for the fabrication of gas gaps earlier. We have also used glass manufactured by the same company (M/s Asahi Float Glass). However, RPCs of this large area had required design of and development of special handling system and jigs for their assembly and handling. We have successfully designed and developed this infrastructure. We did not face any problem with the rest of the RPC fabrication aspects. We have also developed a new cosmic ray test stand to handle these large size RPCs. Shown in Figure 3.41 are pictures of a  $200\text{ cm} \times 200\text{ cm}$  RPC being assembled (left panel) and three such RPCs are being tested in a cosmic ray test stand (right panel).



Figure 3.41: A  $200\text{ cm} \times 200\text{ cm}$  RPC being fabricated (left panel) and three such RPCs are under test in a cosmic ray test stand (right panel).

One of the useful parameters of the RPC operating at its designed conditions, particularly from the point of view of its front-end electronics design, is its mean signal charge or pulse height as seen by the preamplifier. We have studied this parameter for a  $200\text{ cm} \times 200\text{ cm}$  RPC. We captured about 2000 samples of the preamplifier (voltage gain of about 80) output pulses on a digital storage oscilloscope. A sample of these pulses is shown on the left panel of Figure 3.42. We have obtained their peak pulse heights by analysing the data using a software script. Shown on the right panel of Figure 3.42 is their peak pulse height distribution. We have obtained from this plot, the mean pulse height of the RPC signal across a  $50\Omega$  load to be about 3mV. This information was used during design of a front-end ASIC for the ICAL detector.

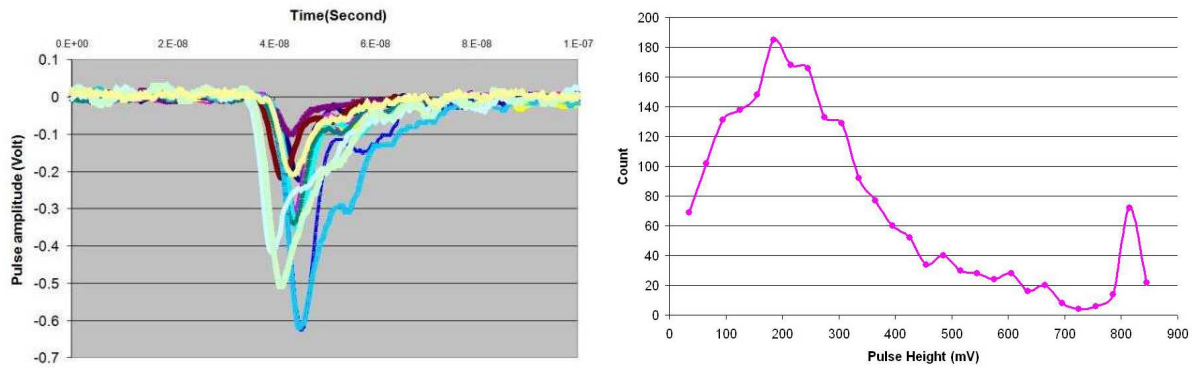


Figure 3.42: Preamplifier output traces of a  $200\text{ cm} \times 200\text{ cm}$  RPC (left panel) and distribution (histogram) of their peak pulse heights (right panel).

Three,  $200\text{ cm} \times 200\text{ cm}$  RPCs are in continuous operation for about four months. Long-term stability of these RPCs is being monitored using their noise rates and chamber currents, measured along with ambient conditions such temperature and relative humidity. Time profile of noise rate of a typical RPC channel, along with the ambient temperature is shown in the Figure 3.43. All three RPCs are showing stable behaviour as shown by this plot.

### 3.9.1 Studies of $\text{SF}_6$ on the RPC performance

To begin with, we have operated the RPCs in the avalanche mode using a binary gas mixture of Freon (R134a) and Isobutane in the proportion of 95.5 : 4.5 by volume. It is reported widely in the literature [138][139] that addition of even small quantities of Sulphur Hexafluoride ( $\text{SF}_6$ ) as quenching gas to the RPC gas mixtures brings stability

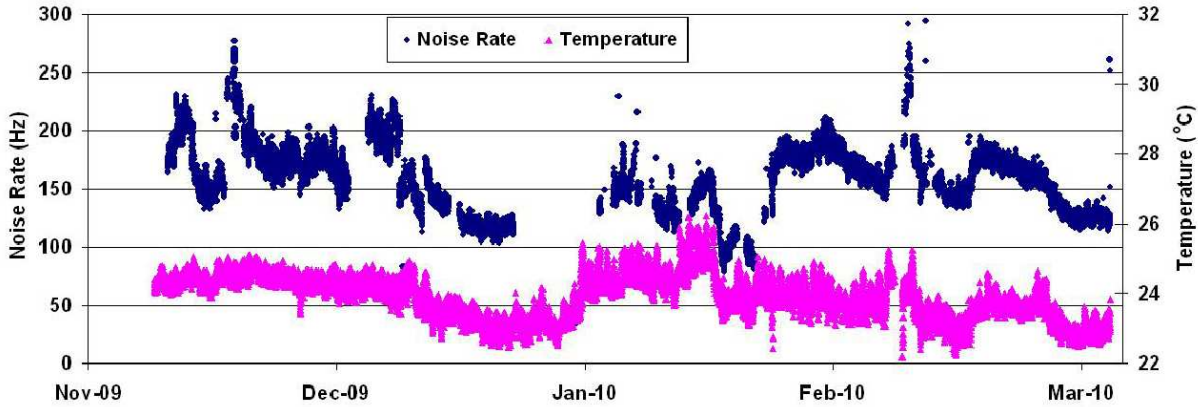


Figure 3.43: Time profile of noise rate of a  $200\text{ cm} \times 200\text{ cm}$  RPC channel, along with the ambient temperature.

to the RPC operation.  $\text{SF}_6$  which is commonly encountered as a high voltage dielectric in the high voltage supplies of particle accelerators, also helps improve the overall insulation characteristics of the RPC gas gap. It works better than Isobutane in containing photon initiated streamers in the RPC operating in avalanche mode due to its high electron affinity ( $1.05 \pm 0.10\text{ eV}$ ). Though this will suppress production of large fast charges in the gas volume and hence result in reduction of charge gain of the RPC, it will extend the streamer free operation and its operating high voltage range [140] [141]. Reduction of the total charge released in the gas gap for each detector count, slows the overall aging of the chamber [142].

Though we had done some preliminary studies on the effect of  $\text{SF}_6$  on the RPC operation and characteristics using  $100\text{ cm} \times 100\text{ cm}$  RPCs earlier, we have now carried out more comprehensive studies using the  $200\text{ cm} \times 200\text{ cm}$  RPCs. We describe below some of the more prominent among these studies and their results.

Shown in Figure 3.44 are oscilloscope screen shots of pulses from an RPC, operated in the avalanche mode, without and with  $\text{SF}_6$  in its gas mixture. When the RPC is operated without  $\text{SF}_6$ , streamer pulses followed by regular avalanche pulses, as shown in the left panel are seen very often. By adding a fraction of a percent of  $\text{SF}_6$  in the gas mixture, these pulses could be almost completely eliminated, as shown in the right panel.

We show in the left panel of Figure 3.45, the voltage-current characteristics of an RPC without and with  $\text{SF}_6$  gas mixtures. The current through the RPC depends, among other factors, on the quenching gases used. Usually one or more of the standard

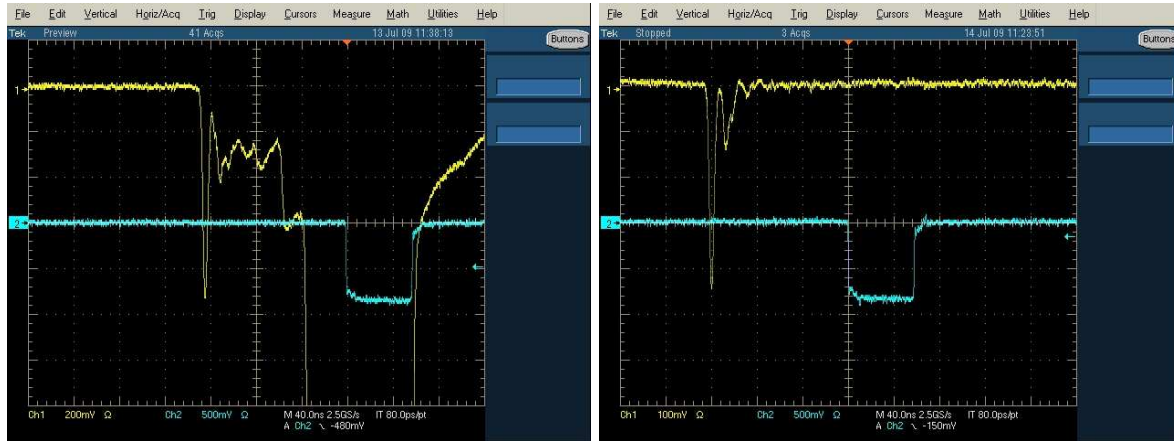


Figure 3.44: Oscilloscope screen shots of signal from RPC, operated without (left panel) and with (right panel) gas mixture containing SF<sub>6</sub>.

quenching gases are used to achieve and optimise many performance characteristics of the RPC. SF<sub>6</sub> is one of the most effective quenching as well as insulating gas especially at higher operating voltages. As can be seen in the figure, it helps bring down the RPC current. At lower operating voltages, however, the currents will be similar with or without SF<sub>6</sub> in the gas mixture, because almost the entire current is contributed by the ohmic component and the component from the gas amplification is insignificant. The chamber current as function of SF<sub>6</sub> fraction in the gas mixture is shown in the right panel and shows the expected trend.

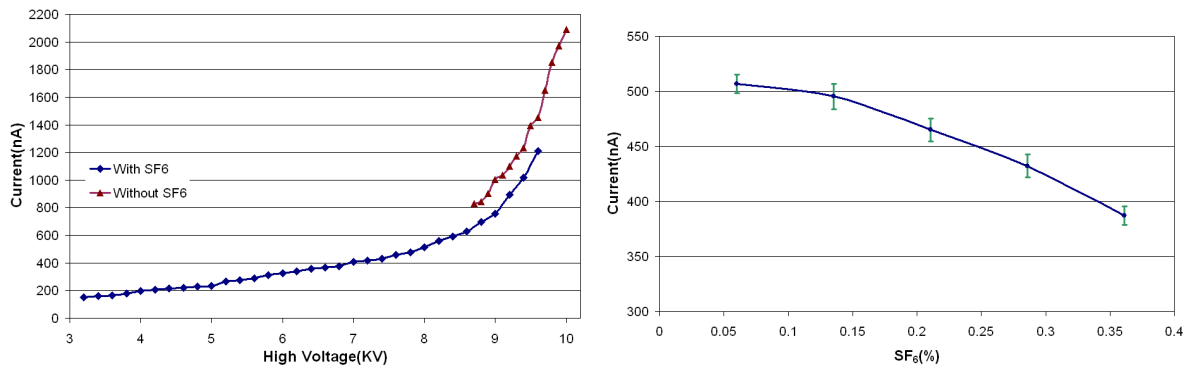


Figure 3.45: RPC current characteristics without and with SF<sub>6</sub> gas mixture.

Charge spectra of the RPC operated in the avalanche mode with a gas mixture of varying SF<sub>6</sub> fractions are shown in the left panel of Figure 3.46. A drastic reduction in the charge yield of the RPC is clearly seen as we increase the fraction of SF<sub>6</sub> even marginally. Shown in the right panel are the most probable and maximum values of the charge spectra, which help in quantifying the effect of SF<sub>6</sub>.

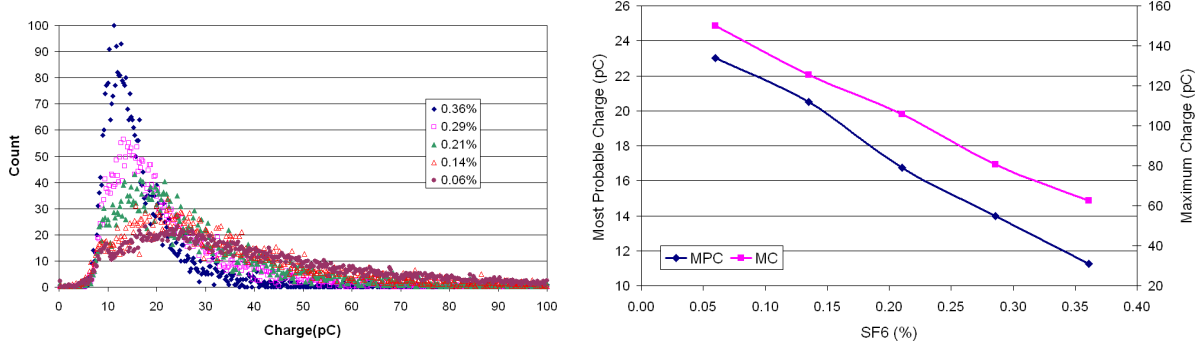


Figure 3.46: Effect of SF<sub>6</sub> in the gas mixture on RPC charge yield. The plot shown in the left panel is a superposition of charge distributions of RPC operated at various SF<sub>6</sub> concentrations. In the right panel, we show the extracted parameters of the distributions, such as most probable and maximum charge.

Two most important parameters of the RPC as a function of SF<sub>6</sub> concentration in the gas mixture are shown in Figure 3.47. The efficiency of the central pickup strip (S32) of the x-plane (to be read on the primary y-axis) and cross-talk of the adjoining pickup strips (S31 and S33) of the same plane (to be read on the secondary y-axis) recorded by a cosmic ray muon telescope, are shown in the left panel. The telescope window which is defined by a 2 cm wide *finger* paddle, was centred on the 3 cm wide central strip. The efficiency and cross-talk are defined as the ratio of number of coincident pulses of the strips with that telescope trigger to the number of trigger pulses. While the efficiency of the central strip has dropped only by a few percent for an increase of 0.3% in SF<sub>6</sub> fraction, the cross-talk from the adjoining strips fell by more than 40% for the same change in SF<sub>6</sub> concentration. This indicates that SF<sub>6</sub> helps a great deal in containing the avalanche to a smaller area and thus improves spacial resolution of the RPC.

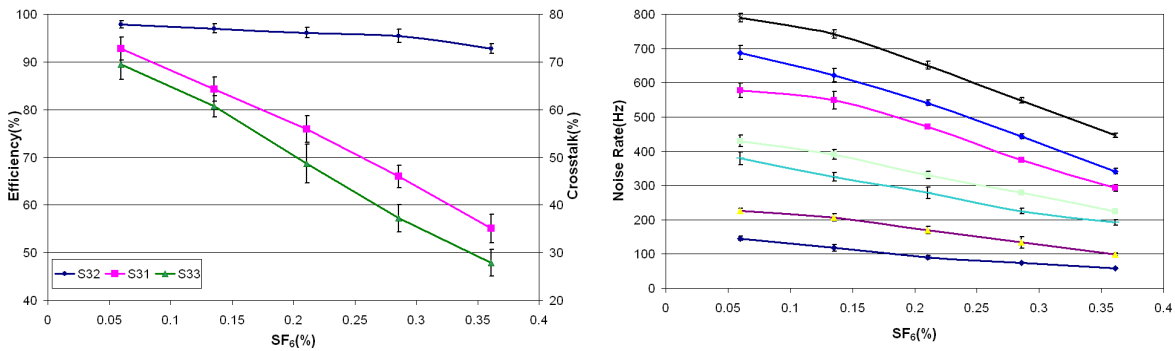


Figure 3.47: Effect of SF<sub>6</sub> in the gas mixture on RPC efficiency (left panel) and noise rate (right panel) characteristics.

Noise rates of several strips for the same change mentioned above in the SF<sub>6</sub> con-

centration, are shown in the right panel. The reduction in the noise rates is consistent with the change in the overall charge yield shown earlier in this section.

The timing performance of the RPC is a crucial factor in deciding its suitability for a particular detector application. This capability of the RPC can be fine tuned by judiciously choosing the fraction of SF<sub>6</sub> fraction in its gas mixture, as shown in Figure 3.48. The pulse response time (left panel) of the RPC is delayed by about 2 ns for an increase of 0.3% in the fraction of SF<sub>6</sub>. The avalanche needs additional time till the charge developed crosses the readout threshold as its rate development is reduced with the increase of SF<sub>6</sub>. This is also accompanied by a marginal deterioration in the timing resolution of the order of a couple of hundred pico seconds.

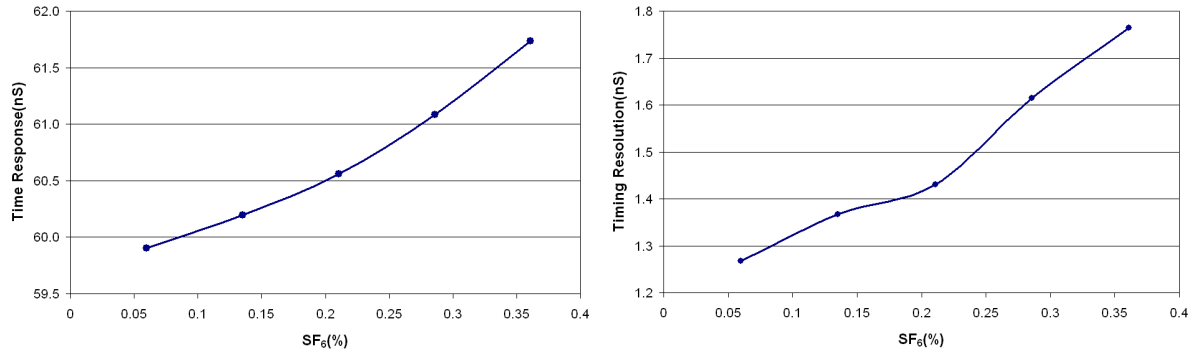


Figure 3.48: Effect of SF<sub>6</sub> in the gas mixture on RPC timing characteristics. While the time response plot is shown in the left panel, time resolution as a function of SF<sub>6</sub> fraction in the gas mixture is shown in the right panel.

## 3.10 Chapter summary

We began our work by developing a large number of single gap glass RPCs of about 30 cm × 30 cm in area and characterising them by operating in the streamer mode. We have successfully demonstrated efficient tracking of cosmic ray muons using a stack of these RPCs. Subsequently, we were faced with a severe problem with regard to their long-term operation in this mode. We have done extensive studies on electrodes from the damaged RPCs as well as several local and imported glass samples. Results from the studies did not show any appreciable differences among various glass samples. We then fabricated a few RPCs of 40 cm × 30 cm in area using Japanese glass and operated them in the avalanche mode continuously for more than two years without

any problem of detector aging. We then developed, built and characterised large area RPCs of dimensions  $100\text{ cm} \times 100\text{ cm}$  required for the ICAL prototype detector stack successfully [143].

RPC fabrication involves deploying a large number of materials as well as many assembly procedures. We have studied a number of different type and quality of these materials and optimised most of these items. We have also designed and developed a large number of assembly and quality control procedures and invented a number of useful jigs that are extremely useful in production of good quality detectors. We have collaborated with local industries to develop a suitable paint as well as its application methods on glass electrodes used for large scale RPC fabrication. We have also designed and developed three generations of gas mixing, distribution and recycling systems needed for RPC operation.

Equipped with various sophisticated materials, processes and infrastructure that we had built over the past few years, we have finally fabricated a couple of  $200\text{ cm} \times 200\text{ cm}$  chambers and evaluated their performance in detail. These detectors are operating flawlessly till now, essentially concluding the most crucial detector R&D phase of the ICAL detector construction.

## ICAL prototype detector stack

The INO collaboration has proposed to build a prototype of the magnetised iron calorimeter (ICAL) to study cosmic ray muons, in order to understand and estimate the performance of the final detector. It was also envisaged that this prototype detector will be used to test the results obtained from the physics and detector simulation studies that are currently underway as well as provide some measured data to help refine the simulations. The detector, of about  $1\text{ m}^3$  in active volume and which can house 12 layers of RPCs each of about  $100\text{ cm} \times 100\text{ cm}$  in area, was assembled at the site in VECC, Kolkata using 5 cm iron plates between the RPC layers. The magnet, which is required to generate about 1.3 T magnetic field has been designed, fabricated, tested and installed in the detector [144].

Meanwhile, we have setup a detector stack using 12 RPC layers of  $100\text{ cm} \times 100\text{ cm}$  in area, but without magnetic field capability, in order to study their long-term performance and the data readout aspects. In fact, as already reported in Section 3.2, we had earlier successfully built a stack comprising of small area RPCs and tracked cosmic ray muons using the same.

We describe the design and construction of this large, magnet-less detector stack in this chapter [145]. While, various components and sub-systems that make up this detector stack are described, the emphasis is mainly laid on the readout electronics, data acquisition, monitoring and trigger systems, which were indigenously designed. We report the validation studies on the readout electronics in this chapter, while leaving the analysis and results on the RPC performance data for the next chapter.

## 4.1 Assembly of 100 cm × 100 cm RPCs

Based on our detector R&D and development of various materials and fabrication procedures (refer Chapter 3), we have built RPCs of 100 cm × 100 cm in area, which are needed for the detector stack. The RPC gas gaps were fabricated using 3 mm thick Asahi Float glass sheets procured from local market. The glass sheets were coated with a semi-resistive paint using an automatic plant. Both the paint and the plant were developed in collaboration with local industries. Polycarbonate buttons, spacers and gas nozzles, which were developed indigenously and manufactured by another local industry, were used to assemble the gas gaps. The gaps were fabricated with the help of a pneumatic jig, which ensured that the gap between the glass sheets is uniform throughout gas volume as well as all the joints are glued well. Custom built honeycomb panels, built as a composite of plastic core padded on both sides with copper sheets, were used for signal pickup as well as for providing the mechanical rigidity to the assembled chamber. Two panels, each grooved with 30 mm signal pickup strips were mounted on either side of the gas gap and orthogonal to each other in order to record particle hit coordinates in both X- and Y-planes. Polyester films were used to isolate the signal pickup panels from the RPC gas gap surfaces, which are maintained at high voltage while the RPC is in operation.

Figure 4.1 shows the mechanical drawings of a base chassis made of aluminum honeycomb panels, on which the RPCs are assembled. The low voltage power supply (for preamplifiers) and high voltage (for RPC) as well as the inlet and outlet gas connectors are all terminated on the chassis as shown in the left panel. The right panel shows the placement of an RPC gas gap on the chassis. The front-end preamplifier boards are mounted in the area between the RPC gas gap boundaries and the front and left edges of the chassis. The other two edges of the chassis are sealed along with the top honeycomb panel, using an adhesive aluminum tape in order to provide the necessary electromagnetic induction (EMI) shielding for the assembled chamber. It may be noted that in this design, the preamplifier boards occupy substantial area on the chamber, which essentially amounts to dead space for charge particle detection. However, front-end electronics for the ICAL detector is being designed based on ASICs and the same will be integrated within the RPC foot-print itself.

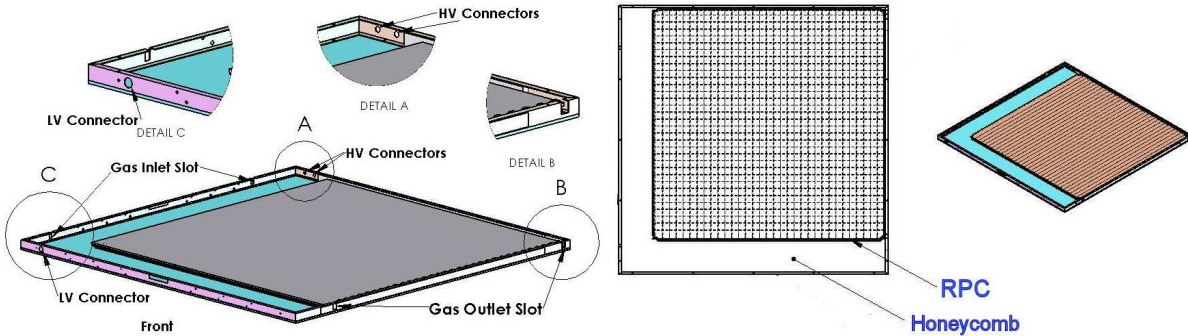


Figure 4.1: Mechanical assembly drawings of 100 cm × 100 cm RPCs used for constructing the ICAL prototype detector stack.

## 4.2 Construction of the detector stack

We have constructed a suitable stand using aluminum sections to house 12 RPCs of 100 cm × 100 cm in area. The stand facilitates easy insertion, removal and precise alignment of the RPCs to the level of a few mm, which is essential to configure the detector to track cosmic ray muons. The inter-layer gap is fixed at 160 mm. A picture of the stack in operation is shown in Figure 4.2.



Figure 4.2: Fully installed ICAL prototype detector stack along with the gas system (left) and DAQ and power supply systems (right). The front-end electronics racks are built on either side of the detector stack - one each for X- and Y-readout planes.

As can be seen in the figure, two multi-level racks built again using aluminum sections, are anchored to either sides of the front-face of the detector stack. All the front-end electronics circuit boards along with the necessary cabling are installed in

these racks. This arrangement has helped in reducing the analog signal cable lengths from the on-detector preamplifier boards to the front-end electronics racks and improved the signal fidelity. In addition it offers high flexibility to service the front-end electronics system.

## 4.3 Segmentation of the prototype detector

We pick up the signals both on the anode side (negative polarity signals) as well as on the cathode side (positive polarity signals) of the RPC, using pickup panels which are mounted orthogonal to each other on either side of the gas gap. In all, there are 64 pickup strips or electronic channels to be readout - 32 on either readout plane. Therefore, we have to handle 768 electronic readout channels from this detector stack. The channels are read out in groups of eight, each group processed by one 8-in-1 fast preamplifier board.

Figure 4.3 shows this arrangement as a schematic for one side of the stack. The RPC identification and its corresponding assigned gas channel numbers are also shown, layer-wise, in the figure.

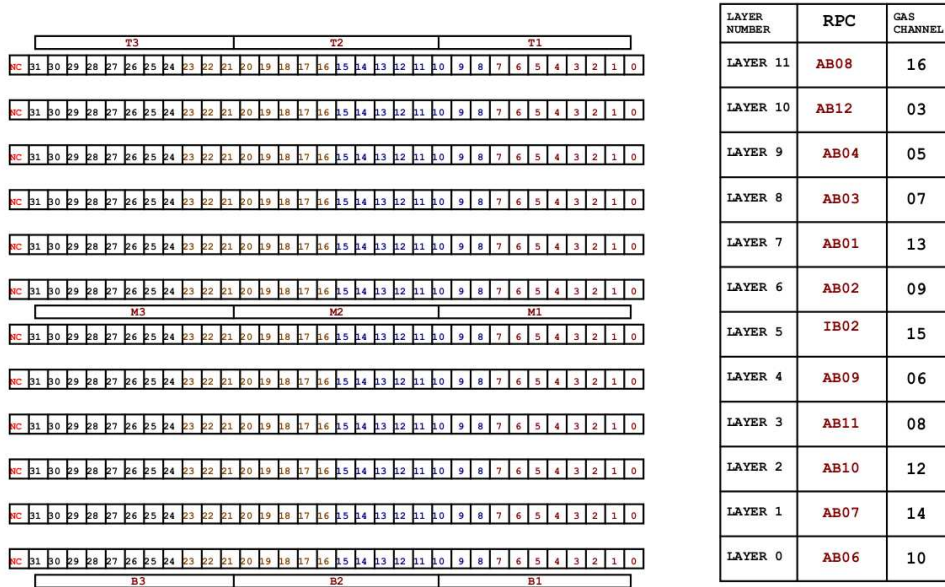


Figure 4.3: Segmentation scheme of the ICAL prototype detector stack. Only the X-readout plane view is shown here for brevity.

## 4.4 Gas system for the prototype detector

All the RPCs in the detector stack are operated in the avalanche mode, using a gas mixture of R134a : Isobutane : SF<sub>6</sub> in the proportion 95.5 : 4.2 : 0.3. The second generation gas mixing and distribution system, described in Section 3.5.1 and shown in Figure 4.2 is used to supply gas to the RPCs in this stack.

The input gas lines - one per RPC are routed from the gas system. The exhaust gas from the RPCs is collected individually through output bubblers into a manifold, before venting it to the atmosphere. The entire gas line plumbing is done using stainless steel tubes, in order to avoid possible seepage of moisture into the gas lines. Bleeder bubblers are mounted on the RPC gas input channels for protecting the chamber in case of high pressure built up on the gas line due to blockages etc. All the input gas channels have been precisely calibrated over their entire dynamic range by water displacement and the tube methods, which are detailed in Section 3.5.2. The entire operation of setting the individual gas fractions as well as round-the-clock monitoring of the gas system parameters are controlled by a PC host using a dedicated hardware interface and graphical user interface (GUI) based application software.

## 4.5 Power supply and monitor systems

The required field across the RPC glass electrodes is setup by applying a differential high voltage of  $\pm 4.9$  kV, using contacts on the semi-resistive coat. The chamber current drawn during the operation is typically in the range of 100 nA per RPC. In order to carry out RPC plateau studies and due to other operational reasons, we required a provision of ramping up/down the high voltage at a required step size. Also since the stability of an RPC could be ascertained by its chamber current, a facility to monitor the output supply voltages and load currents - channel-wise, was an essential feature of the high voltage power supply.

The front-end electronics for the detector stack, comprising of preamplifiers, analog and digital front-end sub-systems as well as signal routers, require d.c. power supplies such as  $\pm 6$  Volts and  $\pm 8$  Volts. Average load currents on these power rails are 25 and 90 Amps for  $\pm 6$  Volts and 15 and 25 Amps for  $\pm 8$  Volts, respectively. Essential require-

ments of the low voltage power supply system are fine control of supply voltages at the load points and the monitoring of supply voltages and load currents.

Both the power supply systems were designed using commercial components from CAEN [146] and shown in Figure 4.4. The high voltage system comprises of two 12-channel high voltage supply modules - one each for either polarity, plugged into an SY2527 power supply mainframe (shown in the left panel in the figure). The low voltage power supply system similarly comprises of several supply modules, plugged into an Easy system crate. The 48 volts raw d.c. power is supplied to the Easy system using a 3-phase AC/DC converter. The system is controlled and connected to the SY1527 mainframe, through a branch controller installed in the latter.

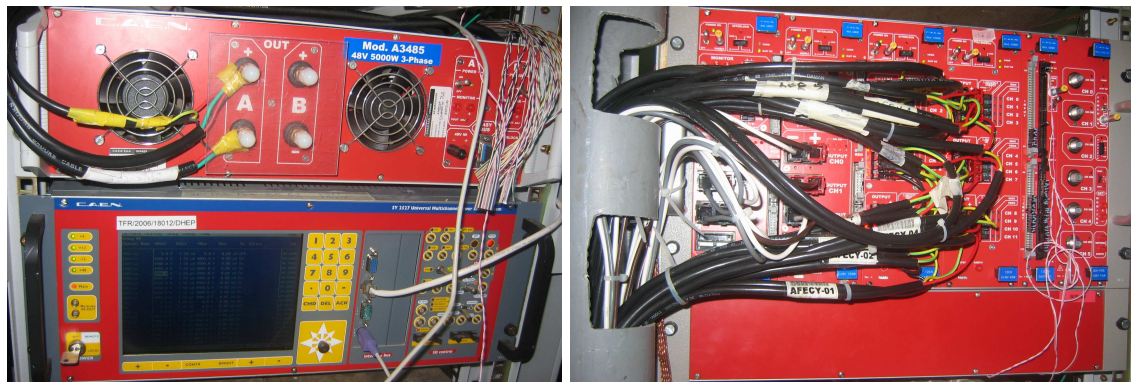


Figure 4.4: Commercial components based high voltage (left panel) and low voltage (right panel) power supply systems for the ICAL prototype detector stack.

Based on the power supply requirements of individual front-end electronics modules, a suitable scheme was designed to distribute power from the power supplies to various modules (Figure 4.5). Multiple bus-bars made of thick copper strips were used for this purpose so that the ohmic voltage drops across the connecting conductors could be minimised. While the input power lines from the power supplies were connected on one end of these bus-bars, power supplies needed by various front-end boards were directly tapped from these bus-bars. This bus-bar based low voltage power supply distribution design has also resulted in improved ground quality to the electronics and data acquisition system.

Both the low voltage and high voltage power supply systems support control and monitoring of various parameters and values through Ethernet ports. We have developed a comprehensive PC based software system on this interface, using which the required voltages are set on various output supply channels. The set voltages and load

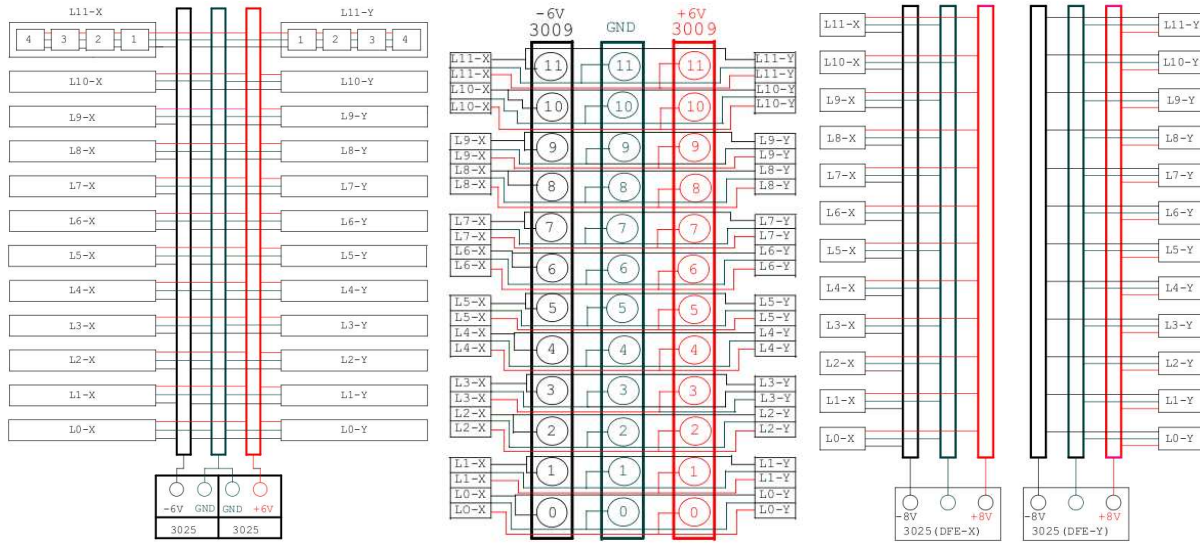


Figure 4.5: Low voltage distribution scheme and networks for the preamplifiers (left panel), analog (middle panel) and digital (right panel) front-end subsystems.

currents are logged in on round the clock basis, which are used to correlate them with long-term behaviour of the RPCs along with ambient conditions etc. Typical screen shots of low voltage and high voltage power supply system monitor consoles are given in Figure 4.6.

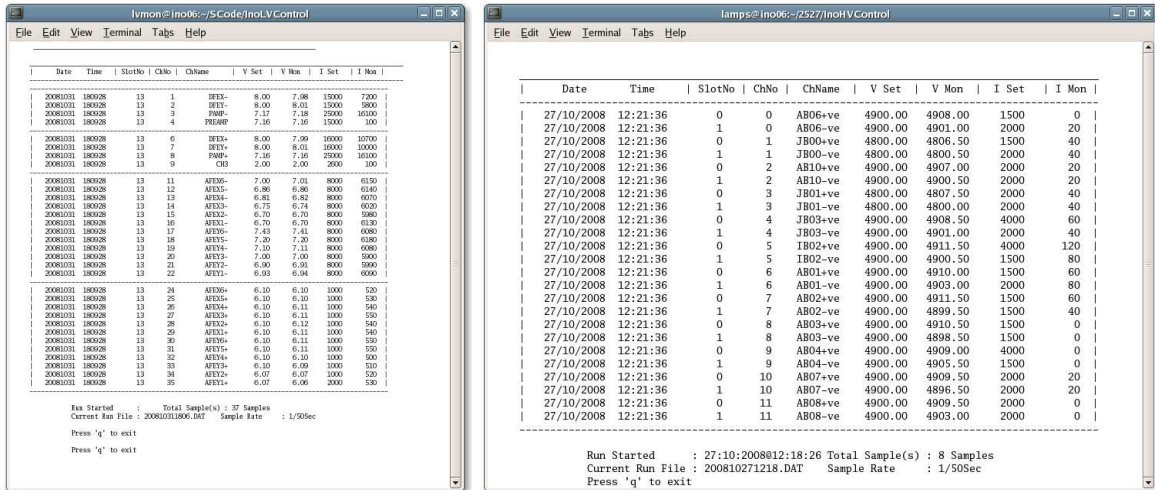


Figure 4.6: Screen shots of low voltage (left panel) and high voltage (right panel) power supply system monitor consoles. These are made accessible on the intranet for facilitating remote monitoring and control.

## 4.6 Electronics and data acquisition system

The main objective of the data acquisition system designed for the prototype detector stack is to generate trigger signal whenever a charged particle passed through the detector leaving a track, based on the hit pattern of the RPC pickup strips and to record strip hit patterns as well as timing of individual RPCs with reference to the global detector trigger. A system schematic of the data readout electronics for the detector stack is shown in Figure 4.7.

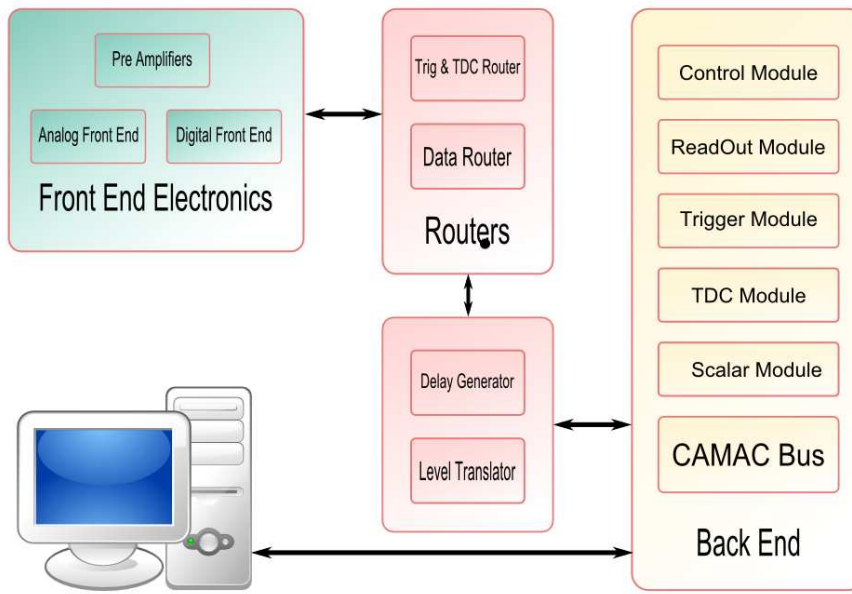


Figure 4.7: Schematic diagram of the front-end and data acquisition systems for the ICAL prototype detector stack. The back-end is based on the CAMAC modular instrumentation standard.

The signal readout chain at the front-end essentially consists of fast, high gain, HMC based preamplifiers and low-level, threshold leading-edge discriminators, followed by the digital front-ends. The digital front-ends built around a couple of Complex Programmable Logic Device (CPLD) chips handle the important tasks of latching the strip hit pattern on master trigger as well as serially transferring data to the back-end system. It is also here that the pre-trigger signals are generated, which are used by the back-end trigger module built using a Field Programmable Gate Array (FPGA) and produces the master trigger. Finally, the digital front-end system also handles the entire signal multiplexing required both during the event data acquisition as well as during strip signal rate monitoring. The RPC timing data on trigger is acquired using commercial TDC modules. The data acquisition is implemented on a CAMAC back-end,

employing many custom built modules, such as control and readout modules. The multiplexed signals from the front-end are sent to the back-end through appropriate router modules. Monitoring of strip signal rates is performed as a periodic background job using scaler modules in the back-end.

Segmentation of the front-end and data acquisition systems in terms of the actual functional circuit boards is given in the Figure 4.8. As indicated in Section 4.3, four preamplifier boards are required per plane per layer. Similarly two analog-front-end (AFE) and one digital front-end (DFE) boards are required in the downstream to process signals from one RPC readout plane. Two control and data router (CDR) modules and one trigger and TDC router (TTR) module are used to multiplex, distribute and transmit data and control signals between the front and back-ends. Further, the TDC (stop) signals are delayed by using four delay generator modules, in order to setup the appropriate timing sequence at the TDC modules used for recording the RPC timing information. Similarly, a signal translator module is also used to convert some of the CDR signals into those compatible to the back-end modules. The CAMAC back-end is configured with a commercial controller as its supervisor, which in turn is driven by a Linux host through an Ethernet port. The back-end system comprises of a master trigger generator, a couple of scalers, a control module and a data readout module, in addition to two commercial TDC modules. In total, about 200 circuit boards and modules of 13 different types were designed and developed by us for this prototype detector. We describe below, in sub-sections, the electronics and data acquisition system in some detail.

#### 4.6.1 Fast preamplifiers

The RPC signal pickup strips which are realised by milling the plastic honeycomb based panels were characterised and found to offer a characteristic impedance of  $50\Omega$ . In the avalanche mode of operation, in which we chose to run the RPCs for ICAL, typical signal range on these strips across a  $50\Omega$  load is 0.5 - 2 mV and rise time of about 1 ns. Hence, there is a need for a high speed, low noise preamplification for the RPC strip signals before it can be further processed by the front-end electronics. We extract these signals into the front-end electronics by terminating the far-end of the strip by a  $50\Omega$  resistor and connecting the near end to a 8-in-1 two-stage Hybrid Micro Cir-

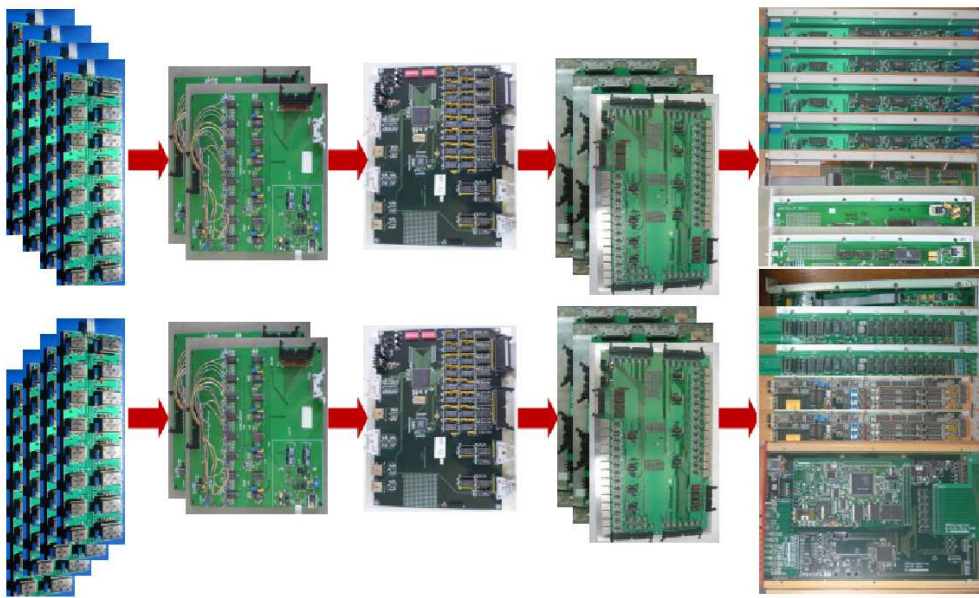


Figure 4.8: Signal flow of the data acquisition system shown using the actual circuit boards. The DAQ sections that these groups of boards represent from left to right are preamplifiers, analog front-end, digital front-end, routers and back-end respectively.

cuits (HMC) based high speed high gain preamplifiers (left panel of Figure 4.9). Two types (BMC 1595 and BMC 1597) of first stage HMCs - one of each for positive and negative polarity strip signals, were designed to provide a nominal gain of 10 and a negative polarity output signal. The second stage HMC (BMC 1513) offers another factor of 10 gain to these signals. All these HMCs<sup>1</sup> share similar design characteristics, such as input signal handing range (100 - 200 mV), bandwidth (350 MHz), rise time (2 ns), power rails ( $\pm 6$  Volts) and power dissipation (120 - 140 mW).

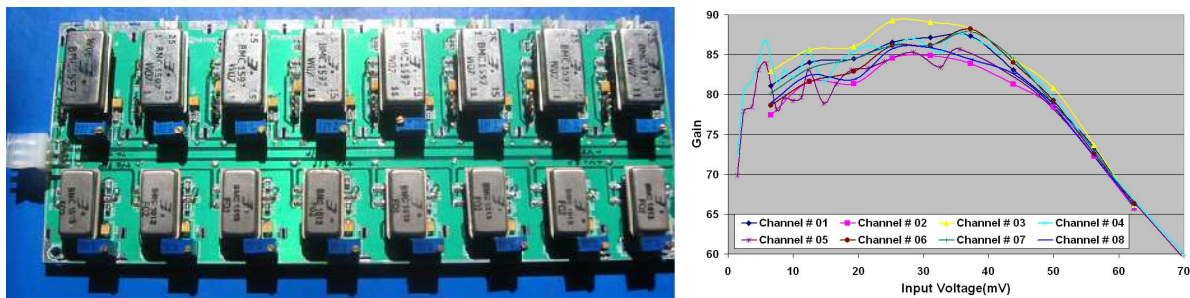


Figure 4.9: HMC based 8-in-1 two-stage preamplifier: the circuit board (left panel) and its gain characteristics (right panel). About 100 such boards were needed to instrument the prototype detector stack.

We have studied gain characteristics of all the preamplifier channels, which have

<sup>1</sup>designed by the Electronics Division of Bhabha Atomic Research Centre (BARC), Mumbai and fabricated at the Bharat Electronics Ltd. (BEL), Bengaluru

shown excellent performance, matching to the design parameters (right panel of Figure 4.9). As can be seen, all the eight channels of the board show a uniform gain of about 90 over a broad range of input signals. The preamplifier boards are fitted inside a galvanised iron (GI) mounting case before installing in the RPC chassis in order to improve the EMI shielding as well as grounding especially at the input side of the board.

### 4.6.2 Analog and digital front-end electronics

The preamplified RPC strip signals are fed to AFE boards. One of the main functions of the AFE board is to convert these amplified analog RPC pulses into logic signals by using low threshold discriminator circuits. The AFE boards also incorporate a primitive trigger logic on board, where discriminator outputs of four channels are shaped to 50 ns pulses and logically *ORed* to generate level-0 trigger signals. The discriminator signals from the AFE boards are further processed by a DFE, which mainly consists of three sections - event data readout, monitoring and level-1 trigger generation. The shaped logic strip signals are registered in a latch which is timed by the final trigger signal. The latched information is then flushed out serially to the back-end along with the board identification code. In the monitor mode, the counting rates of all the strip signals as well as a few fixed frequency calibration signals are monitored sequentially. While, the sequence of signals is initialised by the back-end, the subsequent channels are selected locally in the front-end module itself. This helps reducing communication over-head between the front- and back-ends. Only the multiplexing of these signals is done on the DFEs, while the actual counting is performed by scalers located in the back-end. Both event and monitor data from a DFE are identified by their board identification codes preset by static switches. These two sub-sections are implemented in a CPLD chip (Xilinx XC95288 HQ208 AEM 0049). Finally, the level-0 trigger signals from the AFE are logically *ANDed* to achieve the required  $M$ -fold triggers, where  $M$  is the layer coincidence of  $M$  consecutive signals out of 32 pickup signals. This level-1 trigger logic is implemented using another CPLD chip (Xilinx XC95536 PC44 AEM 0217), thus making it user configurable. A combined signal flow diagram of the AFE and DFE boards is shown in the Figure 4.10.

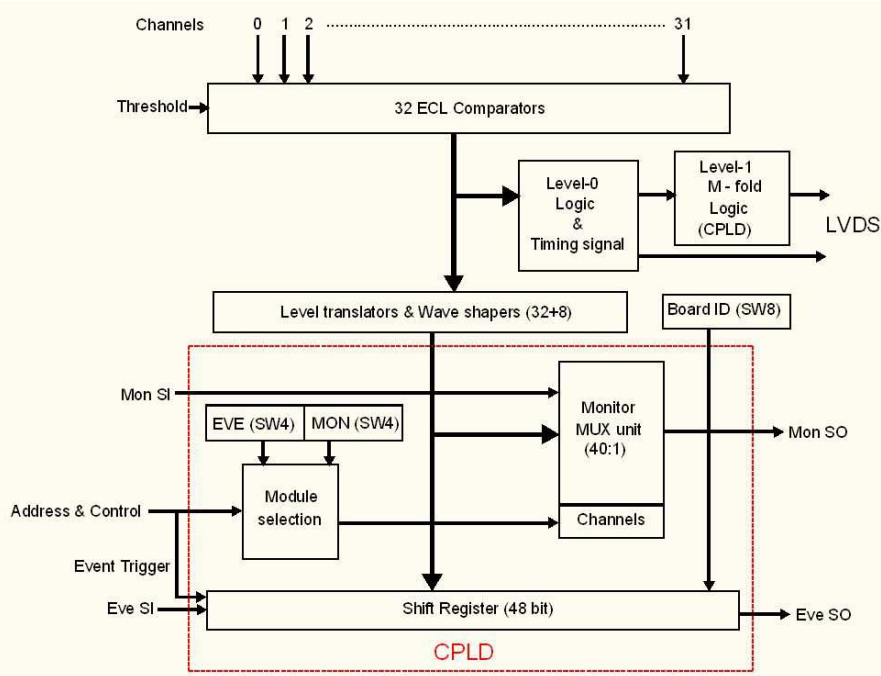


Figure 4.10: Signal flow diagram of the analog and digital front-end sections. Inputs shown at the top of the diagram are the analog signals from the preamplifiers. The daisy-chained control signals from the previous station are shown to enter from the left and exit to the next station from the right side of the diagram.

### 4.6.3 Back-end control and DAQ system

The back-end control and DAQ system is implemented on the CAMAC modular instrumentation standard. This layer completes all the requirements of the data acquisition system, taking inputs from and providing interface services to the front-end, using fast serial links. On the other hand, this layer is interfaced to a PC based host via an intelligent stand alone Ethernet port based CAMAC controller for providing the DAQ, data storage and user interface functions. Apart from this controller, the following modules form the CAMAC back-end system. Functions such as final trigger generation (based on the lower level front-end trigger signals), trigger signal fanout, pre-trigger signal scalers, trigger identification latch etc. are implemented using a FPGA (Altera Flex EPF 10K 50EQC240-2) based Final Trigger Module (FTM)<sup>1</sup>. The Readout Module (RM) supports two serial connections for event data recording and 8 channels for monitoring. During the event process, the serial data from front-end modules are converted to 16-bit parallel data. This data are written into Fan-In-Fan-Out (FIFO) memory buffers of 4K words in size. The data from both FIFOs are read via the CA-

<sup>1</sup>designed by the Electronics Division of Bhabha Atomic Research Centre (BARC), Mumbai

MAC bus in the program. The event data size is normally much smaller than the buffer size. The FIFO overflow can be read from the status port and it also blocks further writing to the FIFO. Generation of all the control lines required for the data readout and monitoring of various status lines as well as fanning out the global trigger signal to all the DAQ subsystems are accomplished by the Control Module (CM). Scaler modules used for monitoring strip signals and TDC modules used for timing measurement are also part of the back-end system. While the CAMAC controller and TDCs were commercial modules, the rest of the modules were developed by us.

## 4.7 Validation of front-end electronics

Studying pulse profiles of the RPC strips - especially of the pulses generated on passage of cosmic ray muons through the chamber, provides invaluable information on the quality and characteristics of the RPC, thus helps in optimisation of RPC operating parameters. The operating parameters include the composition of the gas mixture - especially the concentration of the quenchers, applied field and chamber insulation - both inside the gas volume and outside. We have extensively studied, using the RPC pulse profiles, various characteristics such as rise time (timing), average charge (pulse height), decay constant (pulse shape), impedance matching of the strips, comparison of signal pickup panels and front-end preamplifiers, cross-talk between adjacent strips etc. These measurements have led us to fine-tune the characteristics of various materials used in RPC fabrication, design of various components, process parameters as well as the validation of many front-end electronics designs.

We have programmed an oscilloscope to capture adjacent RPC strip pulse traces on cosmic ray muon trigger. The data is stored in Microsoft Excel worksheets. We typically collected several hundred samples for each study to minimise statistical errors. A Visual Basic script, which runs as a macro in the Excel environment has been developed to scan the pulse profiles, to process the data and extract a number of useful parameters.

Shown in the left panel of Figure 4.11 is a typical amplified strip pulse of an RPC which is operated in the avalanche mode. We processed a large number of pulses to compute its decay time constant. The right panel of Figure 4.11 shows distribution of

this parameter, using which we obtain a mean value of about 10 ns.

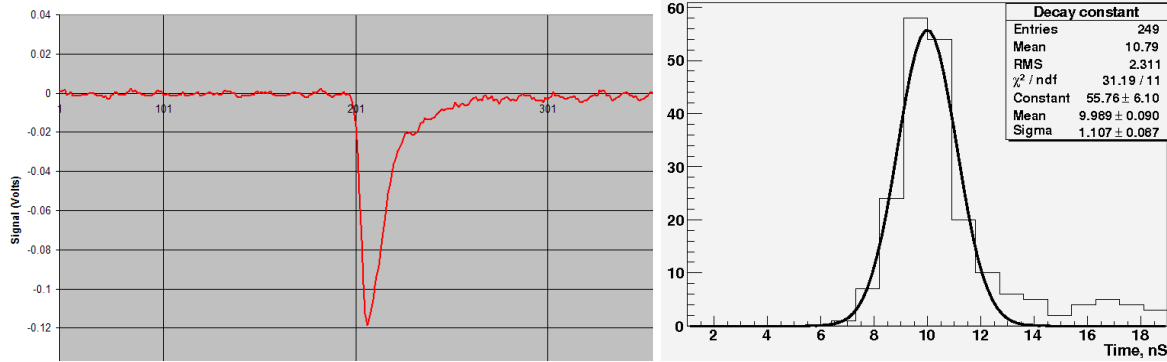


Figure 4.11: Output pulse characteristics of preamplifier. As may be noted from the figure, the pulse amplitude is about -120 mV and pulse width at a threshold of -20 mV is about 18 ns.

A scatter plot of charge versus peak pulse amplitude information recorded by the DAQ system and the oscilloscope respectively for the same events is shown in the left panel of Figure 4.12. The data shows a linear dependence as expected, with a fit value of -7.5 pC/mV. Shown in right panel is a scatter plot of peak pulse amplitude information versus pulse width, at a threshold of -20 mV, extracted from the oscilloscope data.

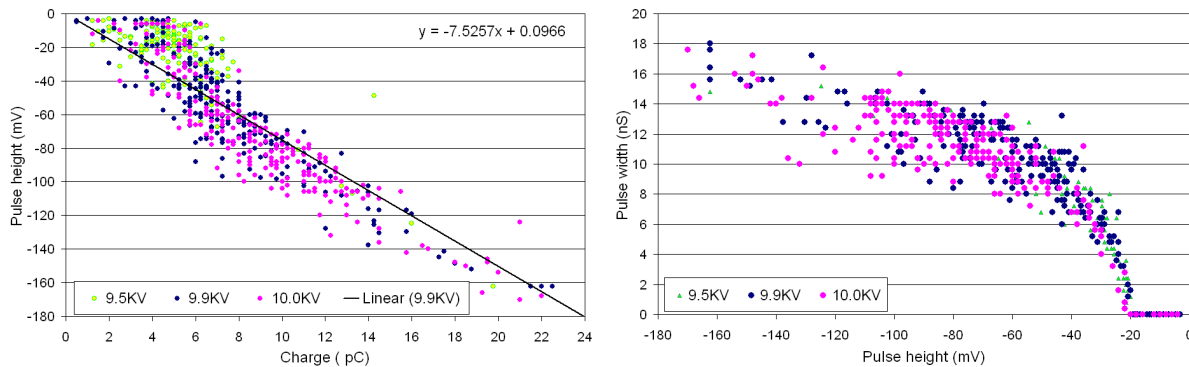


Figure 4.12: Performance studies of the front-end electronics using simultaneous measurements and analysis of RPC parameters using the DAQ system and oscilloscope. The plot in the right panel takes-off from -20 mV on the x-axis, which is the set threshold for the DAQ system.

The RPC pulse may be characterised by the following equation:

$$V(t) = V_0 \exp\left(\frac{-t}{\tau}\right) \quad (4.1)$$

where,  $V(t)$  is the pulse height at a time  $t$ ,  $V_0$  is the peak pulse amplitude and  $\tau$  is

its decay constant (10 ns in our case as shown above). Considering the voltage  $V(t)$  at the threshold level as  $V_{th}$ , we can compute the pulse width at threshold level using the following the equation:

$$t = -\tau \ln\left(\frac{V_{th}}{V_0}\right) \quad (4.2)$$

This logarithmic relation between the peak pulse height and the pulse width at the set threshold level is shown by the plot. Other interesting results obtained by these studies are the relation between the strip hits recorded by the DAQ system versus the peak pulse height and pulse width obtained by the oscilloscope data. Total charge obtained by integrating the area of the captured RPC pulses on the oscilloscope versus the pulse height has also shown very good agreement. Finally, excellent correlation between the hits recorded by the on-line DAQ system versus the hits computed from the oscilloscope data has confirmed the expected functioning of the DAQ system.

## 4.8 Trigger schemes and the system

To begin with, the cosmic ray muon trigger for the detector stack was generated using a scintillator paddle based telescope. A combination of several wide and narrow paddles were carefully placed and aligned to define an aperture for vertically going muons, but only through a single strip and traversing all the 12 RPC layers of the stack. Veto paddles were used to reject events in which, in addition to the single readout strip of interest, one or more other strips are also fired. Even this simple trigger setup was useful in installation, commissioning and debugging of the electronics and data acquisition system of the stack. It enabled the study of many important characteristics of large area RPCs which made up the stack.

We then built a more realistic scintillator paddle based telescope for tracking cosmic ray muons. We have essentially used nine paddles each of 96 cm  $\times$  32 cm in dimension. Using these paddles, we have formed effectively three scintillator layers of 96 cm  $\times$  96 cm, by arranging three each of the above paddles next to each other. The scintillator layers, as shown in Figure 4.3 were arranged one each on top, middle and bottom of the stack. The effective area of these layers - 96 cm  $\times$  96 cm, was designed so that they can be geometrically well aligned inside the RPC area of 100 cm  $\times$  100 cm. In

this, as well as the simpler scheme described above, the signals from the PMTs which were coupled to the scintillators, were processed through modular discriminators and majority logic circuits, in order to generate the trigger pulse, signaling the passage of a cosmic ray muon through the stack. For example, in the present case, the trigger is generated by the following logic equation:

$$\text{Trigger} = (T_1 + T_2 + T_3) * (M_1 + M_2 + M_3) * (B_1 + B_2 + B_3) \quad (4.3)$$

where,  $T_1, T_2, T_3$  are the paddles that make up the top scintillator layer,  $M_1, M_2, M_3$  make up the middle layer and  $B_1, B_2, B_3$  make up the bottom layer of the telescope respectively. The trigger pulse is fanned out to the entire DAQ system using the Control Module (CM) as described in Section 4.6.3. This trigger scheme has helped track cosmic ray muons very efficiently through the stack as a whole. Individual segments of the detector could also be studied in detail for their tracking efficiency and other performance parameters, by quickly making changes in the majority logic circuit, which was used to implement the Equation 4.3.

Finally, we describe the *in-situ* trigger scheme which uses the strip signals of both the readout planes of all the 12 RPCs that make up the detector stack. This scheme is essentially implemented in a distributed manner spanning between the front-end and back-end sections. Eight level-0 trigger primitives are formed in the AFE boards by ORing four strip signals as a group from one readout plane of an RPC, such as:

$$L_{0n} = S_{0+n} + S_{8+n} + S_{16+n} + S_{24+n} \quad n = 1, 2, \dots, 7, 8 \quad (4.4)$$

Thus, two sets of level-0 trigger primitives (eight each per plane) are generated from an RPC layer or 24 sets for the entire detector stack. Using these, level-1 trigger terms are generated in the DFE board. Again, 24 sets of 1-Fold, 2-Fold, 3-Fold and 4-Fold terms are formed - one set per plane, such as:

$$1-Fold = L_{01} + L_{02} + L_{03} + L_{04} + L_{05} + L_{06} + L_{07} + L_{08} \quad (4.5)$$

$$\begin{aligned} 2-Fold = & L_{01} * L_{02} + L_{02} * L_{03} + L_{03} * L_{04} + L_{04} * L_{05} \\ & + L_{05} * L_{06} + L_{06} * L_{07} + L_{07} * L_{08} \end{aligned} \quad (4.6)$$

$$\begin{aligned} 3-Fold = & L_{01} * L_{02} * L_{03} + L_{02} * L_{03} * L_{04} + L_{03} * L_{04} * L_{05} \\ & + L_{04} * L_{05} * L_{06} + L_{05} * L_{06} * L_{07} + L_{06} * L_{07} * L_{08} \end{aligned} \quad (4.7)$$

$$\begin{aligned} 4-Fold = & L_{01} * L_{02} * L_{03} * L_{04} + L_{02} * L_{03} * L_{04} * L_{05} + L_{03} * L_{04} * L_{05} * L_{06} \\ & + L_{04} * L_{05} * L_{06} * L_{07} + L_{05} * L_{06} * L_{07} * L_{08} \end{aligned} \quad (4.8)$$

Finally, 24 level-1 terms each of 1-Fold, 2-Fold, 3-Fold and 4-Fold signals are fed into the CAMAC standard, FPGA based Final Trigger Module (FTM) in the back-end via trigger and TDC router (TTR) boards. The level-2 and the final global trigger is generated by this programmable module. Based on the M-Fold input signals (where  $M$  goes from 1 to 4), an  $M \times N$  level-2 coincidences are implemented here, where  $N$  represents the number of same-side readout planes ( $X$  or  $Y$ ) from where the M-Fold is demanded. The coincidences, which were designed are 1-Fold of any  $N$  out of consecutive 8 planes, 2-Fold of any  $N$  out of consecutive 8 planes, 3-Fold of any  $N$  out of consecutive 6 planes and 4-Fold of any  $N$  out of consecutive 6 planes. All the four level-2 coincidences from both the readout sides are ORed to finally produce the global trigger of the detector stack. The logic diagram of this trigger scheme is shown in Figure 4.13.

The FTM, apart from providing field-programmability of the trigger criteria, also provides facilities to monitor the rates of various intermediate trigger terms, to mask selected input terms etc. Extensive testing of the detector stack and also data taking on the cosmic ray muon tracks of desired criteria were made possible by to the novel design of the flexible trigger scheme in general and the field-programmable FTM in particular.

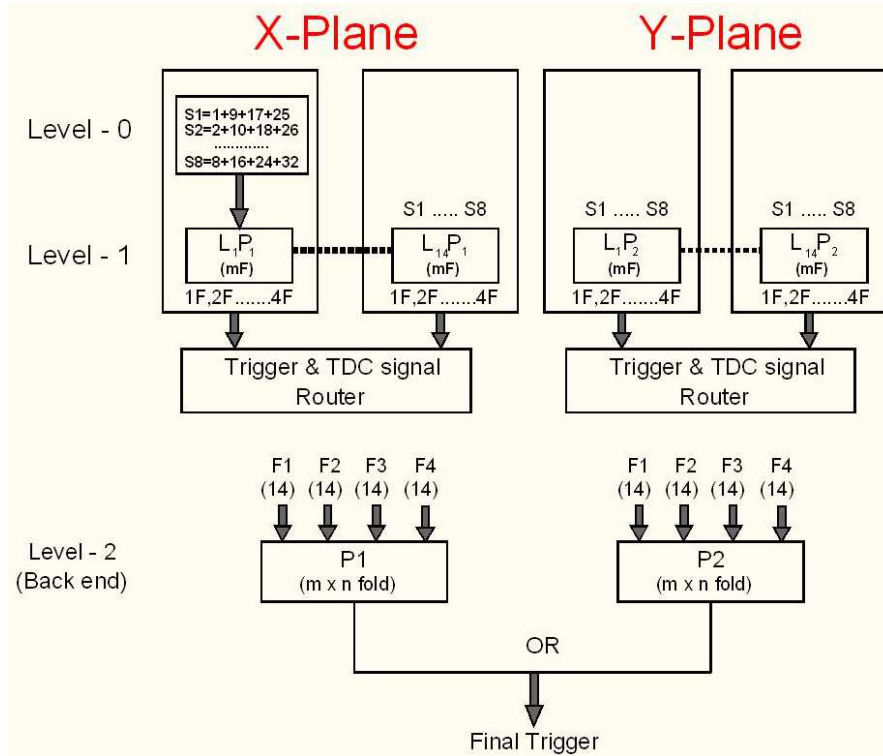


Figure 4.13: Logic diagram of the generation of in-situ trigger signal using the RPC strip signals. Level-0 and level-1 of this three tier trigger system are implemented in the front-end, while level-2 (final) stage is implemented in the back-end

## 4.9 On-line data acquisition software

An on-line data acquisition software was developed in C-language and executed on a Linux host. It was designed to acquire the event data on receiving a trigger and concurrently run various monitoring jobs in the background. The DAQ software essentially spends most of its time executing a small set of the following tasks. It initialises various hardware elements, turns on the desired trigger scheme and sets up appropriate environments for event data as well as monitor data acquisition. The software then initialises the strip rate monitoring cycle and continues to acquire and store this data sequentially. During this time, if a global trigger is signaled by the trigger system, the software acquires the event data, such as the strip hit as well as timing information, stores the same and continues with the background monitoring job. Monitoring of individual strip rates of the RPC is invaluable as it indicates the stability of the chamber under operation.

The cosmic muon events, data of which is being acquired and stored by the on-line DAQ system, are also displayed simultaneously in real time on the web. Two separate

graphical views of both readout planes (X and Y) along with the strips which were hit by the cosmic ray muon track are displayed to scale, thus offering a live display of the tracks on the Internet. This utility has proved to be invaluable to track and monitor the status and health of the detector stack remotely.

The cosmic ray event, strip rate monitor and trigger system data, which are acquired by the on-line DAQ program are saved in a well defined format, so that it can be retrieved easily and analysed by the off-line analysis programs. This data format is given in Appendix B.5.

## 4.10 Ambient parameter monitor system

Monitoring of ambient laboratory parameters such as temperature, relative humidity and barometric pressure along with important operating parameters of the RPCs such as applied high voltage, chamber current, noise rate and efficiency, is one of the most important tasks of the on-line monitoring system designed for the detector stack. A number of useful correlations between these parameters could be established using these data. In addition, we can also use the measured ambient parameters along with the RPC operating voltage in order to correlate the RPC efficiency with the changes in the ambient parameters.

We have procured ambient parameter sensors (shown in the left panel of Figure 4.14) for barometric pressure (accuracy of  $\pm 0.15$  mbar), temperature ( $\pm 0.2^\circ\text{C}$ ) and relative humidity ( $\pm 3\%$ ) [148] and interfaced them to the monitor data acquisition system for recording these data on a round-the-clock basis.

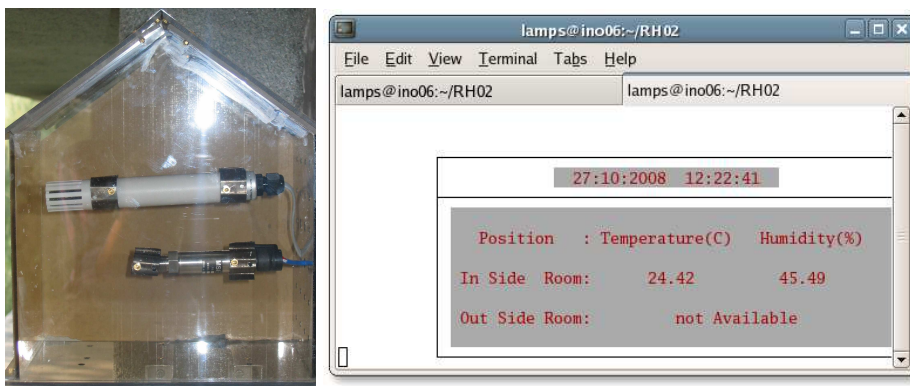


Figure 4.14: Barometric pressure, temperature and humidity sensors (left panel) and the monitoring console of these devices (right panel).

A data-logging software utility (shown in the right panel of Figure 4.14) was developed to acquire various ambient parameters data from their respective sensors and data interfaces, display the current values on the console and also store the data for further off-line processing. Analysis, results and calibration using this data are discussed in Section 5.6.

## 4.11 On-line utilities and services

A number of state-of-the-art on-line tools and utilities were designed or set up to augment the DAQ system of the detector stack. Backed with optimal design of the DAQ software and its data format, these utilities have helped extending the reach and access to the status, performance and monitor data of the detector stack to the INO collaborators located both in India and abroad.

All the R&D studies in the RPC laboratories along with the results obtained are recorded in the web based on-line electronic log book, called ELOG [147], which was set up and configured. ELOG is part of a family of applications known as *weblogs* and is released under the GNU Public License. Various folders and sub-folders for logging information from different INO collaboration groups as well as for their individual activities were created under the home page for convenience. Appropriate account handling mechanisms and access controls were created. Shown in Figure 4.15 is a picture of ELOG screen, where an index of entries related to the TIFR group's RPC R&D activities is listed.

In addition, control and monitoring consoles of low voltage and high voltage power supplies, ambient parameters and gas systems are also accessible remotely, though on the intranet, in order to avoid accidentally changing the crucial settings of the detector stack.

Event and monitoring data, which is acquired by the on-line software are stored in local hard disk. This data is automatically mirrored periodically into a central computing cluster. This arrangement allows many collaborators to run their off-line detailed analysis programs simultaneously on the data just recorded without loading the on-line host for data access.

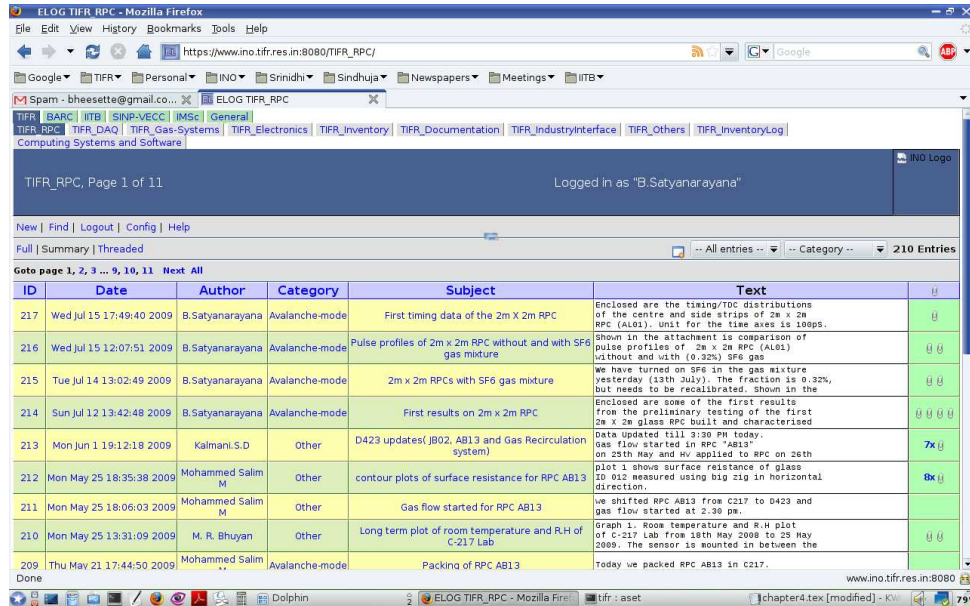


Figure 4.15: A screen shot of INO's on-line web based ELOG book. Apart from plain text, the ELOG entries could comprise of tables, plots, pictures and even audio-video objects.

## 4.12 Chapter summary

We have built a detector stack consisting of 12 RPC layers of  $100\text{ cm} \times 100\text{ cm}$  in area, but without a magnetic field. All the electronics, trigger, data acquisition, monitoring and power supply systems required for this detector stack were designed, fabricated, integrated and commissioned. The stack is in un-interrupted operation now for about a couple of years. Some of the parameters that are tracked on a day-to-day basis are the RPC efficiencies for cosmic ray muons, absolute and relative timing resolutions as well as the stability of RPCs based on the monitoring data of the individual strip rates. Apart from studying various characteristics and long term stability of the RPCs under test, the stack is also being used to study and optimise a number of parameters concerning the RPC gap, chamber design, gas mixture, readout electronics etc.

One major drawback of the data acquisition system described in Section 4.6.3 was that it could not handle the cosmic ray muon trigger rate which was provided by the trigger systems. The bottle-neck turned out to be the commercial CAMAC crate controller architecture. We have therefore recently redesigned the back-end control and DAQ system based on the fast VME modular instrumentation standard. While, we have maintained complete compatibility of the new system with the existing front-end

system, we have designed the Control Module (CM), Readout Module (RM) and Final Trigger Module (FTM) using the commercial general purpose VME modules. We have replaced the rest of the commercial CAMAC modules by their VME counter parts.

We have designed a new Graphical User Interface (GUI) based on-line DAQ software on the Qt[149] and ROOT platforms, incorporating not only the on-line features of the DAQ software described in Section 4.9, but also most of the features of the off-line data analysis utility called *BigStack*, reported in the next chapter. The new DAQ system is able to handle event rates of over 100 Hz. Detailed discussion on this new VME based DAQ system and the on-line program is beyond scope of this thesis.

## Data analysis and results

The ICAL prototype detector stack is in continuous operation for about two years. During this period, several changes were implemented in the configuration of the stack and its operating conditions. As new RPCs were made, they were installed and tested in the stack. Many changes were made in the detector to optimise the gas composition, front-end electronics, data acquisition and trigger systems. This has resulted in better performance of the RPCs, improved electronic noise levels, acquisition of many additional event and monitoring parameters and increased recorded trigger rate. Therefore, the goals of the data analysis, and hence the analysis code used, have varied and evolved over this entire period to incorporate these changes.

This chapter is devoted for the data analysis and the results obtained from various studies that we have taken up. We start this chapter with a brief description of the code developed exclusively for this data analysis, followed by basic data analysis procedure. We then describe some of the routine analysis methods and results for testing and characterising newly built RPCs. We then discuss detailed analysis of the huge volume of cosmic ray muon data, which is being collected by the stack and present some of the important results. Long-term monitoring of many crucial RPC operating parameters along with the ambient parameters is one of the important tasks of the detector stack. We propose a scheme by which apart from using this data to monitor the stability of operation of the chambers, the ambient parameters can also be used to compute the effective RPC parameters. Finally, we hint at a possibility of using the cosmic ray muon data to take up modest physics analysis.

## 5.1 *BigStack*: The ROOT based software package

We have developed a ROOT based sophisticated software package, called *BigStack* to analyse the event, monitor and trigger data collected by the on-line data acquisition software (refer Section 4.9) of the prototype detector stack. The format of the data stored by the on-line software is given in Appendix B.5. In the case of event data, the package interactively displays cosmic ray muon events and fitted event tracks and produces a consolidated run summary sheet in which all the extracted RPC characteristics as well as the operating parameters are given. Along with, all the strip-hits, charge and TDC time-profiles and distributions as well as scatter plots of parameters of interest are produced as ROOT histograms as well as plots. The analysis software also handles the RPC strip rate monitor data, to produce time profiles of this data and the rate distributions over a period of time, in addition to producing the run summary sheets. The package can also be executed in a batch mode, to carry out detailed analysis of high volume data in order to study specific performance aspects of the detector stack.

This package utilises a finely segmented input configuration file through which various input parameters, required functions and user interface options of the package can be conveniently controlled. This design has also helped in achieving a user-friendly and uniform data analysis procedure even during construction phase of the detector stack. In addition to being modular in design, the code required minimal changes to implement the continuously changing detector configuration. Some of the important elements of the configuration file include, RPC identification and the applied high voltage, run number and the type of data to analyse, control switches for single step and auto interactive analysis, flags for creating a number of output files. The RPCs are aligned as accurately as mechanically possible in the stack. However, their precise position offsets as obtained from the initial detailed analysis of the data are also stored in the configuration file so that they can be used for data analysis of subsequent runs.

Another input data file used by the *BigStack* utility is the pickup strip database file. Precise measurements concerning the individual strip positions and widths are recorded for all the pickup panels, which are used to assemble the RPCs. *BigStack* utility computes coordinates of the pickup strips using these measurements, which

in turn are used in the tracking and detailed analysis of the cosmic ray muon events recorded by the stack (Section 5.4).

## 5.2 Basic data analysis procedure

In the interactive single step analysis mode of the event data, the events are replayed one at a time, allowing for a careful study of the tracks as well as hot or dead channels etc. Optionally the event tracks could be fitted and reconstructed in two or three dimensions for better visualisation. It is also possible to run the analysis in the auto mode, using which the analysis can continue with a pre-selected number of events at a time. Figure 5.1 shows some of the interesting cosmic ray muon events recorded by the detector stack. The *BigStack* utility displays the events in two separate frames to scale, as seen by the X- and Y-readout planes respectively. While the channel number shown on the X-axis corresponds to a pickup strip width of 30 mm, the layers represented by the Y-axis are separated by 160 mm. Identification numbers of the RPCs representing various layers are also indicated.

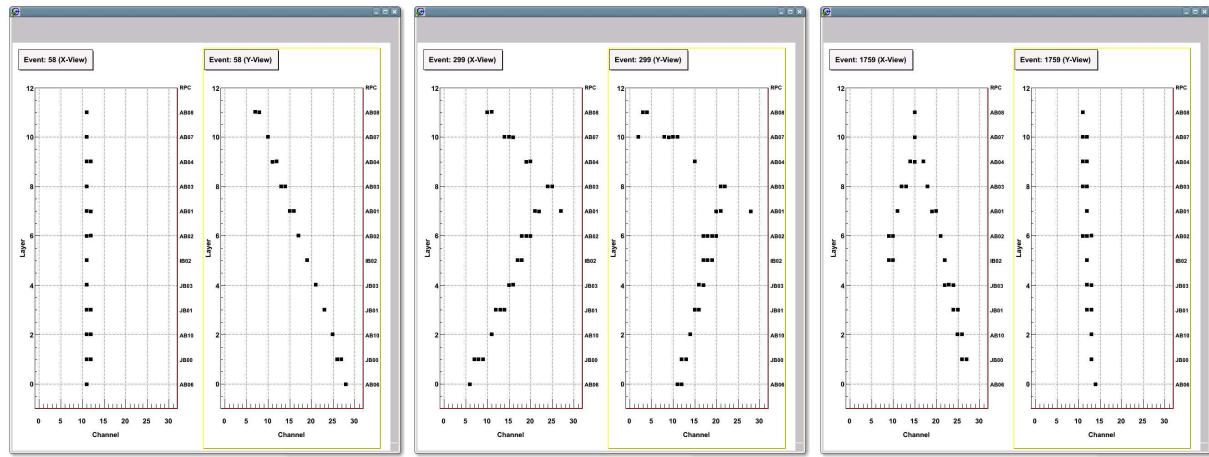


Figure 5.1: A few typical cosmic ray muon events recorded by the prototype detector stack. Shown in the left panel is a single muon track passing through the entire detector. The event in the middle panel is of two muon tracks, both partially tracked by the detector. The right panel demonstrates the capability of the detector to capture particle interactions inside its volume.

Every new chamber, as part of its preliminary acceptance and characterisation process, undergoes a cosmic ray muon detection efficiency study, as a function of its applied high voltage. This study essentially involves recording and analysing data on the

current, strip hits, charge, timing and noise rate of the chamber at various applied high voltages. We fix the operating point for a chamber at a voltage where the efficiency is well above 90%. Efficiency plateau is the region where efficiency is fairly constant over a wide range of the operating voltage of the RPC. We also derive, from these plateau studies, the best timing resolution of the chamber in addition to confirming its other operating and performance characteristics. Shown in Figure 5.2 is a typical efficiency plateau characteristics of a  $200\text{ cm} \times 200\text{ cm}$  chamber.

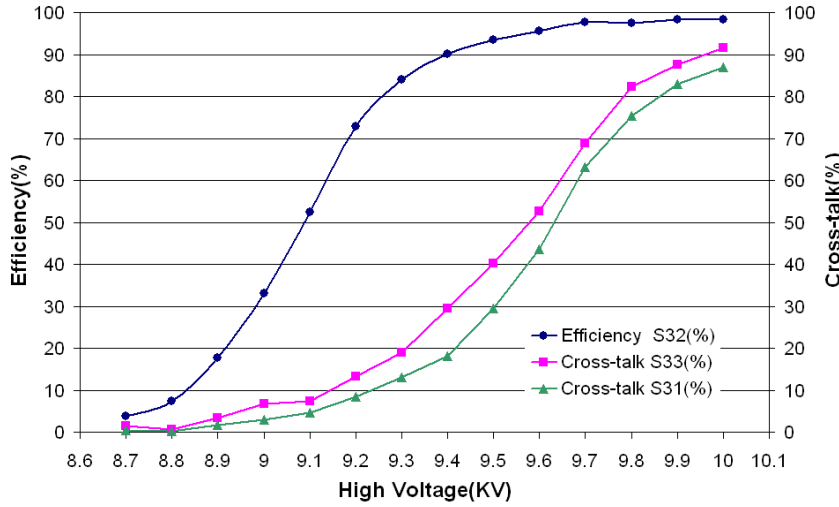


Figure 5.2: Typical efficiency plateau plot of a  $200\text{ cm} \times 200\text{ cm}$  RPC operated in avalanche mode with binary gas mixture of Freon (R134a) and Isobutane. The cosmic ray telescope was intended to be aligned on the strip (S32). But, geometrical misalignment of telescope and the SF<sub>6</sub>-less gas mixture contribute to *apparently* large cross-talk on the neighbouring strips (S31 and S33).

## 5.3 Charge and timing studies of the RPCs

The charge and timing are the two most important parameters in the characterisation studies for an RPC detector. The noise rate, chamber efficiency for detection of charge particles and other derived characteristics depend on the production and efficient processing of the charge induced on the pickup strips for typical charged particles or minimum ionising particles. Similarly, the timing characteristics of the RPC, even while it is deployed in a detector as a *trigger* element, is another important consideration. For example, it is this capability of the RPC, which will be exploited in the ICAL detector for determining the directionality of the particles - whether the particle is traversing

the detector from top to bottom or vice versa. This is an important measurement in the context of atmospheric neutrino studies (Section 1.9).

Shown in Figure 5.3 are the charge and timing distributions of an RPC under test, recorded on cosmic ray muon trigger. It is interesting to note the Landau distribution in case of charge plot. The sigma of the fitted distribution is about 11% of the most probable value. We obtain a typical time resolution of about 1.7 ns from a Gaussian fit of the timing distribution.

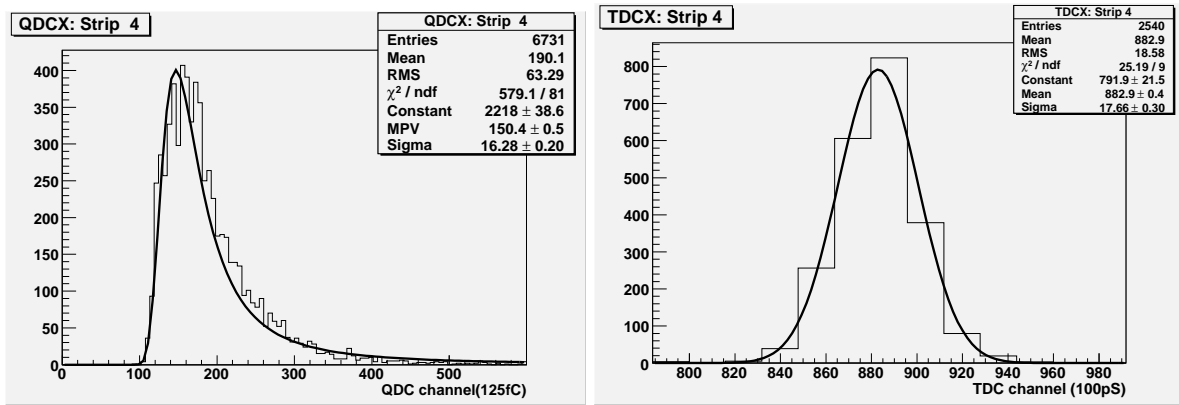


Figure 5.3: Typical charge and timing characteristics of an RPC. It may be noted that the charge distribution is of a single strip, while the timing data is obtained from an entire readout plane by logically summing up all the strip signals.

Time resolution plots of all the 12 RPCs in the prototype detector stack are shown in Figure 5.4. The timing data of an RPC as measured by Time-to-Digital Converters (TDCs) is the time interval between the cosmic ray muon trigger generated by multiple scintillator paddle based telescope and the time of the associated hit in that RPC. As indicated by the fit parameters of TDC data distribution, the average time resolution obtained by the RPC stack is in the range of 2 ns.

Figure 5.5 shows the relative time resolution plots of individual RPCs for the same data. In this case, we choose one of the RPCs (for example *AB04* in this case) in the stack as a time reference and measure the relative timing between the reference RPC and individual RPCs. So, the distributions are essentially of the time differences between the two RPCs. As expected these relative time resolution plots are narrower and provide time resolutions of less than 1.5 ns. This value does not include the effect of unequal propagation times of the RPC signals along the pickup strips, depending on the point of signal induction on the strip. This shows that the intrinsic time resolutions of the RPCs are better than that of scintillator paddle detectors used to build the cosmic

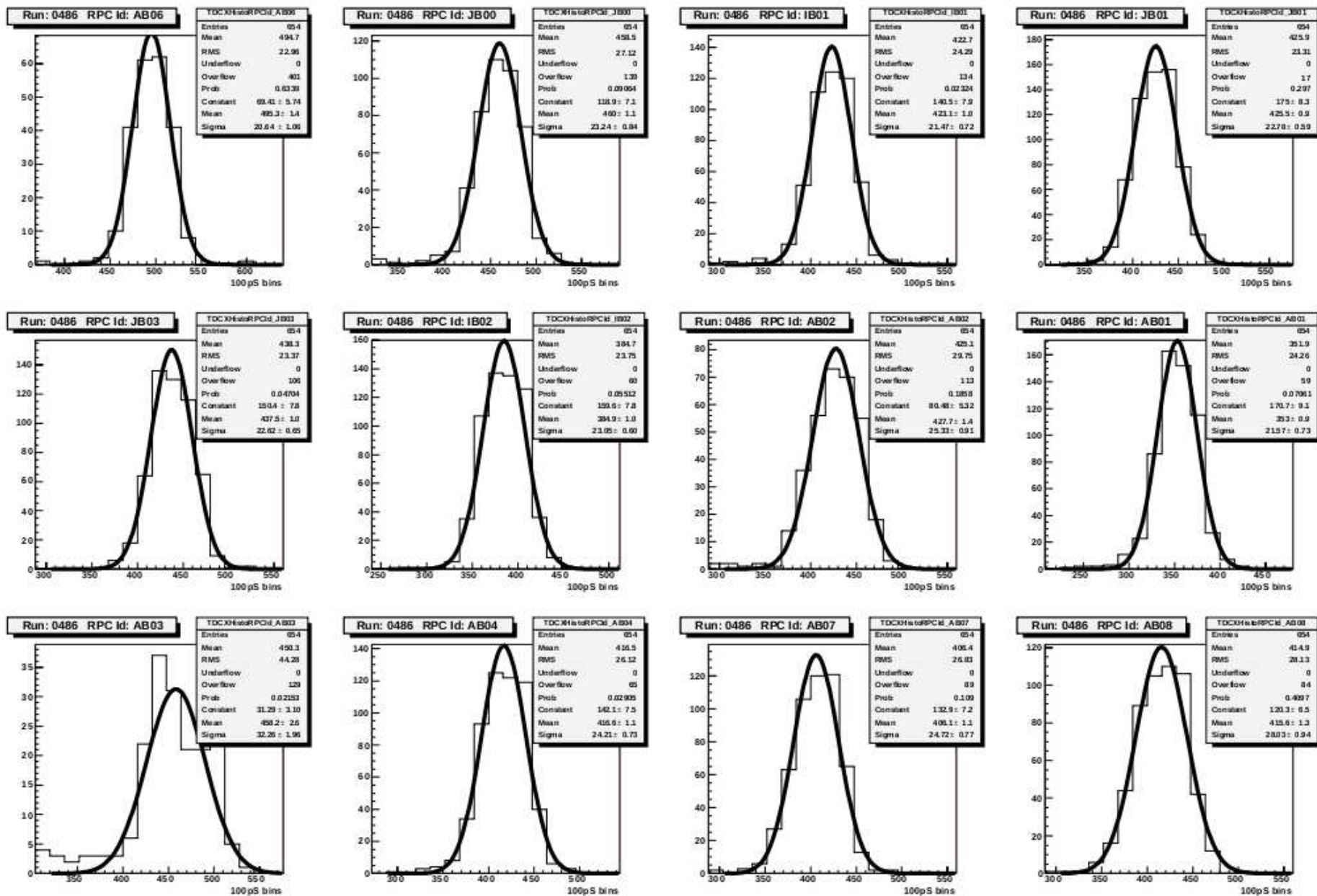


Figure 5.4: Absolute time resolution plots of all the RPCs in the prototype detector stack.

ray muon telescope. A summary of these results is shown in Table 5.1.

Table 5.1: Summary of time resolution measurements of the RPCs in the stack. All the time units are in ns. Columns of particular interest are absolute and relative sigmas.

| RPC Id | HV(kV) | Abs. Mean | Abs. Sigma | Rel. Mean | Rel. Sigma |
|--------|--------|-----------|------------|-----------|------------|
| AB06   | 09.8   | 49.53     | 2.06       | -7.64     | 1.41       |
| JB00   | 09.6   | 46.00     | 2.32       | -4.47     | 1.67       |
| IB01   | 09.8   | 42.31     | 2.15       | -0.64     | 1.63       |
| JB01   | 09.6   | 42.55     | 2.28       | -0.87     | 1.58       |
| JB03   | 09.8   | 43.75     | 2.26       | -2.18     | 1.44       |
| IB02   | 09.8   | 38.49     | 2.31       | 3.27      | 1.38       |
| AB02   | 09.8   | 42.77     | 2.53       | -1.21     | 1.51       |
| AB01   | 09.8   | 35.30     | 2.16       | 6.33      | 1.71       |
| AB03   | 09.8   | 45.82     | 3.23       | -4.55     | 1.99       |
| AB04   | 09.8   | 41.66     | 2.42       | -         | -          |
| AB07   | 09.8   | 40.61     | 2.47       | 0.96      | 1.35       |
| AB08   | 09.8   | 41.56     | 2.80       | 0.31      | 1.82       |

## 5.4 Muon tracking and detailed analysis

Apart from using it for monitoring the day-to-day status as well as long-term stability of the detector stack and its associated electronics, the cosmic ray muon data is also used for detailed analysis of the stack's performance and precision measurements. The cosmic ray muon tracks, which are recorded in the stack are selectively fitted and a number of useful performance parameters are extracted from the huge volume of data.

Given below is the general data analysis scheme for a run:

1. The data is analysed on event-by-event basis.
2. The hits in the detector are originally recorded by the DAQ system in terms of their logical coordinates - layer number and strip (channel) number, both of which start from 0. It may be recalled that the distance between two layers is 160 mm. These are translated into physical coordinates (in mm) as shown below. The offset values used in the calculation of x-coordinate are determined from the residual distribution (Section 5.4.4) and preset in the configuration file for future use.

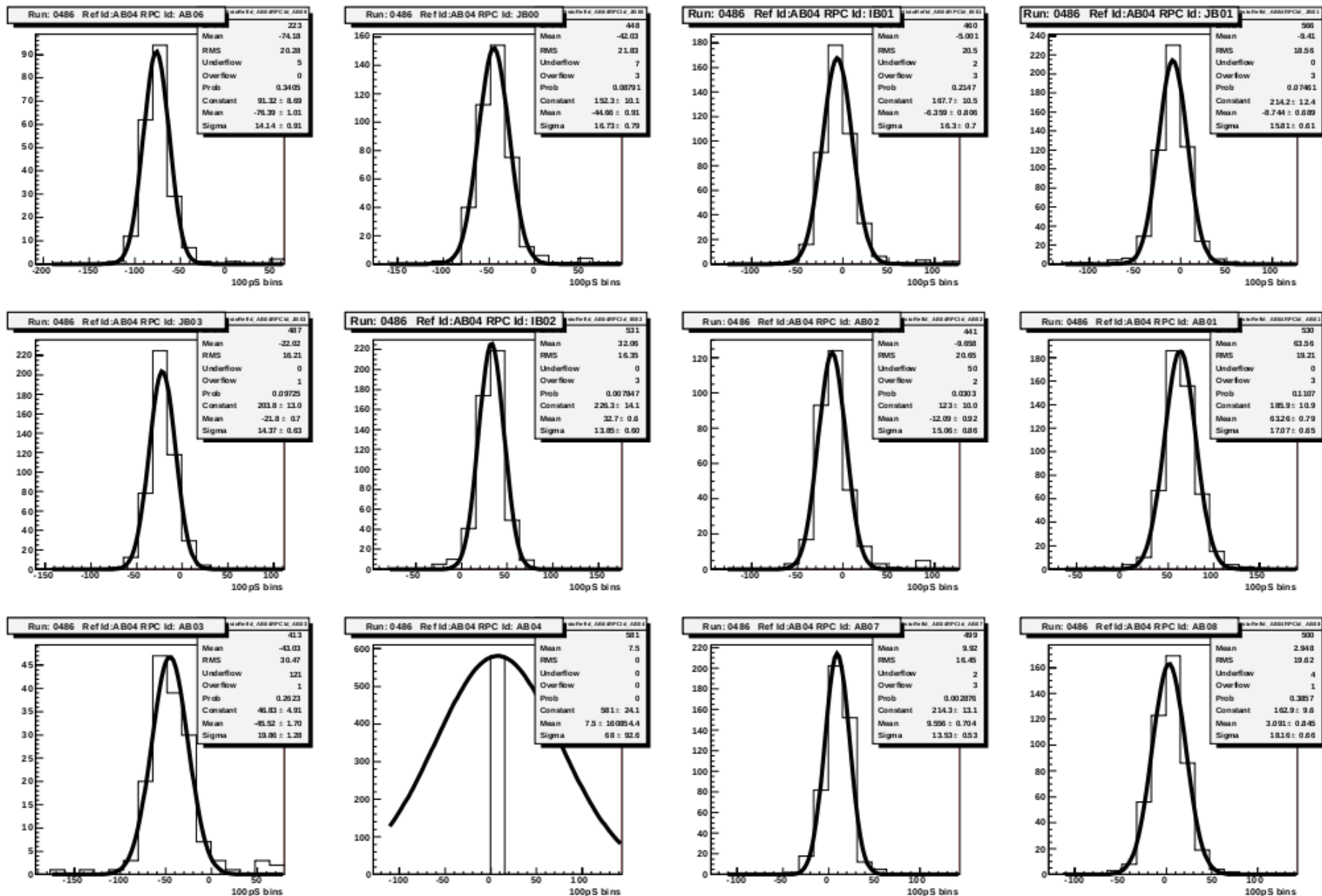


Figure 5.5: Relative time resolution plots of all the RPCs in the prototype detector stack.

$$x\text{-coordinate of a hit} = \text{Mid point of the hit strip} - \text{Offset} \quad (5.1)$$

$$y\text{-coordinate of a hit} = \text{Layer number} * 160. \quad (5.2)$$

$$\text{Error on the } x\text{-coordinate} = \text{Width of the hit strip} / 2 \quad (5.3)$$

$$\text{Error on the } y\text{-coordinate} = 2. \quad (5.4)$$

3. If the number of hit strips in a layer are more than 3, the entire layer is discarded for track fitting. If the number of layers survived for fitting are less than 4, the track fitting for this event in this readout plane is abandoned.
4. Linear fit is then performed on the track.
5. Hits which are more than 50 mm away from the fitted track are rejected. If more than one strip are hit in a layer, all but the hit closest to the fitted track are rejected.
6. The track is re-fitted if the number of surviving layers is more than 4.
7. The event on the readout plane is accepted, if the  $\chi^2/ndf$  is between 0.06 and 0.7.  $\chi^2/ndf$  plots at various stages of analysis and acceptance are shown in Figure 5.6.
8. The track fitting is similarly performed for the second readout plane and then for all the events in a run.

### 5.4.1 Tracking efficiencies of the RPCs

Using the data analysis procedure presented in the previous section, tracking efficiency of RPCs in the detector stack for both the readout planes can be computed. After the track in a readout plane is fitted, the physical coordinates of this track at different layers (or in other words on various RPCs) are calculated. These are translated into logical coordinates of the hit position, in terms of the strip (channel) number, using the pickup strip position data. If this computed strip is also recorded by the DAQ system as the hit strip, then the layer is marked to be efficient for that event or marked inefficient otherwise. Using this procedure, the tracking efficiencies of all layers in a run are calculated. Table 5.2 shows the tracking efficiencies of various RPCs.

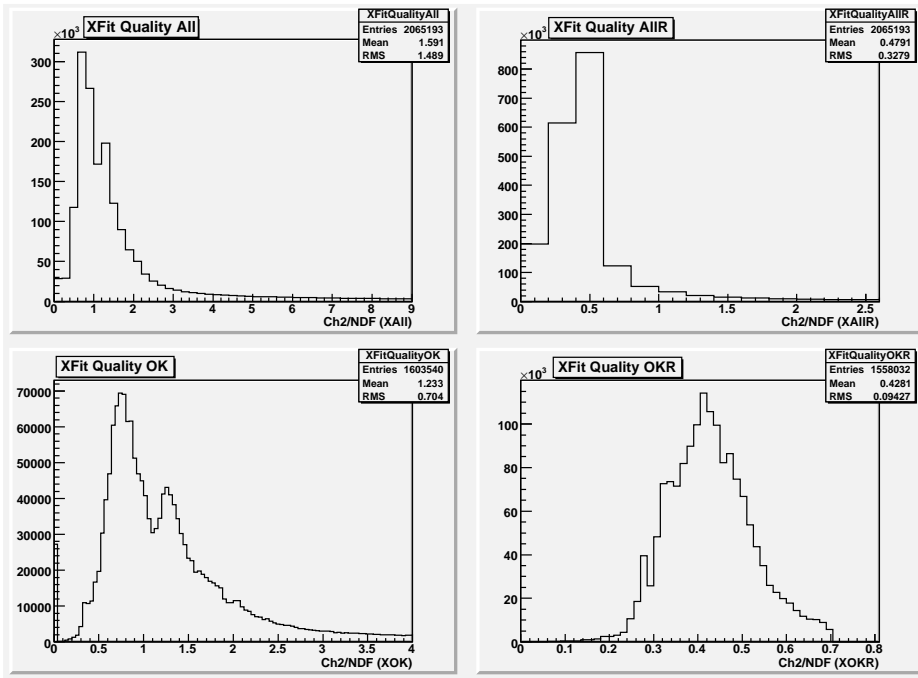


Figure 5.6:  $\chi^2/ndf$  distribution plots. Clock-wise, starting from top-left plot are for: all the fit tracks,  $\chi^2/ndf < 4.0$ , all the re-fit tracks and finally  $0.06 \leq \chi^2/ndf < 0.7$ .

This tracking efficiency is different from the efficiency that we usually obtain from the plateau characteristics of a newly fabricated RPC and is a more realistic parameter from the point of view of its performance in a detector. A small area on the RPC mapped usually by a scintillator paddle based cosmic ray muon telescope window, is tested in case of studying the plateau characteristics. The tracking efficiency as obtained in a detector on the other hand represents the entire surface area of the RPC, as it is calculated based on the cosmic ray muon tracks traversing through its entire area.

#### 5.4.2 Distribution of track impact position

The track impact position on the chamber under test can be determined essentially by the same procedure as above. Strips which lie on the fitted track and recorded by the DAQ system as hits are determined for every event. The frequency distribution of these strips for the X-readout plane is shown in Figure 5.7.

The distribution is on expected lines for the trigger acceptance criterion in force for the detector stack, which in turn determines the fiducial volume of the detector for trigger generation and hence for the data analysis. Cosmic ray trigger for this study was generated by the telescope consisting of nine scintillator paddles (Section 4.8) and

Table 5.2: Tracking efficiencies of the RPCs in the stack as determined by the tracking of cosmic ray muon events. The layer-wise efficiencies are calculated as the ratio of the number of strip hits on the cosmic ray muon track to the number of tracks passed through the detector stack (and through that layer).

| RPC Id | Tracks | Hits   | Efficiency(%) |
|--------|--------|--------|---------------|
| AB06   | 130118 | 122649 | 94.3          |
| AB07   | 130420 | 124796 | 95.7          |
| AB10   | 130457 | 126355 | 96.9          |
| AB11   | 130472 | 126390 | 96.9          |
| AB09   | 130472 | 125840 | 96.4          |
| IB02   | 130465 | 126660 | 97.1          |
| AB02   | 130464 | 127473 | 97.7          |
| AB01   | 130456 | 127668 | 97.9          |
| AB03   | 130439 | 126573 | 97.0          |
| AB04   | 130404 | 127115 | 97.5          |
| AB12   | 130286 | 122066 | 93.7          |
| AB08   | 129272 | 123490 | 95.5          |

whose trigger logic equation is given by 4.3.

### 5.4.3 Study of RPC cluster size

The chamber cluster size or strip multiplicity, which may be defined as the average number of strips fired for a minimum ionising particle hit, is practically computed as the average value of the cluster size distribution. Apart from its dependence on gas mixture and surface resistivity of the electrode coating among other factors, the cluster size is a function of the applied high voltage and can be used as one of the criteria to accept a chamber during large scale production. Usually a chamber is accepted if the cluster size is below three strips at the knee of the efficiency plateau.

Typical cluster size or strip multiplicity plot of an RPC is shown in Figure 5.4.3. Arithmetic means of the cluster size distributions of all the RPCs under test in the prototype detector stack are given in the Table 5.3. Events whose fitted tracks satisfy the condition  $0.06 \leq \chi^2/ndf < 0.7$  are only selected for calculating the strip multiplicity. The average strip multiplicity of the RPCs for cosmic ray muon data is found to be about 1.4.

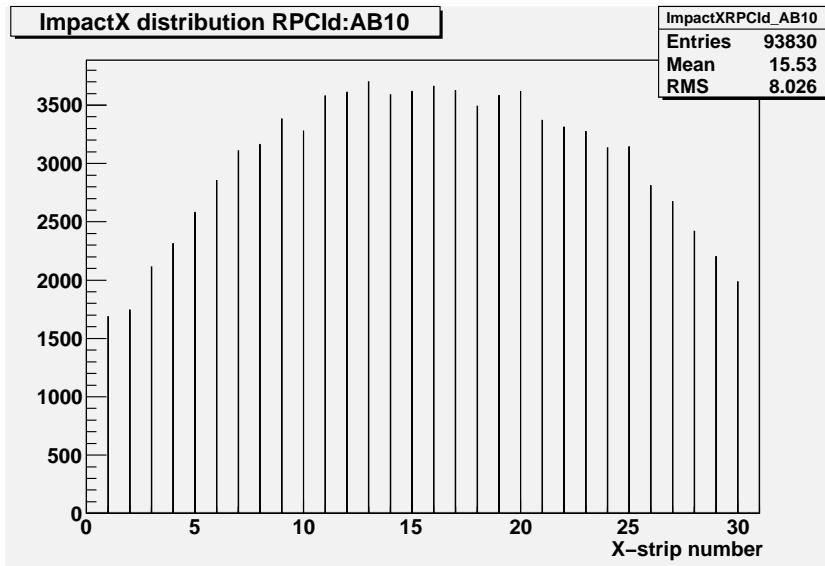


Figure 5.7: Track impact position distribution of an RPC in the stack using cosmic ray muon data.

Table 5.3: Average cluster sizes of all the RPCs in the prototype detector stack.

| RPC  | AB08 | AB07 | AB04 | AB03 | AB09 | IB02 |
|------|------|------|------|------|------|------|
| Size | 1.5  | 1.2  | 1.4  | 1.3  | 1.4  | 2.0  |
| RPC  | AB02 | AB01 | AB06 | AB12 | AB10 | AB11 |
| Size | 1.4  | 1.4  | 1.1  | 1.2  | 1.2  | 1.2  |

#### 5.4.4 Residual distribution of muon tracks

We have also studied the distribution of the residuals between the fitted track and hit pickup strip coordinates. Residual of a hit strip in a layer is defined as the difference between the centre of the strip and the fitted track hit position on that particular layer.

Typical residual distribution plot of a layer in a cosmic ray muon tracking run is shown in Figure 5.9. The shape and width of the distribution is as expected for actual width of our pickup strips being 28 mm and separated by 2 mm gaps. The distribution also peaks at the origin or centre of the strip, which is the minimum logical unit of the hit position on the RPC. The residuals determined from the analysis of large volume of data, are stored in the *BigStack*'s configuration file and are used for applying appropriate corrections while determining the strip coordinates during analysis of detector stack data in future.

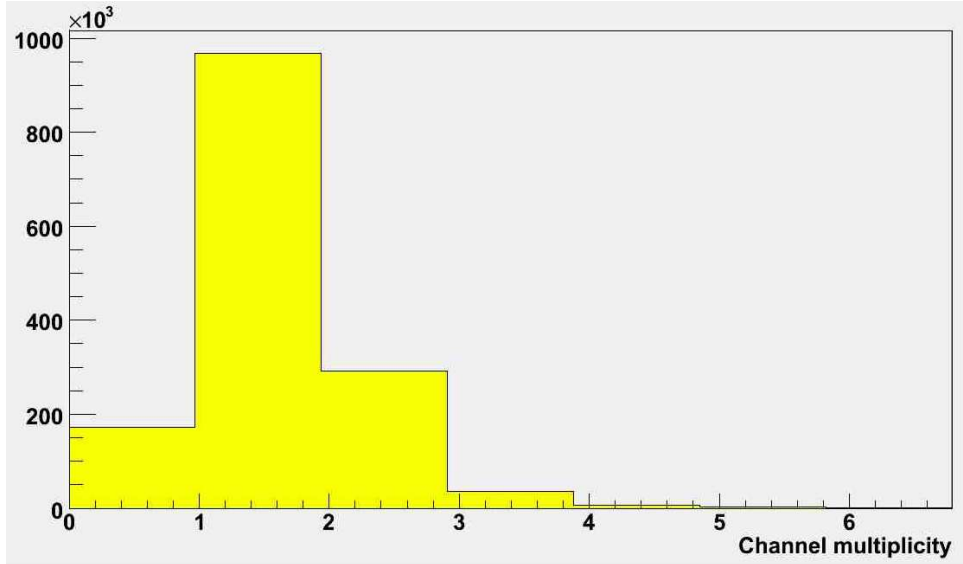


Figure 5.8: Typical cluster size or strip multiplicity distribution plot of an RPC.

#### 5.4.5 RPC *tomography* using cosmic ray muons

Uniformity of response is one of the most important requirements for large RPC systems, such as those planned to be deployed in ICAL detector [150]. More than half a million cosmic ray muon events are recorded per day by the detector stack. These tracks are used to build a surface profile or tomography of the RPCs under test. After the cosmic ray muon tracks are fitted in both readout planes, the X and Y coordinates of the hit on a layer (or RPC) are used to build the profile. A typical surface map of an RPC is shown in Figure 5.10.

The map represents uniform response of the RPC for charged particle detection over its entire active area. The width (28 mm) of the pickup strips used for the RPC readout, the inter-strip gap (2 mm) as well as the dead space due to button-shaped spacers (11 mm in diameter) are clearly visible in the surface map.

## 5.5 Long-term monitoring of detector stack

The RPC detectors are expected to work stably for 10-15 years in the ICAL experiment. Therefore, studying the stability of their operation over long periods of time is essential. The individual strip counting rates (or noise rates) provide an excellent tool for monitoring the long term stability of the RPC detectors. While the event data on cosmic ray muon trigger is acquired asynchronously, the on-line data acquisition system

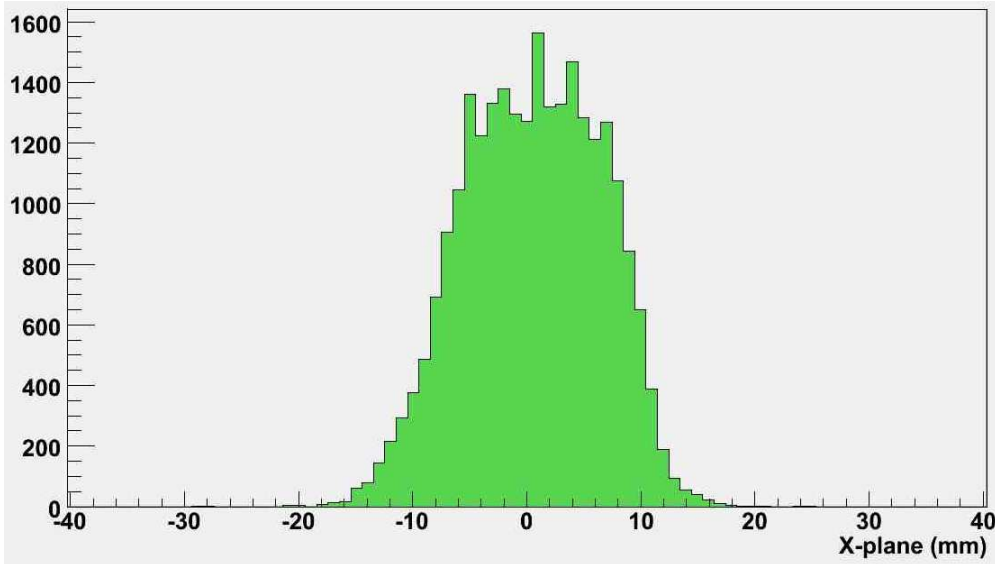


Figure 5.9: Residual distribution of cosmic ray muon track position through an RPC. Most of hits are distributed within 20 mm, and the RMS is about 6 mm.

also monitors for a given time interval and records individual strip rates periodically. Figure 5.11 shows the time profile and histogram of noise rate of an RPC’s pickup strip. As can be clearly seen from the profile plot, the noise rate reflects effect of 24-hour day-night variations in the ambient conditions.

Another operating parameter, which is typically used for monitoring the long-term stability of the RPC is its chamber current. For instance, aging of an RPC is diagnosed by its shooting chamber current (Section 3.3. As described in Section 4.5, the applied voltage and the chamber currents are monitored on round-the-clock basis and are logged in. Shown in the Figure 5.12 are these parameters for one of the RPCs (called *AB02*) in the detector stack, plotted as a function of time for over a period of about two years. As can be seen from the plot, the RPC exhibits excellent stability over this period, represented by its uniform chamber current.

Time profiles of the cosmic ray muon trigger rate as well as the detection efficiencies of the RPCs in the detector stack are also similarly monitored. The purpose of monitoring these parameters as a function of time is to ensure that these values remain uniform over a period of time. The analysis program also builds strip hit maps (lego plots) for all the RPCs in the detector stack for a given run. These plots are used to study and ensure that the entire area of the chamber is active and sensitive to the cosmic ray muons and that there are no dead or hot zones.

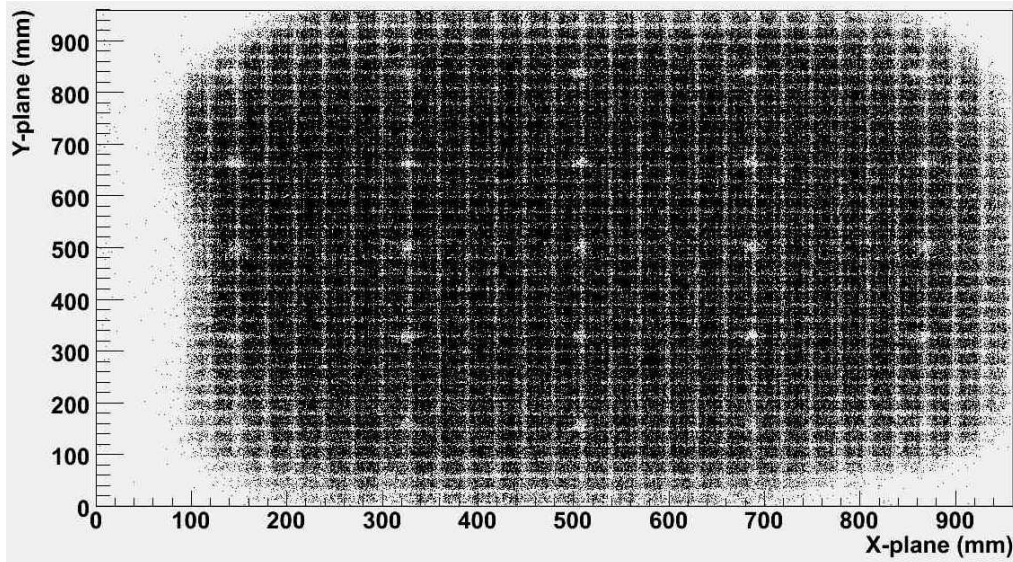


Figure 5.10: Surface map or tomograph of an RPC using cosmic ray muons.

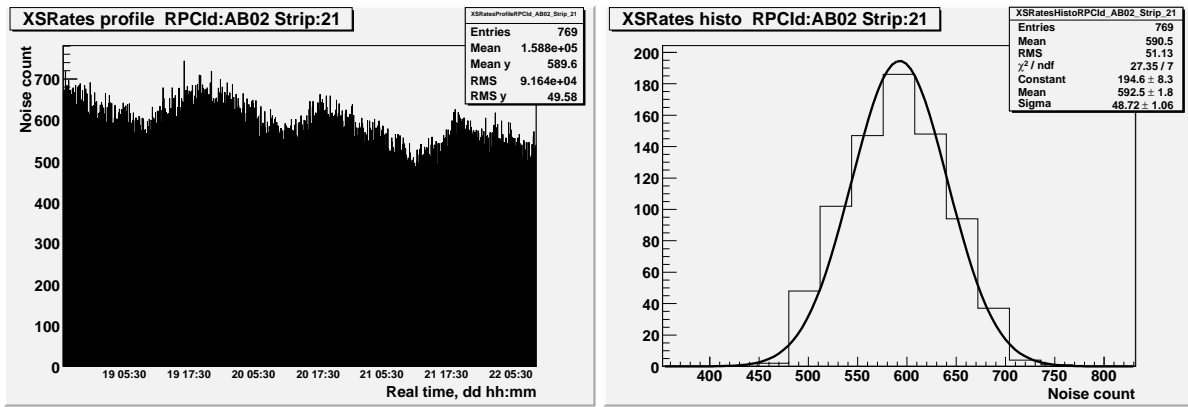


Figure 5.11: Typical strip noise rate time profile (left panel) and distribution plots (right panel). It may be noted that the mean value of the distribution corresponds to the noise count for 10 secs of an RPC strip of  $100 \text{ cm} \times 3 \text{ cm}$  in dimension. We therefore obtain a nominal counting rate of about  $0.2 \text{ Hz/cm}^2$  from this plot.

## 5.6 Ambient parameters and the RPC performance

The operating parameters of the RPCs - dark current and noise rates in particular, show variations during a 24-hour time period. The ambient parameters that exhibit similar behaviour are temperature, relative humidity and barometric pressure. Since the RPC is a gas based detector, variations in the ambient parameters are expected to have considerable effect on its operation [151]. Shown in Figure 5.13, for example, are plots of the noise rate of an RPC strip for a period of about two days and laboratory temperature (in  $^\circ\text{C}$ ) for the same period. One can see an excellent correlation between these parameters.

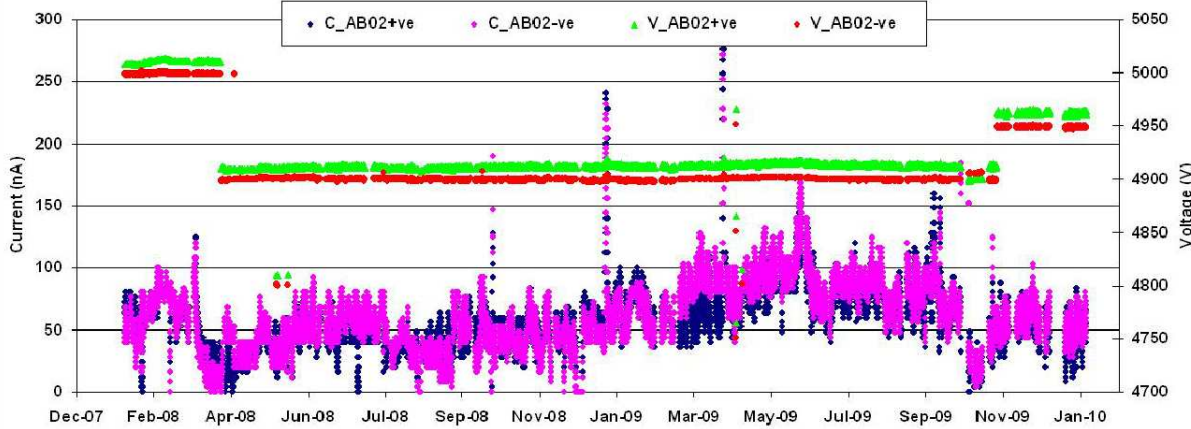


Figure 5.12: Applied voltage and chamber current profile plot of an RPC in the detector stack. As the RPC is powered by a differential high voltage, monitored voltages and currents for both polarity supplies are plotted. The average chamber current is about 50 nA.

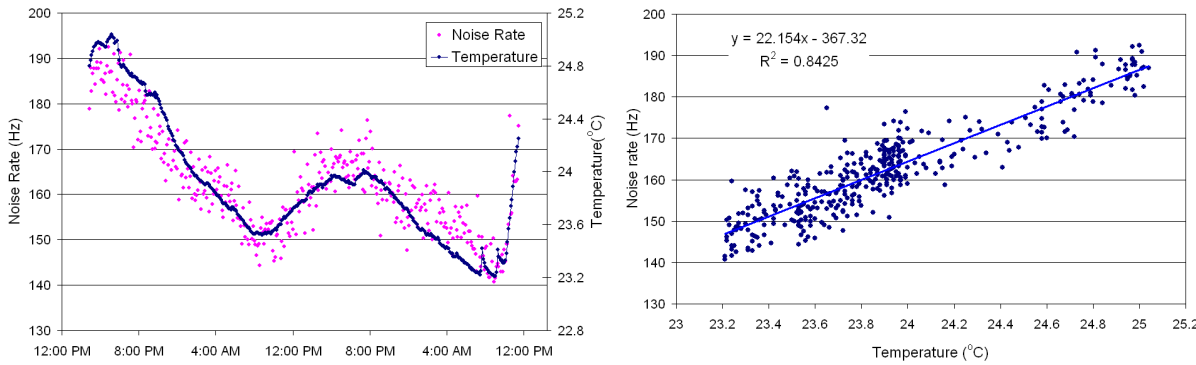


Figure 5.13: Correlation between ambient laboratory temperature and RPC strip rates. Shown in the left panel is the time profile of noise rate and temperature, while in the right panel we show the scatter plot of the same data.

We can also use the measured parameters of temperature and barometric pressure along with the RPC operating voltage in order to correct the RPC efficiency for the changes in the ambient parameters [152]. For example, if we have applied  $V_0$  as the high voltage to the RPC when the temperature and pressure are  $T_0$  and  $P_0$  respectively, then we can compute the operating voltage that we need to apply to the RPC in order to maintain the same efficiency, while the temperature and pressure have changed to  $T$  and  $P$  respectively as:

$$V = V_0 \times \frac{T_0}{T} \times \frac{P}{P_0} \quad (5.5)$$

Alternately we can compute the effective applied voltage  $V_{eff}$ , which is referred to

$T_0$  and  $P_0$ , when the applied voltage is  $V$  at temperature  $T$  and pressure  $P$  as:

$$V_{eff} = V \times \frac{T}{T_0} \times \frac{P_0}{P} \quad (5.6)$$

This of course will account for the gas behaviour only due to the changes in the ambient parameters.

## 5.7 Preliminary physics studies using muon data

As mentioned in Section 4.12, we could increase the recordable trigger rate of the detector stack's data acquisition system to about 300 events/s by migrating from CAMAC to the high-speed VME back-end. This large volume of cosmic ray muon data enabled us to take up some preliminary, but interesting physics analysis jobs.

In the ICAL detector, the up-going muons, which are produced by the  $\nu_\mu$  interaction inside the detector volume, must be discriminated from the down-going cosmic ray stopping muons. This can be achieved by using the length of the track left in the detector by the traversing particles as well as time resolution of the RPC detectors. We are currently working on determining the  $\beta (= v/c)$  value of the cosmic ray muons using even this modest detector consisting of 12 RPC layers. This is being done by computing the expected flight times between consecutive layers and minimising the difference between these values and the observed data. Offsets of the DAQ channels - including the TDC, through which timing data are measured are determined using an external precise pulse generator. The observed data are corrected for these offsets.

Another study we plan to take up soon is the angular distribution of muons. The scheme involves fitting and finding the angles of the muon tracks in the detector. The detector will be divided into towers of  $m \times n$  strips. The muon angles are binned in terms of these towers so that we could study various interesting aspects such as east-west asymmetry.

## 5.8 Chapter summary

The prototype detector stack is in operation for a couple of years and is currently tracking about half a million cosmic ray muons per day. Apart from studying various char-

acteristics and long-term stability of the RPCs under test, the stack is also being used to study and optimise a number of parameters concerning the RPC gap, chamber design, gas mixture, readout electronics etc. We have studied the timing resolution of these large area RPCs relative to the scintillator paddle based trigger signal as well as to other RPCs. We have recorded the RPC strip rate profiles and shown that the noise rates are very stable over long periods, implying the stability of operation of the RPCs under test. Their sensitivity to ambient parameters has been demonstrated. The cosmic ray muon track data was used to build a tomography of the RPC, in which the pitch of the pickup strips used for the RPC readout as well as the dead space due to the button-shaped spacers were clearly visible. We have also studied the distribution of the residuals between the track and hit pickup strip coordinates, distribution of the track impact positions on the readout panels and the average strip multiplicity for the cosmic ray muon data.

Increasing the cosmic ray muon trigger rate of the detector stack by switching over to the high speed VME based data acquisition system, has opened up the possibility of using the detector to initiate physics studies using the large sample of cosmic ray muon events. While we have shown a flavour of these studies in this chapter, we wish to continue these studies.

# Summary and future outlook

## 6.1 Summary

The India-based Neutrino Observatory (INO) has conceived the magnetised Iron Calorimeter (ICAL) detector on a scale that no other basic sciences project in India has attempted. ICAL is not only designed to complement the capabilities of other existing and planned neutrino detectors around the world, but also to specifically address many unexplored challenges of this field. The ICAL detector is contemplated as both a detector for atmospheric neutrinos and as a future end detector for a neutrino factory beam.

The ambitious ICAL detector, of  $48\text{ m} \times 16\text{ m} \times 14.5\text{ m}$  in volume and 50 kt in weight will employ about 30,000 RPCs of about  $2\text{ m} \times 2\text{ m}$  in area as sensitive detector elements to track particles produced by the neutrino interactions inside the detector mass. This amounts to total sensitive detector coverage of about  $100,000\text{ m}^2$ , which would be one of the largest covered area by a detector anywhere in the world. The choice of RPCs for ICAL among other options such as scintillators is driven by their inherent advantages, such as two-dimensional readout from a single detector, excellent spacial and time resolutions, simple and low cost of large scale production and operation. The challenge therefore is to design, develop, characterise large area RPCs and bring the technology to a stage that it can be transferred for large scale industrial production, which is needed to meet the demand for the ICAL detector. A dedicated R&D programme was undertaken to meet the above challenge. This thesis in essence has documented this entire research and design work, the analysis of RPC characterisation data and the results obtained.

We began our work by developing a large number of single gap glass RPCs of about  $30\text{ cm} \times 30\text{ cm}$  in area and initially operated them in the streamer mode. The modeled d.c. characteristics of these detectors were studied and confirmed. The noise rate was established to be a reliable way of monitoring the stability of the RPC operation. Cosmic ray particle detection efficiency characteristics with several gas mixtures were studied and their efficiency knees and plateaus were established. We have also shown that the timing resolution  $\sigma$  of the RPC improves with the detector bias voltage and reaches a value of about 1.2 ns at its plateau region, where the recorded efficiencies were over 90%. The charge spectra and its linearity as a function of the applied voltage as well as the inter-strip cross-talk were measured and the latter was found to be about 6%. We have in the process, developed considerable infrastructure such as a cosmic ray muon telescope, a sophisticated data acquisition system, a gas mixing and distribution system.

We have also successfully demonstrated efficient tracking of cosmic ray muons using a stack of 10 RPCs of  $30\text{ cm} \times 30\text{ cm}$  in area. The RPCs were mounted such that the signal pickup strips of all the chambers were accurately aligned geometrically. The chambers were operated in the streamer mode, using a mixture of Argon, Isobutane and Freon (30 : 8 : 62 by volume). The cosmic ray muon trigger signal was generated by a telescope comprising of a set of scintillator paddles. The detector could be triggered by muons arriving at different angles, easily by relocating the telescope window. The information recorded in these tests was also used to extract many RPC parameters of interest such as efficiency, noise rate, timing, total hit distributions, strip hit multiplicity distribution patterns and their long-term stability.

Even though the results obtained from the characterisation tests mentioned above were comparable to those obtained by other researchers, we faced a severe problem with regard to their long-term operation. Glass RPCs operating in the streamer mode are known to be stable and have a long lifetime (more than 10 years) as evidenced by the successful operation of these chambers in the Belle experiment. However, our prototype detectors showed signs of sudden aging when operated continuously even for a few months. There was a simultaneous sharp increase in the noise rates and drop in the efficiencies. The chambers could not generally be revived.

We have done extensive studies on the inner surfaces of electrodes from the dam-

aged RPCs as well as a large number of local and imported glass samples using Atomic Force Microscope (AFM) and Scanning Electron Microscope (SEM) techniques. Element analysis was also performed using X-Ray Diffraction (XRD) technique both on damaged electrodes and raw glass samples. The structures shown in the AFM and SEM scans were found to be rich in Fluorine, confirming our hypothesis that Freon (R134a) gas contaminated with moisture forms Hydrogen Fluoride (HF), which damaged the RPC. The structures on the damaged electrodes were found to be loose deposits on the electrodes rather than permanent damaged regions on the glass. Even after taking a number of steps towards monitoring and addressing the problem of moisture in the input gases, the detector aging continued. Results from the studies on glass surface quality and elemental analysis, using the above mentioned techniques did not reveal any appreciable differences among various glass samples.

We then fabricated a few RPCs of  $40\text{ cm} \times 30\text{ cm}$  in area, using glass sheets procured from Japan. The same procedures for fabrication and testing as in the case of earlier RPCs were followed for these chambers. Two of these chambers were continuously operated in the avalanche mode for more than two years, in which a gas mixture of Freon (R134a) and Isobutane in the proportion 95.5 : 4.5 by volume was used. The performance of these chambers, characterised by their efficiency, leakage currents and noise rates, remained stable over the entire period of these tests. A comprehensive monitoring system for the periodic recording of the operating parameters of the RPCs together with the ambient parameters such as temperature, pressure and relative humidity - both inside and outside the laboratory, has been designed and implemented. Using these data, several important correlations between the ambient parameters and the RPC operating characteristics could be established.

Large area RPCs of dimensions  $100\text{ cm} \times 100\text{ cm}$  required for the ICAL prototype detector stack were successfully developed, built and characterised. They were operated stably in the avalanche mode for a long period of time without any signs of aging. A detector stack of 12 such RPCs, read out by an indigenously built electronics, data acquisition, trigger, slow control and monitoring systems is tracking cosmic ray muons for about two years now. Hybrid Micro Circuit (HMC) and Complex Programmable Logic Device (CPLD) based front-end electronics was designed for processing particle hit and timing information from 768 detector signals. Custom-built CAMAC and VME

based data acquisition systems were the other highlights of this detector. The detector stack is triggered on cosmic ray muons using scintillator detectors (of  $9\text{ m}^2$  in area) as well as RPC pickup strip hit pattern based trigger systems. Monitoring the stability of the detector as well as laboratory ambient parameters such as temperature, relative humidity and barometric pressure, are the other important tasks of the on-line data acquisition system. The entire status of the experiment, its parameters along with the on-line display of muon tracks are made available on the web so that they are accessible to all the members of the collaboration.

The recorded data is stored in a customised format by the on-line software and is analysed off-line in detail using sophisticated ROOT based analysis software. Some of the aspects that are analysed on day to day basis are the RPC tracking efficiencies for cosmic ray muons, absolute and relative timing resolutions as well as the stability of RPCs based on the monitoring data of the individual strip rates.

The detector is currently tracking about half a million cosmic ray muons per day. These tracks are used to build a *tomography* of the RPC. Pitch (30 mm) of the pickup strips used for the RPC readout as well as the dead space due to the button-shaped spacers (11 mm in diameter) were clearly visible in the map. We have also studied the distribution of the residuals between the track and hit pickup strip coordinates. The width of the distribution is as expected for pickup strip widths of 28 mm resulting in an RMS of about 6 mm. The average strip multiplicity for the cosmic ray muon data is also found to be a little over 1. We studied the timing resolution of these large area RPCs. It was found to be less than 2 ns with reference to scintillator paddle based trigger signal. However, this value improves to better than 1.5 ns if computed relative to another RPC in the stack. We have recorded the RPC strip rate profiles and shown that the noise rates are very stable over long periods, implying the stability of operation of the RPCs under test. Their sensitivity to ambient parameters such as temperature, humidity and barometric pressure was well demonstrated. Apart from studying various characteristics and long term stability of the RPCs under test, the stack is also being used to study and optimise a number of parameters concerning the RPC gap, chamber design, gas mixture and readout electronics.

RPC fabrication involves deploying a large number of materials as well as many assembly procedures, which influence its characteristics and long-term performance.

The production of high performance and reliable chambers therefore involves choosing the right type and quality of materials as well as optimising various assembly and quality control procedures involved in the fabrication. These include materials such as glass used for electrodes, spacers, buttons and gas nozzles which are needed for assembling the chamber and individual gases used for operation of the chambers. Other materials and procedures crucial for RPC fabrication are resistive coat on the electrodes, epoxies used for gluing together different types of materials, pickup panels used for external signal pickup from the chambers and polyester films used for insulating the pickup panels from the resistive coated electrodes. We have studied a number of different types of these materials and optimised their quality, design or construction. We have also designed and developed a large number of assembly and quality control procedures and developed a number of jigs that are extremely useful in production of good quality detectors. Assembling and gluing of chambers and leak testing of the finished chambers are some of these important assembly procedures. A vacuum jig based on a simple but novel technique to maintain uniform pressure on the glass electrodes was designed and developed, resulting in the uniform spacing between them as well as reliable gluing of RPC gas gap. We have worked closely with various R&D institutions as well as many local industrial houses in developing these materials and designing and developing the assembly procedures.

Resistive coating of the outer surfaces of the electrodes plays a very crucial role in the operation of the RPC detector. After our initial R&D work in developing a suitable coat and its application method, we have collaborated with a local paint industry to develop a suitable paint as well as its application methods, which will be more adaptable for large scale production of the RPCs. We have also started designing paint automation techniques and developed prototype robotic machines for the purpose with help of local industry. We have also explored the alternate and cost effective technique of coating the glass surface using screen printing method. This method can also be used to coat the paint on a PET film which can then be stuck on the glass electrode surfaces.

The RPCs are extremely disproportionate and heavy detector modules and hence pose serious problems in terms of mechanical rigidity and difficulties in the packing, transportation and installation of the modules in the experiment. In addition, in spite of gluing the glass sheets together with a matrix of buttons throughout the area and

using spacers on the four edges, the chamber tends to bulge outwards when the gas is flown through the chamber. These considerations call for a suitable and light weight casing for the chamber. Plastic honeycomb panels laminated on one side by aluminum sheet and the other side by copper sheet were developed with help of an industry. Pickup strips of 30 mm width are realised by machining the copper sheet. The honeycomb panels were found to be an excellent solution to the problem of mechanical support to the RPC. They are lighter but still, offered better rigidity to the detector compared to aluminum. However, in the current design and quantity of utilisation of the panels, this solution turns out to be expensive. We are therefore working on cheaper variants of this design as well as on optimising their production process, in order to bring down their cost.

Proper and efficient functioning of the RPC detector demands pre-mixing or on-line mixing of individual gases in appropriate proportion, together with a controlled flow of mixed gases through the detector. The gas flow could be either in open loop mode or in closed loop mode. In the former, gas mixture leaving the detector is collected in a manifold and vented to atmosphere, whereas in the later, it is collected and re-circulated after appropriately purifying it and adding small fractions of fresh gases. We have designed and developed three generations of gas mixing, distribution and recycling systems. The first generation unit features a single output channel and employs rota-meters to mix the input gas in the required proportion. The mixed gas is stored in a reservoir cylinder and subsequently let flow through the output channel.

We had then designed and developed a more sophisticated PC based gas mixing and distribution system, which works on four different input gases and supplies the mixed gas through 16 output channels. It features Mass Flow Controllers to precisely mix the gases to required proportion and 0.3 mm diameter stainless steel capillaries to ensure uniform gas flow through output channels. We have also succeeded in precisely calibrating all the input gas channels over their entire dynamic range by water displacement and other methods. Units of this design were turned out to be workhorses not only for our RPC R&D programme, but for many laboratories in the country.

The gas volume of the ICAL detector is going to be more than  $200 \text{ m}^3$ . The open-loop systems described above therefore are not suitable to be adapted to this massive underground detector due to considerations such as high recurring costs, potential

environmental hazard and safety. Therefore, we have developed an appropriate technique and are currently building a system to recycle the gas mixture. The exhaust gas from the RPC is collected, individual gases separated using fractional condensation method and reused as source. The pilot unit of this design has been successfully tested and is currently being used.

Equipped with various sophisticated materials, processes and infrastructure that we had built over the past few years, we have finally aimed for the final frontier. It is proposed to use RPCs of about  $2\text{ m} \times 2\text{ m}$  in area for ICAL as active detector elements. We have fabricated a few of these chambers and evaluated their performance in detail. We had scaled up and fine tuned a number of parameters, tools and jigs concerning the gas gap assembly, electrode coating, signal pickup and RPC design, in order to fabricate detectors four times larger in area compared to those developed earlier. These detectors are operating flawlessly till now, essentially concluding the detector R&D phase of the ICAL detector construction.

## 6.2 Future outlook

As mentioned in Chapter 4, an ICAL prototype detector, of about  $1\text{ m}^3$  in active volume and which can house 12 layers of RPCs each of about  $100\text{ cm} \times 100\text{ cm}$  in area, was assembled. The magnet, which is required to generate about 1.3 T magnetic field has also been designed, fabricated, tested and installed in the detector. It will be interesting to study the performance of the RPCs in this detector under the influence of magnetic field. Degradation of RPC characteristics such as the spacial and time resolutions, if any may be studied.

As mentioned earlier, we have successfully built and characterised the RPCs that are comparable to the world's largest in area. However, we would now focus on simulating their detector physics, characteristics and problems. Though a lot of work in this direction is already done by other researchers in the field [153] [154] [34] [155], it is imperative that we develop our own understanding and experience in this field, since we plan to deploy these devices in huge number in the ICAL detector. Some of the aspects which will be of particular interest for us are optimisation of gas mixture and flow rate on the characteristics and long term performance of the RPCs. The character-

isation of RPC signal induction and transmission to the front-end electronics and their performance in terms of its various components such as electrodes, electrode coating and pickup panels needs to be explored further. These studies not only will improve our knowledge on the detector physics of these devices but also will result in smooth and cost effective running of ICAL detector.

The 12-layer RPC detector stack, which was described in Chapter 4 is currently tracking about half a million cosmic ray muons per day, collecting wealth of data. This data was analysed under the scope of this thesis, mainly to study and characterise the performance of RPCs and their readout electronics. Another important activity that is already in progress is to analyse the data to study the angular distribution of muons and to look for the east-west asymmetry at least to begin with. Even more ambitious problems could also be taken up using data from this modest detector, if these initial studies turn out to be encouraging.

Optimised front-end electronics plays a crucial role in the efficient deployment of as well as to preserve the novel characteristics of these detectors in the large scale experiments. We strongly believe that RPC characteristics such as its time resolution, cross-talk and stability of long-term operation could be improved substantially, if it is equipped with a superior front-end electronics. As part of the aggressive detector R&D programme, we have taken up design and fabrication of a multi-channel ASIC front-end chip, comprising of differential design, high-gain, high-speed preamplifier and comparator stages. The prototype production of this chip is in progress. A comprehensive programme is in full swing to design and develop front-end electronics, data acquisition, trigger, slow control and monitor systems needed for ICAL detector.

We described our work on design and development of gas systems, including the open-loop gas recovery and recycling system in Section 3.5. We have also started developing a prototype unit of a closed-loop system, in which the recovered gas from the RPCs is purified *on-line* before letting it into the input gas circuit. Mixed with a small fraction (5 to 10%) of fresh gas mixture, this recovered and purified gas is recycled. We are currently doing extensive studies and tests on this as well as the open-loop system, using a Residual Gas Analyser (RGA) setup, which we built in-house.

---

# Neutrino oscillations

Two neutrino mixing is analogous to the mixing of linearly polarized light propagating through an optically active medium [13]. Light propagation can be described in the basis of linearly polarized plane waves or, equally well, in a basis of circular polarization plane waves. Plane polarized light incident on such a medium can be resolved into left and right handed circularly polarized light which propagate with different velocities. Hence the plane polarized light evolves, as it propagates, to elliptically polarized light, circularly or even plane polarized in an orthogonal direction. Similarly, an electron neutrino could convert into a muon neutrino and back again to its original state as it propagates.

We will illustrate the phenomenon of neutrino oscillation between two neutrino flavours, say electron neutrino and muon neutrino [156]. The time evolution of a stationary state  $|\psi_k\rangle$  (in units such that  $\hbar = c = 1$ ) is given by:

$$|\psi_k(t)\rangle = |\psi_k\rangle \exp(-iE_k t), \quad (\text{A.1})$$

where  $E_k$  is the energy eigenvalue corresponding to  $|\psi_k\rangle$ . The stationary state vectors at different times differ only by an overall phase change. The time evolution of a non-stationary state  $|\psi\rangle$ , however is more complicated. For such a state, we can write at  $t = 0$ :

$$|\psi(0)\rangle = \sum_k a_k |\psi_k\rangle, \quad (\text{A.2})$$

where  $a_k$  are constants. Using Equation A.1 we can write:

$$|\psi(t)\rangle = \sum_k a_k |\psi_k\rangle \exp(-iE_k t). \quad (\text{A.3})$$

The assumption is that the flavour eigenstates - electron and muon neutrinos ( $\nu_e$  and  $\nu_\mu$ ), are not the mass eigenstates (i.e., the stationary states)  $m_1$  and  $m_2$ , but their superpositions:

$$|\nu_e\rangle = |\nu_1\rangle c + |\nu_2\rangle s; \quad (\text{A.4})$$

$$|\nu_\mu\rangle = -|\nu_1\rangle s + |\nu_2\rangle c, \quad (\text{A.5})$$

where  $c = \cos \theta$  and  $s = \sin \theta$ . In the case of two flavours, a single angle  $\theta$ , suffices to completely specify one basis in terms of the other.

We will now consider the state vector of a  $\nu_e$  produced at  $t = 0$ . Thus, initially:

$$|\psi(0)\rangle = |\nu_e\rangle = c|\psi_1\rangle + s|\psi_2\rangle. \quad (\text{A.6})$$

If the stationary states  $|\psi_1\rangle$  and  $|\psi_2\rangle$  correspond to energies  $E_1$  and  $E_2$ , respectively, then at a later time,  $t$  the state vector can be written down as:

$$|\psi(t)\rangle = c|\psi_1\rangle \exp(-iE_1 t) + s|\psi_2\rangle \exp(-iE_2 t). \quad (\text{A.7})$$

The probability,  $P(\nu_e, 0; \nu_\mu, t)$ , of the state  $|\psi(t)\rangle$  (originating as a  $\nu_e$  at  $t = 0$ ) appearing as a  $\nu_\mu$  is  $|\langle \nu_\mu | \psi(t) \rangle|^2$  and can be expressed as:

$$P(\nu_e, 0; \nu_\mu, t) = c^2 s^2 |-\exp(-iE_1 t) + \exp(-iE_2 t)|^2. \quad (\text{A.8})$$

To make the notation simple, we denote the probability  $P(\nu_e, 0; \nu_\mu, t) = P_{e\mu}$  and similarly for other flavours.

The neutrinos are expected to have small masses,  $m_i$ , and are in the ultra-relativistic regime ( $E_i \simeq p + m_i^2/(2p)$ ) where  $p$  ( $\gg m_i$ ) is the magnitude of the neutrino momentum. In this situation:

$$P_{e\mu} = 4c^2 s^2 \sin^2 \left( \frac{\delta_{21}}{4p} t \right) = \sin^2 2\theta \sin^2 \left( \frac{\pi x}{\lambda_{21}} \right), \quad (\text{A.9})$$

where  $\delta_{21} = (m_2^2 - m_1^2)$  is the *mass-squared difference* and

$$\lambda_{21} = 2.54m \left( \frac{E}{\text{MeV}} \right) \left( \frac{\text{eV}^2}{\delta_{21}} \right), \quad (\text{A.10})$$

is the so-called *oscillation length* expressed here in terms of the neutrino energy  $E \approx p$ . We use  $x$  and  $t$  interchangeably, since the neutrinos move with essentially the speed of light ( $c = 1$ ). On the right hand side of Equation A.9 the first factor is a consequence of the *mixing* while the second factor leads to the *oscillatory* behaviour.

From Equation A.9, we have

$$P_{ee} = 1 - P_{e\mu} = 1 - \sin^2 2\theta \sin^2 \left( \frac{\pi x}{\lambda_{21}} \right). \quad (\text{A.11})$$

It is seen from the above that  $P_{ee}$  can be less than or equal to unity. The essential ingredients for this are twofold:

1. The neutrinos must be massive and *non-degenerate*.
2. The mass eigenstates of the neutrinos -  $\nu_1, \nu_2$  - must be different from the flavour eigenstates -  $\nu_e, \nu_\mu$ .

Of the variants of this basic theme of neutrino flavour change, the most prominent is the Mikheyev-Smirnov-Wolfenstein (MSW) [157] matter induced resonant effect. It is based on the concept that interactions affect the inertia or mass of a particle. The MSW effect (*matter effect*) is particularly important for solar neutrinos during their passage through the sun.

For case of three neutrino flavours there are seven independent parameters *viz.* the three mass parameters, three mixing angles  $\theta_{12}, \theta_{13}$  and  $\theta_{23}$  as well as a CP phase. A large mixing angle implies a large mixing between the eigenstates. The mass parameters are represented as mass-squared differences  $\delta_{ij}^2$ , which are defined as  $m_i^2 - m_j^2$ .



---

# Technical information

## B.1 Gases used in ICAL detector

Table B.1: Important properties of gases used in ICAL detector. Note<sup>1</sup>: Triple point: -49.4°C at 2.2 bar, Sub. point: -63.9°C.

| Property        | Unit               | R134a  | Isobutane  | Argon   | SF <sub>6</sub>                                       |
|-----------------|--------------------|--|--|---|---|
| Mol. weight     |                    | 102.3  | 58.12  | 39.948  | 146.05  |
| Structure       |                    | Ring   | Ring   |   | Ring  |
| Gas density     | kg/m <sup>3</sup>  | 4.25   | 2.82   | 1.78  | 6.27  |
| Liquid density  | kg/m <sup>3</sup>  | 1206   | 593  |   | 1880  |
| Viscosity       | cP                 | 0.012  | 0.006  | 0.02  | 0.015   |
| Boiling point   | °C/bar             | -26.3  | -11.7  | -185.8  | Note <sup>1</sup>                                     |
| Heat of vapour. | kJ/mol             | 22.021   | 23.300   | 6.43  | 23.681  |
| Critical temp.  | °C                 | 101.1  | 134.9  | -122.13   | 45.5  |
| Critical pres.  | bar                | 40.6   | 36.84  | 48.98   | 37.59   |
| GWP             | CO <sub>2</sub> =1 | 4200   |  |   | 22,400  |
| Purity level    | %                  | 99   | 99.9   | 99.999  | 99.9  |
| Impurities      |                    | O <sub>2</sub> , H <sub>2</sub> O,<br>N <sub>2</sub> , CF <sub>4</sub> | CH <sub>4</sub> , H <sub>2</sub> ,<br>H <sub>2</sub> O, N <sub>2</sub> | N <sub>2</sub> , O <sub>2</sub> ,<br>H <sub>2</sub> O, HC | H <sub>2</sub> O, O <sub>2</sub> ,<br>CF <sub>4</sub> |

## B.2 Paint used in spray painting technique

Table B.2: Specifications of the paint used for spray painting of glass electrodes.

| S.No. | Test                           | Specifications            | Result         |
|-------|--------------------------------|---------------------------|----------------|
| A.    | <i>Liquid paint properties</i> |                           |                |
| 1.    | Supply viscosity               | 35±5 s at 30°C            | 32 s           |
| 2.    | Weight/10 l                    | 9.5±3% kg                 | 9.45 kg        |
| 3.    | Percentage of solids           | 28±3% at 105°C for 3 h    | 27.5%          |
| 4.    | Percentage of thinner          | 100±20% by volume         | 100% by volume |
| 5.    | Hegman gauge                   | ≤35 µm                    | 30µm           |
| 6.    | Recommended thinner            | 1000053                   | Satisfactory   |
| 7.    | Colour/shade                   | Black                     | Black          |
| 8.    | Drying characteristics         | Surface dry: 10 min       | Satisfactory   |
|       |                                | Tack free: 30 min         | Satisfactory   |
|       |                                | Hard dry: 18 min          | Satisfactory   |
| 9.    | Application viscosity          | 16±2 s at 30°C            | 15 s           |
| B.    | <i>Dry film properties</i>     |                           |                |
| 10.   | Finish                         | Smooth & Matt             | Satisfactory   |
| 11.   | Adhesion on glass              | 2 × 2 × 10 mm             | Passes 0/100   |
| 12.   | Dry film resistivity           | 1500±500 kΩ at 2.5" apart | 1350-1500 kΩ   |
| 13.   | Recommended DFT                | 16 ±2 µm                  | 15 µm          |

## B.3 GE LEXAN polycarbonate material

Table B.3: Technical specifications of the GE made LEXAN polycarbonate material.

| Property          | Units     | Test ref. | Min. spec. | Max. spec. | Lot avg. |
|-------------------|-----------|-----------|------------|------------|----------|
| Flexural modulus  | MPa       | ISO-178   | 2000       | 3500       | 2922     |
| MVI 300°C/1.2 kg  | cc/10 min | ISO-1133  | 5          | 8          | 6        |
| Flexural strength | MPa       | ISO-178   | 70         | 90         | 85       |

## B.4 Garware EMCL insulating film

Table B.4: Technical specifications of the Garware made EMCL grade insulating film.

| S.No. | Property           | Unit                    | Target  | Min. | Max.  | Test method  |
|-------|--------------------|-------------------------|---------|------|-------|--------------|
| 1.    | Thickness          | $\mu\text{m}$           | 100.0   | 98.0 | 102.0 | ASTM E 252   |
| 2.    | Yield              | $\text{m}^2/\text{kg}$  | 7.1     | 7.0  | 7.3   | Weight basis |
| 3.    | Tensile strength   | $\text{kg}/\text{cm}^2$ |         |      |       | ASTM D 882   |
|       | MD                 |                         | 2000    | 1800 | 2200  |              |
|       | TD                 |                         | 2000    | 1800 | 2200  |              |
| 4.    | Elongation         | %                       |         |      |       | ASTM D 882   |
|       | MD                 |                         | 135     | 100  | 170   |              |
|       | TD                 |                         | 120     | 90   | 150   |              |
| 5.    | Shrinkage @150°C   | %                       |         |      |       | ASTM D 1204  |
|       | MD                 |                         | 1.1     | 0.8  | 1.4   |              |
|       | TD                 |                         | 0.4     | 0.2  | 0.6   |              |
| 6.    | Shrinkage @190°C   | %                       |         |      |       | ASTM D 1204  |
|       | MD                 |                         | 2.0     | 1.6  | 2.4   |              |
|       | TD                 |                         | 1.0     | 0.6  | 1.4   |              |
| 7.    | Haze               | %                       | 2.0     | 1.5  | 2.5   | ASTM D 1003  |
| 8.    | Coeff. of friction |                         | 0.45    | 0.30 | 0.60  | ASTM D 1894  |
| 9.    | Standard length    | m                       | 1500    |      |       |              |
| 10.   | Width tolerance    | mm                      | $\pm 2$ |      |       |              |

## B.5 Data format of the on-line DAQ software

Table B.5: Event data format. Packet size: 167 words.

| <b>Index</b> | <b>Data description</b>   |
|--------------|---|
| 01           | 0xAAAA  |
| 02           | 0x5555  |
| 03           | Year  |
| 04           | Run number  |
| 05-06        | 32-bit event counter  |
| 05           | Event number-1 (Lower word)   |
| 06           | Event number-2 (Higher word)  |
| 07-11        | PC time (Binary), RTC time (BCD)  |
| 07           | RT-1 [N.A] [ $\mu$ s - 3,2,1]   |
| 08           | RT-2 [0.1s] [ms - 3,2,1]  |
| 09           | RT-3 [M2M1S2S1] [M2M1S2S1]  |
| 10           | RT-4 [D2D1H2H1] [D2D1H2H1]  |
| 11           | RT-5 [Y2Y1m2m1] [xxxxD4D3]  |
| 12           | Data size (155 from here on)  |
| 13-14        | Two word Event Counter -  |
|              | Master trigger scaler counter (Hardware)  |
| 15-16        | Two word Event Counter -  |
|              | Scintillator trigger counter (Hardware)   |
| 17-28        | 6 Spare scalers data (two words/channel)  |
| 29-44        | TDC-1 to TDC-14, Cal 1, Cal 2 (X-plane)   |
| 45-60        | TDC-1 to TDC-14, Cal 1, Cal 2 (Y-plane)   |
| 61-108       | Latch information from 16 front-end boards of X-plane<br>1st word:  6 bits board Id 6 bits mon counter 1F 2F 3F 4F <br>(Board Id : MSB=0 → X-plane, MSB=1 → Y-plane)<br>2nd word: 32 to 17 RPC latch information<br>3rd word: 16 to 1 RPC latch information |
| 109-156      | Latch information from 16 front end boards of Y-plane<br>Same as in X-Plane   |
| 157-167      | 11 words of information from final trigger module   |

Table B.6: Monitor data format. Packet size: 52 words.

| Index | Data description   |
|-------|--|
| 01    | 0x5555   |
| 02    | 0xAAAA   |
| 03    | Run number   |
| 04    | Year   |
| 05    | Monitor Record number  |
| 06-10 | PC time (Binary) RTC time (BCD)  |
| 06    | RT-1 [N.A] [ $\mu$ s - 3,2,1]  |
| 07    | RT-2 [0.1s] [ms - 3,2,1]   |
| 08    | RT-3 [M2M1S2S1] [M2M1S2S1]   |
| 09    | RT-4 [D2D1H2H1] [D2D1H2H1]   |
| 10    | RT-5 [Y2Y1m2m1] [xxxxD4D3]   |
| 11    | Monitor time duration (in 1/10th of s)   |
| 12    | Data size (40 from here on)  |
| 13-20 | Final trigger module scaler data<br>F1X to F4X and F1Y to F4Y  |
| 21-36 | X-plane monitor data:<br>Board code and Channel code<br>(Higher byte: Board Id = 0 to 15,<br>MSB=0 → X-plane, MSB=1 → Y-plane)<br>(Lower byte: Channel number 0 to 39) |
| 21    | Board code and Channel code<br>(Higher byte: Board Id = 0 to 15,<br>MSB=0 → X-plane, MSB=1 → Y-plane)<br>(Lower byte: Channel number 0 to 39)                          |
| 22    | Monitor scaler data  |
| 23-36 | Sr.No. 21 & 22 repeated 7 times  |
| 37-52 | Y-plane monitor data:<br>Board code and Channel code<br>(Higher byte: Board Id = 0 to 15,<br>MSB=0 → X-plane, MSB=1 → Y-plane)<br>(Lower byte: Channel number 0 to 39) |
| 37    | Board code and Channel code<br>(Higher byte: Board Id = 0 to 15,<br>MSB=0 → X-plane, MSB=1 → Y-plane)<br>(Lower byte: Channel number 0 to 39)                          |
| 38    | Monitor scaler data  |
| 39-52 | Sr.No. 37 & 38 repeated 7 times  |



---

# Publications and proceedings

## C.1 Publications and communications

1. Cosmic Ray test of INO RPC stack, Manuscript in preparation for NIMA
2. Development of 2 m×2 m size Glass RPCs for INO, Manuscript in preparation for NIMA
3. VME based DAQ system for INO RPC stack, Manuscript in preparation for NIMA
4. Performance of the Prototype Gas Recirculation System with built-in RGA for INO RPC system, Manuscript in preparation for NIMA
5. Beta measurement of cosmic muons using INO RPC detector stack, Manuscript in preparation for NIMA
6. INO prototype detector and data acquisition system, NIMA **602**, (2009), 784-787
7. Development of glass Resistive Plate Chambers for INO experiment, NIMA **602**, (2009), 744-748
8. Development of conductive coated polyester film as RPC electrodes using screen printing, NIMA **602**, (2009), 835-838
9. On-line gas mixing and multi-channel distribution system, NIMA **602**, (2009), 845-849
10. RPC exhaust gas recovery by open loop method, NIMA **602**, (2009), 809-813

11. Preliminary results from INO detector R&D programme, *Pramana* **69**, (2007), 1015-1023
12. On aging problem of glass Resistive Plate Chambers, *Nucl. Phys.* **B158**, (2006), 195-198

## C.2 Proceedings

1. INO Update, 5th Plenary Meeting of the International Design Study for the Neutrino Factory (IDS-NF5), April 8-10, 2010, Fermilab, USA
2. Design of a Frontend *Anusparsh* ASIC for Glass Resistive Plate Chamber for INO's ICAL Experiment, DAE-BRNS Natl. Symp. on Nucl. Inst. (NSNI-2010), BARC, Mumbai, February 24-26, 2010
3. Glass RPC Detector R&D for a Mega Neutrino Detector, IEEE Nucl. Sci. Symp. and Medical Imaging Conf., Florida, USA, October 2009
4. Detector and electronics R&D for the INO's ICAL detector, Intl. School on High Energy Astrophysics, Kodaikanal, December 1-11, 2009
5. Development of prototype RPC and LVDS/NIM-ECL translator for the INO-DAQ system, DAE Symposium in High Energy Physics, BHU, Varanasi, December 14-18, 2008
6. Development of Glass Resistive Plate Chambers for INO, Intl. Conf. on High Energy Phys., Univ. of Pennsylvania, USA, July 2008, arXiv:**0810:4693**
7. Development and characterisation of large area glass Resistive Plate Chambers for the ICAL detector at INO, Nuclear Physics Symposium, Sambalpur University, Sambalpur, December 11-15, 2007
8. Electronics and data acquisition system for prototype INO-ICAL detector, Nuclear Physics Symposium, Sambalpur University, Sambalpur, December 11-15, 2007
9. The INO project, JIGSAW-2007, TIFR, Mumbai, February 12-23, 2007

10. Development of Resistive Plate Chambers for the INO detector, JIGSAW-2007, TIFR, Mumbai, February 12-23, 2007
11. Experiences of using float glass as electrodes for radiation detectors, JIGSAW-2007, TIFR, Mumbai, February 12-23, 2007,
12. On aging problem of glass Resistive Plate Chambers, JIGSAW-2007, TIFR, Mumbai, February 12-23, 2007
13. Status of INO RPC R&D activities, JIGSAW-2007, TIFR, Mumbai, February 12-23, 2007
14. Introduction to Resistive Plate Chambers, Perspectives of Neutrino Physics and India-based Neutrino Observatory, Sambalpur University, Sambalpur, February 17-18, 2007
15. Electronics and data acquisition systems for RPC detectors, Perspectives of Neutrino Physics and India-based Neutrino Observatory, Sambalpur University, Sambalpur, February 17-18, 2007
16. Design and development of a family of ultra fast amplifier Hybrid Micro Circuits for INO experiments, Nuclear Physics Symposium, University of Baroda, Vadodara, December 11-15, 2006
17. Scintillator paddles as trigger detectors for RPCs, Nuclear Physics Symposium, University of Baroda, Vadodara, December 11-15, 2006
18. Integration and commissioning of data acquisition system for the INO prototype detector, DAE Symposium in High Energy Physics, IIT Kharagpur, December 11-15, 2006
19. Results from long term stability tests of Resistive Plate Chambers, DAE Symposium in High Energy Physics, IIT Kharagpur, December 11-15, 2006
20. Glass characterisation techniques used in the Resistive Plate Chamber development, DAE Symposium in High Energy Physics, IIT Kharagpur, December 11-15, 2006

21. Experience of using float glass for electrodes in radiation detectors, NSGC-06, BARC, Mumbai, September 15-16, 2006
22. Development of Resistive Plate Chambers for the INO detector, 50th DAE-BRNS Symposium on Nuclear Physics, BARC, Mumbai, December 12-16, 2005
23. Design of electronics, trigger and data acquisition system for the proposed INO prototype detector, DAE Symposium on High Energy Physics, SINP, Kolkata, December 2004
24. Results from development of glass RPCs for INO detector, DAE Symposium on High Energy Physics, SINP, Kolkata, December 2004

### C.3 Technical notes

1. Report on proposed INO ICAL electronics, April 2009
2. A short report on the performance of BARC HMCs for INO detectors, March 2008
3. How-to-BigStack, User manual for *BigStack* analysis package, 2007
4. How-to-ProcessTraces, User manual for *ProcessTraces* analysis script, 2007
5. Calibration procedure and test results of *NINO* amplifier, July 2007
6. On data format of *InoDaq* and *rpcanal* packages, 2006
7. Quality control procedures for RPC production, 2006
8. Glass surface quality and element analysis, September 2006

# Bibliography

- [1] David Caldwell (Ed.), Current Aspects of Neutrino Physics, Springer, (2001)
- [2] C.D.Ellis and W.A.Wooster, Proc. R.Soc. (Lond.) A **117**, (1927), 109; L.Meitner and W.Orthmann, Z. Phys. **60**, (1930), 143
- [3] N.Bohr, J. Chem. Soc. **135**, (1932), 349
- [4] Letter to the participants of workshop at Tübingen, Germany, (1930)
- [5] H.A.Bethe and R.E.Peierls, Nature **133**, (1934), 532
- [6] Frederick Reines and Clyde L. Cowan, Jr., Nature **178**, (1956), 446
- [7] G.Danby *et al.*, Phys. Rev. Lett. **9**, (1962), 36
- [8] K.Kodama *et al.*, Phys. Lett. **B504**, (2001), 218
- [9] C.Athanassopoulos *et al.*, Phys. Rev. Lett. **81**, (1998) 1774; Phys. Rev. **C58**, (1998) 2489.
- [10] P.W.Higgs, Phys. Rev. Lett. **12**, (1964), 132
- [11] G.Rajasekaran, Pramana **55**, (2000), 19
- [12] A.Raychaudhuri, Proc. Ind. Natl. Sci. Acad. **70A**, (2004), 179
- [13] G.Rajasekaran, Resonance, **10**, (2005), 49
- [14] <http://en.wikipedia.org/wiki/Neutrino>
- [15] V.M.Lobashev *et al.*, Nucl. Phys. **A 719**, (2004), 153
- [16] C.L. Bennett *et al.*, Astrophys. J. **583** (2003) 1
- [17] C.V.Achar *et al.*, Physics Letters **18**, (1965), 196
- [18] INO Collaboration, Detailed Project Report **I**, (2007)

- [19] INO Collaboration, INO Project Report **INO/2006/01**, (2006) and references therein; V.M.Datar, Proc. Nucl. Phys. Symposium, Vadodara, (2006); India-based Neutrino Observatory (INO) web pages: <http://www.ino.tifr.res.in> and <http://www.imsc.res.in/> ino
- [20] H.Murayama and T.Yanagida Phys. Lett. **B520**, (2001), 263
- [21] R.P.Kokoulin and A.A.Petrukhin, Sov. J. Part. Nucl. **21**, (1990), 332
- [22] INO Collaboration, Detailed Project Report on INO-ICAL Detector Structure **II**, (2008)
- [23] Magnet6.0 Code, Infolytica Corporation, USA
- [24] G.Charpak *et al.*, NIM **62**, (1968), 217
- [25] J.Keuffel, Phys. Rev. **73** (1948), 531
- [26] V.Parchomchuk *et al.*, NIM **93**, (1971), 269
- [27] Y.Pestov, NIM **196**, (1982), 45
- [28] Y.Pestov, Proc. Intl. Winter Meeting on Nucl. Phys., Bormio, Italy, (1998)
- [29] Y.Ivaniouchenkov *et al.*, NIMA **422**, (1999), 300
- [30] A.Arefiev *et al.*, NIMA **348**, (1994), 318
- [31] R.Santonico and R.Cardarelli, NIM **187**, (1981), 377
- [32] R.Cardarelli *et al.*, NIMA **263**, (1988), 20
- [33] E.C.Zeballos *et al.*, NIMA **396**, (1997), 93
- [34] Christian Lippmann, Ph.D. Thesis, (2003)
- [35] P.Fonte, NIMA **456**, (2000), 6
- [36] W.R.Leo, Techniques for Nuclear and Particle Physics Experiments, 2nd Ed., Narosa Publ. House, (1995)
- [37] V.Ammosov *et al.*, arXiv:hep-ex/0204026, (2002)
- [38] G.L.Bruno, Ph.D. Thesis, (2000-2001)
- [39] R.Cardarelli *et al.*, NIMA **333**, (1993), 399
- [40] R.Cardarelli *et al.*, NIMA **382**, (1996), 470
- [41] P.Fonte, IEEE Trans. on Nucl. Sci. **49** (2002), 881

- [42] K.Abe *et al.*, *Scientifica Acta* **13**, (1998), 281
- [43] CMS Collaboration, *CERN/LHCC* **97-32**, (1997)
- [44] E.C.Zeballos *et al.*, *NIMA* **392**, (1997), 150
- [45] G.Charpak and F.Sauli, *Phys. Lett.* **B78**, (1978), 523
- [46] P.Fonte *et al.*, *NIMA* **449**, (2000), 295
- [47] E.C.Zeballos *et al.*, *NIMA* **374**, (1996), 132
- [48] V.Peskov and P. Fonte, Proc. Intl. Conf. on Position-Sensitive Detectors, London, England, (1999)
- [49] L3 Collaboration, *NIMA* **456**, (2000), 113
- [50] BaBar Collaboration, *NIMA* **479**, (2002), 1
- [51] M.Yamaga *et al.*, *NIMA* **456**, (2000), 109
- [52] YBJ-ARGO Collaboration, *NIMA* **562**, (2006), 92; *ibid.*, **588**, (2008), 7
- [53] OPERA Collaboration, OPERA Proposal **CERN/SPSC 2000-028**, (2008); *NIMA* **602**, (2009), 631
- [54] Yuguang Xie *et al.*, *NIMA* **599**, (2009), 20
- [55] Jiawen Zhang *et al.*, *NIMA* **540**, (2005), 102
- [56] ALICE Collaboration, *NIMA* **604**, (2009), 301
- [57] A.Antonelli *et al.*, *NIMA* **337**, (1993), 34
- [58] E.Gorini, *NIMB* **23A**, (1991), 249
- [59] G.Bressi, *NIMA* **261**, (1987), 449
- [60] M.Ambrosio, *Scientifica Acta* **13**, (1998), 245
- [61] T&T Collaboration, *NIMA* **344**, (1994), 350
- [62] G.Agnetto *et al.*, *NIMA* **359**, (1995), 596
- [63] AUGER Collaboration, Proc. Workshop on RPCs and Related Detectors, Pavia, (1995)
- [64] C.Aramo, *Scientifica Acta* **13**, (1998), 257
- [65] ATLAS Muon collaboration, *CERN/LHCC* **97-22**, (1997)

- [66] ATLAS Collaboration, JINST **S08003**, (2008)
- [67] A.Aloisio *et al.*, NIMA **535**, (2004), 265
- [68] CMS Muon collaboration, CERN/LHCC **97-32**, (1997)
- [69] CMS Collaboration, JINST **S08004**, (2008)
- [70] LHCb Collaboration, **CERN-LHCC-2001-010**, (2001)
- [71] A.Bizzeti *et al.*, LHCb Note, LHCb-2001/027, (2001)
- [72] ALICE collaboration, **CERN/LHCC 2000-012**, (2000)
- [73] A.N.Akindinov *et al.*, NIMA **533**, (2004), 74
- [74] M.Bogomilov *et al.*, Proc. Workshop on RPCs and Related Detectors, Coimbra, Portugal, (2001)
- [75] M.Bogomilov *et al.*, NIMA **508**, (2003), 152
- [76] STAR TOF Collaboration, (2004)
- [77] B.Bonner *et al.*, NIMA **508**, (2003), 181
- [78] Byungsik Hong, NIMA **602**, (2009), 644
- [79] Diego González Díaz, Ph.D. Thesis, (2006)
- [80] D.Belver *et al.*, NIMA **602**, (2009), 687
- [81] A.Schütttauf *et al.*, NIMA **602**, (2009), 679
- [82] Jingbo Wang *et al.*, Proc. Workshop on RPCs and Related Detectors, GSI, Germany, (2010)
- [83] Daniel Bemmerer *et al.*, Proc. Workshop on RPCs and Related Detectors, GSI, Germany, (2010)
- [84] M/s Asahi Float Glass (India) Ltd., Mumbai, India
- [85] Developed by M/s General Electric Plastics in 1966 and now owned by M/s Saudi Basic Industries Corp.
- [86] A.Abashian *et al.*, NIMA **479**, (2002), 117
- [87] Manufactured by M/s Riken-Keiki, Japan
- [88] Supplied by M/s Nikunj Eximp Enterprises (Private) Ltd., Mumbai, India and M/s Steel Plant Specialities, Mumbai, India

- [89] Manufactured by The Dow Chemical Company, USA
- [90] Supplied by M/s Praxair India (Private) Ltd., Mumbai, India
- [91] M/s Alpha Pneumatics, Mumbai, India
- [92] M/s Saint-Gobain Performance Plastics, France
- [93] Manufactured by M/s 80/20 Inc., USA
- [94] Physics Analysis Workstation, <http://wwwasd.web.cern.ch/wwwasd/paw/>
- [95] An Object-Oriented Analysis Framework, <http://root.cern.ch/root/>
- [96] Daniel Marlow, Rice University Seminar, July 9, (1999)
- [97] Sarika Bhide *et al.*, *Pramana* **69**, (2007), 1015
- [98] Sarika Bhide *et al.*, *Nucl. Phys. B* **158**, (2006), 195
- [99] M.Ambrosio *et al.* *IEEE Trans. Nucl. Science*, **50**, (2003), 820
- [100] H.Sakai *et al.*, *NIMA* **484**, (2002), 153
- [101] T.Kubo *et al.*, arXiv:hep-ex/0211020 v1, (2002)
- [102] Manufactured by M/s Hemaki Lab-Services (Private) Ltd., Mumbai, India
- [103] S.D.Kalmani *et al.*, *NIMA* **602**, (2009), 845
- [104] A.Candela *et al.*, *NIMA* **533**, (2004), 116
- [105] Manufactured by M/s Tylan Corp., Torrance, CA, USA
- [106] <http://www.qualiflow.com/support/mfc-principles.pdf>
- [107] Manufactured by M/s Shaw Moisture Meters, England, United Kingdom
- [108] M.Ahart *et al.*, *KEK Belle Note* **135**, (1996)
- [109] [http://en.wikipedia.org/wiki/Hagen-Poiseuille\\_equation](http://en.wikipedia.org/wiki/Hagen-Poiseuille_equation)
- [110] Manufactured by M/s Parker Hannifin Corp., Cleaveland, USA
- [111] Manufactured by M/s Dow Corning, Valencia, CA, USA
- [112] M.Bosteels *et al.*, CMS Note 1999/018, (1999); L.Basset *et al.*, CMS Note 2000/040, (2000); I. Crotty *et al.*, CMS Note 2001/019, (2001)
- [113] Avinash Joshi *et al.*, *NIMA* **602**, (2009), 809

- [114] Avinash Joshi, Proc. Workshop on RPCs and Related Detectors, GSI, Germany, (2010)
- [115] Manufactured by M/s Danfoss A/S, Denmark
- [116] Sarika Bhide *et al.*, Proc. Natl. Symp. on Science & Technology of Glass/Glass-Ceramics (NSGC-06), Mumbai, INDIA, (2006)
- [117] W.Riegler, NIMA **491**, (2002), 258
- [118] G.Aielli *et al.*, NIMA **515**, (2003), 335
- [119] Y.Hoshi *et al*, Proc. Workshop on RPCs and Related Detectors, Coimbra, (2001)
- [120] G.C.Trincherio *et al.*, NIMA **508**, (2003), 102
- [121] S.Park *et al.*, NIMA **550**, (2005), 555
- [122] G.Bencivenni *et al.*, NIMA **332**, (1993), 368; NIMA **345**, (1994), 456
- [123] C.Gustavino *et al.*, INFN Technical note, INFN/TC-99/14, (1999)
- [124] A.Abashian *et al.*, NIMA **449**, (2000), 112
- [125] M/s Kansai-Nerolac, Mumbai, India, <http://www.nerolac.com>
- [126] M/s Pankaj Enterprises, Navi Mumbai, India
- [127] S.D.Kalmani *et al.*, NIMA **602**, (2009), 835
- [128] M/s Grafica Flextronica, Mumbai, India, <http://www.graficaindia.com>
- [129] Manufactured by M/s Dozentech, Korea
- [130] M/S Oswin Plastics Pvt. Ltd., Mumbai, India
- [131] Satyanarayana Bheesette, Proc. 34th Intl. Conf. on High Energy Phys., Philadelphia USA, arXiv:**0810:4693**, (2008)
- [132] Carlo Gustavino, Laboratori Nazionali del Gran Sasso, Italy, Private communication, (2006)
- [133] Manufactured by M/s DuPont Teijin Films, USA
- [134] Manufactured by M/s Garware Polyester Ltd., Mumbai, India
- [135] Standard test method for dielectric breakdown voltage and dielectric strength of solid electrical insulating materials at commercial power frequencies, ASTM standard, D149-97a

- [136] M/s Multivac (India) Pvt. Ltd., Gurgaon, India
- [137] M/s Honeycomb (India) Pvt. Ltd., Bengaluru, India
- [138] C.C.Bueno *et al.*, Proc. Intl. Nucl. Atlantic Conf., Brazil, (2007)
- [139] K.Abe *et al.*, NIMA **455** (2000), 397
- [140] P.Camarri *et al.*, NIMA **414**, (1998), 317
- [141] G.Aielli *et al.*, NIMA **493**, (2002), 137
- [142] A.Mengucci *et al.*, NIMA **583**, (2007), 264
- [143] V.M.Datar *et al.*, NIMA **602**, (2009), 744
- [144] M.S.Bhatia *et al.*, Internal note
- [145] Anita Behere *et al.*, NIMA **602**, (2009), 784
- [146] M/s CAEN S.p.A, Viareggio, Italy
- [147] <https://midas.psi.ch/elog/>
- [148] RH-02 Temperature and Humidity Data Logger, M/s Pico Technology, <http://www.picotech.com/humidity.html>
- [149] Qt Development Frameworks (Nokia Corporation), <http://qt.nokia.com/>
- [150] G.Aielli *et al.*, NIMA **456**, (2000), 40
- [151] M.Ćwiok *et al.*, NIMA **508**, (2003), 38
- [152] P.Camarri, University of Roma Tor Vergata and INFN, Italy, Private communication, (2005)
- [153] W.Riegler, LHCb Muon 2000-112, (2000)
- [154] W.Riegler *et al.*, NIMA **500**, (2003), 144
- [155] M.Abbrescia et al, NIMA **409**, (1998), 1
- [156] A.Raychaudhuri, Proc. DAE Symp. on Nucl. Phys., Varanasi, (2004)
- [157] M.Mikheyev and A.Simrnov, Sov. J. Nucl. Phys. **42**, (1986), 913; L.Wolfenstein, Phys. Rev. **D17**, (1978) 2369; *ibid.* **D20**, (1979), 2634

# Acknowledgements

I wish to place on record my deep sense of gratitude to my internal guide Prof. Raghava Varma for his initiative, encouragement and determination to help me. Had I not met him, my dream of doing a Ph.D. would have possibly remained just one. My external guide Prof. Naba Mondal is a lot more than just that to me. We worked together building several front-ranking high energy physics experiments for over 26 years. He continues to lead mega experimental science projects with deep commitment and involvement, inspiring a lot of us.

I am thankful to my Research Progress Committee (RPC!) members Prof. Uma Sankar and Prof. Basant Kumar Nandi for their help and guidance. Thanks are also due to the faculty of my graduate courses, my thesis referees and examiners.

I am grateful to the Tata Institute of Fundamental Research, Mumbai and the Indian Institute of Technology Bombay, for providing me with all the facilities required for carrying out this research work. I am grateful to Prof. Mustansir Barma, Director, Prof. S.Ramakrishnan, former Dean and Prof. E.V.Sampathkumaran, Dean, Natural Sciences Faculty, TIFR in particular for their constant support.

In a way, this work has resulted from an ongoing large collaborative effort to build a massive neutrino experiment in the country. I wish to acknowledge many crucial contributions made by my colleagues, in particular the detector and electronics R&D team members - Suresh Kalmani, Nagaraj Panyam, Venkatesam Reddy, Piyush Verma, Mandar Saraf, Ravindra Shinde, Sarika Bhide, G.K.Padmashree, Manas Bhuyan, Shekhar Lahamge, Sonal Dhuldhaj, Asmita Redij, Noopur Srivastava, Deepak Samuel, S.R.Joshi, Santosh Chavan, Vishal Asgolkar, Ganesh Ghodke, Darshana Koli, Suresh Upadhyaya, Shobha Rao, B.K.Nagesh, Vidhya Lotankar, Gobinda Majumder, Vivek Datar, M.S. Bhatia, Vinay Chandratre, Menka Tewani, Anita Behere, S.M.Raut, R.Sashtrakar and P.K.Mukhopadhyay. I thank other members of the INO collaboration, including G. Rajasekaran, M.V.N.Murthy, D.Indumathi, Sudeb Bhattacharya, Y.P.Viyogi, Amol Dighe and J.B.Singh for their encouragement and many useful discussions.

Thanks are due to many colleagues from the Department of Condensed Matter Physics & Materials Science as well as from the Department of Chemical Sciences, who have helped me with various characterisation studies on glass samples. I also wish to acknowledge many useful discussions with Shri Avinash Joshi (M/s Alpha Pneumatics, Mumbai) on gas systems.

I had taught, trained and guided dozens of INO and TIFR graduate students, undergraduate and summer students as well as faculty members and engineers during the past several years in our RPC detector R&D laboratories. I thank them all, as my interactions with them have actually enriched my own understanding of the subject of

this thesis. Special mention is due to Satyajit Jena, Sumanta Pal and Salim Mohammed.

Since I began to work on the development of Resistive Plate Chambers, I had opportunities to interact with many experts in the field. I wish to particularly thank Prof. Rinaldo Santanico, Prof. Kazuo Abe, Prof. Carlo Gustavino, Dr. Ian Crotty, Dr. Christian Lippmann, Dr. Adam Para, Dr. Valery Makeev, Dr. M.C.S.Williams, Dr. Archana Sharma, Dr. Werner Riegler, Dr. P.Camarri and Prof. Jianxin Cai. I have learnt invaluable tips and traps of the *trade* from them.

It all began for me in Kolar Gold Fields. What can be a better start for an electronics engineer right out of a college, than building a series of experiments deploying state-of-the-art technologies to do cutting-edge physics? And my first teachers were then our collaborators from Osaka City University, Japan - Prof. Yoshio Hayashi and Prof. Saburo Kawakami. It was indeed this training that I received from these amazingly versatile experimentalists, which has molded me into what I am even today.

I would like to sincerely thank my department colleagues Profs. Sunil Gupta, Tariq Aziz, B.S.Acharya, Shashi Dugad, Sudeshna Banerjee, Atul Gurtu, K.Sudhakar and Kajari Mazumdar as well as Mandakini Patil, S.R.Chendvankar and P.K.Mohanty for their affection and encouragement.

Many of my colleagues and friends selflessly wished for a long time that I pursue my Ph.D. and they had also kept track of my progress or often lack of it, more accurately than myself. I am grateful indeed to Profs. Deepak Mathur, Mayank Vahia, Sugata Sanyal, Arun Grover and Ms. Punita Punia. I know they will feel very happy as I am reaching this milestone. I am indebted to them all for celebrating my achievements.

I am proud of my joint family, my small village, my childhood friends, my schools and colleges, my teachers and my classmates. I am indeed very fortunate to have received love and affection all throughout my childhood, school and college days from everyone I met.

Last, but most importantly I owe most of my accomplishments - including this one, to my wife Lakshmi and to our kids Srinidhi and Sindhuja. Due to my self-imposed working style and hours, most often, I could not honour even the minimum family commitments and end up being a guilty witness to their endless patience and silent sacrifices.

**Satyanarayana Bheesette**

Dated: 16th December 2009